Towards increased understanding of low-power induction and synchronous reluctance machines

Citation for published version (APA):
Sprangers, R. L. J. (2015). *Towards increased understanding of low-power induction and synchronous reluctance machines: harmonic modeling of complex electromagnetic phenomena*. [Phd Thesis 1 (Research TU/e / Graduation TU/e), Electrical Engineering]. Technische Universiteit Eindhoven.

Document status and date:
Published: 01/01/2015

Document Version:
Publisher’s PDF, also known as Version of Record (includes final page, issue and volume numbers)

Please check the document version of this publication:

• A submitted manuscript is the version of the article upon submission and before peer-review. There can be important differences between the submitted version and the official published version of record. People interested in the research are advised to contact the author for the final version of the publication, or visit the DOI to the publisher's website.
• The final author version and the galley proof are versions of the publication after peer review.
• The final published version features the final layout of the paper including the volume, issue and page numbers.

Link to publication

General rights
Copyright and moral rights for the publications made accessible in the public portal are retained by the authors and/or other copyright owners and it is a condition of accessing publications that users recognise and abide by the legal requirements associated with these rights.

- Users may download and print one copy of any publication from the public portal for the purpose of private study or research.
- You may not further distribute the material or use it for any profit-making activity or commercial gain
- You may freely distribute the URL identifying the publication in the public portal.

If the publication is distributed under the terms of Article 25fa of the Dutch Copyright Act, indicated by the “Taverne” license above, please follow below link for the End User Agreement:

www.tue.nl/taverne

Take down policy
If you believe that this document breaches copyright please contact us at:

openaccess@tue.nl

providing details and we will investigate your claim.

Download date: 05. Oct. 2023

Towards Increased Understanding of Low-Power Induction and Synchronous Reluctance Machines

Harmonic Modeling of Complex Electromagnetic Phenomena

PROEFSCHRIFT

ter verkrijging van de graad van doctor
aan de Technische Universiteit Eindhoven,
op gezag van de rector magnificus prof.dr.ir. F.P.T. Baaijens,
voor een commissie aangewezen door het College voor Promoties,
in het openbaar te verdedigen
op donderdag 17 september 2015 om 16:00 uur

door

Ruud Leonardus Johannes Sprangers

geboren te Waspik

Dit proefschrift is goedgekeurd door de promotoren en de samenstelling van de promotiecommissie is als volgt:

voorzitter:	prof.dr.ir. A.C.P.M. Backx
promotor:	prof.dr. E.A. Lomonova M.Sc.
copromotor:	dr. J.J.H. Paulides, M.Phil.
leden:	prof.dr. J. Pyrhönen (Lappeenranta University of Technology)
	prof.dr. M.J. Kamper (Stellenbosch University)
	dr.ir. M.C. van Beurden
adviseurs:	Dr.-Ing. A. Lange (Mahr GmbH)
	dr.ir. B.L.J. Gysen (Prodrive Technologies)

Towards Increased Understanding of Low-Power Induction and Synchronous Reluctance Machines

Harmonic Modeling of Complex Electromagnetic Phenomena

VOSTERMANS
VENTILATION

This research is funded by Vostermans Ventilation B.V. in Venlo, The Netherlands.

R.L.J. Sprangers, Towards Increased Understanding of Low-Power Induction and Synchronous Reluctance Machines: Harmonic Modeling of Complex Electromagnetic Phenomena, Eindhoven University of Technology, 2015.

A catalogue record is available from the Eindhoven University of Technology Library.
ISBN: 978-90-386-3914-7

Summary

Towards Increased Understanding of Low-Power Induction and Synchronous Reluctance Machines

Harmonic Modeling of Complex Electromagnetic Phenomena

Due to the electrification of our society, the global demand for electric energy is rising. This challenging need requires significantly more electric-energy production, preferably from renewable energy sources. The share of such sources in global electric-energy production is therefore expected to raise up to one third by 2040. In the mean time, the available electric energy should be used as efficiently as possible, to reduce the stress on existing production facilities, and to limit the increase in electricity cost for end-consumers.

Between 43% and 46% of the global-generated electric energy is estimated to be converted into mechanical energy by electric-motor-driven systems. To increase the energy-efficiency of such systems, minimum energy performance standards (MEPS) have been set by governments world-wide. These MEPS force electric-motor manufacturers to reconsider the design of existing motor technologies, such as induction motors (IMs), or to embrace other motor technologies, such as permanent-magnet synchronous motors (PMSMs) or synchronous reluctance motors (SynRMs). The availability of fast, accurate, and reliable analysis models is of fundamental importance during the motor design stage. To close the gap between strongly simplified analytical models and time-consuming numerical models, this thesis discusses the development of semi-analytical models based on harmonic modeling. In particular, the work focuses on harmonic modeling of the slotted electromagnetic structures of IMs and SynRMs in 2D polar coordinates.

In Chapter 2, an extension of the existing magnetic-field solution for electromagnetic structures in 2D polar coordinates is presented. The new formulation accounts for circumferential variations of the magnetic permeability, and represents an important step towards incorporating magnetic saturation. An overview of prior approaches to harmonic modeling of slotted electromagnetic structures is also given. The existing methods, namely the Anisotropic Layer Theory (ALT) and the Mode-Matching Theory (MMT), are compared to the new approach, referred to as Inhomogeneous Region Modeling (IRM), based on results obtained for a benchmark topology. It is shown that ALT and MMT models can either represent the influence of global saturation or the effect of leakage and fringing flux, respectively, whereas IRM models can represent both these phenomena at once. However, for the analysis of the benchmark topology, the required calculation time of the IRM model is seven times longer than the calculation time of the most time-consuming existing approach.

The implementation of the ALT and MMT approaches for IM analysis is discussed in detail in Chapter 3. One of the challenges for the MMT implementation is the polar representation of the geometry. Two different representations are analysed, and the most suitable one is selected. Additionally, methods to calculate the fundamental air-gap flux-density, flux linkage, and electromagnetic torque are given for each modeling approach. The results of the calculations are validated against 2D Finite Element Analysis (2D FEA) predictions based on four benchmark motor geometries.

To analyse IMs in loaded operating conditions, two methods are proposed for the calculation of induced rotor-bar currents in Chapter 4. The first method uses an equivalent rotor-bar circuit to calculate the rotor-bar current indirectly. The parameters of the circuit, representing the rotor-bar induced voltage due to the stator magnetic field and the rotor-bar synchronous inductance due to the rotor magnetic field, are calculated using the MMT model in two calculation steps. Further, the second method uses a direct coupling between the magnetic-field model, either ALT or MMT, and the stator and rotor electric-circuit models. Both methods are validated against 2D FEA predictions in terms of induced rotor current and electromagnetic torque production for various operating conditions.

In Chapter 5, a semi-analytical framework for analysis of three-phase IMs is presented, based on a combination of the MMT model, the ALT model, and direct electric-circuit coupling. Leakage and fringing flux phenomena are modeled using the MMT approach, and their influence on motor performance is parameterized in terms of Carter's factor and leakage inductance. Further, the ALT approach is used to predict the global influence of saturation, while taking the leakage and fringing flux parameters into consideration. Also, to account for the influence of rotor skewing on the fundamental electromagnetic torque, the circuit coupling between the ALT model, and the stator and rotor electric circuits is extended to a multi-slice circuit coupling. The calculation results of the framework, obtained for four benchmark IMs, are validated against FEA predictions and measurement results. It is shown that the results are acceptably accurate, although material parameter uncertainties lead to discrepancies between the predicted motor performance characteristics and the measured ones.

Finally, a semi-analytical framework for analysis of SynRMs, based on the IRM approach, is introduced in Chapter 6. The polar representation of the SynRM geometry is discussed and focuses on equal average width of the rotor flux-barriers. Also, methods to calculate the electromagnetic torque and the d- and q-axis flux linkage and inductance are addressed. The proposed framework is then used to model a benchmark SynRM topology, and the obtained calculation results are validated against 2D FEA calculations. It is shown that the chosen polar representation leads to small discrepancies in the d-axis parameter estimation, whereas the q-axis parameters are obtained relatively accurately.

Contents

List of symbols

Matrices and column vectors

Symbol	Description
$\mathbf{a}$	Field coefficient matrix
$\mathbf{b}$	Field coefficient matrix
$\mathbf{E}$	Known coefficient matrix
$\mathbf{G}$	Source term coefficient matrix
$\mathbf{I}$	Identity matrix
$\mathbf{K}_\theta$	Diagonal spatial harmonic order matrix
$\mathbf{S}$	Intermediate matrix
$\mathbf{V}$	Intermediate matrix
$\mathbf{W}$	Eigenvector matrix
$\mathbf{X}$	Unknown coefficient column vector
$\mathbf{Y}$	Fixed term column vector
$\boldsymbol{\lambda}$	Diagonal eigenvalue vector
$\boldsymbol{\mu}_{c,r}$	Radial permeability Toeplitz matrix
$\boldsymbol{\mu}_{c,\theta}$	Circumferential permeability Toeplitz matrix

Parameters with Roman symbols

Symbol	Unit	Description
a	[$*$]	Field coefficient
$\vec{A}$	[Wb m^{-1}]	Magnetic vector potential
b	[$*$]	Field coefficient
b	[m]	Width
b_o	[m]	Slot opening width
$\vec{B}$	[T]	Magnetic flux density vector
$\vec{B}_{rem}$	[T]	Remanent magnetization vector
B_{rg}	[T]	Radial air gap flux density

($*$) Unit depends on the context

$B_{rg,1}$	[T]	Fundamental radial air gap flux density
$B_{rg,rms}$	[T]	RMS radial air gap flux density
c	[∗]	Field coefficient
c_{dir}	[-]	Direction of current flow
C	[∗]	Coefficient
C_{it}	[-]	Relaxation constant
C_{per}	[-]	Number of periodic sections
C_{spm}	[s min^{-1}]	Seconds per minute
d	[∗]	Field coefficient
d	[m]	Thickness
D	[m]	Diameter
D_{in}	[m]	Inner diameter
D_{out}	[m]	Outer diameter
D_{pri}	[m]	Primary winding diameter
D_{sec}	[m]	Secondary winding diameter
E	[V]	Induced voltage
$\vec{E}$	[V m^{-1}]	Electric field strength vector
f	[Hz]	Frequency
$\vec{F}$	[N]	Force vector
G	[∗]	Source term function
h	[m]	Height
h_0	[m]	Region radial position
h_c	[m]	Region radial height
h_r	[m]	Rotor lamination height
$\vec{H}$	[A m^{-1}]	Magnetic field strength vector
I	[A]	RMS current
I_r	[A]	Stator referred rotor current (rms)
j	[-]	Region index number
j	[m^{-2}]	Current density coefficient
$\vec{J}$	[A m^{-2}]	Current density vector
J_{bnd}	[A m^{-1}]	Linear current density on a boundary
J_{lin}	[A m^{-1}]	Linear current density
k	[-]	Region index number
k	[∗]	Coefficient
k_C	[-]	Carter factor
k_R	[-]	Skin effect resistance factor
k_{sf}	[-]	Lamination stacking factor
k_{so}	[-]	Slot opening region index number
k_{sc}	[-]	Slot region index number
k_{w1}	[-]	Fundamental winding factor
K	[∗]	Circumferential source/material distribution
K	[-]	Number of permeability sections
l	[m]	Length
l_{sl}	[m]	Effective slot length
l_{stk}	[m]	Stack length
l_{wire}	[m]	Stator phase winding wire length

L	[H]	Inductance
L_{ew}	[H]	Stator end winding inductance
L_m	[H]	Magnetizing inductance
$L_{\sigma,s}$	[H]	Stator phase leakage inductance
$L'_{\sigma,r}$	[H]	Rotor leakage inductance, stator referred
m	[-]	Spatial harmonic ordinal number (subregion)
m	[-]	Number of phases
m	[kg]	Mass
$\vec{M}$	$[\mathrm{A\,m^{-1}}]$	Magnetization vector
$\vec{M}_0$	$[\mathrm{A\,m^{-1}}]$	Residual magnetization vector
$\vec{M}_s$	$[\mathrm{A\,m^{-1}}]$	Material magnetization vector
n	[-]	Spatial harmonic ordinal number
n	[rpm]	Speed
Υ_{bar}	[-]	Number of flux barrier/guides
n_f	[-]	Fundamental spatial harmonic
n_{slice}	[-]	Model slice index
N_{ph}	[-]	Number of winding turns per phase
N_{pri}	[-]	Number of primary turns
N_{sec}	[-]	Number of secondary turns
N_{sh}	[-]	Number of positive spatial harmonics
N_{slice}	[-]	Number of model slices
N_{sr}	[-]	Number of rotor slots in the model
N_{ss}	[-]	Number of stator slots in the model
$N_{A,B,C}$	[-]	Set of all slots belonging to phase A,B or C
p	[-]	Number of pole pairs
p	$[\mathrm{W\ m^{-3}}]$	Loss density
pf	[-]	Power factor
P	[W]	Active power
q	[-]	Number of slots per pole per phase
Q	[-]	Number of slots
Q	[VAr]	Reactive power
r	[m]	Polar or cylindrical coordinate
r_0	[m]	Normalizing radius
r_b	[m]	Barrier outer radius
r_{bnd}	[m]	Boundary radius
r_i	[m]	Region inner radius
r_{mid}	[m]	Region center radius
r_o	[m]	Region outer radius
r_{sh}	[m]	Shaft radius
r_{ro}	[m]	Rotor outer radius
r_{si}	[m]	Stator inner radius
r_{so}	[m]	Stator outer radius
R	$[\Omega]$	Resistance
R_{Fe}	$[\Omega]$	Core loss resistance
R_s	$[\Omega]$	Stator phase resistance
R'_r	$[\Omega]$	Stator referred rotor resistance

s	[-]	Slip
S	[m^2]	Surface area
t	[s]	Time
t_{exc}	[s]	Model execution time
T	[Nm]	Torque
T	[°C]	Temperature
$\mathbb{T}$	[T^2]	Maxwell's Stress Tensor
$\vec{u}$	[-]	Unit vector
V	[V]	RMS voltage
V	[m^3]	Volume
w	[-]	Circumferential periodicity
w_{syn}	[rad s^{-1}]	Synchronous angular velocity
$w_{r,m}$	[rad s^{-1}]	Mechanical angular velocity
w_s	[rad s^{-1}]	Stator electric angular frequency
z	[m]	Cylindrical coordinate
z_Q	[-]	Number of conductors
Z	[Ω]	Impedance

Parameters with Greek symbols

Symbol	Unit	Description
α	[-]	Permeability ratio coefficient
α_T	[-]	Temperature coefficient
β_c	[rad]	Cut-out angle
γ_{skew}	[rad]	Rotor bar inclination angle
δ_c	[rad]	Current angle in dq reference frame (electrical)
Δ_{cur}	[rad]	Current angle (electrical)
$\Delta\theta_{slice}$	[rad]	Model slice rotor displacement
Δ_θ	[rad]	Rotor displacement angle
ε_{des}	[-]	Maximum permeability error
θ	[rad]	Polar or cylindrical coordinate
η	[%]	Efficiency
θ	[rad]	Angle
θ_0	[rad]	Region angular position
θ_c	[rad]	Region angular width
θ_{exc}	[rad]	Excitation current angular width
θ_m	[rad]	Circumferential midpoint angle
θ_{offset}	[rad]	Electrical offset angle
θ_p	[rad]	Fundamental pole angle of a region
θ_r	[rad]	Angle between A-axis and d-axis
θ_{sb}	[rad]	Subregion starting angle
θ_{se}	[rad]	Subregion ending angle
θ_{slice}	[rad]	Skewing angle per slice
θ_{skew}	[rad]	Rotor bar skew angle
θ_{sp}	[rad]	Slot pitch angle

θ_t	[rad]	Tooth angle
θ_w	[rad]	Region angular width
$\theta_{\mu,b}$	[rad]	Permeability section starting angle
$\theta_{\mu,e}$	[rad]	Permeability section ending angle
κ	[-]	Carter coefficient intermediate factor
κ	[-]	Permeability section index number
λ	[Wb]	Flux linkage
μ	$[\mathrm{H\,m^{-1}}]$	Magnetic permeability
μ^{rec}	$[\mathrm{m\,H^{-1}}]$	Reciprocal of the magnetic permeability
μ_0	$[\mathrm{H\,m^{-1}}]$	Magnetic permeability of vacuum
μ_{new}	$[\mathrm{H\,m^{-1}}]$	New permeability value
μ_r	[-]	Relative magnetic permeability
μ_{rr}	$[\mathrm{H\,m^{-1}}]$	Radial magnetic permeability
$\mu_{\theta\theta}$	$[\mathrm{H\,m^{-1}}]$	Circumferential magnetic permeability
ν	[-]	Subregion index, slot index
$\mathcal{V}$	[-]	Number of subregions
ξ	[-]	Skin effect coefficient
σ	$[\mathrm{S\,m^{-1}}]$	Conductivity
τ_{skew}	[m]	Rotor skew pitch at rotor surface
τ_{sp}	[m]	Slot pitch at stator/rotor surface
υ	[-]	Rotor barrier/guide index number
ϕ	[deg]	Electric phase angle
φ	[rad]	Phase angle between current and voltage
χ	[-]	Magnetic susceptibility

Common subscripts and superscripts

Sub-/superscript	Description
amb	Ambient
A	Phase A
B	Phase B
bar	Rotor bar
bd	Barrier, d-axis
$bearing$	Bearing loss
bq	Barrier, q-axis
c	Cut-out
C	Phase C
d	direct axis
dr	Rotor tooth
ds	Stator tooth
$eddy$	Eddy current
em	Electromagnetic
eq	Equivalent
er	Equivalent end ring
exc	Excess

Fe	Iron loss
g	Air gap
gd	Guide, d-axis
gq	Guide, q-axis
hys	Hysteresis
in	Input
$iron$	Soft-magnetic material
i	Region index number
j	Region index number
k	Region index number
k_{so}	Slot opening region index number
k_{sc}	Slot region index number
lam	Lamination
LR	Locked-rotor
m	Spatial harmonic ordinal number
m	Magnetizing
max	Maximum
$mech$	Mechanical
min	Minimum
ml	Mechanical loss
n	Spatial harmonic ordinal number
N	Nominal
n_{slice}	Model slice index
NL	No-load
nom	Nominal
Ohm	Ohmic loss
op	Operating
or	Rotor slot opening
os	Stator slot opening
ph	Phase
q	Quadrature axis
r	Rotor
$ring$	Rotor end ring
rns	Ring sample
s	Stator
sr	Rotor slot
ss	Stator slot
$stray$	Stray loss
w	Inner web
$wind$	End winding
yr	Rotor yoke
ys	Stator yoke
κ	Permeability section index number
ν	Subregion index, slot index
σ	Leakage
υ	Rotor barrier/guide index number

List of abbreviations

Abbreviation	Description
1D	One-dimensional
2D	Two-dimensional
3D	Three-dimensional
ac	Alternating-current
ALA	Axially Laminated Anisotropy
ALT	Anisotropic Layer Theory
av	Average
BC	Boundary Condition
BM	Benchmark Motor
dc	Direct-current
DOL	Direct-on-line
emf	electromotive force
FEA	Finite Element Analysis
FFF	Fast Fourier Factorization
fund.	Fundamental
GUI	Graphical User Interface
HM	Harmonic Modeling
IEC	International Electrotechnical Commission
IM	Induction Motor
IRM	Inhomogeneous Region Modeling
KVL	Kirchhoff's Voltage Law
LIM	Linear Induction Motor
MEC	Magnetic Equivalent Circuit
MEPS	Minimum Energy Performance Standard
MMT	Mode-Matching Theory
mmf	magnetomotive force
MST	Maxwell's Stress Tensor
MWFA	Modified Winding Function Approach
nonl.	nonlinear
PC	Personal Computer
PM	Permanent Magnet
PMSM	Permanent Magnet Synchronous Motor
p.u.	Per unit

RCWA	Rigorous Coupled Wave Analysis
rms	Root Mean Square
SEC	Steinmetz Equivalent Circuit
SynRM	Synchronous Reluctance Motor
TLA	Transverse Laminated Anisotropy
VSD	Variable Speed Drive
WFA	Winding Function Approach

Chapter 1

Introduction

1.1 Background

The electrification of our society is advancing rapidly. Not only does this change the way we communicate, gather information or drive our cars, even the toys which our babies and toddlers are given to play with often contain a considerable amount of electronics. Electricity and electronic devices are all around us and have become inseparable from our daily lives. Consequently, the amount of electric energy required to fulfill our needs is rising. According to [1], the global demand for energy is set to grow by 37% by the year 2040 in the current scenario, whereas electricity is mentioned as the fastest-growing final form of energy. On the one hand, the increasing electricity demand requires significantly more electric energy production. On the other hand, traditional power plants based on fossil fuel sources are not preferred due to their associated environmental impact. A strong growth in the use of renewable energy sources is therefore expected in the upcoming decades, raising its share in global electric energy production up to one-third by 2040 [1]. In the mean time, to reduce the stress on existing and near-future production facilities, it is of critical importance that the available electric energy is utilized as efficiently as possible. Furthermore, the price of electric energy is expected to increase due to high fossil fuel prices and the required investment in renewable energy sources. Therefore, more efficient use of electric energy will be even more important for energy consumers.

1.1.1 Energy-efficient electric motors

The largest consumer of electric energy is represented by electric-motor-driven systems, which are estimated to account for between 43% and 46% of the total global electric energy consumption [2]. In an ideal case, all the electric energy supplied to an electric motor is converted into mechanical energy. In practice, however, this process is accompanied by many different energy-loss mechanisms, which transform useful electric energy into undesired heat. To maximize the efficiency of a motor, these energy losses should be minimized. Therefore, to force motor manufacturers to produce more energy-efficient electric motors, minimum energy performance standards (MEPS) have been set by governments world-wide using efficiency standards defined by the International Electrotechnical Commission (IEC) in the IEC 60034-30 standard [3].

In Europe, the MEPS for rotating electric motors are documented in [4]. They are mandatory for single-speed, three-phase induction motors (IM) with two, four or six poles, a rated voltage up to 1000 V and a rated power between 0.75 kW and 375 kW. Furthermore, the motor should be intended for continuous duty operation. Several exceptions are excluded for the requirements, as documented in [4] and updated in [5]. For example, these exceptions apply for motors that are completely integrated into a system, such as fans, pumps, compressors etc., and motor that operate under extreme conditions. For motors that are not excluded, the efficiency requirements posed by [4] are applied in three stages:

1. From June 16, 2011, electric motors in the power range from 0.75 - 375 kW should comply with the IE2 efficiency class;
2. From January 1, 2015, electric motors in the power range from 7.5 - 375 kW should comply with either the IE3 efficiency class for direct-on-line (DOL) operation or the IE2 efficiency class in combination with a variable speed drive (VSD);
3. From January 1, 2017, electric motors in the power range from 0.75 - 375 kW should comply with either the IE3 efficiency class for DOL operation or the IE2 efficiency class in combination with a VSD.

To determine the motor efficiencies, the methods specified in the IEC 60034-2-1:2014 standard [6] should be used. Finally, it should be noted that IEC 60034-30 was recently replaced by IEC 60034-30-1 [7]. This new standard expands the product range covered by the previous standard by considering all types of DOL motors, instead of only three-phase, squirrel-cage IM, for a larger power range, namely 0.12 - 1000 kW. Also, it sets the definition for the IE4 efficiency class and presents an informative introduction of the IE5 efficiency class. Another standard, IEC 60034-30-2, is currently under preparation and will cover motors driven by variable voltage and frequency supplies.

To comply with the MEPS, motor manufacturers need to reconsider their products. The traditional IM, which is one of the most widely used electric motors in industrial applications, is generally not efficient enough to comply with the IE2 and IE3 efficiency classes. On the other hand, it does provide several important features, including high reliability, relatively low production costs and its inherent DOL operating ability. Therefore, during the past decade, a significant amount of research was devoted to the improvement of IM efficiency. For example, the use of copper instead of aluminium for the die-cast rotor cage and the application of premium soft-magnetic materials for the motor laminations was investigated [8, 9, 10, 11, 12]. Also, increasing the size of the motor, by increasing its stack length [13] or outer diameter [14], has been considered as a solution to improve IM efficiency. A comprehensive overview of additional possibilities for IM efficiency improvement is provided in [15].

Besides IMs, other motor types have received even more attention during recent years in research and development. An overview of various motor technologies considered suitable for meeting the efficiency demands is presented in [16]. In general, the main interest of motor manufacturers seems to be in two kinds of synchronous motors: the Permanent-Magnet Synchronous Motor (PMSM) and the Synchronous Reluctance Motor (SynRM). The advantage of a PMSM is that the magnetization of the motor is provided by permanent magnets (PMs), placed on the rotor surface or inside the rotor. Therefore, in comparison to IMs, rotor winding conduction losses are eliminated, whereas the stator winding conduction losses are reduced since only the current required to produce electromagnetic torque needs to be supplied (assuming no field weakening takes place). This also allows the design of PMSMs with a high power factor. A disadvantage is that they are relatively expensive, especially when equipped with rare-earth PMs. Therefore, cheaper magnet types, such as ferrite magnets, are currently being considered as an alternative, although their energy density is significantly lower [17]. Also, PMs are sensitive to over-temperature and uncontrolled peak current conditions, for example during short-circuits. Such conditions could lead to permanent demagnetization of the PMs, which is catastrophic for the motor performance.

In the SynRM, the rotor consists of soft-magnetic material and air, and the torque production is based on reluctance torque. Therefore, SynRMs benefit from the absence of rotor winding conduction losses, but the stator still needs to supply current for the magnetization as well as torque production. Due to the absence of PMs, the SynRM is not as sensitive to rotor over-temperature and current peaks as the PMSM, whereas its production costs are limited due to the simpler rotor construction. A disadvantage of the SynRM, however, is its relatively low power factor. The power factor can be increased by designing the motor for low q-axis inductance, although this generally leads to a lower d-axis inductance as well, which results in lower output torque [18]. A popular solution to the low power factor is to add ferrite magnets to the barriers of the SynRM to reduce the q-axis flux. Although these PM-assisted SynRMs seem promising [19, 20], they partially take away the advantages of the SynRM in terms of production complexity and fault tolerance. Furthermore, another disadvantage of the SynRM is its mechanical instability. Due to the thin soft-magnetic connections between the rotor flux guides, adequate mechanical design is required to guarantee sufficient strength, especially for higher operating speeds [21, 22].

Finally, one additional disadvantage that PMSMs and SynRMs have in common is their need for a VSD. Without additional measures, they can not be operated directly from the grid. Therefore, if DOL operation is desired, a damper cage similar to the squirrel cage of an IM can be added to the rotor of certain types of synchronous motors. In recent publications, such a solution is investigated for both PMSMs [23, 24, 25, 26, 27] and SynRMs [28, 29]. Some drawbacks of the line-start synchronous machines, however, are large torque pulsations during start-up and the limitations regarding load inertia in order to obtain successful synchronization [25, 27].

1.1.2 Intended application

The research presented in this thesis is conducted in close co-operation with Vostermans Ventilation B.V., located in Venlo, The Netherlands. Therefore, the intended application for the developed analysis tools is the design of electric motors for ventilation systems. An overview of a typical, direct-drive ventilation system is shown in Figure 1.1. Further, a typical torque-speed characteristic of the considered load, a fan, is shown in Figure 1.2, where the nominal torque and speed are indicated by T_N and n_N, respectively. Since the required torque depends quadratically on the operating speed, the required start-up torque is gen-

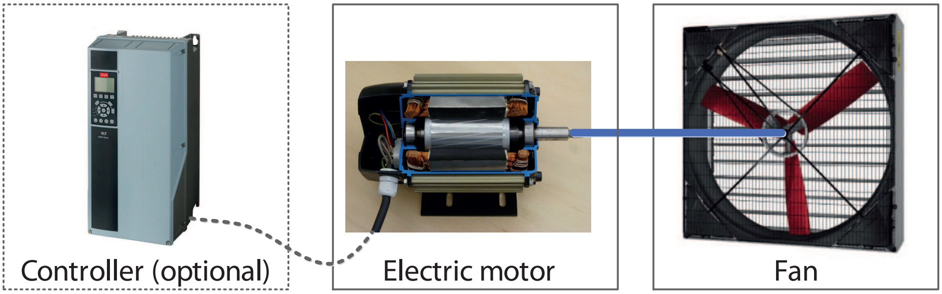

Figure 1.1: Overview of a typical, direct-drive ventilation system.

erally low. However, the inertia of the fan is generally significantly larger than the inertia of the rotor.

Currently, the fan is driven by an IM, often in combination with a controller. This allows the fan to run directly from the grid, which provides a back-up in case the controller fails. The mechanical power requirements for the considered ventilation systems range between 0.1 - 5 kW, whereas the speed requirements vary up to approximately 3000 rpm. Therefore, the considered electric motors can be classified as low-power, low-speed motors. Although the MEPS discussed in [4] and [5] are not mandatory for electric motors embedded in a ventilation system, it is still desired to increase the efficiency of the electric motors according to these requirements. To design more efficient electric motors, the complex electromagnetic phenomena that determine the fundamental characteristics of the machine and its parasitic effects should be well understood. Such understanding can be obtained from (semi-)analytical models. On the one hand, these types of models can provide their users with a mathematical description of the relation between the electromagnetic phenomena and their effect on the motor characteristics. Such descriptions allow for an increased insight in the machine behaviour. On the other hand, (semi-)analytical models also force their users to carefully consider which effects they want to model and which assumptions can or cannot be made during the modeling process. Further, an additional advantages of (semi-)analytical models is that they are often considerably more time-efficient

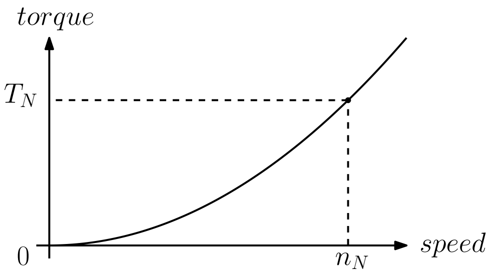

Figure 1.2: Typical torque-speed characteristic of a fan.

than fully numerical approaches such as Finite Element Analysis (FEA). This makes them especially suited for exploration of large design spaces within a limited amount of time. The research presented in this thesis therefore focuses on the (semi-)analytical modeling of IMs and SynRMs.

1.2 Literature overview

The literature overview presented in this section focuses on three aspects, namely IM modeling, SynRM modeling and harmonic modeling. It should be noted that this overview is by no means a complete one and the referenced literature only represents a selection of the available literature. However, it does provide insight in the advantages, disadvantages and past development of various modeling approaches.

1.2.1 Induction motors

Near the end of the 19^{th} century, the first alternating-current IMs without commutators were independently invented by Ferraris [30] and Tesla [31]. Although the initial designs were far from perfect, the principle behind the machine was picked up by industry for further development. In 1889, the first short-circuit rotor was invented by Dolivo-Dobrovolsky [32], which led to the development of the squirrel-cage IM. The interest in the motor grew and eventually, it became one of the most frequently used electric motors in industry. Along with the development of the IM, a countless number of researchers and engineers have worked on its design, analysis, and control. As a results, many different models and modeling approaches have been developed. Here, an overview is given of several research trends that have developed throughout the years, focusing mainly on models that have served a purpose in the design of IMs.

Steinmetz equivalent circuit model:

One of the first and most commonly used models for IMs was developed by Steinmetz [33] and is known as the Steinmetz Equivalent Circuit (SEC). Due to its analytical nature, it can be evaluated very quickly and it provides valuable insight in the behavior of the machine. For example, such insights allow experienced designers to estimate the influence of design changes or varying operating conditions on the performance of the motor. The model itself is based on the transformer equivalent circuit, with the necessary adjustments to transpose the rotating field and induced rotor currents to the stator reference frame. It consists of several lumped parameters, representing the stator resistance, R_s, the stator leakage inductance, $L_{\sigma,s}$, the magnetizing inductance, L_m, the core loss resistance, R_{Fe}, the rotor resistance, R_r', and the rotor leakage inductance, $L_{\sigma,r}'$. A graphical overview of the SEC and its parameters is shown Figure 1.3.

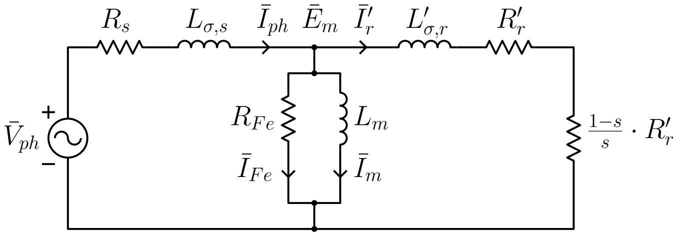

Figure 1.3: Steinmetz Equivalent Circuit of a three-phase induction motor.

To obtain accurate calculation results, the lumped parameter values should be determined accurately. For an existing IM, this can be done by means of measurements and empirical corrections. During machine design, however, a prototype machine is generally not available for measurements. Therefore, empirical equations and simplified models are conventionally used to estimate the parameters. The leakage inductances are split up into separate parts, each modeling a different leakage flux component and calculated independently of each other. The influences of saturation, skin effect and higher harmonics are taken into account by correction coefficients or extensions of the standard equivalent circuit. An overview of calculation procedures and models for the calculation of the lumped parameters are extensively described in literature, for example in [34, 35, 36, 37, 38, 39, 40]. In practice, however, the obtained parameter values often require tuning to match the calculation results with measurement results.

Another limitation of the SEC is that it represents the magnetic field inside the motor from a high abstraction level. More detailed knowledge about the magnetic-field distribution, for example the flux densities in different motor parts, is usually desired for design purposes. Therefore, many induction-motor models focus on magnetic-field prediction and are often used in combination with the SEC or an extension of the SEC to calculate the IM performance.

Magnetic equivalent circuit model:

A widely used approach for magnetic analysis of electric machines is Magnetic Equivalent Circuit (MEC) modeling. In principle, this method is based on the 1D representation of a magnetic-flux flow by means of a reluctance element. To predict the flux distribution in the machine, its geometry is divided into a number of sections and each section is represented by one or more reluctance elements, each modeling a part of the magnetic flux. These elements are then connected accordingly, whereas magnetic-field sources, generally a current-carrying coil or a PM, are represented by magnetomotive force (mmf). The resulting network of reluctance elements and mmf sources is analogous to an electric circuit with resistors and voltages source, and can be solved similarly to obtain the magnetic flux through each reluctance element. Before the introduction of digital computers, MEC models were often used to perform manual calculations. Therefore, the first MEC models for IMs were simple in nature, considering only the fundamental

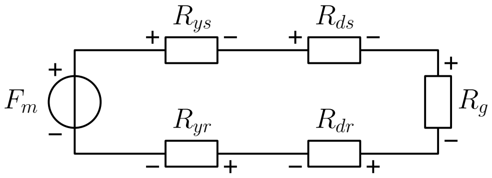

Figure 1.4: Magnetic equivalent circuit for the main flux of an induction motor.

magnetic flux and representing the reluctance of the main flux path using five reluctance elements, namely: the stator yoke reluctance, R_{ys}, the stator tooth reluctance, R_{ds}, the air-gap reluctance, R_g, the rotor tooth reluctance, R_{dr}, and the rotor yoke reluctance, R_{yr}. A graphical overview of this model is shown in Figure 1.4. Nowadays, these simple MEC models are still very useful, especially for fast calculation of the main flux during motor design [37, 40].

One of the advantages of MEC modeling is that the reluctance of an element can be made flux-dependent, such that magnetic material nonlinearities can be incorporated. In [41], Ostovic uses this property to propose a number of MEC-based models for various electric machines, applied for analysis of their dynamic behavior in saturated operating conditions. These models are significantly more advanced than the conventional main flux models and therefore allow for a more accurate estimation of the flux distribution in the motor and the influence of saturation on motor performance. Based on the work of Ostovic [41], a number of subsequent publications is observed, for example for the design of inverter-fed asynchronous machine [42, 43], a permanent-magnet motor [44, 45], and a linear stepping motor [46]. MEC models for real-time simulation and transient simulation of IMs are presented in [47] and [48], respectively.

Furthermore, a work on the development of a software package for the design of electromagnetic devices was presented by Perho [49] in 2002. The work aims to generalize the construction of a MEC and its coupling to the electric domain. The effects of eddy-currents in iron parts are also treated, based on the work of Atkins [50]. The resulting reluctance model was implemented for two IMs and validated against measurement results. Also, the calculation of SEC model parameters from the results of the MEC is discussed in detail. A framework for MEC modeling along three dimensions of an electromagnetic structure was presented by Armhein [51]. It was attempted to generalize the model construction for design purposes. In another publication [52], Armhein presents a force calculation method for MEC based on Maxwell's Stress Tensor (MST). The results of the model, implemented for an IM, are discussed in [53].

Despite all previously mentioned research, MEC-based models still have a few important disadvantages. One of these disadvantages is that a discretization of the motor geometry is required. For a coarse discretization, MEC-based models are time-efficient, but the accuracy of the results is limited. Also, a-priori knowledge of the magnetic-field distribution is required to properly define the reluctance elements. To improve the accuracy and reduce the need for a-priori knowledge, a finer discretization can be used, for example by means of mesh-based discretization. However, these improvements are obtained at the expense of an increased calculation time. Further, effects such as flux fringing are considered by two (or three) 1D flux paths, whereas their actual 2D (or 3D) nature is not directly represented. To obtain a better representation of the magnetic-field distribution, a hybrid combination of MEC modeling and harmonic modeling can be used, as discussed in [54, 55]. However, this approach still requires a MEC-based field solution in the slots and slot openings of an electric motor.

Anisotropic Layer Theory:

In 1953, a method for induction-motor performance analysis was proposed by Mishkin [56]. The method is based on harmonic representation of the fundamental magnetic flux and considers the slotted sections of the machine by homogeneous, anisotropic layers. The characteristics of the layer materials are artificial ones, reflecting averaged values of the real (mixed) characteristics. However, large deviations between the new theory and the conventional circle diagram were shown for large values of slip, which Mishkin attributed to the ignored skin effect in the circle diagram method. The theory was extended by Cullen and Barton in [57], where the tooth area was divided into two separate layers for the tooth tips and the slots. The resulting model takes better account of tooth-tip leakage flux. In a comparison to Mishkin's results, it was shown that the deviation seen before is mainly caused by the absence of tooth-tip leakage flux in Mishkin's single-layer slot model. The contribution of the skin effect to the deviation is shown to be much smaller than assumed by Mishkin [56]. Cullen and Barton [57] ignored the end effects of the machine.

In the same publication, Cullen and Barton noted the analogy between Mishkin's layer theory and the transmission line theory used for microwave analysis. It was shown that the application of the concept of wave impedance to the IM gives results identical to the conventional SEC with skin-effect correction. The analogy was further extended by the definition of general equations for the transfer matrix of a layer [58]. The combination of the transfer matrix and the concept of wave impedance allows for the calculation of electrical quantities, which led to the definition of an equivalent T-circuit for every layer. The parameters were calculated as seen from the machine terminals [59], and it was shown that the SEC can be derived from the layer theory by making some simplifying assumptions.

The concept of using anisotropic layers to represent slotted machine regions has often been applied to the analysis of linear induction motors (LIMs). In 1969, Preston and Reece described a method for including the transverse edge effect in LIMs [60]. The method is based on the axial repetition of the 1D model, while changing the sign after every repetition. A 2D model was suggested in a response to [60] by Freeman and Lowther [61], and applied for analysis of transverse-flux tubular motors by Eastham and Alwash [62].

A method similar to Mishkin's, but including both magnetic and electric anisotropy, was proposed by Weh [63]. In [64], a multi-layer model for induction machines is described with magnetic and electric anisotropy along all three axes of the machine by Williamson and identified as the Anisotropic Layer Theory (ALT). The current distributions along both the circumferential and the transverse directions are represented by current sheets and expressed by Fourier series. The transmission line equivalent circuit is derived and applied to evaluate the model. In a subsequent paper [65], Williamson focused on the application of the model for rotating induction machines. Williamson extended the previous model by including the effects of rotor skew and discrete rotor current, and derived the conventional SEC from the extended model. Similar multi-layer models for IMs have also been developed by Gieras [66, 67]. He considered taking into account the higher spatial harmonics and their representation in an extended SEC model. In [68], the method is applied in cylindrical coordinates. Using an iterative method, the permeabilities of the layers are updated as a function of the magnetic flux. This allows for saturation of the main flux path to be taken into account. It is shown that the calculated magnetizing characteristics are in good agreement with measurement results for a wide variety of three-phase IMs.

In a more recent publication by Magill, the ALT was suggested for synthesis-based design of electric machines rather than analysis based design [69]. Further, a combination of the ALT and mode-matching harmonic modeling was presented in [70], whereas a comparison of two different ALT models for analysis of IM performance was presented in [71]. In the latter, one of the models directly includes the induced rotor current by solving the diffusion equation in polar coordinates and considering an average conductivity in the rotor. However, it was shown that such an approach is not entirely valid due to the discrete nature of the rotor bars in the actual machine, especially for high-slip operation.

Winding Function Approach:

Another method for analysis of IM performance that has received a substantial amount of research interest is the Winding Function Approach (WFA). This method is not very effective for accurate magnetic-field analysis, but it is very useful to study other design-related problems, such as rotor eccentricity and the influence of stator and rotor slotting on current and voltage waveforms. The principles of the WFA are explained in detail by Schmitz and Novotny [72]. The method is based on the calculation of a winding function for every winding in the machine using the circumferential distribution of the conductors. The stator and rotor are assumed to be two concentric cylinders with infinite permeability, separated by an air gap. The self- and mutual inductances of all the windings in the machine can be calculated from the winding function.

The WFA was used by Toliyat in his work on concentrated winding induction machines for adjustable speed drives [73]. Later, a systematic procedure for modeling of IMs was published [74]. The suitability of the method for winding fault analysis was pointed out and several research papers on this topic were presented

[75, 76, 77, 78]. Further, the WFA was used to model rotor eccentricity. Firstly, this was done using the conventional WFA [79, 80], which has the drawback of not taking the air-gap variation into account. The problem was solved by the development of the Modified WFA (MWFA) [81, 82]. The MWFA was applied in various studies on the effects of rotor eccentricity [83, 84, 85]. A comprehensive overview of eccentricity fault simulations is given in [86]. Also, the WFA was extended for a skewed rotor with uniform air-gap in [87] and for a skewed rotor with non-uniform air-gap in [88]. Attempts to include saturation were discussed in [89, 90] and are based on the work presented in [91]. Finally, a combination of a mode-matching harmonic model and the WFA to calculate induced voltage and inductance for an axial flux PM machine is presented in [92].

Finite Element Analysis:

Since the 1980's, the available amount of computational power has grown heavily and as a result, numerical techniques such as Finite Element Analysis (FEA) have emerged [49]. In comparison to other magnetic-field modeling methods, FEA gives relatively accurate results due to its ability to model complex geometries and nonlinear soft-magnetic material properties. Some of its disadvantages, however, include the requirement of a detailed geometry mesh, relatively time-consuming calculations and the discrete nature of the obtained field solution. Nevertheless, FEA has developed into a generally applicable modeling technique and is being used by many researchers and engineers for analysis, design fine-tuning, and validation of analytical or semi-analytical models. A detailed explanation of the FEA approach and its development can be found in [93]. Furthermore, the implementation of an induction-motor model using 2D FEA, including the interaction between the electric circuits and the magnetic model, is presented in [94]. In this thesis, 2D FEA is mainly used as a means to validate the developed models. All employed FEA models are implemented using commercial software packages, namely Cedrat Flux2D and Cedrat FluxSkewed.

1.2.2 Synchronous reluctance motors

The rotors of the first SynRMs, designed in the 19th century, were mere salient-pole rotors. They were used in situations where accurate speed control was required and often provided with a damper cage to assist in synchronizing with the stator magnetic field. Their performance, however, was relatively poor due to their low inductance ratio and therefore, they were not able to compete with other motor types, such as direct-current (dc) motors and IMs, in applications that required high motor performance. In 1923, however, a different type of SynRM rotor was proposed by Kostko [95]. Stating that the salient-pole rotors do not represent the correct method to create a high-performance SynRM, he introduced the first version of a distributed anisotropy rotor. This type of rotor has flux barriers to block the q-axis flux, whereas soft-magnetic flux guides provide a low-reluctance flux path along the d-axis. The advantage of the distributed anisotropy rotors is that the achievable inductance ratio is much higher. Therefore, the same approach is currently still used in modern SynRMs, albeit with a significant number of improvements to boost its performance.

In the past, high-performance SynRMs have not been used very extensively due to limited control possibilities. However, the development of variable-frequency motor drives for IMs has led to a renewed interest in SynRMs. With such a drive, the magnetic field of the stator is synchronized with the rotor (using position feedback) instead of using a damper cage to synchronize the rotor with the magnetic field of the stator. As a results, the research on design of distributed anisotropy rotors was boosted and developed into two different types of SynRM rotors, namely Axially Laminated Anisotropy (ALA) rotors and Transversely Laminated Anisotropy (TLA) rotors. In ALA-type rotors, axial sheets of soft-magnetic material and magnetically insulating material are stacked onto each other alternately along the radial direction. Early research work in the field of distributed anisotropy rotor mainly focused on this type of rotor due to its high inductance ratios [96, 97, 98]. However, ALA-type rotors are more difficult to manufacture than TLA-type rotors and tend to produce higher rotor iron-losses [37]. For example, such losses were experimentally shown in [99, 100] and predicted using a simplified model in [101]. In [100], it is also shown that for a smaller number of properly shaped flux barriers and guides, such as in a TLA-type rotor, rotor iron-losses can be strongly reduced.

In TLA-type SynRMs, the rotor consists of transversal sheets of soft-magnetic material, which are stacked onto each other in the axial direction. Such laminations can be produced and stacked using conventional techniques. Therefore, their production cost is low, especially in comparison to ALA-type rotors. Consequently, the research on SynRMs slowly diverted towards the TLA-type. In the studies conducted by Fratta and Vagati, design criteria for these SynRMs are derived while focusing on minimization of the q-axis flux [102] and torque ripple reduction [103, 104]. The employed analytical models are largely based on magnetic equivalent circuits for the flux barriers of the rotor, whereas the soft-magnetic material is assumed infinitely permeable. Although the presented methods provide valuable insight in design choices, they are not capable of accurately predicting the SynRM performance due to the neglected saturation effect. Therefore, refinement of the designs by means of FEA is required, e.g. as discussed in [105].

In fact, a significant number of studies performed throughout the past two decades use 2D FEA for analysis, design and optimization of SynRMs. This trend is mainly motivated by its flexibility with respect to complex motor geometries and its ability to consider nonlinear soft-magnetic materials. For example, the influence of rotor dimensions and saturation on the d- and q-axis inductance are discussed in [18], whereas the ratio between the flux barrier width and the flux guide width is investigated as a design parameters in [106]. Further, the effects of stator winding chording and rotor skew on average torque and torque ripple are discussed in [107] and the influence of various rotor flux barrier parameters are investigated in [108, 109, 110, 111]. Finally, a design optimization based on asymmetric flux barriers is presented in [112], whereas various FEA-based optimization procedures are presented in [113, 114, 115, 116].

Besides FEA-based analysis, several analytical approaches have also been studied. An analytical procedure for SynRM design optimization, based on the calculation of the required magnetomotive force to obtain predefined d- and q-axis flux levels, is discussed in [117, 118]. Furthermore, analytical models based on winding function theory are presented in [119, 120], where the latter one combined it with MEC and conformal mapping to represent the influence of the rotor barriers. However, neither of these two approaches include magnetic saturation in a rigorous manner. Finally, a simple harmonic model is implemented in [121], where the complex SynRM rotor is replaced by a solid rotor in order to determine optimal placement of the flux guides.

1.2.3 Harmonic modeling

In 1929, one of the first applications of harmonic modeling to magnetic-field calculation was presented by Hague, who predicted the field produced by arbitrarily positioned, current-carrying wires between two parallel or concentric iron surfaces [122]. A few decades later, the method was exploited for analysis of IMs, which eventually led to the definition of the ALT method described in Section 1.2.1. The analysis of many different induction-based actuators has been considered, including rotating IMs [65], linear IMs [60], tubular actuators [62] and high-speed, solid rotor IMs [123].

Besides induction devices, harmonic modeling has been applied to many other periodic motor and actuator structures as well. Boules used the method to calculate the magnetic-field distribution of a permanent-magnet motor in Cartesian [124] and polar [125] coordinates. His approach was extended and improved in a number of subsequent publications, accounting for the relative permeability of the magnets [126, 127], Halbach arrays [128], armature reaction [129] and the effect of stator slotting [130]. The latter, however, slotting is accounted for by means of a relative permeance function, which is modulated on to the air-gap flux-density distribution, B_g, obtained from a slotless motor model. In comparison to Carter's factor, which only accounts for the average effective air-gap increase, this permeance function takes local disturbances in B_g due to stator slotting into account. However, it does not account for the magnetic-flux distribution inside the stator slots. A different, more rigorous method is presented by Ackermann in [131], where each slot is considered as a separate model region and the boundary conditions between the air-gap region and each slot region is solved using mode-matching. The presented boundary-condition equations are solved iteratively and therefore, the model is very time-consuming. However, this problem is solved in [132] by considering the boundary conditions in matrix form and solving the matrix equation directly.

The resulting mode-matching model is time-efficient and produces an accurate prediction of the magnetic-field distribution in the air gap and slots of an electric motor or actuator. Therefore, this approach has received a significant amount of attention from the research community. For example, the method has been used for analysis of PMSMs [133, 134, 135, 136], linear PM motors [137], flux switching PM machines [138, 139, 140] and axial flux PM machines [141]. Furthermore, a method to calculate induced rotor-bar currents in induction machines by means of the diffusion equation is presented in [142], under the assumptions of a smooth stator surface and single stator spatial harmonic excitation. Finally, a general formulation of the harmonic modeling method in 2D applications is presented in [143], whereas an extension of the Mode-Matching Theory (MMT) to 3D applications is presented in [144, 145].

One of the main assumptions required to implement MMT models for slotted motor structures is the assumption of infinite magnetic permeability in the soft-magnetic parts of the motor or actuator. To overcome this limitation, a different approach is required. In the optics community, a method known as Rigorous Coupled Wave Analysis (RCWA) exists, which has been extensively used to model wave propagation in periodic structures with low to moderate index contrast [146]. The electromagnetic-field quantities are expressed in terms of complex Fourier series and in fact, the method is very similar to the layered harmonic modeling approach used for electric machine analysis. Furthermore, the material properties such as permittivity, permeability and conductivity are also expressed in terms of complex Fourier series.

1.3 Scientific objectives

Harmonic modeling has proven to be a powerful method for analysis of electromagnetic motors and actuators. However, its current state-of-the-art requires several assumptions that significantly limit the validity of the method for specific modeling cases. For example, the finite magnetic permeability of soft-magnetic materials in slotted motor structures is not considered, which could lead to significant discrepancies when analysing induction and synchronous reluctance motors. Therefore, the applicability and implementation of the harmonic modeling method for these motor types is investigated in this thesis. An overview of the scientific objectives and their resulting contributions is presented:

1. **To extend the harmonic modeling method for rotating electric machines with circumferential magnetic permeability variations:**
   For electromagnetic motors and actuators, the Mode-Matching Theory (MMT) approach is often used to account for circumferential magnetic permeability variations. In this thesis, the following improvements for harmonic modeling are investigated:

   - to allow for variation of the magnetic permeability in the circumferential direction within a model region;
   - to account for soft-magnetic materials with a finite magnetic permeability in slotted structures;
   - to obtain the magnetic-field distribution in soft-magnetic materials with uniform relative permeabilities.

   To realize these improvements, the circumferential distribution of the magnetic permeability is written in terms of complex Fourier series. The magnetic-field solution is then redefined such that it takes the permeability variation into account. A detailed description of the obtained solution for regions with inhomogeneous material properties is presented in Chapter 2 and compared against the results calculated by the Anisotropic Layer Theory (ALT) and MMT approaches for a benchmark topology. This comparison shows that the proposed method is superior in accuracy, but requires significantly more computation time.

2. **To investigate the capabilities and limitations of existing harmonic modeling approaches for induction-motor analysis:**
   Existing harmonic modeling approaches generally deal with slotted magnetic structures in two ways: either the slotted motor sections are homogenized by assuming homogeneous, anisotropic material properties (ALT), or the soft-magnetic material is assumed to be infinitely permeable such that it can be accounted for by means of boundary conditions (MMT). As discussed in Section 1.2.1, the ALT has been extensively applied to IM analysis in the past. For the MMT, however, this is not the case. Both modeling approaches are

implemented and validated against 2D Finite Element Analysis (FEA) predictions in Chapter 3. Based on results obtained for a set of four benchmark IMs, conclusions are drawn about the advantages and disadvantages of each approach.

3. **To include the interaction between the magnetic models and electric-circuit models of the stator and rotor windings:**
   The induced currents in the rotor bars of an IM depend on numerous parameters, including the operating speed of the motor, the amplitude of the magnetic field and the impedance of the rotor squirrel cage. Therefore, its magnitude and phase angle can, in general, not be defined in advance. To overcome this limitation, two methods are proposed to calculate the induced rotor-bar currents in Chapter 4. The first method presents an indirect approach, where the influence of the magnetic fields produced by stator and rotor currents are modeled separately. Using the calculation results, an equivalent rotor-bar circuit is then defined and analysed to obtain the rotor-bar current. Due to the nature of this method, it can only be applied for simulations with fixed stator current. Further, the second method presents a direct approach. The stator and rotor electric circuits are coupled to the magnetic model by means of voltage equations. This method can be applied for simulations with fixed stator current as well as fixed stator voltage. Both methods are implemented for the benchmark IMs and validated against 2D FEA predictions.

4. **To implement and validate a semi-analytical framework for induction-motor analysis based on harmonic modeling:**
   To create a semi-analytical framework for induction-motor analysis based on harmonic modeling, the advantages of the ALT and MMT are combined. The MMT approach is used to predict leakage and fringing flux effects, whereas the ALT approach is used to predict the global effect of saturation and skewing on the fundamental magnetic field in the motor. The results of calculations performed on four benchmark IMs are validated against 2D FEA calculation, skewed FEA calculation and measurement results. The implementation details of the framework and the results of framework validation are thoroughly discussed in Chapter 5.

5. **To implement a semi-analytical framework for synchronous reluctance motor analysis including finite soft-magnetic material permeability:**
   For accurate SynRM analysis, it is important to take the finite permeability of the soft-magnetic material in the motor into account. Therefore, a semi-analytical framework for SynRM analysis is implemented based on the magnetic-field solution for inhomogeneous regions presented in Section 2.4. The implementation of this framework requires a suitable polar representation of the SynRM geometry, which is derived in terms of geometric parameters of the actual motor in Chapter 6. Further, the resulting model is applied to a benchmark SynRM and validated against 2D FEA calculations.

Chapter 2

Harmonic modeling of magnetic structures in polar coordinates

The contents of this chapter are published in:

R. L. J. Sprangers, J. J. H. Paulides, B. L. J. Gysen and E. A. Lomonova, "Towards Magnetic Saturation in Semi-Analytical Harmonic Modeling,", *IEEE Trans. Magn.*, accepted: to be published.

2.1 Introduction

In recent literature, it was shown that harmonic modeling (HM) provides a suitable alternative to FEA in terms of accuracy and calculation time. However, one of the main limitations of HM is the required assumption of infinitely permeable soft-magnetic material to account for slotting. For PM-based devices, this assumption leads to relatively small discrepancies when calculating the back-emf, since the reluctance of the air gap and PMs is dominant. On the other hand, saturation of the iron core does influence the electric loading. Furthermore, for induction- and reluctance-based motors, the air gap is generally small to improve the performance of the machine. As a consequence, the influence of the finite soft-magnetic material permeability on the motor performance is much larger. Therefore, to obtain accurate calculation results for these types of machines, an extension of the previously used magnetic-field solutions is desired.

Two generalized solutions are presented for the magnetic-field distribution in a polar coordinate system. The first solution is based on the state-of-the-art harmonic modeling for electromagnetic actuators and is valid for regions with homogeneous, but possibly anisotropic, material properties. Therefore, it is referred to as the magnetic-field solution for homogeneous regions. The second solution presents an extension of the state-of-the-art and accounts for inhomogeneous material properties by considering circumferential variation of the magnetic permeability. Therefore, this solution is referred to as the magnetic-field solution for inhomogeneous regions. In both cases, separation of variables is applied, such that the circumferential dependency of the magnetic field can be expressed in terms of Fourier series. Further, the radial dependency of the magnetic field is derived analytically from Maxwell's equations in quasi-static form. To obtain the magnetic-field solutions, the unknown coefficients in the aforementioned expressions are solved using boundary conditions. A general description of each magnetic-field solution, boundary conditions and numerical implementation issues is given.

Finally, it should be mentioned that harmonic modeling is considered to be a semi-analytical modeling technique. Since the magnetic-field solutions discussed in this chapter all contain infinite series, truncation is required for any practical implementation of the models. Therefore, the resulting magnetic-field solution is always an approximation of the true analytical magnetic-field solution.

2.2 Assumptions and limitations

The electromagnetic field inside an electric motor is mathematically described by Maxwell's equations. If the frequency of the field variation is low enough, it may be assumed that the time required for the field to penetrate a device is negligible. For typical rotating electrical machines, this is generally the case [41] and therefore, they are considered quasi-static. Consequently, the magnetic-field equations derived later in this chapter are based on these quasi-static Maxwell equations.

Additionally, for many rotating electric machines, the geometry and its magnetic-field distribution do not vary significantly in the axial direction. Therefore, it is often justified to assume that the structure is infinite and invariant in the axial direction, such that the 3D geometry of the motor can be represented in a 2D polar coordinate system. Naturally, end effects are not taken into account by the 2D model, which may lead to incorrect calculation results if the axial length of the machine is short. Further, the influence of skewing is also neglected, which may lead to an overestimation of the average torque and torque ripple amplitude. A common solution to consider skewing is the use of a multi-slice model, as will be explained in more detail in Chapter 5.

If the geometry of the modeled motor exhibits periodicity, only one period of the geometry needs to be considered in the magnetic-field model. This periodic section is then divided into a finite number of regions with fixed angular width and radial height, each representing a part of the motor. To limit the number of regions, a suitable polar representation of the motor geometry is required. However, the chosen polar representation also affects the accuracy of the calculation results. Suitable polar representations of common IM and SynRM geometries are discussed in detail in Chapters 3 and 6, respectively. Further, a distinction is made between periodic regions and nonperiodic regions. Periodic regions are periodic in the circumferential direction, whereas nonperiodic regions are circumferentially bounded by infinitely permeable material. Also, a local coordinate system, $\left(r, \theta^k\right)$ is defined for each region k. For periodic regions, the local coordinate system is equal to the global polar coordinate system, (r, θ). For nonperiodic regions, however, the local coordinate system is circumferentially shifted with respect to the global coordinate system by θ_0^k.

Within each region, magnetic-field sources can be defined in terms of a current density, $\vec{J}$, or a remanent magnetization, $\vec{M}_0$. To comply with the assumed 2D polar coordinate system, current-density sources are assumed to be solely directed along the axial direction, whereas magnetization sources are assumed to be directed in the radial and/or circumferential direction. Also, all source terms are assumed to be invariant in the radial direction within a region, to limit the complexity of the magnetic-field solution. Moreover, in case of slotting, the current density within a slot is assumed to be homogeneously distributed. Due to the assumed homogeneous current density, skin and proximity effects are not taken into account by the model, although analytical corrections can be applied to (partially) compensate for such effects.

Within each region, all material properties are assumed to be linear and invariant in the radial direction. The conventional formulation of the magnetic-field solution used for HM assumes that the material properties are invariant in the circumferential direction as well. Therefore, it is referred to as the magnetic-field

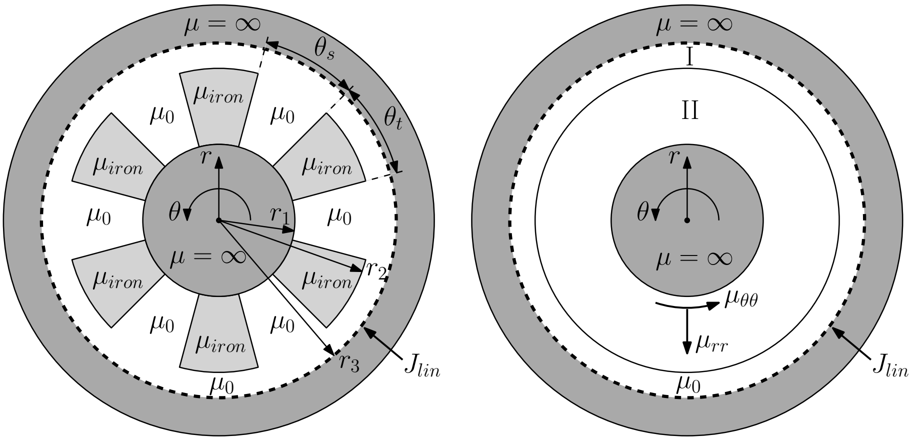

(a) Benchmark topology (b) ALT model

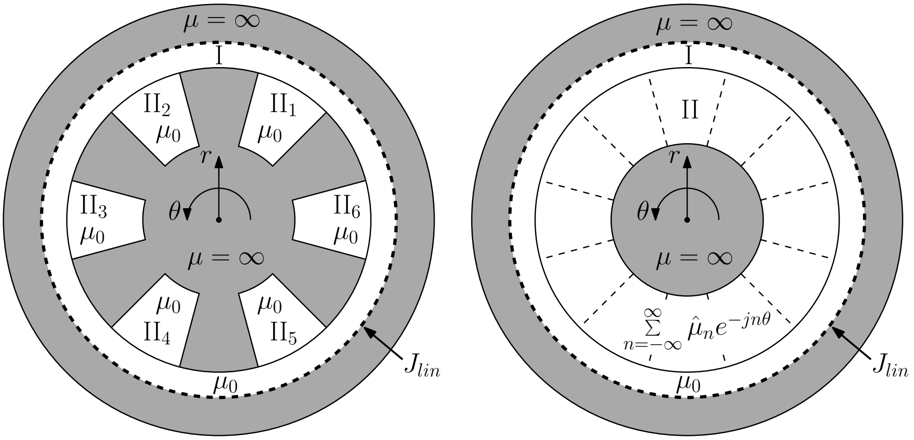

(c) MMT model (d) IRM model

Figure 2.1: Benchmark topology for comparison of the ALT, MMT and IRM modeling approaches and their respective model representations.

solution for homogeneous regions. To deal with magnetic structures with varying magnetic permeability, e.g. due to slotting, two different approaches are generally considered, namely Anisotropic Layer Theory (ALT) and Mode-Matching Theory (MMT). The ALT approach assumes that each region with permeability variations can be modeled as a homogeneous region with artificial, anisotropic material parameters. For example, the benchmark topology shown in Figure 2.1a is represented by the ALT model shown in Figure 2.1b, where region I represents the air gap and region II depicts the rotor slot/tooth region. Further, the MMT approach assumes that low permeability sections (e.g. slots or slot openings) can be represented by subregions, whereas high permeability sections (e.g. teeth or tooth tips) are assumed to be infinitely permeable. Each subregion should interface with a high permeability region at its circumferential boundaries. An example of an MMT model representation for the benchmark topology of Figure 2.1a is shown in Figure 2.1c.

The assumed circumferential invariance of the magnetic material properties in a region can, however, also be omitted. To this extent, a new formulation of the magnetic-field solution for HM in a polar coordinate system is presented. The circumferential magnetic permeability variation is expressed in terms of Fourier series, such that it can be included in the magnetic-field solution by means of convolution. This extended magnetic-field solution can be used to model regions with inhomogeneous material properties and is therefore referred to as the magnetic-field solution for inhomogeneous regions. Based on this solution, a new modeling approach for magnetic structures with varying magnetic material properties is defined, namely Inhomogeneous Region Modeling (IRM). An example of an IRM model representation for the benchmark topology of Figure 2.1a is shown in Figure 2.1d.

In this chapter, firstly the conventional magnetic-field solution for homogeneous regions, required for the ALT and MMT modeling approaches, is discussed. Secondly, the extended magnetic-field solution for inhomogeneous regions, required for the IRM modeling approach, is presented. To solve the unknown coefficients in the magnetic-field solution of each region, boundary conditions are used. Therefore, the required boundary conditions and their numerical implementation are briefly discussed next. Finally, a comparison between the conventional HM approaches, ALT and MMT, and the newly proposed IRM approach is given in terms of accuracy and calculation time for the benchmark topology shown in Figure 2.1a.

2.3 Magnetic field in homogeneous regions

A general description of the magnetic-field solution for homogeneous regions in a polar coordinate system is provided in this section. The solution includes polar anisotropy of the magnetic permeability and is used for the implementation of the ALT and MMT models discussed throughout this thesis. Firstly, the magnetic-field equation, required to solve the radial dependence of the magnetic field, is derived from the basic laws of electromagnetism. Secondly, a semi-analytical representation of the magnetic field and field sources is provided in terms of sine and cosine Fourier series. The magnetic-field equation is then solved to obtain an analytical expression for the magnetic field, including anisotropic magnetic permeability. The resulting magnetic-field solution is given in terms of the axial magnetic vector potential and the radial and circumferential components of the magnetic-flux density.

2.3.1 Deriving the magnetic-field equation

For the considered quasi-static problem, Ampère's law is given in differential form by

$$\nabla \times \vec{H} = \vec{J}, \tag{2.1}$$

where $\vec{H}$ is the magnetic-field strength and $\vec{J}$ is the electric-current density. Also, the relation between $\vec{H}$, the magnetic-flux density, $\vec{B}$, and the magnetization $\vec{M}$ is given by

$$\vec{B} = \mu_0 \left(\vec{H} + \vec{M} \right), \tag{2.2}$$

where μ_0 is the permeability of vacuum. The magnetization can be separated into two parts, namely $\vec{M}_0$ and $\vec{M}_s$. The first term, $\vec{M}_0$, represents a permanent-magnet source and is linked to the remanent magnetic-flux density, $\vec{B}_{rem}$, of a hard-magnetic material as

$$\vec{M}_0 = \frac{\vec{B}_{rem}}{\mu_0}. \tag{2.3}$$

Further, the secondary magnetization term, $\vec{M}_s$, appears when a magnetic field is applied to a magnetic material. The relation between $\vec{M}_s$ and $\vec{H}$ is given by

$$\vec{M}_s = \chi \vec{H}, \tag{2.4}$$

where χ is the magnetic susceptibility of the material. Substituting (2.3) and (2.4) into (2.2), the relation between $\vec{B}$, $\vec{H}$ and $\vec{M}$ can be rewritten as

$$\vec{B} = \mu \vec{H} + \mu_0 \vec{M}_0, \tag{2.5}$$

where $\mu = \mu_0 \mu_r$ is the magnetic permeability of the material and $\mu_r = (1 + \chi)$ represents the relative magnetic permeability of the material.

To take anisotropic materials into account, μ is written in tensor form as

$$\bar{\bar{\mu}} = \begin{bmatrix} \mu_{rr} & \mu_{r\theta} & \mu_{rz} \\ \mu_{\theta r} & \mu_{\theta\theta} & \mu_{\theta z} \\ \mu_{zr} & \mu_{z\theta} & \mu_{zz} \end{bmatrix}. \tag{2.6}$$

For the considered magnetic-field problems, it is assumed that there is no cross-coupling between the components of $\vec{H}$ and $\vec{B}$, such that $\mu_{r\theta} = \mu_{rz} = \mu_{\theta r} = \mu_{\theta z} = \mu_{zr} = \mu_{z\theta} = 0$. For a polar coordinate system, the permeability tensor then reduces to

$$\bar{\bar{\mu}} = \begin{bmatrix} \mu_{rr} & 0 \\ 0 & \mu_{\theta\theta} \end{bmatrix}, \tag{2.7}$$

where μ_{rr} and $\mu_{\theta\theta}$ are the magnetic permeabilities in the radial and circumferential directions, respectively.

Based on Gauss's law for magnetism, given in differential form by

$$\nabla \cdot \vec{B} = 0, \tag{2.8}$$

the magnetic vector potential, $\vec{A}$, can be defined as

$$\vec{B} = \nabla \times \vec{A}. \tag{2.9}$$

To limit the number of possible solutions for $\vec{A}$, the Coulomb gauge, given by

$$\nabla \cdot \vec{A} = 0, \tag{2.10}$$

is used to define the divergence of $\vec{A}$. Then, combining (2.1), (2.5), (2.7), (2.9) and (2.10), the magnetic-field equation for the considered polar coordinate system results in

$$\frac{\partial^2 A_z}{\partial r^2} + \frac{1}{r}\frac{\partial A_z}{\partial r} + \alpha^2 \frac{1}{r^2}\frac{\partial^2 A_z}{\partial \theta^2} = -\mu_0 \frac{1}{r}\left(M_\theta - \alpha^2 \frac{\partial M_r}{\partial \theta}\right) - \mu_{\theta\theta} J_z, \tag{2.11}$$

where α is given by

$$\alpha = \sqrt{\frac{\mu_{\theta\theta}}{\mu_{rr}}}. \tag{2.12}$$

A unique solution for $\vec{A}$ can be obtained for a specific situation by means of boundary conditions.

2.3.2 Semi-analytical magnetic-field representation

In case of 2D analysis, the magnetic-field solution for each homogeneous region k can be expressed in terms of Fourier series as [147]

$$\vec{A}^k = A_z^k \left(r, \theta^k\right) \vec{u}_z, \tag{2.13}$$

$$\begin{aligned} A_z^k \left(r, \theta^k\right) = &\sum_{n=1}^{\infty} \left[A_{zcn}^k (r) \cos\left(w_n^k \theta^k\right) + A_{zsn}^k (r) \sin\left(w_n^k \theta^k\right)\right] \\ &+ A_{z0}^k (r), \end{aligned} \tag{2.14}$$

where A_{zcn}^k, A_{zsn}^k and A_{z0}^k represent the Fourier-series coefficients of A_z^k. The (dimensionless) circumferential periodicity of each harmonic order n is given by

$$w_n^k = \frac{n\pi}{\theta_p^k}, \tag{2.15}$$

where θ_p^k represents the fundamental pole angle of region k. Further, a local coordinate system, $\left(r, \theta^k\right)$, is defined for each region, where θ^k is the circumferential position in the local coordinate system. Similar to $\vec{A}^k$, a semi-analytical expression for $\vec{B}$ is given by

$$\vec{B}^k = B_r^k\left(r,\theta^k\right)\vec{u}_r + B_{\theta^k}^k\left(r,\theta\right)\vec{u}_\theta, \tag{2.16}$$

$$B_r^k\left(r,\theta^k\right) = \sum_{n=1}^{\infty}\left[B_{rcn}^k\left(r\right)\cos\left(w_n^k\theta^k\right) + B_{rsn}^k\left(r\right)\sin\left(w_n^k\theta^k\right)\right], \tag{2.17}$$

$$B_\theta^k\left(r,\theta^k\right) = \sum_{n=1}^{\infty}\left[B_{\theta cn}^k\left(r\right)\cos\left(w_n^k\theta^k\right) + B_{\theta sn}^k\left(r\right)\sin\left(w_n^k\theta^k\right)\right] + B_{\theta 0}^k, \tag{2.18}$$

where B_{rcn}^k, B_{rsn}^k, $B_{\theta cn}^k$, $B_{\theta sn}^k$ and $B_{\theta 0}^k$ represent the Fourier-series coefficients of B_r^k and B_θ^k for each region.

Expressions for the Fourier-series coefficients of A_z^k, B_r^k and B_θ^k are derived by solving the magnetic-field equation. Firstly however, to comply with the solution of $\vec{A}^k$, any circumferential distribution of the source terms $\vec{M}_0^k$ and $\vec{J}^k$ should be expressed as a Fourier series as well. For regions with one or more permanent-magnet sources, $\vec{M}_0^k$ is therefore defined as

$$\vec{M}_0^k = M_r^k\left(\theta^k\right)\vec{u}_r + M_\theta^k\left(\theta^k\right)\vec{u}_\theta, \tag{2.19}$$

$$M_r^k\left(\theta^k\right) = \sum_{n=1}^{\infty}\left[M_{rcn}^k\cos\left(w_n^k\theta^k\right) + M_{rsn}^k\sin\left(w_n^k\theta^k\right)\right] + M_{r0}^k, \tag{2.20}$$

$$M_\theta^k\left(\theta^k\right) = \sum_{n=1}^{\infty}\left[M_{\theta cn}^k\cos\left(w_n^k\theta^k\right) + M_{\theta sn}^k\sin\left(w_n^k\theta^k\right)\right] + M_{\theta 0}^k, \tag{2.21}$$

where M_{rcn}^k, M_{rsn}^k, M_{r0}^k, $M_{\theta cn}^k$, $M_{\theta sn}^k$ and $M_{\theta 0}^k$ represent the Fourier-series coefficients of M_r^k and M_θ^k, respectively. Further, for regions with one or more current-density sources, $\vec{J}^k$ is defined as

$$\vec{J}^k = J_z^k\left(\theta^k\right)\vec{u}_z, \tag{2.22}$$

$$J_z^k\left(\theta^k\right) = \sum_{n=1}^{\infty}\left[J_{zcn}^k\cos\left(w_n^k\theta^k\right) + J_{zsn}^k\sin\left(w_n^k\theta^k\right)\right] + J_{z0}^k, \tag{2.23}$$

where J_{zcn}^k, J_{zsn}^k and J_{z0}^k are the Fourier-series coefficients of $J_z^k\left(\theta\right)$.

Assuming that the distribution of the sources within a region is known, the dc, sine and cosine coefficients are calculated using

$$K_0 = \frac{1}{2\theta_p^k}\int_0^{2\theta_p^k} K\left(\theta\right)d\theta^k, \tag{2.24}$$

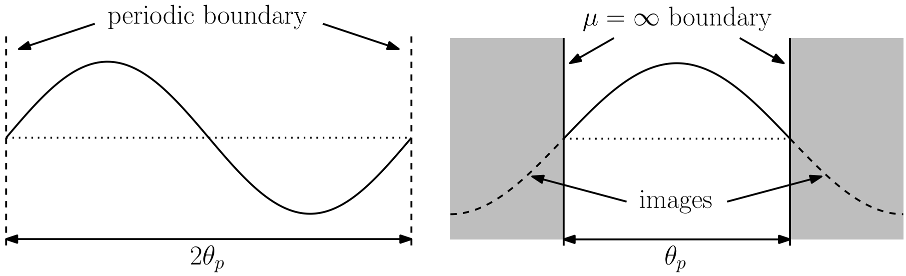

(a) Periodic region (b) Nonperiodic region

Figure 2.2: Definition of the fundamental pole angle, θ_p, for a) periodic and b) nonperiodic regions.

$$K_{cn} = \frac{1}{\theta_p^k} \int_0^{2\theta_p^k} K(\theta) \cos\left(w_n^k \theta^k\right) d\theta^k, \tag{2.25}$$

$$K_{sn} = \frac{1}{\theta_p^k} \int_0^{2\theta_p^k} K(\theta) \sin\left(w_n^k \theta^k\right) d\theta^k, \tag{2.26}$$

where $K(\theta)$ represents any source term, including M_r, M_θ and J_z. For periodic regions, θ_p^k is equal to half of the period, as shown in Figure 2.2a. For regions bounded by infinitely permeable material in the circumferential direction, however, the imaging method [122, 147] is used to obtain a periodic representation of the source terms. This representation is then used to evaluate (2.24) to (2.26) and obtain the source-term Fourier-series coefficients. The fundamental spatial harmonic of these nonperiodic regions spans twice the region width, such that θ_p^k is equal to the region width as shown in Figure 2.2a

2.3.3 Magnetic-field solution

The magnetic-field equation given by (2.11) is solved using (2.14). As a result, semi-analytical expressions for the Fourier-series coefficients, A_{zcn}^k, A_{zsn}^k and A_{z0}^k, are obtained as

$$A_{zcn}^k(r) = -\frac{1}{w_n^k}\left(a_n^k r^{\alpha^k w_n^k} + b_n^k r^{-\alpha^k w_n^k} + rG_{rsn}^k(r)\right), \tag{2.27}$$

$$A_{zsn}^k(r) = -\frac{1}{w_n^k}\left(c_n^k r^{\alpha^k w_n^k} + d_n^k r^{-\alpha^k w_n^k} - rG_{rcn}^k(r)\right), \tag{2.28}$$

$$A_{z0}^k(r) = -\mu_{\theta\theta}^k \frac{J_{z0}^k}{4} r^2 - \mu_0 M_{\theta 0}^k r + B_0^k \ln(r) + A_0^k. \tag{2.29}$$

Furthermore, expressions for the Fourier-series coefficients of $B_r^k(r)$ and $B_\theta^k(r)$ are obtained using (2.9) and given by

$$B_{rcn}^k(r) = -c_n^k r^{\alpha^k w_n^k - 1} - d_n^k r^{-\alpha^k w_n^k - 1} + G_{rcn}^k(r), \tag{2.30}$$

$$B_{rsn}^k(r) = a_n^k r^{\alpha^k w_n^k - 1} + b_n^k r^{-\alpha^k w_n^k - 1} + G_{rsn}^k(r), \tag{2.31}$$

$$B_{\theta cn}^k(r) = \alpha^k a_n^k r^{\alpha^k w_n^k - 1} - \alpha^k b_n^k r^{-\alpha^k w_n^k - 1} + G_{\theta cn}^k(r), \tag{2.32}$$

$$B_{\theta sn}^k(r) = \alpha^k c_n^k r^{\alpha^k w_n^k - 1} - \alpha^k d_n^k r^{-\alpha^k w_n^k - 1} + G_{\theta sn}^k(r), \tag{2.33}$$

$$B_{\theta 0}^k(r) = \mu_{\theta\theta}^k \frac{J_{z0}^k}{2} r + \mu_0 M_{\theta 0}^k - \frac{B_0^k}{r}. \tag{2.34}$$

In (2.27) to (2.34), the terms G_{rcn}^k, G_{rsn}^k, $G_{\theta cn}^k$ and $G_{\theta sn}^k$ describe the contribution of the field sources to the field solution and are given by

$$G_{rsn}^k(r) = \begin{cases} -\mu_0 \frac{M_{rsn}^k - w_n^k M_{\theta cn}^k}{2} \ln(r) + \mu_{\theta\theta}^k w_n^k \frac{J_{zcn}^k}{3} r & \alpha^k \left(w_n^k\right)^2 = 1, \\ \mu_0 \frac{4M_{rsn}^k - w_n^k M_{\theta cn}^k}{3} + \mu_{\theta\theta}^k w_n^k \frac{J_{zcn}^k}{4} r \ln(r) & \alpha^k \left(w_n^k\right)^2 = 4, \\ -\mu_0 w_n^k \frac{\alpha^k w_n^k M_{rsn}^k - M_{\theta cn}^k}{1 - \alpha^k (w_n^k)^2} + \mu_{\theta\theta}^k w_n^k \frac{J_{zcn}^k}{4 - \alpha^k (w_n^k)^2} r & \text{else}, \end{cases} \tag{2.35}$$

$$G_{rcn}^k(r) = \begin{cases} -\mu_0 \frac{M_{rcn}^k + w_n^k M_{\theta sn}^k}{2} \ln(r) - \mu_{\theta\theta}^k w_n^k \frac{J_{zsn}^k}{3} r & \alpha^k \left(w_n^k\right)^2 = 1, \\ \mu_0 \frac{4M_{rcn}^k + w_n^k M_{\theta sn}^k}{3} - \mu_{\theta\theta}^k w_n^k \frac{J_{zsn}^k}{4} r \ln(r) & \alpha^k \left(w_n^k\right)^2 = 4, \\ -\mu_0 w_n^k \frac{\alpha^k w_n^k M_{rcn}^k + M_{\theta sn}^k}{1 - \alpha^k (w_n^k)^2} - \mu_{\theta\theta}^k w_n^k \frac{J_{zsn}^k}{4 - \alpha^k (w_n^k)^2} r & \text{else}, \end{cases} \tag{2.36}$$

$$G_{\theta sn}^k(r) = \begin{cases} \mu_0 \frac{\alpha^k w_n^k M_{rcn}^k + M_{\theta sn}^k}{2} (\ln(r) + 1) + \mu_{\theta\theta}^k \frac{2J_{zsn}^k}{3} r & \alpha^k \left(w_n^k\right)^2 = 1, \\ -\mu_0 \frac{\alpha^k w_n^k M_{rcn}^k + M_{\theta sn}^k}{3} + \mu_{\theta\theta}^k \frac{J_{zsn}^k}{4} r (1 + 2\ln(r)) & \alpha^k \left(w_n^k\right)^2 = 4, \\ \mu_0 \frac{\alpha^k w_n^k M_{rcn}^k + M_{\theta sn}^k}{1 - \alpha^k (w_n^k)^2} + \mu_{\theta\theta}^k \frac{2J_{zsn}^k}{4 - \alpha^k (w_n^k)^2} r & \text{else}, \end{cases} \tag{2.37}$$

$$G_{\theta cn}^k(r) = \begin{cases} -\mu_0 \frac{\alpha^k w_n^k M_{rsn}^k - M_{\theta cn}^k}{2} (1 + \ln(r)) + \mu_{\theta\theta}^k \frac{2J_{zcn}^k}{3} r & \alpha^k \left(w_n^k\right)^2 = 1, \\ \mu_0 \frac{\alpha^k w_n^k M_{rsn}^k - M_{\theta cn}^k}{3} + \mu_{\theta\theta}^k \frac{J_{zcn}^k}{4} r (1 + 2\ln(r)) & \alpha^k \left(w_n^k\right)^2 = 4, \\ -\mu_0 \frac{\alpha^k w_n^k M_{rsn}^k - M_{\theta cn}^k}{1 - \alpha^k (w_n^k)^2} + \mu_{\theta\theta}^k \frac{2J_{zcn}^k}{4 - \alpha^k (w_n^k)^2} r & \text{else}. \end{cases} \tag{2.38}$$

The coefficients a_n^k, b_n^k, c_n^k and d_n^k are initially unknown and will be solved numerically by means of boundary conditions. The boundary conditions and their resulting system matrix equation are discussed in Section 2.5.

2.4 Magnetic field in inhomogeneous regions

In this section, a new formulation of the magnetic-field solution for HM in polar coordinates is presented. In contrast to the conventional magnetic-field solution for HM, as presented in the previous section, the new formulation takes circumferential variation of the magnetic permeability into account. It can be applied to regions which are inhomogeneous along the circumferential direction, for example to solve the magnetic field inside regions that consisting of both slots and soft-magnetic teeth. Firstly, a semi-analytical description of the magnetic field and its source terms is provided, followed by the derivation of the magnetic-field equation. Secondly, the Toeplitz matrices, which appear in the magnetic-field solution due to the permeability variation, are discussed. Then, the magnetic-field equation is solved analytically and the solutions of the magnetic vector potential, the magnetic-flux density and the magnetic-field strength expressed analytically in matrix form.

2.4.1 Semi-analytical magnetic-field representation

For each inhomogeneous region k, the solution of the axial component of the magnetic vector potential is defined by a complex Fourier series as

$$A_z^k(r,\theta) = \sum_{n=-\infty}^{\infty} \hat{A}_{z,n}^k(r)\, e^{-jn\theta}, \tag{2.39}$$

where n is the harmonic ordinal number. Similarly, the radial and circumferential components of the magnetic-flux density and the magnetic-field strength are represented as

$$B_r^k(r,\theta) = \sum_{n=-\infty}^{\infty} \hat{B}_{r,n}^k(r)\, e^{-jn\theta}, \tag{2.40}$$

$$B_\theta^k(r,\theta) = \sum_{n=-\infty}^{\infty} \hat{B}_{\theta,n}^k(r)\, e^{-jn\theta}, \tag{2.41}$$

$$H_r^k(r,\theta) = \sum_{n=-\infty}^{\infty} \hat{H}_{r,n}^k(r)\, e^{-jn\theta}, \tag{2.42}$$

$$H_\theta^k(r,\theta) = \sum_{n=-\infty}^{\infty} \hat{H}_{\theta,n}^k(r)\, e^{-jn\theta}. \tag{2.43}$$

The terms $\hat{A}^k_{z,n}$, $\hat{B}^k_{r,n}$, $\hat{B}^k_{\theta,n}$, $\hat{H}^k_{r,n}$ and $\hat{H}^k_{\theta,n}$ are the complex Fourier-series coefficients. It should be noted here that all inhomogeneous regions considered in this thesis are assumed to have periodic circumferential boundaries. In this case, the average values of the magnetic-field quantities, represented by $n = 0$, are zero.

Complex Fourier-series representations of the source-term components $J^k_z(\theta)$, $M^k_r(\theta)$ and $M^k_\theta(\theta)$ are given by

$$J^k_z(\theta) = \sum_{n=-\infty}^{\infty} \hat{J}^k_{z,n} e^{-jn\theta}, \tag{2.44}$$

$$M^k_r(\theta) = \sum_{n=-\infty}^{\infty} \hat{M}^k_{r,n} e^{-jn\theta}, \tag{2.45}$$

$$M^k_\theta(\theta) = \sum_{n=-\infty}^{\infty} \hat{M}^k_{\theta,n} e^{-jn\theta}, \tag{2.46}$$

where $\hat{J}^k_{z,n}$, $\hat{M}^k_{r,n}$ and $\hat{M}^k_{\theta,n}$ are the complex Fourier-series coefficients. Further, to include the circumferential variation of the magnetic permeability, its circumferential distribution is represented as a complex Fourier series as well. For $\mu^k(\theta)$, the Fourier-series expansion is given by

$$\mu^k(\theta) = \sum_{n=-\infty}^{\infty} \hat{\mu}^k_n e^{-jn\theta}, \tag{2.47}$$

where $\hat{\mu}^k_n$ represents the complex Fourier-series coefficients of the permeability distribution. For the reciprocal of the permeability distribution, $1/\mu^k(\theta)$, the Fourier-series expansion is given by

$$\frac{1}{\mu^k(\theta)} = \sum_{n=-\infty}^{\infty} \hat{\mu}^{rec,k}_n e^{-jn\theta}, \tag{2.48}$$

where $\hat{\mu}^{rec,k}_n$ represents the complex Fourier-series coefficients of the reciprocal permeability distribution. Assuming that the distribution of sources and material properties is known, the complex Fourier-series coefficients of each source term, $J^k_z(\theta)$, $M^k_r(\theta)$ or $M^k_\theta(\theta)$, or permeability distribution, $\mu^k(\theta)$ or $1/\mu^k(\theta)$, are calculated for each value of n as

$$\hat{K}^k_n = \frac{1}{2\pi} \int_{-\pi}^{\pi} K^k(\theta) e^{jn\theta} d\theta, \tag{2.49}$$

where $K^k(\theta)$ is any circumferential source or material property distribution.

Similar to the magnetic-field equation for homogeneous regions, the magnetic-field equation for inhomogeneous regions is derived from the quasi-static form of Ampère's law. However, since the magnetic permeability of the material is described as a Fourier-series summation, a product of two sums appears in the right-hand side of (2.5). Using Cauchy's product theorem, (2.5) is rewritten in terms of Fourier-series coefficients for each value of n as

$$\hat{B}_{r,n}(r) = \sum_{n'=-\infty}^{\infty} \hat{\mu}_{n-n'} \hat{H}_{r,n'}(r) + \mu_0 \hat{M}_{r,n}, \tag{2.50}$$

$$\hat{B}_{\theta,n}(r) = \sum_{n'=-\infty}^{\infty} \hat{\mu}_{n-n'} \hat{H}_{\theta,n'}(r) + \mu_0 \hat{M}_{\theta,n}. \tag{2.51}$$

The summations in (2.50) and (2.51) represent a convolution. For conciseness, (2.50) and (2.51) are written in matrix form as

$$\mathbf{B}_r = \boldsymbol{\mu}_{c,r} \mathbf{H}_r + \mu_0 \mathbf{M}_r, \tag{2.52}$$

$$\mathbf{B}_\theta = \boldsymbol{\mu}_{c,\theta} \mathbf{H}_\theta + \mu_0 \mathbf{M}_\theta, \tag{2.53}$$

where $\mathbf{B}_r$, $\mathbf{B}_\theta$, $\mathbf{H}_r$, $\mathbf{H}_\theta$, $\mathbf{M}_r$ and $\mathbf{M}_\theta$ are column vectors representing $\hat{B}_{r,n}$, $\hat{B}_{\theta,n}$, $\hat{H}_{r,n}$, $\hat{H}_{\theta,n}$, $\hat{M}_{r,n}$ and $\hat{M}_{\theta,n}$ for each value of n. Furthermore, $\boldsymbol{\mu}_{c,r}$ and $\boldsymbol{\mu}_{c,\theta}$ are the magnetic permeability Toeplitz matrices. The definition of these Toeplitz matrices is discussed in Section 2.4.2, as special care should be taken in order to avoid convergence problems. Firstly, however, the derivation of the magnetic-field equation is described.

Following the previous trend, (2.9) is rewritten in matrix form as

$$\mathbf{B}_r = \frac{1}{r} \frac{\partial \mathbf{A}_z}{\partial \theta} = -j \frac{1}{r} \mathbf{K}_\theta \mathbf{A}_z, \tag{2.54}$$

$$\mathbf{B}_\theta = -\frac{\partial \mathbf{A}_z}{\partial r}, \tag{2.55}$$

where $\mathbf{K}_\theta$ is the diagonal matrix of n, given by

$$\mathbf{K}_\theta = \begin{bmatrix} -N_{sh} & \dots & 0 \\ \vdots & \ddots & \vdots \\ 0 & \dots & N_{sh} \end{bmatrix}, \tag{2.56}$$

where N_{sh} denotes the number of positive spatial harmonics. Then, substituting (2.54) into (2.52) and (2.55) into (2.53), expressions for $\mathbf{H}_r$ and $\mathbf{H}_\theta$ are obtained as

$$\mathbf{H}_r = -j \frac{1}{r} \boldsymbol{\mu}_{c,r}^{-1} \mathbf{K}_\theta \mathbf{A}_z - \mu_0 \boldsymbol{\mu}_{c,r}^{-1} \mathbf{M}_r, \tag{2.57}$$

$$\mathbf{H}_\theta = -\boldsymbol{\mu}_{c,\theta}^{-1} \frac{\partial \mathbf{A}_z}{\partial r} - \mu_0 \boldsymbol{\mu}_{c,\theta}^{-1} \mathbf{M}_\theta. \tag{2.58}$$

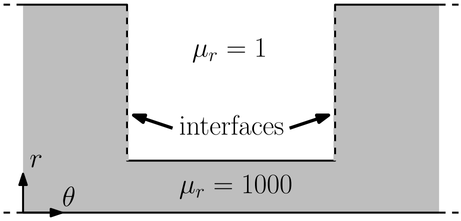

Figure 2.3: An example of discrete circumferential interfaces for a low-permeability slot in a high-permeability material.

Finally, (2.1) is rewritten in matrix form as

$$\frac{\partial \mathbf{H}_\theta}{\partial r} + \frac{1}{r}\mathbf{H}_\theta + j\frac{1}{r}\mathbf{K}_\theta \mathbf{H}_r = \mathbf{J}_z. \tag{2.59}$$

After substituting (2.57) and (2.58) into (2.59), the magnetic-field equation for inhomogeneous regions is obtained as

$$\frac{\partial^2 \mathbf{A}_z}{\partial r^2} + \frac{1}{r}\frac{\partial \mathbf{A}_z}{\partial r} - \frac{1}{r^2}\mathbf{V}\mathbf{A}_z = -\boldsymbol{\mu}_{c,\theta}\mathbf{J}_z - \mu_0\frac{1}{r}\mathbf{M}_\theta - j\mu_0\frac{1}{r}\mathbf{S}\mathbf{M}_r, \tag{2.60}$$

where $\mathbf{V} = \boldsymbol{\mu}_{c,\theta}\mathbf{K}_\theta\boldsymbol{\mu}_{c,r}^{-1}\mathbf{K}_\theta$ and $\mathbf{S} = \boldsymbol{\mu}_{c,\theta}\mathbf{K}_\theta\boldsymbol{\mu}_{c,r}^{-1}$.

2.4.2 Permeability Toeplitz matrices

On the discrete boundary between two permeability values, μ_1 and μ_2, the obtained magnetic-field solution is assumed to obey the continuity conditions given by

$$B_n^{\mu_2} - B_n^{\mu_1} = 0, \tag{2.61}$$
$$H_t^{\mu_2} - H_t^{\mu_1} = 0, \tag{2.62}$$

where B_n represents the magnetic-flux density normal to the boundary surface and H_t is the magnetic-field strength tangential to the boundary surface. Consequently, H_n and B_t are discontinuous across the boundary due to the difference in permeability. To reduce convergence problems in the magnetic-field description at these boundaries, care should be taken in the calculation of the magnetic permeability Toeplitz matrices, $\boldsymbol{\mu}_{c,r}$ and $\boldsymbol{\mu}_{c,\theta}$. At the boundary between, for example, a low permeability material (air, copper, etc.) and a high permeability material (soft-magnetic iron), such as shown in Figure 2.3, two different cases may arise. The first case is represented by (2.52), where the continuity conditions dictate that a discontinuous quantity, B_r, results from the convolution of the discontinuous permeability distribution and a continuous quantity, H_r. Therefore, the left- and right-hand sides of (2.52) will converge at the same rate, such that the Toeplitz matrix $\boldsymbol{\mu}_{c,r}$ can be expressed as

$$\boldsymbol{\mu}_{c,r} = \boldsymbol{\mu} = \begin{bmatrix} \hat{\mu}_0 & \cdots & \hat{\mu}_{-2N_{sh}} \\ \vdots & \ddots & \vdots \\ \hat{\mu}_{2N_{sh}} & \cdots & \hat{\mu}_0 \end{bmatrix}, \tag{2.63}$$

where N_{sh} is the number of positive spatial harmonics. The coefficients of $\boldsymbol{\mu}$ are equal to the Fourier coefficients of $\mu(\theta)$ for the indicated values of n, as defined by (2.47).

The second case is represented by (2.53), where the continuity conditions imply that a continuous quantity, B_θ, results from the convolution of the discontinuous permeability distribution and a discontinuous quantity, H_θ. Therefore, the right-hand side of (2.53) converges slower than the left-hand side. To solve this problem, a method called Fast Fourier Factorization (FFF) was independently proposed in [148] and [149], whereas a mathematical foundation for the method is presented in [150]. According to FFF, $\boldsymbol{\mu}_{c,\theta}$ should be calculated as the inverse of the Toeplitz matrix of the reciprocal of $\mu(\theta)$, and is expressed as

$$\boldsymbol{\mu}_{c,\theta} = \left(\boldsymbol{\mu}_{c,\theta}^{rec}\right)^{-1} = \begin{bmatrix} \hat{\mu}_0^{rec} & \cdots & \hat{\mu}_{-2N_{sh}}^{rec} \\ \vdots & \ddots & \vdots \\ \hat{\mu}_{2N_{sh}}^{rec} & \cdots & \hat{\mu}_0^{rec} \end{bmatrix}^{-1}. \tag{2.64}$$

The coefficients of $\boldsymbol{\mu}_{c,\theta}^{rec}$ are equal to the Fourier coefficients of $1/\mu(\theta)$ for the indicated values of n, as defined by (2.48).

2.4.3 Magnetic-field solution

The magnetic-field solution for inhomogeneous region k is obtained by solving the magnetic-field equation posed by (2.60). The solution of the complex Fourier coefficients of A_z^k is expressed in matrix form as

$$\mathbf{A}_z^k = \mathbf{W}^k r^{\boldsymbol{\lambda}^k} \mathbf{a}^k + \mathbf{W}^k r^{-\boldsymbol{\lambda}^k} \mathbf{b}^k + r^2 \mathbf{G}_1^k + r \mathbf{G}_2^k. \tag{2.65}$$

Furthermore, the solution of the complex Fourier coefficients of B_r^k, B_θ^k, H_r^k and H_θ^k are given in matrix form by

$$\mathbf{B}_r^k = -j\frac{1}{r}\left(\mathbf{K}_\theta \mathbf{W}^k r^{\boldsymbol{\lambda}^k} \mathbf{a}^k + \mathbf{K}_\theta \mathbf{W}^k r^{-\boldsymbol{\lambda}^k} \mathbf{b}^k + r^2 \mathbf{K}_\theta \mathbf{G}_1^k + r \mathbf{K}_\theta \mathbf{G}_2^k\right), \tag{2.66}$$

$$\mathbf{B}_\theta^k = -\mathbf{W}^k \boldsymbol{\lambda}^k r^{\boldsymbol{\lambda}^k - 1} \mathbf{a}^k + \mathbf{W}^k \boldsymbol{\lambda}^k r^{-\boldsymbol{\lambda}^k - 1} \mathbf{b}^k - 2r \mathbf{G}_1^k - \mathbf{G}_2^k, \tag{2.67}$$

$$\begin{aligned} \mathbf{H}_r^k = \left(\boldsymbol{\mu}_{c,r}^k\right)^{-1} \Big[& -j\frac{1}{r}\Big(\mathbf{K}_\theta \mathbf{W}^k r^{\boldsymbol{\lambda}^k} \mathbf{a}^k + \mathbf{K}_\theta \mathbf{W}^k r^{-\boldsymbol{\lambda}^k} \mathbf{b}^k + r^2 \mathbf{K}_\theta \mathbf{G}_1^k \\ & + r \mathbf{K}_\theta \mathbf{G}_2^k\Big) - \mu_0 \mathbf{M}_r^k\Big], \end{aligned} \tag{2.68}$$

$$\begin{aligned} \mathbf{H}_\theta^k = \left(\boldsymbol{\mu}_{c,r}^k\right)^{-1} \Big[& -\mathbf{W}^k \boldsymbol{\lambda}^k r^{\boldsymbol{\lambda}^k - 1} \mathbf{a}^k + \mathbf{W}^k \boldsymbol{\lambda}^k r^{-\boldsymbol{\lambda}^k - 1} \mathbf{b}^k - 2r \mathbf{G}_1^k \\ & - \mathbf{G}_2^k - \mu_0 \mathbf{M}_\theta^k\Big]. \end{aligned} \tag{2.69}$$

The matrices $\mathbf{W}^k$ and $\boldsymbol{\lambda}^k$ represent the eigenvector matrix and the diagonal eigenvalue matrix of $(\mathbf{V}^k)^{\frac{1}{2}}$, respectively, and are obtained using eigendecomposition. For regions without circumferential magnetic permeability variation, e.g. the air gap of an electric motor, $\boldsymbol{\lambda}^k = \mathbf{K}_\theta$ and $\mathbf{W}^k$ is equal to an identity matrix of the size of $\mathbf{K}_\theta$. Also, the matrices $\mathbf{a}^k$ and $\mathbf{b}^k$ represent the unknown coefficient of the solution, to be solved by means of boundary conditions. Finally, the matrices $\mathbf{G}_1^k$ and $\mathbf{G}_2^k$ represent the contribution of the field sources and are calculated as

$$\mathbf{G}_1^k = -\left(4\mathbf{I} - \mathbf{V}^k\right)^{-1} \boldsymbol{\mu}_{c,\theta}^k \mathbf{J}_z^k, \tag{2.70}$$

$$\mathbf{G}_2^k = -\,\mu_0 \left(\mathbf{I} - \mathbf{V}^k\right)^{-1} \left(\mathbf{M}_\theta^k + \jmath \mathbf{S}^k \mathbf{M}_r^k\right), \tag{2.71}$$

where $\mathbf{I}$ is a diagonal identity matrix of the same size as $\mathbf{V}^k$.

2.5 Solving the boundary-condition equations

To determine the unknown coefficients in the magnetic-field solution, a system of equations that includes these coefficients is obtained using boundary conditions (BCs). Since the BCs along the circumferential direction of both periodic and nonperiodic regions are inherently satisfied by the chosen magnetic-field solution, only the BCs along the radial direction are used to generate the equation matrices. Different types of boundary conditions are distinguished, namely:

- Neumann boundary conditions
- Dirichlet boundary conditions
- Interface boundary conditions
- Mixed boundaries

A short overview of these boundary conditions is given here.

2.5.1 Neumann boundary conditions

For a function that describes the solution of an ordinary or partial differential equation, a Neumann boundary condition specifies the normal derivative of the function on the boundary of a domain. For the considered magnetic-field solution, this means that the partial derivative of A_z with respect to r should be specified. Furthermore, it is given by (2.9) that

$$\frac{\partial A_z}{\partial r} = -B_\theta = -\mu H_\theta. \tag{2.72}$$

Therefore, the Neumann boundary condition can be fulfilled by specifying B_θ or H_θ at the radius of a boundary, r_{bnd}. In this thesis, Neumann BCs are used to describe the magnetic field at the boundary of a region that interface with infinitely permeable magnetic material. In such materials, the magnetic-field strength is equal to zero. Therefore, the corresponding Neumann BC is given by

$$H_\theta^k\left(r,\theta^k\right)\big|_{r=r_{bnd}} = 0, \qquad \text{for} \quad 0 \leq \theta^k \leq \theta_w^k, \tag{2.73}$$

where θ_w^k is the width of region k.

2.5.2 Dirichlet boundary conditions

For Dirichlet boundary conditions, the value of a function that describes the solution of an ordinary or partial differential equation is specified on the boundary of a domain. This means that A_z should be defined for the considered magnetic-field solution. Furthermore, since the derivative of A_z with respect to θ can be evaluated analytically, it is found from (2.9) that for each harmonic n

$$\frac{\partial \hat{A}_{z,n} e^{-jn\theta}}{\partial \theta} = -\frac{1}{jn}\hat{A}_{z,n}e^{-jn\theta} = r\hat{B}_{r,n} = r\mu\hat{H}_{r,n}. \tag{2.74}$$

The Dirichlet boundary condition can thus be fulfilled by specifying B_r or H_r at the boundary radius, r_{bnd}. Therefore, Dirichlet BCs are used in this thesis to set the normal magnetic-flux density on a radial boundary to zero, such that the magnetic flux does not enter or leave the domain through the boundary. In such a case, the Dirichlet BC is given by

$$B_r^k\left(r,\theta^k\right)\big|_{r=r_{bnd}} = 0, \qquad \text{for} \quad 0 \leq \theta^k \leq \theta_w^k. \tag{2.75}$$

2.5.3 Interface boundary conditions

On the boundary between two equally wide, adjacent regions, k and $k+1$, interface boundary conditions are applied. If there is no surface current density on the boundary, the interface conditions are continuous and given by

$$B_r^{k+1} - B_r^k\big|_{r=r_{bnd}} = 0, \tag{2.76}$$

$$H_\theta^{k+1} - H_\theta^k\big|_{r=r_{bnd}} = 0. \tag{2.77}$$

However, if a linear surface current density, J_{bnd}, is present on the boundary, H_θ becomes discontinuous across the boundary. In this case, the interface boundary conditions are given by

$$B_r^{k+1} - B_r^k\big|_{r=r_{bnd}} = 0, \tag{2.78}$$

$$H_\theta^{k+1} - H_\theta^k\big|_{r=r_{bnd}} = J_{bnd}. \tag{2.79}$$

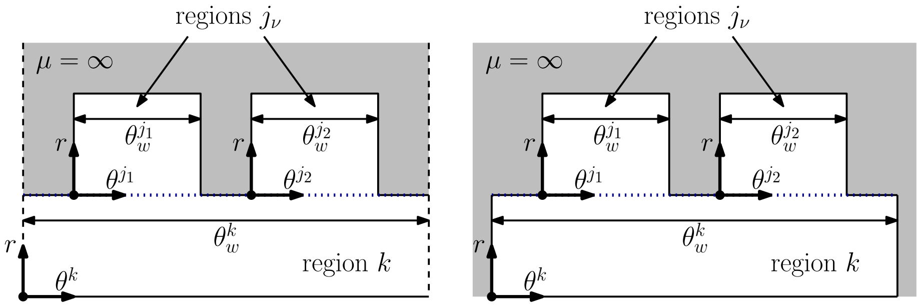

(a) Periodic region k (b) Nonperiodic region k

Figure 2.4: An example of a mixed boundary-condition problem for a) periodic region k and b) nonperiodic region k.

In this thesis, interface boundary conditions are applied on the boundaries between the periodic regions of the ALT and IRM models and between the equally wide, nonperiodic regions of the MMT models.

2.5.4 Mixed boundary conditions

If a region k interfaces with one or more regions of unequal width, mixed boundary conditions are applied. In this thesis, mixed boundary conditions are considered as a combination between interface boundary conditions and Neumann boundary conditions. They are applied to the boundary between a periodic region and one or more nonperiodic regions, as depicted by the example in Figure 2.4a. However, they may also be applied to the boundary between two or more nonperiodic regions, as shown by the example in Figure 2.4b. For both situations, k and j are region indices, whereas ν is the subregion index. Using these notations, the mixed boundary conditions are given by

$$\begin{aligned} B_r^{j_\nu}\left(r,\theta^{j_\nu}\right)\Big|_{r=r_{bnd}} &= \\ B_r^{k}\left(r,\theta^{k}\right)\Big|_{r=r_{bnd}} & \end{aligned} \quad \text{for} \quad \begin{cases} \theta^k = \theta^{j_\nu} + \left(\theta_0^{j_\nu} - \theta_0^k\right) & \text{and} \\ 0 \le \theta^{j_\nu} \le \theta_w^{j_\nu} & \text{and} \\ \nu = 1, ..., \mathcal{V}, & \end{cases} \tag{2.80}$$

$$H_\theta^k\left(r,\theta^k\right)\Big|_{r=r_{bnd}} = \begin{cases} \sum_{\nu=1}^{\mathcal{V}} H_\theta^{j_\nu}\left(r,\theta^{j_\nu}\right)\Big|_{r=r_{bnd}} & \text{for} \quad \begin{cases} \theta^k = \theta^{j_\nu} + \left(\theta_0^{j_\nu} - \theta_0^k\right) & \text{and} \\ 0 \le \theta^{j_\nu} \le \theta_w^{j_\nu}, & \end{cases} \\ 0 & \text{elsewhere}, \end{cases} \tag{2.81}$$

where θ_w is the angular width of a region and θ_0 is the angular position of the region with respect to the global coordinate system. Evaluating (2.80) and (2.81) for the field solution in homogeneous regions, a relation between the Fourier coefficients in k and j_ν is obtained using correlation functions. These functions serve to match the spatial modes of the magnetic-field solutions in k and j_ν, and are given in Appendix A.4.

If a nonperiodic region is situated between two mixed boundaries, additional equations are required in order to solve the constants $B_0^{j_\nu}$ and $A_0^{j_\nu}$. For $B_0^{j_\nu}$, these equations can be obtained using conservation of magnetic flux and Ampère's law, respectively given in integral form by

$$\oiint \vec{B} \cdot d\vec{S} = 0, \tag{2.82}$$

$$\oint \vec{H} \cdot d\vec{l} = \oiint \vec{J} \cdot d\vec{S}, \tag{2.83}$$

where the influence of PMs is embedded in the magnetic-field solutions obtained for $\vec{B}$ and $\vec{H}$. Further, the additional equations to obtain $A_0^{j_\nu}$ are found using continuity of the magnetic vector potential, given by

$$\int\limits_0^{\theta_w^{j_\nu}} A_z^{j_\nu}\left(r_{bnd}, \theta^{j_\nu}\right) d\theta^{j_\nu} = \int\limits_{\theta_p^{j_\nu}}^{\theta_p^{j_\nu}+\theta_w^{j_\nu}} A_z^{k}\left(r_{bnd}, \theta^{k}\right) d\theta^{k}. \tag{2.84}$$

A more thorough discussion of the boundary conditions for mixed boundaries can be found in [147]. Furthermore, some examples for the boundary conditions in specific modeling cases are given in Appendix A.

2.5.5 Numerical implementation

The equations obtained from the boundary conditions are expressed in matrix form as

$$\mathbf{E}\mathbf{X} = \mathbf{Y}, \tag{2.85}$$

where $\mathbf{X}$ and $\mathbf{Y}$ are column vectors representing the unknown coefficients and fixed values in the boundary-condition equations, respectively. Further, $\mathbf{E}$ is a square matrix representing the multiplication factors for the unknown coefficient. For any practical implementation of the presented magnetic-field solutions, the infinite Fourier summations are truncated. Consequently, the size of $\mathbf{X}$, $\mathbf{Y}$ and $\mathbf{E}$ is determined by the number of model regions and the number of positive spatial harmonics, N_{sh}. To obtain accurate calculation results, a large N_{sh} is required for the truncated Fourier summations in order to approximate an infinite summation. However, increasing N_{sh} also increases the required calculation time. Therefore,

N_{sh} should be carefully selected by checking the convergence of the calculation results for various values of N_{sh}.

Furthermore, large N_{sh} may also cause $\mathbf{E}$ to be ill-conditioned, leading to inaccuracies when solving the system of equations numerically. For the considered magnetic-field solution, the boundary conditions contain terms of the forms $a_n r^{x(n)}$ and $b_n r^{-x(n)}$, where $x\left(n\right)$ is a linear function of the spatial harmonic order, n. Consequently, for a given value of r, one of these terms will exponentially increase as a function of n, whereas the other term will exponentially decrease as a function of n. For large values of N_{sh}, the difference between the terms becomes so large that an accurate, numerical representation of both terms is not possible. As a result, the accuracy of the numerical results reduces. To improve the numerical accuracy, the unknown coefficients represented by $\mathbf{X}$ are scaled such that r is normalized. For the exponentially growing terms, r is normalized such that its resulting value is ≤ 1, whereas for exponentially decaying terms, r is normalized such that its resulting value is ≥ 1. For the given magnetic-field solution, scaling can therefore be applied to the unknown coefficients of region k as

$$\mathbf{a}^k_{n,scaled} = \left(r^k_o\right)^{x(n)} \mathbf{a}^k_n, \tag{2.86}$$

$$\mathbf{b}^k_{n,scaled} = \left(r^k_i\right)^{-x(n)} \mathbf{b}^k_n, \tag{2.87}$$

where r^k_i and r^k_o are the inner and outer radius of the region, respectively.

The number of spatial harmonics used in periodic regions, N^k_{sh}, should be equal for each periodic region, whereas the number of harmonics used in a nonperiodic region, $N^{j_\nu}_{sh}$, may differ. In fact, the ratio between $N^{j_\nu}_{sh}$ and N^k_{sh} influences the accuracy of the magnetic-field solution. To minimize the error, $N^{j_\nu}_{sh}$ should approximately be chosen according to [147]

$$N^{j_\nu}_{sh} = \left\lceil \frac{\theta^{j_\nu}_w}{\theta^k_w} N^k_{sh} \right\rceil . \tag{2.88}$$

If a region is very narrow, (2.88) gives $N^{j_\nu}_{sh} = 1$ even for large values of N^k_{sh}. In such cases, however, it is often beneficial to set $N^{j_\nu}_{sh}$ to 2 or 3. The effect of the selected number of harmonics is discussed in more detail in [151, 152]

Finally, there are several methods to solve (2.85) for $\mathbf{X}$. In principle, $\mathbf{X}$ can be obtained as

$$\mathbf{X} = \mathbf{E}^{-1}\mathbf{Y}, \tag{2.89}$$

although generally, the calculation of the inverse of $\mathbf{E}$ is computationally expensive. As an alternative, matrix decomposition methods, such as LU or QR decomposition, can be applied to $\mathbf{E}$ to solve for $\mathbf{X}$ faster. The models presented in this thesis are implemented in a Matlab software environment, where an operation called 'backslash-division' can be used. This operation starts an algorithm that automatically selects a suitable decomposition method and uses it to solve the system of equations.

Table 2.1: Parameters of the benchmark topology for comparison of the ALT, MMT and IRM modeling approaches.

Symbol	Value	Unit	Description
r_1	25	mm	Rotor yoke radius
r_2	39	mm	Rotor outer radius
r_3	40	mm	Stator inner radius
θ_{sl}	$\pi/6$	rad	Slot angle
θ_t	$\pi/6$	rad	Tooth angle

2.6 Benchmark comparison of harmonic models

In slotted electromagnetic motors and actuators, the soft-magnetic material that guides the magnetic flux is interrupted by regions with a low magnetic permeability. These regions often provide space for the conductive material of the windings or serve to prevent magnetic flux from flowing into a certain direction, such as in a SynRM. To analyse these slotted structures using harmonic modeling, three different approaches are considered, namely:

- Anisotropic Layer Theory (ALT)
- Mode-Matching Theory (MMT)
- Inhomogeneous Region Modeling (IRM)

To illustrate the advantages and disadvantages of these modeling approaches, each one has been implemented for a benchmark topology. Without stepping into details of each model implementation, a short description of the modeling differences is given. A more elaborate discussion of model implementations for each modeling approach is provided in Chapters 3 and 6 for more challenging magnetic structures. The purpose of this section, however, is to provide a comparison of the abilities of each approach, which is presented in terms of accuracy and required calculation time. For accuracy calculations, FEA simulations results are used as a reference.

2.6.1 Benchmark topology and implementation

The benchmark topology for comparison of the harmonic modeling approaches is shown in Figure 2.1a. It consists of an infinitely permeable stator, an air gap and a slotted rotor structure with an infinitely permeable back-iron, and its geometrical parameters are given in Table 2.1. For modeling purposes, the geometry can be divided into two regions, namely the air-gap region and the rotor tooth/slot region. The infinitely permeable stator and rotor back-iron are accounted for by Neumann boundary conditions. Further, the excitation of the model is provided

Table 2.2: Hardware specifications of the PC used for the benchmark comparison of the ALT, MMT and IRM modeling approaches.

Component	**Specification values**
Processor	Intel Core i7 870 (64 bit, 2.93 GHz)
Memory	16 GB
Graphics card	NVIDIA Quadro NVS 295
Operating System	Windows 7 Enterprise 64-bits

by a linear current density, J_{lin}, on the interface between the air gap and the stator. The circumferential distribution of J_{lin} is given by

$$J_{lin} = \begin{cases} \frac{z_Q I}{\theta_{exc} r_3} & \text{for} \quad -\frac{\theta_{exc}}{2} \leq \theta \leq \frac{\theta_{exc}}{2}, \\ -\frac{z_Q I}{\theta_{exc} r_3} & \text{for} \quad \left(\pi - \frac{\theta_{exc}}{2}\right) \leq \theta \leq \left(\pi + \frac{\theta_{exc}}{2}\right), \\ 0 & \text{otherwise}, \end{cases} \tag{2.90}$$

where $z_Q I = 1000$ represents the total excitation current and $\theta_{exc} = 2\pi/36$ is the angular width of the positive and negative excitation currents.

In the rotor tooth/slot region, the permeability varies between μ_0 and μ_{iron}. Each harmonic modeling approach deals with this variation in a different manner. Firstly, the ALT approach replaces the varying material properties by homogeneous material properties with an artificial anisotropy. The resulting anisotropic material properties represent the effective influence of the material variation. However, the exact distribution of the flux in the teeth and slots is not obtained. Secondly, the MMT approach only models the air gap and the rotor slots, whereas the rotor teeth are assumed to be infinitely permeable. Consequently, only the magnetic-field distribution in the air gap and the rotor slots is obtained. Also, the influence of a finite μ_{iron} is not taken into account. Finally, the IRM approach uses complex Fourier series to describe the permeability variation. Therefore, the magnetic-field distribution inside both rotor teeth and slots is obtained.

It should be noted that the same number of air-gap spatial harmonics is used for each model, namely $N_{sh}^{\mathrm{I}} = 50$. For the ALT and IRM models, this means that N_{sh}^{I} spatial harmonics are also used for the rotor tooth/slot region. For the MMT model, however, the number of spatial harmonics per rotor slot is determined using (2.88). Further, an overview of the specifications of the computer used to obtained the calculation results is given in Table 2.2.

2.6.2 Comparison of modeling results

For comparison of the modeling results, two rotor tooth relative permeability values are considered, namely $\mu_{r,iron} = 1000$ and $\mu_{r,iron} = 100$. With each model, the radial air-gap flux-density distribution, B_{rg}, is calculated at $r = (r_3 + r_2)/2$ and validated against FEA predictions. The calculation results are shown in

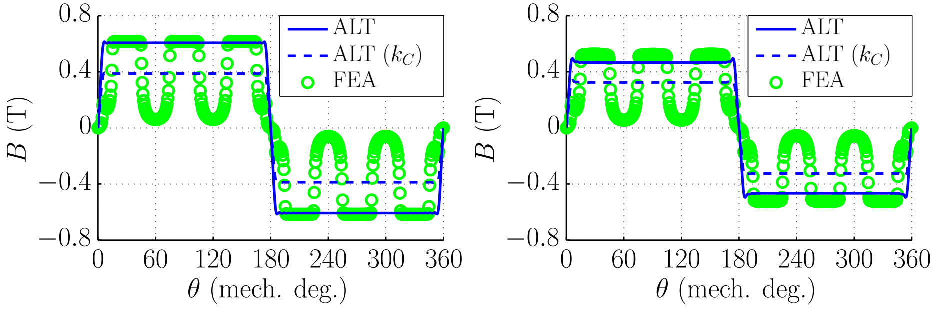

(a) (b)

Figure 2.5: Comparison of the radial air-gap flux-density calculated by ALT and linear 2D FEA for a) $\mu_{r,iron} = 1000$ and b) $\mu_{r,iron} = 100$.

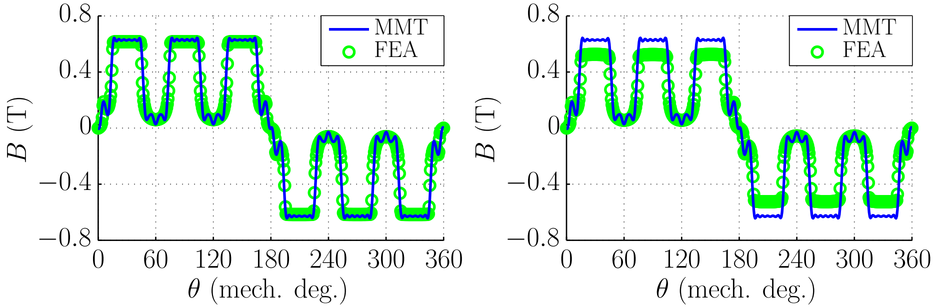

(a) (b)

Figure 2.6: Comparison of the radial air-gap flux-density calculated by MMT and linear 2D FEA for a) $\mu_{r,iron} = 1000$ and b) $\mu_{r,iron} = 100$.

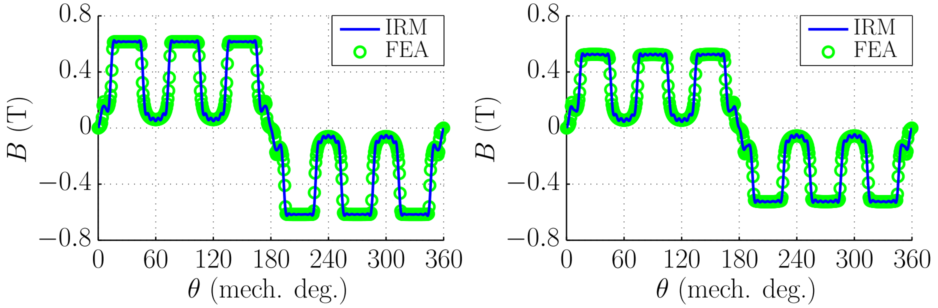

(a) (b)

Figure 2.7: Comparison of the radial air-gap flux-density calculated by IRM and linear 2D FEA for a) $\mu_{r,iron} = 1000$ and b) $\mu_{r,iron} = 100$.

Table 2.3: Comparison of the benchmark calculation results obtained from 2D FEA, ALT, MMT and IRM for $\mu_{r,iron} = 1000$.

Symbol	**Value**					**Unit**	**Description**
-	FEA	ALT	ALT	MMT	IRM	-	Model
k_C	-	1	1.59	-	-	-	Carter factor
B_{rg}^1	0.49	0.77	0.49	0.50	0.50	T	Fundamental B_{rg}
B_{rg}^{rms}	0.45	0.60	0.38	0.47	0.46	T	rms value B_{rg}
t_{exc}	1.4e3	6	6	18	129	ms	Execution time

Table 2.4: Comparison of the benchmark calculation results obtained from 2D FEA, ALT, MMT and IRM for $\mu_{r,iron} = 100$.

Symbol	**Value**					**Unit**	**Description**
-	FEA	ALT	ALT	MMT	IRM	-	Model
k_C	-	1	1.59	-	-	-	Carter factor
B_{rg}^1	0.42	0.59	0.41	0.50	0.42	T	Fundamental B_{rg}
B_{rg}^{rms}	0.38	0.46	0.32	0.47	0.39	T	rms value B_{rg}
t_{exc}	1.4e3	6	6	18	123	ms	Execution time

Figures 2.5 to 2.7. Furthermore, Tables 2.3 and 2.4 show a comparison of the results in terms of fundamental and effective radial air-gap flux-density, B_{rg}^1 and B_{rg}^{rms} respectively, and the required execution time of each model, t_{exc}.

For the ALT model, it can be seen that the influence of the rotor slots is not apparent in the air-gap magnetic-flux-density distribution. This means that fringing of the air-gap flux, due to the rotor slots, is not considered by the model. On average, this leads to an overestimation of both B_{rg}^1 and B_{rg}^{rms}. However, the simulation results obtained for $\mu_{r,iron} = 100$ do show decreased values of B_{rg}^1 and B_{rg}^{rms} in comparison to the results obtained for $\mu_{r,iron} = 1000$. To account for the global influence of flux fringing, the air-gap permeability of the ALT model is divided by Carter's factor, k_C. This coefficient is obtained from the MMT model using the methods described in Chapter 5. It can be seen from Tables 2.3 and 2.4 that this correction works well for B_{rg}^1, whereas B_{rg}^{rms} is underestimated. Further, it can be seen that the MMT model does consider the influence of the rotor slots on the air-gap magnetic-flux distribution. For $\mu_{r,iron} = 1000$, a good agreement is therefore obtained between the MMT model and FEA predictions. For $\mu_{r,iron} = 100$, however, it can clearly be seen that the assumption of infinitely permeable rotor teeth in the MMT model leads to a significant discrepancy. Finally, for the IRM model, it can be seen that a good agreement is obtained for both values of μ_{iron}. This shows that the IRM approach is able to accurately model the fringing flux as well as the influence of finite soft-magnetic material permeability in slotted structures. In terms of execution time, however, the IRM model requires significantly more time than the ALT and MMT models.

In the comparison, the execution time required for the FEA simulation is also given. It should be noted, however, that the mesh of the employed FEA model is not optimized for short execution time. Nevertheless, the advantage of the harmonic models over the FEA model is still apparent, especially for the ALT and MMT models.

Chapter 3

Harmonic modeling for Induction Motors

The contents of this chapter are published in:

R. L. J. Sprangers, J. J. H. Paulides, K. Boynov, E. A. Lomonova and J. Waarma, "Comparison of two anisotropic layer models applied to induction motors," *IEEE Trans. Ind. Appl.*, vol. 50, no. 4, pp. 2533-2543, July/August 2014.

R. L. J. Sprangers, J. J. H. Paulides, B. L. J. Gysen and E. A. Lomonova, "A fast semi-analytical model for the slotted structure of induction motors with 36/28 stator/rotor slot combination," in *Proceedings of Electrimacs 2014*, pp. 209-214, May 2014.

R. L. J. Sprangers, J. J. H. Paulides, B. L. J. Gysen and E. A. Lomonova, "A fast semi-analytical model for the slotted structure of induction motors," *Elsevier Mathematics and Computers in Simulation*, under review.

3.1 Introduction

To predict the performance of an IM, a suitable electromagnetic model is required. As discussed in Chapter 1, various approaches to obtain such a model have been studied in the past. One of these approaches, namely the ALT, represents an early form of harmonic modeling for slotted electric-motor structures. Further, two additional forms of harmonic modeling for slotted electric-motor structures were discussed in Chapter 2, namely the MMT and the IRM. In this chapter, the applicability of the ALT and the MMT for IM analysis are investigated in detail. The IRM is not considered for IM analysis, as a combination of ALT and MMT models is believed to be sufficient. The implementation of such a combined model will be presented in Chapter 5. Besides, the additional computation time required by IRM models makes it less attractive to be used for IM analysis, due to the relatively simple stator and rotor structure.

Two IM models are discussed in this chapter, namely the ALT model and the MMT model. For ALT models, slotted magnetic structures are dealt with through artificial homogenization of the material properties. The soft-magnetic material properties of the ALT model discussed in this chapter are updated iteratively based on nonlinear soft-magnetic material charactetistics. The advantage of this model, therefore, is its ability to account for global saturation of the fundamental magnetic-flux path in the IM. However, due to the homogenization of the slotted motor sections, leakage and fringing flux are not properly accounted for.

Further, MMT models deal with slotted magnetic structures by assuming that the soft-magnetic material that interfaces the slots at their circumferential boundaries is infinitely permeable. For the MMT model discussed here, this means that each slot is represented by one or more nonperiodic regions. The amplitude of the harmonics in the slot regions are correlated with the amplitude of the harmonics in the air gap using correlations functions. The advantage of the MMT model is its relatively accurate prediction of the magnetic-field distribution in the air gap and slots of the motor, which makes it suitable for prediction of leakage and fringing flux. The influence of finite soft-magnetic material permeability, however, is not taken into account.

The implementation of both models will be thoroughly discussed. Firstly, however, a general description of the geometry of a low-power IM is given, followed by the definition of four benchmark motor topologies. Finally, a short description of the 2D FEA models, implemented for each benchmark motor, is also given. These models are used to validate the calculation results of the ALT and MMT models.

3.2 Geometry and benchmark definitions

To implement the IM models in a general way, the IM geometry is parameterized. For a typical low-power IM, as shown in Figure 3.4, the geometry can roughly be divided into seven parts, namely:

1. The stator core, consisting of a yoke, teeth and tooth tips
2. The stator slots, containing the stator windings
3. The stator slot-openings
4. The air gap between the stator and rotor
5. The rotor slot-openings
6. The rotor slots, containing the squirrel-cage rotor conductors
7. The rotor core, consisting of a yoke, teeth and tooth tips

Based on the typical IM geometry, a number of geometric parameters is defined. An overview of these parameters is given in Figure 3.1 and Table 3.1. The values in Table 3.1 represent a set of four benchmark motors, which will be further introduced in Section 3.2.1.

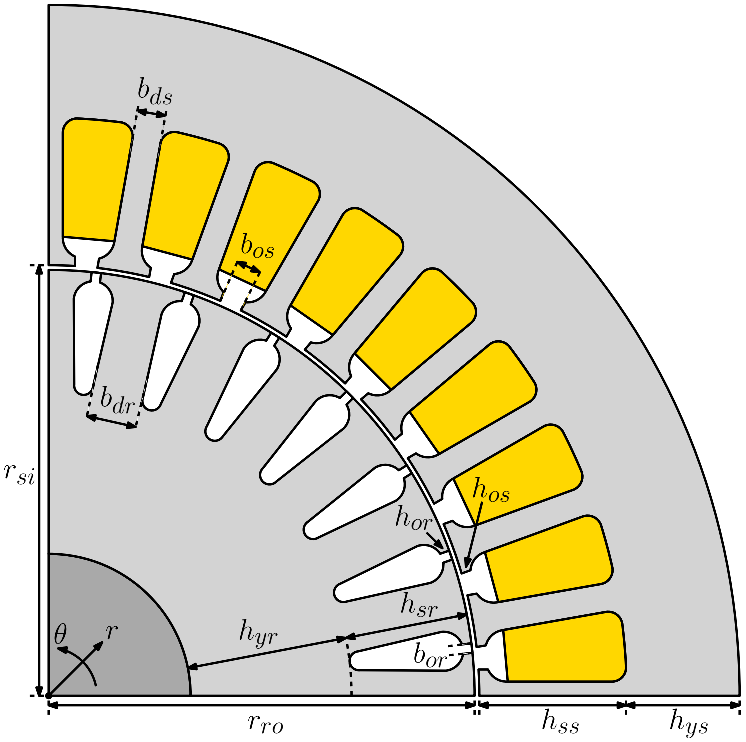

Figure 3.1: Geometric parameters of a typical, low-power induction motor.

Table 3.1: Geometric parameters of a typical induction motor geometry, expressed as radial and circumferential distances.

Symbol	**Value**				**Unit**	**Description**
-	1	2	3	4	-	Benchmark motor
Q_s	36	36	24	36	-	Stator slot number
Q_r	26	26	17	28	-	Rotor slot number
r_{si}	45	45	35	40	mm	Stator inner radius
r_{ro}	44.66	44.75	34.44	39.44	mm	Rotor outer radius
h_{ss}	14.3	14.3	15.0	15.5	mm	Stator slot height
h_{sr}	15.1	15.1	10.9	15.1	mm	Rotor slot height
h_{ys}	8.25	8.25	13.8	12.0	mm	Stator yoke height
h_{yr}	14.6	14.6	13.8	9.6	mm	Rotor yoke height
b_{ds}	3.8	3.8	4.8	3.63	mm	Stator tooth width
b_{dr}	5.75	5.75	5.34	4.39	mm	Rotor tooth width
b_{os}	2.3	2.3	2.05	2.3	mm	Stator slot opening width
b_{or}	1	1	1.2	1	mm	Rotor slot opening width
h_{os}	0.62	0.62	0.63	0.67	mm	Stator slot opening height
h_{or}	0.56	0.65	0.87	0.26	mm	Rotor slot opening height
l_{stk}	45	100	50	100	mm	Stack length
z_Q	185	68	160	44	-	Conductors per slot

The stator excitation of the motor is defined by the number of conductors per slot, z_Q, and the rms phase current, I_{ph}. For sinusoidal, balanced stator currents, the current density in the slots belonging to phases A, B and C are represented by a phasor, given by

$$\bar{J}_A = \frac{\bar{I}_A z_Q}{S_{ss}}, \tag{3.1}$$

$$\bar{J}_B = \frac{\bar{I}_B z_Q}{S_{ss}}, \tag{3.2}$$

$$\bar{J}_C = \frac{\bar{I}_C z_Q}{S_{ss}}, \tag{3.3}$$

where $\bar{I}_A$, $\bar{I}_B$ and $\bar{I}_C$ are the current phasors of phases A, B and C and S_{ss} is the surface area of the stator slots in the model. For current-fed simulations, fixed three-phase current phasors are defined for each phase as

$$\bar{I}_A = \sqrt{2} I_{ph} e^{j\Delta_{cur,s}}, \tag{3.4}$$

$$\bar{I}_B = \sqrt{2} I_{ph} e^{j\left(\Delta_{cur,s} - \frac{2\pi}{3}\right)}, \tag{3.5}$$

$$\bar{I}_C = \sqrt{2} I_{ph} e^{j\left(\Delta_{cur,s} + \frac{2\pi}{3}\right)}, \tag{3.6}$$

where $\Delta_{cur,s}$ is the stator current angle, which can be varied in order to change the orientation of the stator magnetic field. For voltage-fed simulations, the current depends on the impedance seen by the voltage sources. A method to calculate $\bar{I}_A$, $\bar{I}_B$ and $\bar{I}_C$ for voltage-fed simulations is discussed in Section 4.4.

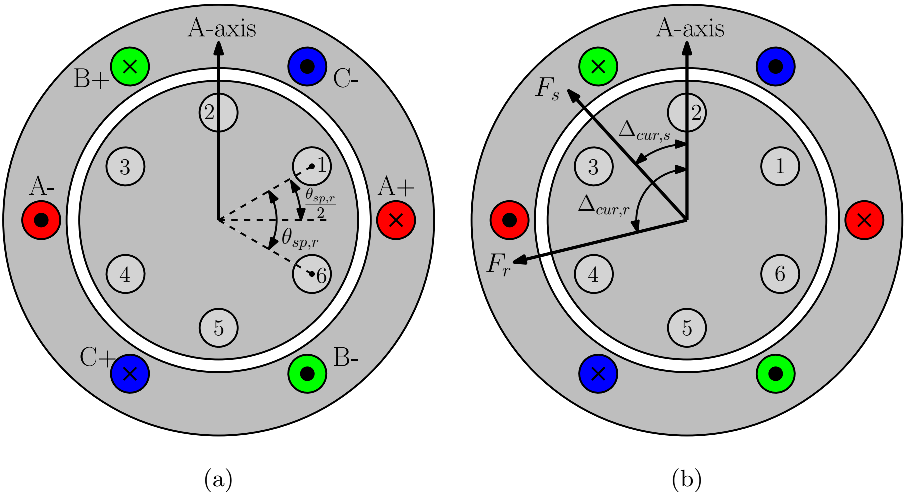

Figure 3.2: a) Simplified induction motor example and b) its stator and rotor magnetic-field representation.

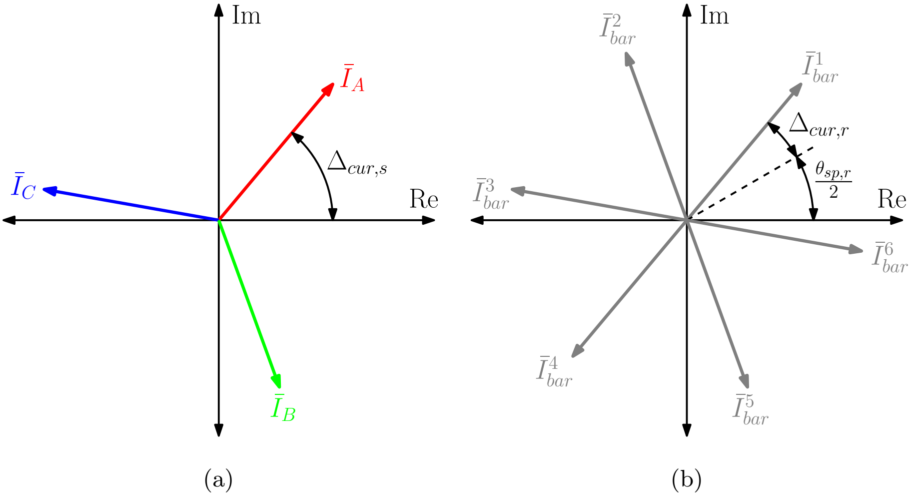

Figure 3.3: Phasor diagram of a) the stator phase current and b) the rotor-bar current for a simplified induction motor example.

Additionally, current will also flow through the bars of the rotor squirrel cage when it is operating under load. Assuming sinusoidal and balanced rotor-bar currents, the current density in the ν^{th} rotor bar is represented as a phasor and obtained as

$$\bar{J}^{\nu}_{bar} = \frac{\bar{I}^{\nu}_{bar}}{S_{sr}}, \tag{3.7}$$

Table 3.2: Parameters of the benchmark induction motors.

Symbol	Value				Unit	Description
-	1	2	3	4	-	Benchmark motor
V_{ph}^{N}	230	230	230	230	V	Nominal rms phase voltage
I_{ph}^{N}	0.7	2.6	1.1	5.0	A	Nominal rms phase current
f_{s}^{N}	50	50	50	50	Hz	Nominal stator frequency
s_N	0.12	0.05	0.09	0.1	-	Nominal slip
P_{mech}^{N}	0.18	0.82	0.28	1.6	kW	Nominal output power
p	3	3	2	2	-	Pole pair number

where $\bar{I}_{bar}^{\nu}$ is the current phasor of the ν^{th} rotor bar and S_{sr} is the surface area of the rotor slots in the model. In practice, the current in the rotor bars depends on the operating conditions of the motor. Two methods to calculate $\bar{I}_{bar}^{\nu}$ for variable load conditions using the models presented in this chapter are discussed in Chapter 4. However, for simulation purposes, fixed sinusoidally distributed rotor-bar currents can also be assigned to each rotor bar using

$$\bar{I}_{bar}^{\nu} = \sqrt{2} I_{bar} e^{j\left(p\left[\frac{\theta_{sp,r}}{2}+(\nu-1)\theta_{sp,r}\right]+\Delta_{cur,r}\right)}, \tag{3.8}$$

where p is the number of pole pairs, I_{bar} is the rms rotor-bar current, $\theta_{sp,r} = 2\pi/Q_r$ is the rotor slot-pitch angle and $\Delta_{cur,r}$ is the rotor current angle, which can be varied to change the orientation of the rotor magnetic field.

To illustrate the interpretation of (3.4) to (3.6) and (3.8) graphically, a simplified example of an IM is introduced in Figure 3.2a. This example contains a three-phase stator winding with $p = 1$, whereas the rotor houses six rotor bars. The parameters $\Delta_{cur,s}$ and $\Delta_{cur,r}$ represent the orientation of stator and rotor magnetic field, respectively, as depicted in Figure 3.2b. In this figure, F_s and F_r are the stator and rotor magnetic field, respectively. Further, according to (3.4) to (3.6) and (3.8), the phasor diagrams of the stator winding and rotor-bar currents are as shown in Figures 3.3a and 3.3b, respectively.

3.2.1 Benchmark motor topologies

For the validation of the ALT and MMT models, four different benchmark motor topologies are defined. The geometrical parameters of these motor are given in Table 3.1, whereas their nominal characteristics are given in Table 3.2. For each benchmark motor, a prototype is available to perform measurements, which will be used to validate the IM analysis framework presented in Chapter 5. Also, a graphical overview of the motor cross-sections is shown in Figure 3.4. For benchmark motors "one", "two" and "four", the definition of the parameters

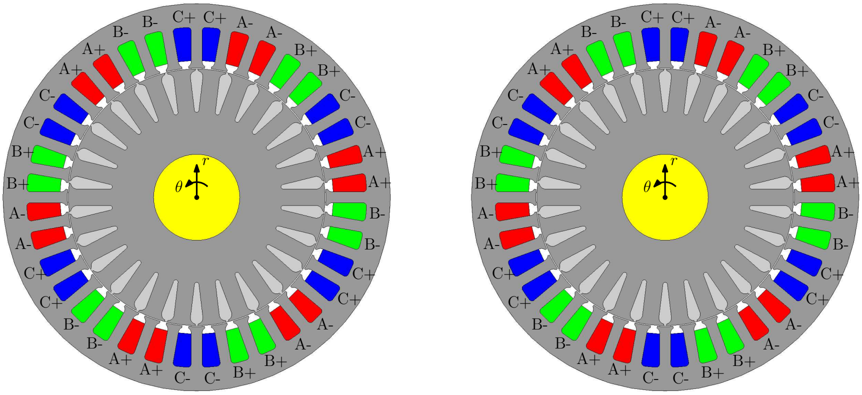

(a) Benchmark motor ”one” (b) Benchmark motor ”two”

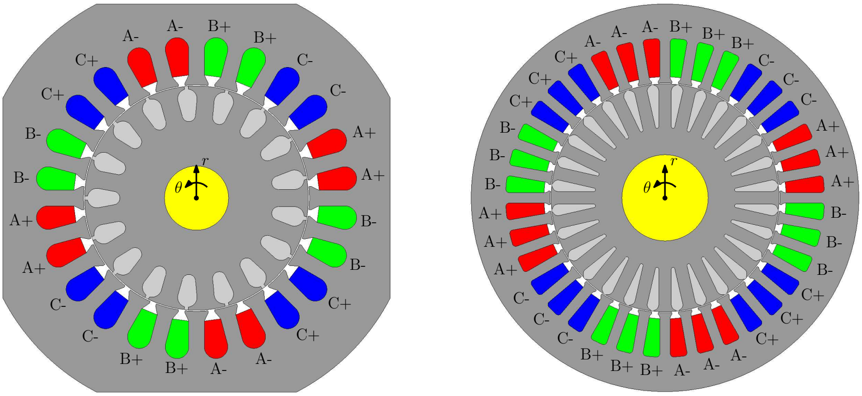

(c) Benchmark motor ”three” (d) Benchmark motor ”four”

Figure 3.4: Overview of the benchmark motor cross-sections.

shown in Table 3.2 is relatively straightforward. For benchmark motor ”three”, however, the height of the stator yoke, h_{ys}, is variable. Therefore, the value of h_{ys} used in the ALT and MMT models is selected as the average of the minimum and maximum stator yoke height.

3.2.2 2D FEA models

The 2D FEA models used to validate the harmonic models use steady-state ac magnetic solutions. This means that all physical quantities, such as voltage, current, magnetic-flux density and magnetic-field strength, are assumed to vary sinusoidally as a function of time. Other (higher) time harmonics and their influence on the performance of the motor are not included. However, the same approximation is used in the harmonic models and therefore, the steady-state ac solutions provided by the FEA models present a suitable basis for comparison. Furthermore, the steady-state harmonic models could be extended to time-stepping transient models if desired, as discussed in [153].

For each benchmark motor, two types of FEA models are considered, namely a current-fed model and a voltage-fed model. In the current-fed model, a sinusoidal three-phase current is directly applied to the stator winding, whereas in the voltage-fed model a sinusoidal three-phase voltage is applied to the stator winding through an electric-circuit model. The bars of the rotor squirrel cage are in both cases modeled as solid conductors, connected at both ends by means of an electric circuit that represents the short-circuit ring. Also, the nonlinearity of the soft-magnetic material is included using the BH-characteristic of the soft-magnetic material. To determine this characteristic, measurements have been performed on ring-core samples, as described in Appendix B. For all benchmark motors, the BH-characteristic measured for material two was used in the FEA simulations.

3.3 The anisotropic layer model

In this section, the implementation and validation of the ALT model for IMs is discussed. The main advantage of this model is its ability to include global saturation of the soft-magnetic material in the motor. Therefore, it is very suitable to analyse the magnetization behavior of an IM, under the assumption that local saturation effects are negligible. On the other hand, the ALT is not suitable for analysis of leakage and fringing fluxes. For these purposes, the MMT model discussed in the next section can be used.

3.3.1 Model representation of the IM geometry

The layers of the model will be referred to as regions. Firstly, the geometry is divided into five regions, namely:

I: Rotor yoke region
II: Rotor slotting region
III: Air-gap region
IV: Stator slotting region
V: Stator yoke region

Each region is represented as a periodic region in the model, such that the region model shown in Figure 3.5 is obtained. Note, that regions II and IV describe the teeth and slots as well as the tooth tips and slot openings of the rotor and stator, respectively.

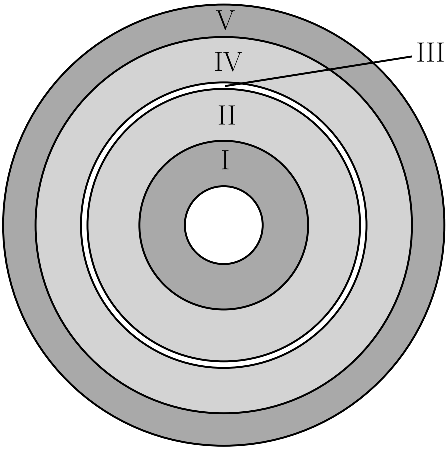

Figure 3.5: Region division for the ALT model of an induction motor.

Secondly, material parameters are assigned to each model region. Regions I, III and V are assumed to have homogeneous, isotropic material properties. Therefore, the relative magnetic permeabilities of the yoke regions, μ_r^I and μ_r^V, are initially set to 1000. These values are updated iteratively to account for global saturation of the yokes, as will be discussed in Section 3.3.3. Further, the relative permeability of the air-gap region, III, is set to $\mu_r^{III} = 1/k_C$, where k_C is Carter's factor. It serves to effectively enlarge the air gap to account for stator and rotor slotting [154]. In the ALT model, however, k_C is applied as a correction of the air-gap permeability instead of the air-gap length, to assure that the radial dimensions of the motor are preserved in the model.

In the slotting regions, both soft-magnetic and conducting materials are present. To account for the effect of both materials on the magnetic-field distribution, artificial, anisotropic material parameters are calculated for the rotor and stator slotting regions. In the circumferential direction, the slots and teeth are considered to be in series. Therefore, the circumferential magnetic permeability, $\mu_{\theta\theta}$, is found for regions II and IV as [68]

$$\mu_{\theta\theta}^{II} = \frac{\mu_{dr}\mu_{sr}\left(b_{dr} + b_{sr}^{av}\right)}{\mu_{dr}b_{sr}^{av} + \mu_{sr}b_{dr}}, \tag{3.9}$$

$$\mu_{\theta\theta}^{IV} = \frac{\mu_{ds}\mu_{ss}\left(b_{ds} + b_{ss}^{av}\right)}{\mu_{ds}b_{ss}^{av} + \mu_{ss}b_{ds}}, \tag{3.10}$$

where $\mu_{ds} = \mu_{r,ds}\mu_0$ and $\mu_{dr} = \mu_{r,dr}\mu_0$ are the stator and rotor tooth permeabilities and $\mu_{ss} = \mu_0$ and $\mu_{sr} = \mu_0$ are the stator and rotor slot permeabilities. Similar to μ_r^I and μ_r^V, the relatively permeability values of the stator and rotor teeth, $\mu_{r,dr}$ and $\mu_{r,ds}$, are initially set to 1000 and updated iteratively to account for global saturation of the teeth. Additionally, b_{ds} and b_{dr} are the stator and rotor tooth width and b_{ss}^{av} and b_{sr}^{av} are the average stator and rotor slot width, calculated as

$$b_{ss}^{av} = \frac{2\pi\left(r_{si} + \frac{h_{ss}}{2}\right)}{Q_s} - b_{ds}, \tag{3.11}$$

$$b_{sr}^{av} = \frac{2\pi\left(r_{ro} - \frac{h_{sr}}{2}\right)}{Q_r} - b_{dr}, \tag{3.12}$$

where r_{si} is the stator inner radius, r_{ro} is the rotor outer radius, h_{ss} and h_{sr} are the stator and rotor slot height, respectively, and Q_s and Q_r are the number of stator and rotor slots, respectively. Furthermore, in the radial direction, the slots and teeth are considered to be in parallel. Therefore, the radial magnetic permeability, μ_{rr} is found for regions II and IV as [68]

$$\mu_{rr}^{II} = \frac{\mu_{dr} b_{dr} + \mu_{sr} b_{sr}^{av}}{b_{dr} + b_{sr}^{av}}, \tag{3.13}$$

$$\mu_{rr}^{IV} = \frac{\mu_{ds} b_{ds} + \mu_{ss} b_{ss}^{av}}{b_{ds} + b_{ss}^{av}}. \tag{3.14}$$

3.3.2 Magnetic-field solution

Since all material properties are homogenized, the magnetic-field solution of each region is given by (2.27) to (2.38). Between the regions, interface boundary conditions are applied, whereas Dirichlet boundary conditions are applied at the inner boundary of I and the outer boundary of V. It is assumed here that the magnetic flux leaking out of the stator and rotor yokes is negligible. An overview of the boundary-condition equations for the ALT model can be found in Appendix A.1.

Additionally, as mentioned in Section 2.2, only one period of the motor geometry needs to be considered in the ALT model. The number of periodic sections in a motor geometry is denoted as C_{per}. If the number of periodic section is not equal to the number of pole pairs, $C_{per} \neq p$, the fundamental spatial harmonic of the model is not equal to the fundamental spatial harmonic of the motor. Therefore, the spatial harmonics used in the model should be multiplied by p/C_{per} to match them with the motor. For the ALT model, only the fundamental spatial harmonic of the motor, represented in the model by $n_f = p/C_{per}$, is considered. Higher spatial harmonics and their interaction with the rotor may also be considered. However, care should be taken, since the applied homogenization looses its validity for higher spatial harmonics.

In regions II and IV, current-density sources are present due to the rotor and stator winding currents, respectively. To obtain the Fourier-series coefficients of these sources, (2.24) to (2.26) should be evaluated for the current-density distributions. Since the regions are periodic and the currents are assumed to be balanced, $J_{z0}^{II} = J_{z0}^{IV} = 0$. Further, (2.25) and (2.26) can be calculated separately for each slot ν in regions II and IV as

$$J_{zcn}^{\mathrm{II},\nu} = j_{zcn}^{\mathrm{II},\nu} \bar{I}_{bar,\nu}, \tag{3.15}$$

$$J_{zsn}^{\mathrm{II},\nu} = j_{zsn}^{\mathrm{II},\nu} \bar{I}_{bar,\nu}, \tag{3.16}$$

$$J_{zcn}^{\mathrm{IV},\nu} = j_{zcn}^{\mathrm{IV},\nu} \bar{I}_{ss,\nu}, \tag{3.17}$$

$$J_{zsn}^{\mathrm{IV},\nu} = j_{zsn}^{\mathrm{IV},\nu} \bar{I}_{ss,\nu}, \tag{3.18}$$

where $\bar{I}_{ss,\nu}$ represents the current phasor in the ν^{th} stator slot, $\bar{I}_{bar,\nu}$ represents the current phasor in the ν^{th} rotor slot and

$$j_{zcn}^{\mathrm{II},\nu} = \frac{1}{S_{sr} w_n^{\mathrm{II}} \theta_p^{\mathrm{II}}} \left[\sin\left(w_n^{\mathrm{II}} \theta_{re,\nu}\right) - \sin\left(w_n^{\mathrm{II}} \theta_{rb,\nu}\right)\right], \tag{3.19}$$

$$j_{zsn}^{\mathrm{IV},\nu} = \frac{1}{S_{sr} w_n^{\mathrm{II}} \theta_p^{\mathrm{II}}} \left[\cos\left(w_n^{\mathrm{II}} \theta_{rb,\nu}\right) - \cos\left(w_n^{\mathrm{II}} \theta_{re,\nu}\right)\right], \tag{3.20}$$

$$j_{zcn}^{\mathrm{IV},\nu} = \frac{z_{Q,s}}{S_{ss} w_n^{\mathrm{IV}} \theta_p^{\mathrm{IV}}} \left[\sin\left(w_n^{\mathrm{IV}} \theta_{se,\nu}\right) - \sin\left(w_n^{\mathrm{IV}} \theta_{sb,\nu}\right)\right], \tag{3.21}$$

$$j_{zsn}^{\mathrm{IV},\nu} = \frac{z_{Q,s}}{S_{ss} w_n^{\mathrm{IV}} \theta_p^{\mathrm{IV}}} \left[\cos\left(w_n^{\mathrm{IV}} \theta_{sb,\nu}\right) - \cos\left(w_n^{\mathrm{IV}} \theta_{se,\nu}\right)\right], \tag{3.22}$$

where $\theta_{sb,\nu}$, $\theta_{se,\nu}$, $\theta_{rb,\nu}$ and $\theta_{re,\nu}$ are the starting and ending angles of the ν^{th} stator and rotor slot, respectively, in the model. Further, the stator and rotor slot areas used to calculate the slot current density, S_{ss} and S_{sr} respectively, are calculated as

$$S_{ss} = \frac{\theta_{ss}}{2} \left[\left(r_{si} + h_{ss}\right)^2 - \left(r_{si} + h_{os}\right)^2\right], \tag{3.23}$$

$$S_{sr} = \frac{\theta_{sr}}{2} \left[\left(r_{ro} - h_{or}\right)^2 - \left(r_{ro} - h_{sr}\right)^2\right], \tag{3.24}$$

where θ_{ss} and θ_{sr} are the stator and rotor slot angles, respectively. For the ALT model, θ_{ss} and θ_{sr} are set equal to the stator and rotor slot opening angle. Finally, to calculate the sine and cosine coefficients of the current densities in regions II and IV, the contributions of each slot in a region are summed as

$$J_{zcn}^{II} = \sum_{\nu=1}^{N_{sr}} J_{zcn}^{II,\nu}, \qquad J_{zsn}^{II} = \sum_{\nu=1}^{N_{sr}} J_{zsn}^{II,\nu}, \tag{3.25}$$

$$J_{zcn}^{IV} = \sum_{\nu=1}^{N_{ss}} J_{zcn}^{IV,\nu}, \qquad J_{zsn}^{IV} = \sum_{\nu=1}^{N_{ss}} J_{zsn}^{IV,\nu}, \tag{3.26}$$

where N_{sr} and N_{ss} represent the number of rotor and stator slots in the model, respectively, and are obtained as

$$N_{sr} = \frac{Q_s}{C_{per}}, \qquad N_{ss} = \frac{Q_r}{C_{per}}. \tag{3.27}$$

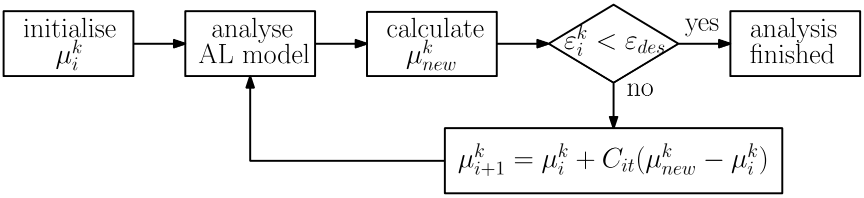

Figure 3.6: Schematic overview of the iterative process to account for global saturation in the ALT model regions.

3.3.3 Global saturation effect

To account for the influence of global saturation on the fundamental magnetic flux, an iterative method, such as proposed in [68], can be used. This method is based on magnetic permeability relaxation in each region that contains soft-magnetic material. A schematic overview of the iterative procedure is shown in Figure 3.6. After setting initial values for μ_1^k for each saturable region, the magnetic-field distribution is analysed using the ALT model. From the results, the peak magnetic-flux density in each saturable region, $\hat{B}$, is calculated. In the rotor and stator yoke regions, $\hat{B}$ is assumed equal to the amplitude of the fundamental circumferential magnetic-flux density, $\hat{B}_{\theta,1}$, at the radial midpoint of the region, r_{mid}^k, and is calculated as

$$\hat{B}_{yr} = \frac{1}{2}\left|B_{\theta cn_f}^{I}\left(r_{mid}^{I}\right) + jB_{\theta sn_f}^{I}\left(r_{mid}^{I}\right)\right|, \tag{3.28}$$

$$\hat{B}_{ys} = \frac{1}{2}\left|B_{\theta cn_f}^{V}\left(r_{mid}^{V}\right) + jB_{\theta sn_f}^{V}\left(r_{mid}^{V}\right)\right|, \tag{3.29}$$

where coefficients $B_{\theta cn_f}^{I}$, $B_{\theta sn_f}^{I}$, $B_{\theta cn_f}^{V}$ and $B_{\theta sn_f}^{V}$ are calculated using (2.32) and (2.33).

Further, in the rotor and stator slot regions, $\hat{B}$ is determined using the amplitude of the fundamental radial magnetic-flux density, $\hat{B}_{r,1}$. For unsaturated and mildly saturated operating conditions, the radial flux mainly passes through the teeth, and therefore

$$\hat{B}_{dr} = \frac{b_{dr} + b_{sr}^{av}}{2b_{dr}}\left|B_{rcn_f}^{II}\left(r_{mid}^{II}\right) + jB_{rsn_f}^{II}\left(r_{mid}^{II}\right)\right|, \tag{3.30}$$

$$\hat{B}_{ds} = \frac{b_{ds} + b_{ss}^{av}}{2b_{ds}}\left|B_{rcn_f}^{IV}\left(r_{mid}^{IV}\right) + jB_{rsn_f}^{IV}\left(r_{mid}^{IV}\right)\right|. \tag{3.31}$$

For deeply saturated operating conditions, part of the radial flux passes through the slots instead of the teeth. To correct for this effect, an estimation of the slot flux could be subtracted from $\hat{B}_{dr}$ and $\hat{B}_{ds}$ [40]. In this thesis, however, such a correction is not considered as the developed models are not yet suitable for analysis of deeply saturated IMs. Besides, an efficient low-power IM design, intended for industrial applications where the overload capability is not relevant,

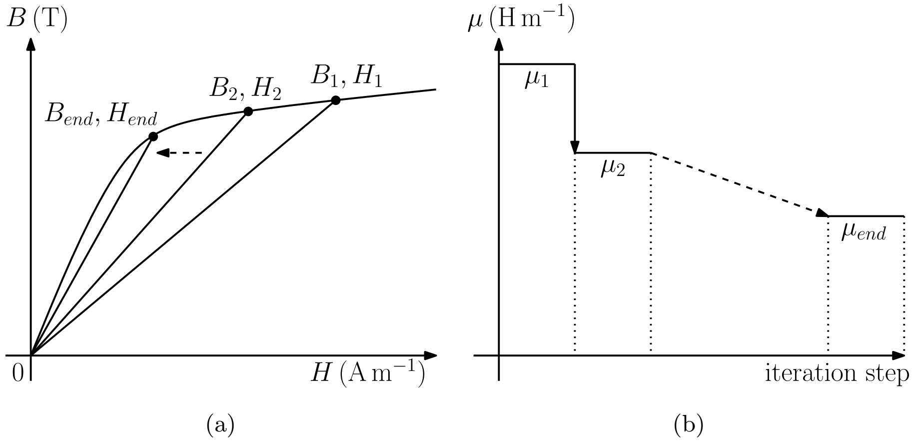

Figure 3.7: Graphical representation of the iterative process to account for global saturation in the ALT model regions.

usually does not saturate deeply during nominal operation, as this would lead to an excessive magnetization current.

Finally, from the computed values of $\hat{B}$, a new relative permeability, μ_{new}^{k}, is obtained for each saturable region by interpolating the μ (B) curve of the soft-magnetic material. These curves are derived from the BH-characteristics of the magnetic material, which are usually either provided by the soft-magnetic material manufacturer or measured on samples of the material. An overview of measurements performed on two different soft-magnetic materials is given in Appendix B. For each saturable region, μ_{new}^{k} is compared to μ_{1}^{k}. If the difference is larger than the maximum error, ε_{des}, the relative permeability is recalculated for the next iteration step, $i+1$, as

$$\mu_{i+1}^{k} = \mu_{i}^{k} + C_{it}\left(\mu_{new}^{k} - \mu_{i}^{k}\right), \tag{3.32}$$

where C_{it} is the relaxation constant. In practice, $C_{it} \approx 0.1\,\text{to}\,0.3$ appears to be suitable for fast convergence in most cases [40], whereas the maximum error is set to $\varepsilon_{des} = 0.001$. After updating the model for μ_{i+1}^{k}, the magnetic-field distribution and the resulting values of μ_{new}^{k} are recalculated. If the error between μ_{i+1}^{k} and μ_{new}^{k} is not smaller than ε_{des} yet, the iterative process is repeated. Once the error is smaller than ε_{des}, the analysis is finished and post-processing can be initiated.

A graphical representation of the iterative process is shown in Figure 3.7, where it is assumed that μ is initially overestimated. As a result, B_1 and H_1 are overestimated and μ_{new} is lower than the assumed permeability, μ_1. Therefore, the permeability is reduced for the next iteration step. Once the simulation has reached convergence, the actual operating point of the magnetic material, represented by B_{end} and H_{end}, and the effective material permeability, μ_{end}, are obtained.

3.3.4 Air-gap magnetic-flux density

The amplitude of the n^{th} spatial harmonic of the radial air-gap magnetic-flux density, $\hat{B}_{g,n}$, is obtained from the ALT model in the center of the air gap as

$$\hat{B}_{g,n} = \frac{1}{2}\left|B_{rcn}^{III}\left(r_{mid}^{III}\right) + jB_{rsn}^{III}\left(r_{mid}^{III}\right)\right|, \tag{3.33}$$

where coefficients B_{rcn}^{III} and B_{rsn}^{III} are calculated using (2.32) and (2.33). To validate $\hat{B}_{g,n}$ for n_{fun}, FEA simulations are performed for no-load operating conditions using the current-fed model of each benchmark motor. To obtain these operating conditions, the rotor slip is assumed very close to zero (1e-5), such that the induced rotor current is approximately zero as well. Further, the stator current is increased from 10% to 100% of the nominal motor current. Similar calculations are performed with the ALT model and compared to FEA results, as shown in terms of per unit (p.u.) values in Figure 3.8. In both simulations, the same BH-characteristic is used for the soft-magnetic material. It can be seen that a very good agreement is obtained, with errors less than 4% with respect to the FEA value obtained for nominal current. The knee-point in the characteristic of each benchmark motor indicates that a part of the main flux path starts to saturate. For benchmark motor "one", some discrepancies are observed around this knee-point, whereas benchmark motor "three" shows an increasing mismatch for stator currents exceeding the knee-point. These small deviations are attributed to the simplified geometry representation used in the ALT model and associated neglected effects, such as local saturation.

3.3.5 Flux linkage

The flux linkage phasors of the ν^{th} stator and rotor slot can be obtained as

$$\bar{\lambda}_{ss}^{\nu,ALT} = \frac{z_{Q,s} l_{sl}}{S_{ss}} \int\limits_{\theta_{sb,\nu}}^{\theta_{se,\nu}} \int\limits_{r_i^{\mathrm{IV}}}^{r_o^{\mathrm{IV}}} A_z\left(r,\theta\right) r dr d\theta, \tag{3.34}$$

$$\bar{\lambda}_{sr}^{\nu,ALT} = \frac{l_{sl}}{S_{sr}} \int\limits_{\theta_{rb,\nu}}^{\theta_{re,\nu}} \int\limits_{r_i^{\mathrm{II}}}^{r_o^{\mathrm{II}}} A_z\left(r,\theta\right) r dr d\theta, \tag{3.35}$$

where $l_{sl} = l_{stk} + 2\left(r_{si} - r_{ro}\right)$ is the effective slot length in the axial direction, taking fringing flux at the machine ends into account.

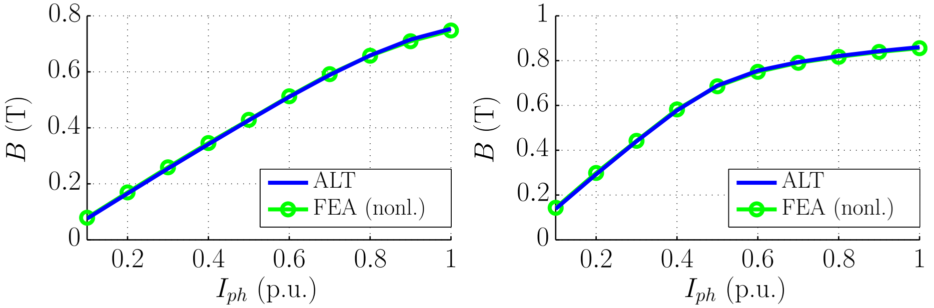

(a) Benchmark motor ”one” (b) Benchmark motor ”two”

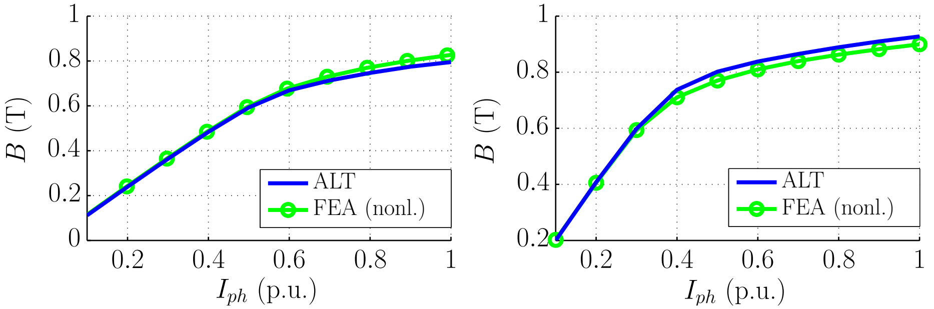

(c) Benchmark motor ”three” (d) Benchmark motor ”four”

Figure 3.8: Comparison of the fundamental air-gap flux-density calculated by ALT and nonlinear 2D FEA for various stator current at no-load operating conditions.

Evaluating (3.35) for the given magnetic-field solution, the expressions for the stator and rotor slot flux linkage become

$$\bar{\lambda}_{ss}^{\nu,ALT} = \sum_{\forall n}\left[C_{sn,s}^{\nu}\left(C_{an}^{\mathrm{IV}}a_n^{\mathrm{IV}} + C_{bn}^{\mathrm{IV}}b_n^{\mathrm{IV}} + \sum_{\nu_s=1}^{N_{ss}} C_{gcn}^{\mathrm{IV},\nu_s}\bar{I}_{ss,\nu_s}\right) + \right.$$
$$\left. C_{cn,s}^{\nu}\left(C_{cn}^{\mathrm{IV}}c_n^{\mathrm{IV}} + C_{dn}^{\mathrm{IV}}d_n^{\mathrm{IV}} + \sum_{\nu_s=1}^{N_{ss}} C_{gsn}^{\mathrm{IV},\nu_s}\bar{I}_{ss,\nu_s}\right)\right], \tag{3.36}$$

$$\bar{\lambda}_{sr}^{\nu,ALT} = \sum_{\forall n}\left[C_{sn,r}^{\nu}\left(C_{an}^{\mathrm{II}}a_n^{\mathrm{II}} + C_{bn}^{\mathrm{II}}b_n^{\mathrm{II}} + \sum_{\nu_r=1}^{N_{sr}} C_{gcn}^{\mathrm{II},\nu_r}\bar{I}_{bar,\nu_r}\right) + \right.$$
$$\left. C_{cn,r}^{\nu}\left(C_{cn}^{\mathrm{II}}c_n^{\mathrm{II}} + C_{dn}^{\mathrm{II}}d_n^{\mathrm{II}} + \sum_{\nu_r=1}^{N_{sr}} C_{gsn}^{\mathrm{II},\nu_r}\bar{I}_{bar,\nu_r}\right)\right], \tag{3.37}$$

where coefficients $C^{\nu}_{sn,s}$, $C^{\nu}_{cn,s}$, $C^{\nu}_{sn,r}$ and $C^{\nu}_{cn,r}$ are calculated as

$$C^{\nu}_{sn,s} = \frac{z_{Q,s} l_{sl}}{\left(w^{\mathrm{IV}}_n\right)^2 S_{ss}} \left(\sin\left(w^{\mathrm{IV}}_n \theta_{se,\nu}\right) - \sin\left(w^{\mathrm{IV}}_n \theta_{sb,\nu}\right)\right), \tag{3.38}$$

$$C^{\nu}_{cn,s} = \frac{z_{Q,s} l_{sl}}{\left(w^{\mathrm{IV}}_n\right)^2 S_{ss}} \left(\cos\left(w^{\mathrm{IV}}_n \theta_{sb,\nu}\right) - \cos\left(w^{\mathrm{IV}}_n \theta_{se,\nu}\right)\right), \tag{3.39}$$

$$C^{\nu}_{sn,r} = \frac{l_{sl}}{\left(w^{\mathrm{II}}_n\right)^2 S_{sr}} \left(\sin\left(w^{\mathrm{II}}_n \theta_{re,\nu}\right) - \sin\left(w^{\mathrm{II}}_n \theta_{rb,\nu}\right)\right), \tag{3.40}$$

$$C^{\nu}_{cn,r} = \frac{l_{sl}}{\left(w^{\mathrm{II}}_n\right)^2 S_{sr}} \left(\cos\left(w^{\mathrm{II}}_n \theta_{rb,\nu}\right) - \cos\left(w^{\mathrm{II}}_n \theta_{re,\nu}\right)\right). \tag{3.41}$$

Further, coefficients C^k_{an}, C^k_{bn}, C^k_{cn} and C^k_{dn} are obtained for $k = \mathrm{II}$ and $k = \mathrm{IV}$ using

$$C^k_{an} = \frac{1}{\left(2 + \alpha^k w^k_n\right)} \left(\left(r^k_o\right)^{\alpha^k w^k_n + 2} - \left(r^k_i\right)^{\alpha^k w^k_n + 2}\right), \tag{3.42}$$

$$C^k_{bn} = \frac{1}{\left(2 - \alpha^k w^k_n\right)} \left(\left(r^k_o\right)^{-\alpha^k w^k_n + 2} - \left(r^k_i\right)^{-\alpha^k w^k_n + 2}\right), \tag{3.43}$$

$$C^k_{cn} = \frac{1}{\left(2 + \alpha^k w^k_n\right)} \left(\left(r^k_o\right)^{\alpha^k w^k_n + 2} - \left(r^k_i\right)^{\alpha^k w^k_n + 2}\right), \tag{3.44}$$

$$C^k_{dn} = \frac{1}{\left(2 - \alpha^k w^k_n\right)} \left(\left(r^k_o\right)^{-\alpha^k w^k_n + 2} - \left(r^k_i\right)^{-\alpha^k w^k_n + 2}\right), \tag{3.45}$$

whereas conditional coefficients $C^{k,\nu}_{gcn}$ and $C^{k,\nu}_{gsn}$ are determined for $k = \mathrm{II}$ and $k = \mathrm{IV}$ as

$$C^{k,\nu}_{gcn} = \begin{cases} \frac{j^{k,\nu}_{zcn}}{12} \left(\left(r^k_o\right)^4 - \left(r^k_i\right)\right)^4 & \alpha^k \left(w^k_n\right)^2 = 1 \\ \frac{j^{k,\nu}_{zcn}}{16} \left[\left(r^k_o\right)^4 \left(\ln\left(r^k_o\right) - \frac{1}{4}\right) - \right. & \alpha^k \left(w^k_n\right)^2 = 4 \\ \qquad \left. \left(r^k_i\right)^4 \left(\ln\left(r^k_i\right) - \frac{1}{4}\right)\right] & \\ \frac{j^{k,\nu}_{zcn}}{16 - 4\left(w^k_n\right)\alpha^k} \left(\left(r^k_o\right)^4 - \left(r^k_i\right)^4\right) & \text{else,} \end{cases} \tag{3.46}$$

$$C^{k,\nu}_{gsn} = \begin{cases} \frac{j^{k,\nu}_{zsn}}{12} \left(\left(r^k_o\right)^4 - \left(r^k_i\right)\right)^4 & \alpha^k \left(w^k_n\right)^2 = 1 \\ \frac{j^{k,\nu}_{zsn}}{16} \left[\left(r^k_o\right)^4 \left(\ln\left(r^k_o\right) - \frac{1}{4}\right) - \right. & \alpha^k \left(w^k_n\right)^2 = 4 \\ \qquad \left. \left(r^k_i\right)^4 \left(\ln\left(r^k_i\right) - \frac{1}{4}\right)\right] & \\ \frac{j^{k,\nu}_{zsn}}{16 - 4\left(w^k_n\right)\alpha^k} \left(\left(r^k_o\right)^4 - \left(r^k_i\right)^4\right) & \text{else.} \end{cases} \tag{3.47}$$

To obtain the flux linkage per stator phase, the flux linkages of all slots belonging to a phase should be summed. The flux linkage phasors of phases A, B and C are therefore calculated as

$$\bar{\lambda}_A^{ALT} = C_{per} \sum_{\forall \nu \in N_A} c_{dir}^{\nu} \bar{\lambda}_{ss}^{ALT}, \tag{3.48}$$

$$\bar{\lambda}_B^{ALT} = C_{per} \sum_{\forall \nu \in N_B} c_{dir}^{\nu} \bar{\lambda}_{ss}^{ALT}, \tag{3.49}$$

$$\bar{\lambda}_C^{ALT} = C_{per} \sum_{\forall \nu \in N_C} c_{dir}^{\nu} \bar{\lambda}_{ss}^{ALT}, \tag{3.50}$$

where N_A, N_B and N_C represent all slots in the model belonging to phases A, B and C, respectively, and c_{dir}^{ν} is the direction of current flow inside the slot. If the slot current is positive, $c_{dir}^{\nu} = 1$, whereas $c_{dir}^{\nu} = -1$ if the slot current is negative. Also, the summation of the slot flux linkages should be multiplied by C_{per} to account for all periodic sections of the motor. It should be noted that it is assumed that each slot contains conductors of only one phase winding. However, the integral presented by (3.35) can be modified to account for multiple phase windings per slot, such as, for example, in case of double layer windings.

In Figure 3.9, the stator flux linkage calculated from the ALT model is compared to similar results obtained from FEA simulations for all four benchmark motors. The operating conditions are equal to those of Section 3.3.4 and it can be seen that a good agreement is obtained. Errors are typically less than 5%, although benchmark motor "three" shows an increased error of approximately 8%. Further, the results show that the fundamental flux distribution is the main contributor to the stator flux linkage for the benchmark motors under no-load operating conditions.

3.3.6 Electromagnetic torque

In literature, many different methods are known to calculate the forces and torques produced by electromagnetic motors and actuators. For the harmonic models presented here, however, Maxwell's Stress Tensor (MST) method is the most suitable approach. Using MST, the force between two unconnected objects is calculated as

$$\vec{F} = \frac{1}{\mu} \oint_S \mathbb{T} \cdot d\vec{S}, \tag{3.51}$$

where S is a surface surrounding one of the objects on which the force is calculated and the magnetic stress tensor, $\mathbb{T}$, given in its general form by

$$\mathbb{T} = \begin{bmatrix} \frac{B_n^2 - B_t^2 - B_l^2}{2} & B_n B_t & B_n B_l \\ B_t B_n & \frac{-B_n^2 + B_t^2 - B_l^2}{2} & B_t B_l \\ B_l B_n & B_l B_t & \frac{-B_n^2 - B_t^2 + B_l^2}{2} \end{bmatrix}, \tag{3.52}$$

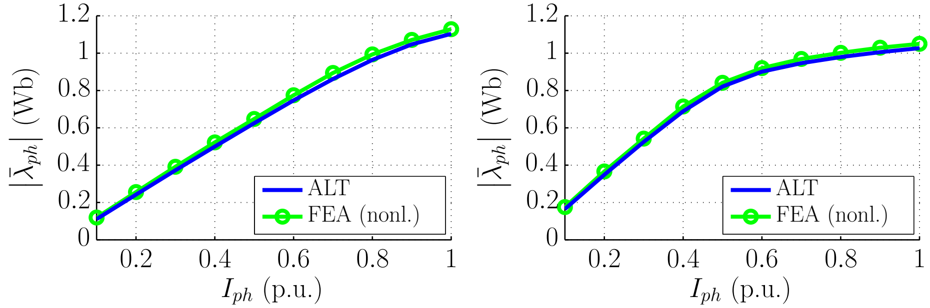

(a) Benchmark motor "one" (b) Benchmark motor "two"

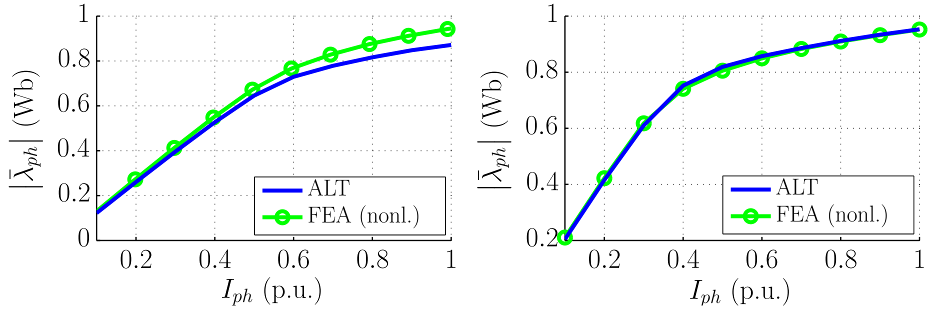

(c) Benchmark motor "three" (d) Benchmark motor "four"

Figure 3.9: Comparison of the stator flux linkage calculated by ALT and nonlinear 2D FEA for various stator current at no-load operating conditions.

where B_n, B_t and B_l represent the normal, tangential and longitudinal components of the magnetic-flux density in a given coordinate system, respectively. For the considered polar coordinate system, $\mathbb{T}$ reduces to

$$\mathbb{T} = \begin{bmatrix} \frac{B_r^2 - B_\theta^2}{2} & B_r B_\theta \\ B_\theta B_r & \frac{-B_r^2 + B_\theta^2}{2} \end{bmatrix}. \tag{3.53}$$

One of the advantages of the MST method is that only the magnetic-field distribution between the considered objects is required. For rotating electric machines, the surface S can therefore be placed inside the air gap, for example in the middle, meaning that only the air-gap magnetic-field distribution is required to determined the produced torque. Since the harmonic models provide a continuous, analytical description of the air-gap magnetic field, (3.51) can be evaluated without distortion due to spatial discretization. Furthermore, an analytical expression for the produced torque can be obtained, which allows very fast post-processing calculations. For the ALT model, the expression for the produced torque, T_{em}, is

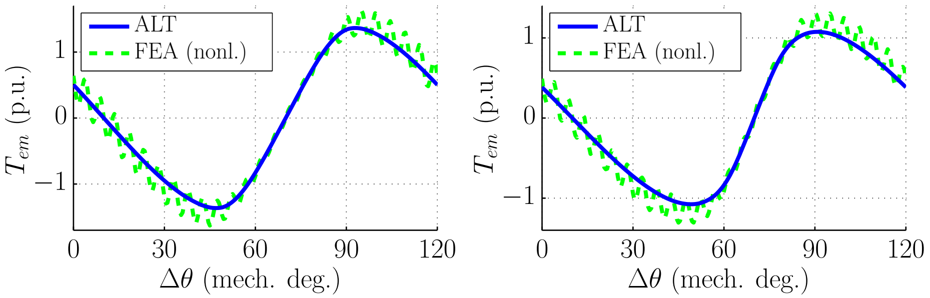

(a) Benchmark motor "one" (b) Benchmark motor "two"

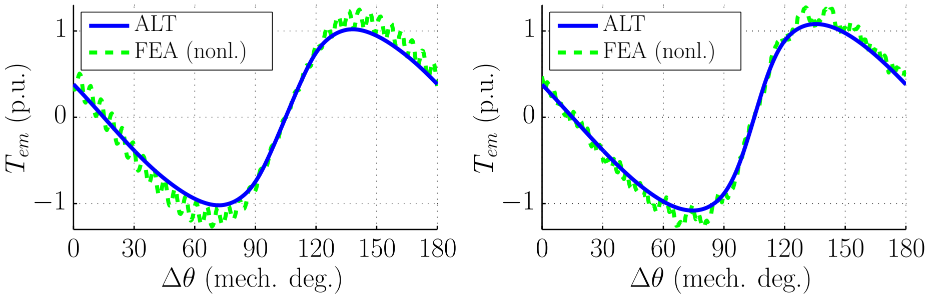

(c) Benchmark motor "three" (d) Benchmark motor "four"

Figure 3.10: Comparison of the electromagnetic torque calculated by ALT and nonlinear 2D FEA for various rotor positions and static stator and rotor current distributions.

given by

$$T_{em} = \frac{2\pi l_{stk}}{\mu^{\mathrm{III}}} \sum_{n=1}^{N_{sh}} \left[\mathrm{Re}\left(b_n^{\mathrm{III}}\right) \mathrm{Re}\left(c_n^{\mathrm{III}}\right) - \mathrm{Re}\left(a_n^{\mathrm{III}}\right) \mathrm{Re}\left(d_n^{\mathrm{III}}\right) \right]. \tag{3.54}$$

To validate the torque predicted by the ALT model, static current distributions are applied to the stator and rotor of each benchmark motor, while the torque is calculated for various rotor positions. For each calculation, the rotor position is increased in steps of 0.2°, from 0 to $360/p$. Furthermore, the stator current distribution is obtained according to (3.4) to (3.6) using $I_{ph} = I_{ph}^N$, whereas the rotor current distribution is obtained according to (3.8) using $I_{bar} = I_{bar}^N$. Similar calculations are also performed using 2D FEA. A comparison of the calculation results in terms of predicted torque is shown in Figure 3.10. For each benchmark motor, it can be seen that the fundamental torque is not completely sinusoidal due to the nonlinearity of the soft-magnetic material. Since global saturation is accounted for, this effect is represented in the results of the ALT model as well. This indicates that the ALT model is suitable for the prediction of the average motor torque. However, it can also be noticed that a significant torque ripple is predicted by FEA due to stator and rotor slotting. Obviously, this ripple is not observed in the ALT model results, since it does not take slotting into account. Therefore, the maximum rms value of the error along the entire waveform is 15%, respectively.

3.4 The mode-matching model

In this section, the implementation and validation of the MMT model for IMs is presented. The main advantage of this model over the ALT model is its ability to include stator and rotor slots in the magnetic-field solution. However, the main disadvantage is that the soft-magnetic material of the motor is assumed to be infinitely permeable. Nevertheless, the model can provide valuable insight in flux leakage and fringing phenomena, which can not be obtained from the ALT model.

3.4.1 Model representation of the IM geometry

To implement the MMT model, a suitable polar representation of the IM geometry is required. Therefore, it is divided into a number of regions that describe the air gap and the stator and rotor slots of the motor. Each region k is defined by its angular width, θ_c, angular position, θ_0, radial height, h_c, and radial position, h_0. Additionally, a local coordinate system, $\left(r, \theta^k\right)$, is defined for each region where

$$\theta^k = \begin{cases} \theta - \theta_0^k - \Delta_\theta & \text{for rotor regions,} \\ \theta - \theta_0^k & \text{for stator and air gap regions,} \end{cases} \tag{3.55}$$

and Δ_θ is the rotor displacement angle. Since the soft-magnetic material is assumed to be infinitely permeable, the teeth and yokes of the stator and rotor do not need to be represented by a model region. Instead, their presence is taken into account by means of boundary conditions.

Cartesian representations of typical stator and rotor slot geometries for low-power IMs are shown in Figure 3.11. In principle, these curved structures can be represented in the harmonic model by a staircase approximation, consisting of many thin regions with constant radial height and angular width. However, such an approach would most likely lead to a large number of regions and, consequently, to a long computation time based on today's computer capabilities. Therefore, a polar slot representation with as few regions as possible is desired, while still representing the magnetic-field distribution with sufficient accuracy. To this extent, two different polar slot representations are investigated, namely the single region slot representation and the double region slot representation.

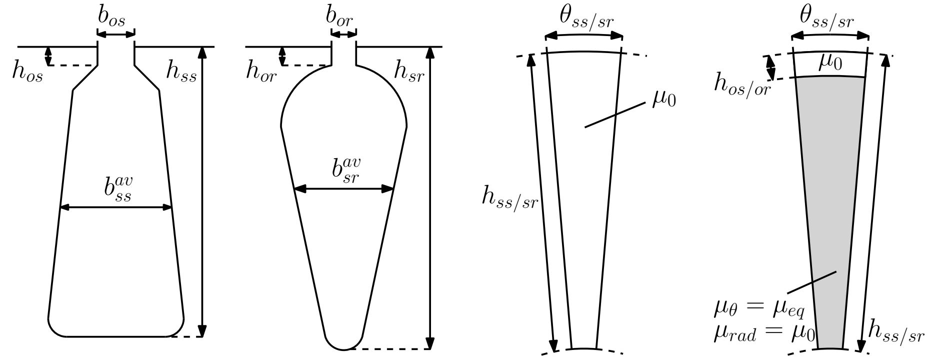

(a) Stator slot (b) Rotor slot (c) Single region (d) Double region

Figure 3.11: Cartesian representations of typical a) stator and b) rotor slot geometries for a low-power induction motor and their c) single and d) double region polar representations.

Single region slot representation

The single region slot representation uses one region to represent an entire slot. An example of such a slot representation is shown in Fig. 3.11c. The advantage of this approach is that the model size is relatively small. However, a trade-off should be made in selecting the modeled stator and rotor slot angles, θ_{ss} and θ_{sr}. On the one hand, to accurately describe the magnetic-field distribution in the air gap and the slot openings, the slot angles should be selected equal or close to the slot opening angles, given for the stator and rotor by

$$\theta_{os} = \frac{b_{os}}{r_{si}}, \qquad \theta_{or} = \frac{b_{or}}{r_{ro}}. \tag{3.56}$$

On the other hand, to properly describe slot-leakage flux in the remainder of the slot, θ_{ss} and θ_{sr} should be selected equal or close to the average slot angles, given for the stator and rotor slots by

$$\theta_{ss}^{av} = \frac{b_{ss}^{av}}{r_{si} + \frac{h_{ss}}{2}}, \qquad \theta_{sr}^{av} = \frac{b_{sr}^{av}}{r_{ro} - \frac{h_{sr}}{2}}. \tag{3.57}$$

To select suitable values for θ_{ss} and θ_{sr}, parameter sweeps can be performed to obtain the electromagnetic torque as a function of the slot angles. Therefore, θ_{ss} is varied in steps from θ_{os} to θ_{ss}^{av} and θ_{sr} is varied from θ_{or} to θ_{sr}^{av}. The proposed MMT model can be used to achieve such calculation results, once it is combined with a method to calculate the induced rotor currents, e.g. using the methods described in Chapter 4. For any value of θ_{ss} and θ_{sr} in the variation range, either the slot-leakage flux is overestimated or the fundamental air-gap flux is underestimated. Therefore, it is expected that the electromagnetic torque, T_{em}, predicted with single region slot representation is generally lower than the one predicted with actual slot geometries. Consequently, the proposed strategy

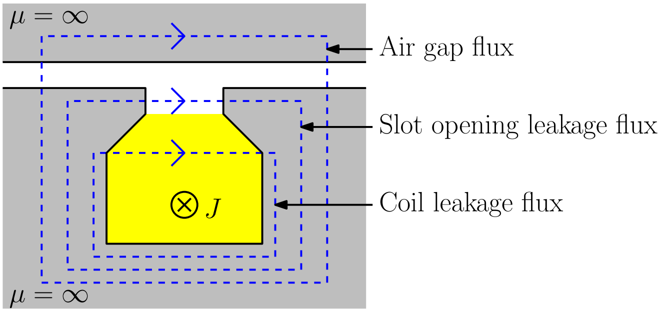

Figure 3.12: Simplified example of a single-slot model.

to obtain the most suitable values for the model slot angles is to select the one which results in the largest T_{em}.

Double region slot representation

To separate the influence of the selected slot angles on the air-gap flux distribution and the slot-leakage flux, two regions can be used to describe a stator or rotor slot instead of one region. An example of such a double region slot representation is shown in Fig. 3.11d. Here, the upper region represents the slot opening, whereas the lower region models the coil area of the slot. To avoid mixed boundary conditions between the upper and lower slot regions, both regions have the same slot angle, selected equal to the slot opening angle. Therefore, the influence of the slot openings on the air-gap magnetic-field distribution is properly included. Further, to avoid overestimation of the slot-leakage flux, an equivalent magnetic permeability, μ_{eq}, is introduced for the circumferential permeability, $\mu_{\theta\theta}$, of the coil area (lower) region. The value of μ_{eq} is calculated for the stator and rotor as

$$\mu_{eq,s} = \frac{b_{os}}{b_{ss}^{av}}\mu_0, \qquad \mu_{eq,r} = \frac{b_{or}}{b_{sr}^{av}}\mu_0. \tag{3.58}$$

It should be noted that the applicability of the proposed approach is currently limited to semi-closed stator and rotor slots. For fully-closed slots, a different procedure is required since the closed slot bridges are generally saturated, even for relatively low values of slot current. However, this is outside the scope of this thesis.

Validation of polar slot representations

To assess the correctness of the polar slot representations, FEA simulations are performed on a single-slot model of the actual slots and the polar slot representations. A simplified example of such a single-slot model is shown in Fig. 3.12. The results are quantified and compared in terms of air-gap flux, coil leakage flux and slot opening leakage flux for all four benchmark motor topologies. In all simulations, the soft-magnetic material surrounding the slot and opposing the

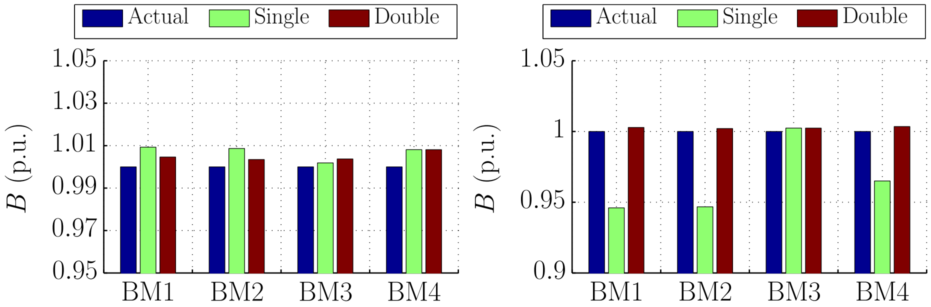

(a) Stator air-gap flux (b) Rotor air-gap flux

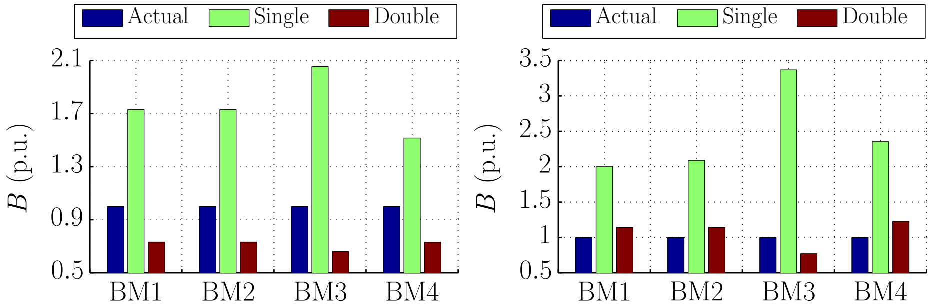

(c) Stator coil leakage flux (d) Rotor coil leakage flux

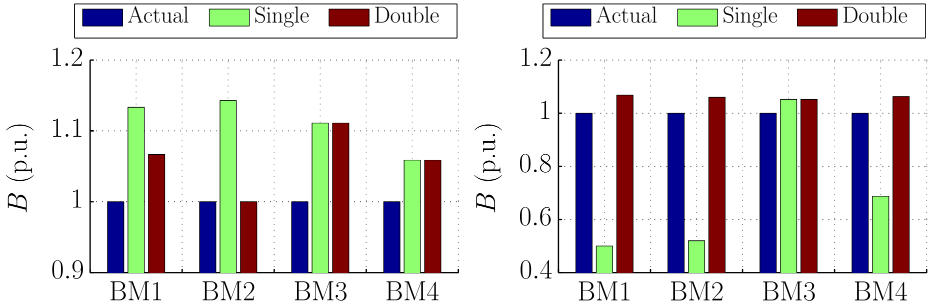

(e) Stator slot opening leakage flux (f) Rotor slot opening leakage flux

Figure 3.13: Validation of the single and double region polar slot representations against the actual slot geometry in terms of air-gap flux, coil leakage flux and slot opening leakage flux.

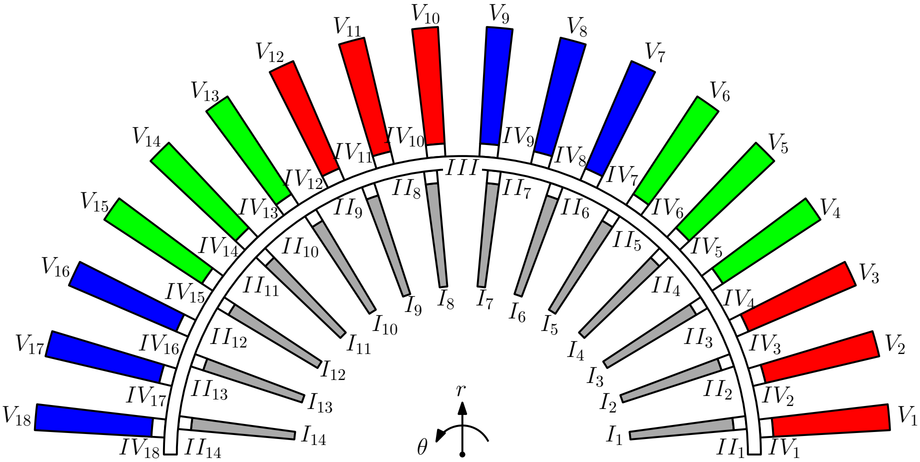

Figure 3.14: Example of a region division with double region polar slot representation.

slot on the other side of the air gap is assumed to be infinitely permeable. Also, the simulations are performed for stator and rotor slots separately. Figure 3.13 shows an overview of the simulation results, normalized with respect to the results obtained for the actual slots. To obtain the results for the single region slot representation, the stator and rotor slot angles are optimized for maximum T_{em}. It can be seen that both polar slot representations give a relatively accurate approximation of the air-gap flux with respect to the actual slots. For the coil and slot opening leakage fluxes, however, the double region polar slot representation is clearly much more accurate than the single region polar slot representation. Combined with the fact that it does not require any initial parameter sweeps, the double region polar slot is considered the favorable polar slot representation. Therefore, the double region representation will be used for the implementation of the benchmark motor topologies. Finally, it should be noted that even for the double region representation, there is still a small discrepancy with the actual slots, especially in term of coil leakage flux as observed in Figs. 3.13c and 3.13d. A different formulation of μ_{eq} could be used to reduce this difference. For example, an analytical or semi-analytical model for a single stator or rotor slot could be used to estimate the slot-leakage flux in advance and calculate a more accurate value for μ_{eq}. However, this is beyond the scope of this thesis.

3.4.2 Magnetic-field solution

To describe the magnetic-field solution for IMs, the geometry is divided into regions according to the selected polar geometry representation. An example of such a region model is shown in Figure 3.14 for benchmark motor "four". In total, a model consists of N_{sr} rotor slot regions, represented by I_ν, N_{sr} rotor slot openings regions, represented by II_ν, one air-gap region, represented by III, N_{ss} stator slot opening regions, represented by IV_ν and N_{ss} stator slot regions, represented by V_ν. Further, the material properties are homogeneous within each region. Therefore, the magnetic-field solution within each region is obtained using (2.27) to (2.38), and are described for each region type in the next subsections.

Magnetic-field solution in the air-gap region

In the air gap, region III, no current-density or remanent-magnetization sources are present, such that $\vec{J}^{\mathrm{III}} = \vec{M}_0^{\mathrm{III}} = 0$. Further, it is bounded in the circumferential direction by periodic boundaries and the permeability of the region is isotropic. Therefore, using (2.12) and (2.15), α^{III} and w_n^{III} are obtained as

$$\alpha^{\mathrm{III}} = 1, \qquad\qquad w_n^{\mathrm{III}} = 2n. \tag{3.59}$$

Considering the periodic boundaries and assuming balanced phase currents, the spatial average of the field quantities should be zero along one period, hence $A_{z0}^{\mathrm{III}} = B_{\theta 0}^{\mathrm{III}} = 0$. The remaining sine and cosine terms of $A_z^{\mathrm{III}}(r,\theta)$ are given by

$$A_{zcn}^{\mathrm{III}}(r) = -\frac{1}{w_n^{\mathrm{III}}}\left(a_n^{\mathrm{III}} r^{2n} + b_n^{\mathrm{III}} r^{-2n}\right), \tag{3.60}$$

$$A_{zsn}^{\mathrm{III}}(r) = -\frac{1}{w_n^{\mathrm{III}}}\left(c_n^{\mathrm{III}} r^{2n} + d_n^{\mathrm{III}} r^{-2n}\right), \tag{3.61}$$

whereas the sine and cosine coefficients of $B_r^{\mathrm{III}}(r,\theta)$ and $B_\theta^{\mathrm{III}}(r,\theta)$ are given by

$$B_{rcn}^{\mathrm{III}}(r) = -c_n^{\mathrm{III}} r^{2n-1} - d_n^{\mathrm{III}} r^{-2n-1}, \tag{3.62}$$

$$B_{rsn}^{\mathrm{III}}(r) = a_n^{\mathrm{III}} r^{2n-1} + b_n^{\mathrm{III}} r^{-2n-1}, \tag{3.63}$$

$$B_{\theta cn}^{\mathrm{III}}(r) = a_n^{\mathrm{III}} r^{2n-1} - b_n^{\mathrm{III}} r^{-2n-1}, \tag{3.64}$$

$$B_{\theta sn}^{\mathrm{III}}(r) = c_n^{\mathrm{III}} r^{2n-1} - d_n^{\mathrm{III}} r^{-2n-1}. \tag{3.65}$$

Magnetic-field solution in the slot opening regions

The rotor and stator slot opening regions, II_ν and IV_ν respectively, are bounded in the circumferential direction by infinitely permeable material. According to boundary conditions, the terms A_{zsm}, B_{rcm} and $B_{\theta sm}$ should therefore be zero for these regions. The spatial frequencies are given by

$$w_m^{\mathrm{II}_\nu} = \frac{m\pi}{\theta_{sr}}, \qquad\qquad w_m^{\mathrm{IV}_\nu} = \frac{m\pi}{\theta_{ss}}, \tag{3.66}$$

where m denotes the spatial ordinal number in each slot opening region, given by $m = 1, 2, 3...\infty$. Also, no current-density or remanent-magnetization sources are present and the magnetic permeability is isotropic, such that $\vec{J}^{\mathrm{II}_\nu} = \vec{J}^{\mathrm{IV}_\nu} =$

$\vec{M}_0^{\mathrm{II}_\nu} = \vec{M}_0^{\mathrm{IV}_\nu} = 0$ and $\alpha^{\mathrm{II}_\nu} = \alpha^{\mathrm{IV}_\nu} = 1$. Therefore, for each slot opening region, denoted by k_{so}, the remaining terms of $A_z^{k_{so}}(r,\theta)$ are given by

$$A_{zcm}^{k_{so}}(r) = -\frac{1}{w_m^{k_{so}}}\left(a_m^{k_{so}} r^{w_m^{k_{so}}} + b_m^{k_{so}} r^{-w_m^{k_{so}}}\right), \tag{3.67}$$

$$A_{z0}^{k_{so}}(r) = B_0^{k_{so}} \ln(r) + A_0^{k_{so}}, \tag{3.68}$$

whereas the remaining terms of $B_r^{k_{so}}(r,\theta)$ and $B_\theta^{k_{so}}(r,\theta)$ are given by

$$B_{rsm}^{k_{so}}(r) = a_m^{k_{so}} r^{w_m^{k_{so}}} + b_m^{k_{so}} r^{-w_m^{k_{so}}}, \tag{3.69}$$

$$B_{\theta cm}^{k_{so}}(r) = a_m^{k_{so}} r^{w_m^{k_{so}}} - b_m^{k_{so}} r^{-w_m^{k_{so}}}, \tag{3.70}$$

$$B_{\theta 0}^{k_{so}}(r) = -\frac{B_0^{k_{so}}}{r}. \tag{3.71}$$

Magnetic-field solution in the slot regions

The rotor and stator slot regions, I_ν and V_ν respectively, are also bounded by infinitely permeable material in the circumferential direction, such that the terms A_{zsm}, B_{rcm} and $B_{\theta sm}$ are zero. However, to correct the slot-leakage flux for the narrow slot regions in the model, the magnetic permeability is considered anisotropic, such that

$$\alpha^{\mathrm{I}_\nu} = \sqrt{\frac{\mu_{eq,r}}{\mu_0}}, \qquad \alpha^{\mathrm{V}_\nu} = \sqrt{\frac{\mu_{eq,s}}{\mu_0}}. \tag{3.72}$$

The spatial frequencies are given by

$$w_m^{\mathrm{I}_\nu} = \frac{m\pi}{\theta_{sr}}, \qquad w_m^{\mathrm{V}_\nu} = \frac{m\pi}{\theta_{ss}}. \tag{3.73}$$

Further, a homogeneous current density $\vec{J}^k = J_0^k \vec{e}_z$ is present in each slot region, whereas $\vec{M}_0^{I_\nu} = \vec{M}_0^{V_\nu} = 0$. For the stator slot regions, $J_0^{V_\nu}$ is equal to J_A, J_B or J_C and for the rotor slot regions $J_0^{I_\nu}$ is equal to J_{bar}^ν. Finally, for each slot region, denoted by k_{sc}, the remaining terms of $A_z^{k_{sc}}(r,\theta)$ are given by

$$A_{zcm}^{k_{sc}}(r) = -\frac{1}{w_m^{k_{sc}}}\left(a_m^{k_{sc}} r^{\alpha^{k_{sc}} w_m^{k_{sc}}} + b_m^{k_{sc}} r^{-\alpha^{k_{sc}} w_m^{k_{sc}}}\right), \tag{3.74}$$

$$A_{z0}^{k_{sc}}(r) = -\mu_{\theta\theta}^{k_{sc}} \frac{J_{z0}^{k_{sc}}}{4} r^2 + B_0^{k_{sc}} \ln(r) + A_0^{k_{sc}}, \tag{3.75}$$

whereas the remaining terms of $B_r^{k_{sc}}(r,\theta)$ and $B_\theta^{k_{sc}}(r,\theta)$ are given by

$$B_{rsm}^{k_{sc}}(r) = a_m^{k_{sc}} r^{\alpha^{k_{sc}} w_m^{k_{sc}}} + b_m^{k_{sc}} r^{-\alpha^{k_{sc}} w_m^{k_{sc}}}, \tag{3.76}$$

$$B_{\theta cm}^{k_{sc}}(r) = \alpha^{k_{sc}} a_m^{k_{sc}} r^{\alpha^{k_{sc}} w_m^{k_{sc}}} - \alpha^{k_{sc}} b_m^{k_{sc}} r^{-\alpha^{k_{sc}} w_m^{k_{sc}}}, \tag{3.77}$$

$$B_{\theta 0}^{k_{sc}}(r) = \mu_{\theta\theta}^{k_{sc}} \frac{J_{z0}^{k_{sc}}}{2} r - \frac{B_0^{k_{sc}}}{r}. \tag{3.78}$$

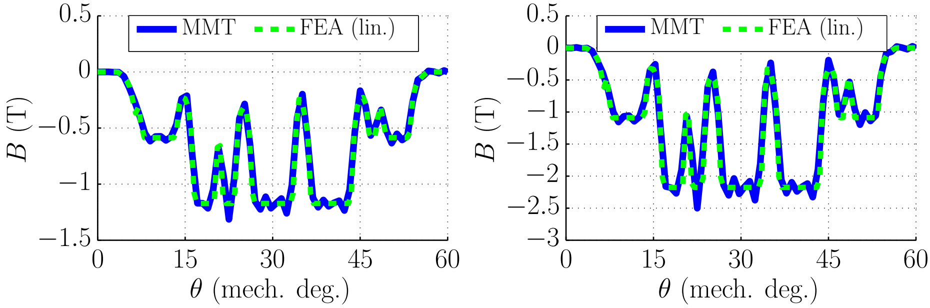

(a) Benchmark motor ”one” (b) Benchmark motor ”two”

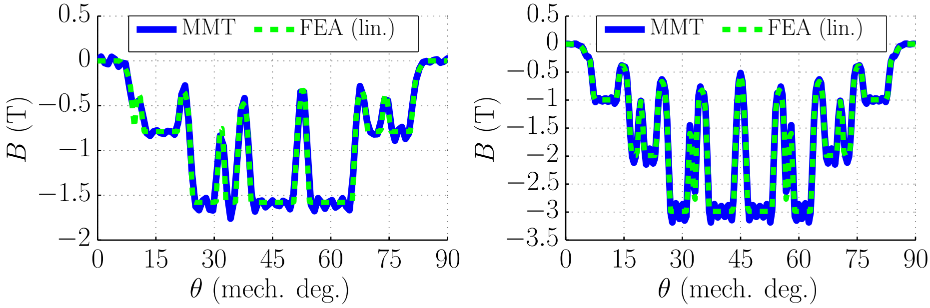

(c) Benchmark motor ”three” (d) Benchmark motor ”four”

Figure 3.15: Comparison of the radial air-gap flux-density distribution calculated by MMT and linear 2D FEA for nominal stator current at no-load operation.

Boundary conditions

The unknown coefficients in (3.60) to (3.65), (3.67) to (3.71) and (3.74) to (3.78) are solved using boundary conditions as discussed in Section 2.5. At the inner boundary of the rotor slot regions and the outer boundaries of the stator slot regions, Neumann boundary conditions are applied. In addition, interface boundary conditions are applied on the boundaries between each slot and slot opening region. Finally, on the interface between the slot opening regions and the air-gap region, mixed boundary conditions are applied. A complete overview of the boundary-condition equations between the regions of the IM mode-matching model is given in Appendix A.2.

3.4.3 Air-gap magnetic-flux density

To validate the magnetic-field solution of the MMT model, the magnetic-flux-density distribution in the air gap is calculated using (3.62) to (3.65), (2.17) and (2.18). Due to the geometry of benchmark motors ”one” and ”two”, periodicity can not be applied and the entire motor geometry should be represented in the MMT model. Consequently, the ratio between the first (but not necessarily fundamental) spatial air-gap harmonic and the first spatial slotting harmonic in the air gap is relatively large. Therefore, to obtain sufficient convergence, a relatively large number of spatial air-gap harmonics, $N_{sh}^{\mathrm{III}} = 150$, needs to be selected. For benchmark motor "three", periodicity can not be applied either, although it has fewer stator and rotor slots than benchmark motors "one" and "two". Therefore, the ratio between the first spatial air-gap harmonic and the first spatial slotting harmonic is naturally lower, such that $N_{sh}^{\mathrm{III}} = 120$ can be selected. Finally, periodicity can be applied for benchmark motor "four", such that the number of spatial air-gap harmonics can be reduced to $N_{sh}^{\mathrm{III}} = 100$. The number of spatial harmonics in the remaining regions is then determined using (2.88).

During the calculations, I_{ph} was set to its nominal value and I_{bar} was set to zero. Similar calculations were also performed with a current-fed, linear FEA model. In this FEA model, the magnetic permeability of the stator and rotor soft-magnetic material is set to a large value (1e8) to closely approximate the infinite permeability assumed in the MMT model. A comparison of the calculation results obtained from both models is shown in Figure 3.15 in terms of the radial magnetic-flux-density distribution along the circumferential axis at $r = (r_{si} + r_{ro})/2$. It can be seen that a good agreement is obtained between the MMT model and the linear FEA predictions. However, due to the truncation of the Fourier series, oscillations appear near fast transitions of the magnetic-flux density. This effect is known as the Gibbs phenomenon [155, 156, 157, 158] and for the given calculation results, it leads to local errors up to 33% with respect to the amplitude of the fundamental magnetic-flux density. The rms value of the error along the entire waveform, however, is limited to a maximum of 8% for the considered benchmark motors.

Further, it can be seen from Figure 3.15 that the flux-density levels predicted by the linear models are high, especially for benchmark motors "two" and "four". In a practical machine, such levels are generally not achieved due to soft-magnetic material saturation. However, it should be noted that Figure 3.15 represents a no-load case, where nominal stator phase current is applied to the stator windings. In an on-load situation, a significant counteracting rotor field would be present, which would lead to much lower flux-density levels.

Finally, a comparison of the fundamental air-gap magnetic-flux-density for various stator currents, ranging from 10% up to 100% of the nominal current, is shown in Figure 3.16. These results are obtained from the MMT, linear FEA and nonlinear FEA models for no-load operating conditions. For the nonlinear simulations, the BH-characteristic of soft-magnetic material two, as presented in Appendix B, is used. From the results, it can be seen that a very good agreement is obtained between the MMT model and the linear FEA model. The obtained errors are all less than 3% with respect to the value obtain by FEA for nominal current. This indicates that the MM model can present an accurate estimation of the influence of slotting on the fundamental air-gap flux in the linear case. For example, the

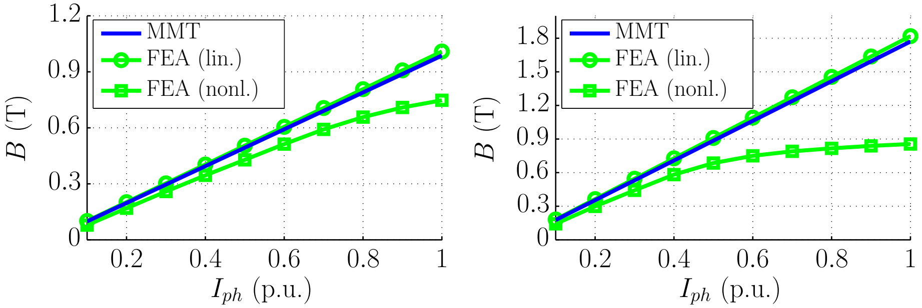

(a) Benchmark motor "one" (b) Benchmark motor "two"

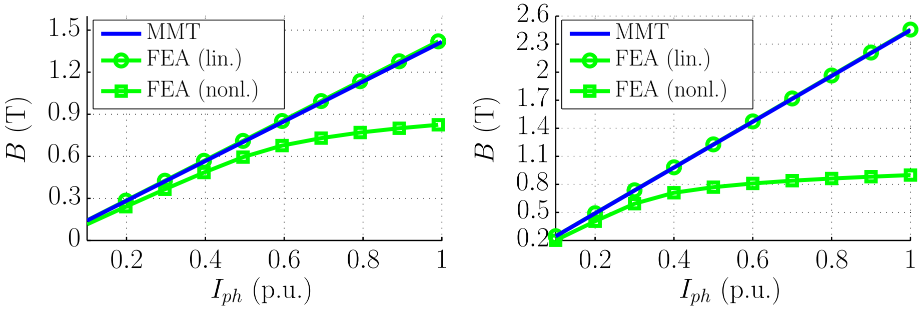

(c) Benchmark motor "three" (d) Benchmark motor "four"

Figure 3.16: Comparison of the fundamental air-gap flux-density calculated by MMT and linear 2D FEA for various stator currents at no-load operation.

MM model could therefore be used as an alternative method to calculate Carter's factor. Also, it can be seen that there is a large discrepancy between the linear models and the nonlinear model due to the neglected saturation effect. However, it should be noted that the results in Figure 3.16 represent no-load operating conditions. For full-load operating conditions, which are of main interest here, the discrepancy will be significantly reduced due to the counteracting magnetic field of the rotor. This conclusion is supported by the fact that there is a relatively good agreement between the linear and nonlinear models for low stator current values.

3.4.4 Flux linkage

The total flux linkage of each ν^{th} stator or rotor slot can be obtained by evaluating

$$\bar{\lambda}_{ss}^{\nu,MMT} = \frac{z_{Q,s} l_{sl}}{S_{ss}} \int_{0}^{\theta_{ss}} \int_{r_i^{\mathrm{V}}}^{r_o^{\mathrm{V}}} A_z\left(r, \theta^{\mathrm{V}_\nu}\right) r dr d\theta^{\mathrm{V}_\nu}, \tag{3.79}$$

$$\bar{\lambda}_{sr}^{\nu,MMT} = \frac{l_{sl}}{S_{sr}} \int\limits_{0}^{\theta_{sr}} \int\limits_{r_i^{\mathrm{I}}}^{r_o^{\mathrm{I}}} A_z\left(r, \theta^{\mathrm{I}_\nu}\right) r dr d\theta^{\mathrm{I}_\nu}. \tag{3.80}$$

For the magnetic-field solution given in Section 3.4.2, this yields

$$\bar{\lambda}_{ss}^{\nu,MMT} = \frac{z_{Q,s} l_{sl} \theta_{ss}}{2 S_{ss}} \left[C_{I,s} J_{z0}^{\mathrm{V}_\nu} + C_{B,s} B_0^{\mathrm{V}_\nu} + C_{A,s} A_0^{\mathrm{V}_\nu}\right], \tag{3.81}$$

$$\bar{\lambda}_{sr}^{\nu,MMT} = \frac{l_{sl} \theta_{sr}}{2 S_{sr}} \left[C_{I,r} J_{z0}^{\mathrm{I}_\nu} + C_{B,r} B_0^{\mathrm{I}_\nu} + C_{A,r} A_0^{\mathrm{I}_\nu}\right], \tag{3.82}$$

where the coefficients $C_{I,s}$, $C_{I,r}$, $C_{B,s}$, $C_{B,r}$, $C_{A,s}$ and $C_{A,r}$ are obtained as

$$C_{I,s} = -\frac{\mu_{\theta\theta}^{\mathrm{V}_\nu}}{8} \left(\left(r_o^{\mathrm{V}_\nu}\right)^4 - \left(r_i^{\mathrm{V}_\nu}\right)^4\right), \tag{3.83}$$

$$C_{I,r} = -\frac{\mu_{\theta\theta}^{\mathrm{I}_\nu}}{8} \left(\left(r_o^{\mathrm{I}_\nu}\right)^4 - \left(r_i^{\mathrm{I}_\nu}\right)^4\right), \tag{3.84}$$

$$C_{B,s} = \left[\left(r_o^{\mathrm{V}_\nu}\right)^2 \left(\ln\left(r_o^{\mathrm{V}_\nu}\right) - \frac{1}{2}\right) - \left(r_i^{\mathrm{V}_\nu}\right)^2 \left(\ln\left(r_i^{\mathrm{V}_\nu}\right) - \frac{1}{2}\right)\right], \tag{3.85}$$

$$C_{B,r} = \left[\left(r_o^{\mathrm{I}_\nu}\right)^2 \left(\ln\left(r_o^{\mathrm{I}_\nu}\right) - \frac{1}{2}\right) - \left(r_i^{\mathrm{I}_\nu}\right)^2 \left(\ln\left(r_i^{\mathrm{I}_\nu}\right) - \frac{1}{2}\right)\right], \tag{3.86}$$

$$C_{A,s} = \left(\left(r_o^{\mathrm{V}_\nu}\right)^2 - \left(r_i^{\mathrm{V}_\nu}\right)^2\right), \tag{3.87}$$

$$C_{A,r} = \left(\left(r_o^{\mathrm{I}_\nu}\right)^2 - \left(r_i^{\mathrm{I}_\nu}\right)^2\right). \tag{3.88}$$

The flux linkage phasor of each stator phase A, B and C is then obtained as

$$\bar{\lambda}_A^{MMT} = C_{per} \sum_{\forall \nu \in N_A} c_{dir}^{\nu} \bar{\lambda}_{ss}^{\nu,MMT}, \tag{3.89}$$

$$\bar{\lambda}_B^{MMT} = C_{per} \sum_{\forall \nu \in N_B} c_{dir}^{\nu} \bar{\lambda}_{ss}^{\nu,MMT}, \tag{3.90}$$

$$\bar{\lambda}_C^{MMT} = C_{per} \sum_{\forall \nu \in N_C} c_{dir}^{\nu} \bar{\lambda}_{ss}^{\nu,MMT}. \tag{3.91}$$

Additionally, the MMT model can also be used to calculate the magnetization flux linkage phasor, $\bar{\lambda}_{ms}^{\nu,MMT}$, due the the fundamental space harmonic of the motor. For each stator or rotor slot, $\bar{\lambda}_{ms}^{\nu,MMT}$, is obtained by evaluating

$$\bar{\lambda}_{m,ss}^{\nu,MMT} = \frac{z_{Q,s} l_{sl}}{\theta_{ss}} \int\limits_{\theta_{sb,\nu}}^{\theta_{se,\nu}} A_z\left(r, \theta\right) r d\theta \Bigg|_{r=r_g}, \tag{3.92}$$

$$\bar{\lambda}_{m,sr}^{\nu,MMT} = \frac{l_{sl}}{\theta_{sr}} \int\limits_{\theta_{rb,\nu}}^{\theta_{re,\nu}} A_z\left(r, \theta\right) r d\theta \Bigg|_{r=r_g}, \tag{3.93}$$

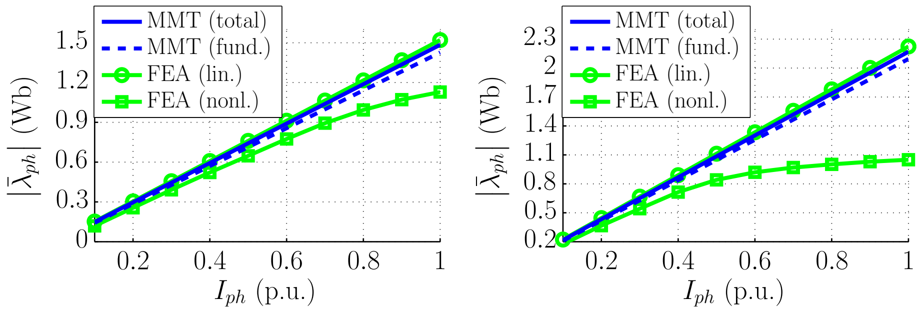

(a) Benchmark motor "one" (b) Benchmark motor "two"

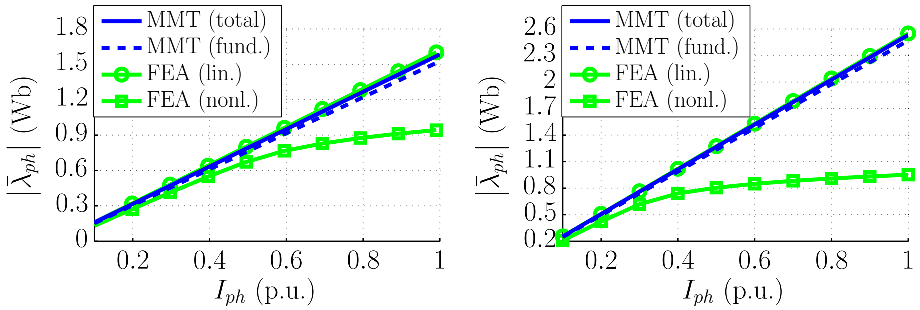

(c) Benchmark motor "three" (d) Benchmark motor "four"

Figure 3.17: Comparison of the stator flux linkage calculated by MMT and linear 2D FEA for various stator currents at no-load operation.

where $r_g = r_{ro} + \frac{g}{2}$. For the given magnetic-field solution, this yields

$$\bar{\lambda}^{\nu,MMT}_{m,ss} = \frac{z_{Q,s} l_{sl}}{\left(w^{\mathrm{III}}_{n_f}\right)^2 \theta_{ss}} \left(C^{m,\nu}_{cos,s} - C^{m,\nu}_{sin,s}\right), \tag{3.94}$$

$$\bar{\lambda}^{\nu,MMT}_{m,sr} = \frac{l_{sl}}{\left(w^{\mathrm{III}}_{n_f}\right)^2 \theta_{sr}} \left(C^{m,\nu}_{cos,r} - C^{m,\nu}_{sin,r}\right), \tag{3.95}$$

where coefficient $C^m_{sin,s}$, $C^m_{sin,r}$, $C^m_{cos,s}$ and $C^m_{cos,r}$ are given by

$$C^{m,\nu}_{sin,s} = \left(a^{\mathrm{III}}_{n_f} r_g^{2n_f} + b^{\mathrm{III}}_{n_f} r_g^{-2n_f}\right)\left(\sin\left(w^{\mathrm{III}}_{n_f}\theta_{se,\nu}\right) - \sin\left(w^{\mathrm{III}}_{n_f}\theta_{sb,\nu}\right)\right), \tag{3.96}$$

$$C^{m,\nu}_{sin,r} = \left(a^{\mathrm{III}}_{n_f} r_g^{2n_f} + b^{\mathrm{III}}_{n_f} r_g^{-2n_f}\right)\left(\sin\left(w^{\mathrm{III}}_{n_f}\theta_{re,\nu}\right) - \sin\left(w^{\mathrm{III}}_{n_f}\theta_{rb,\nu}\right)\right), \tag{3.97}$$

$$C^{m,\nu}_{cos,s} = \left(c^{\mathrm{III}}_{n_f} r_g^{2n_f} + d^{\mathrm{III}}_{n_f} r_g^{-2n_f}\right)\left(\cos\left(w^{\mathrm{III}}_{n_f}\theta_{se,\nu}\right) - \cos\left(w^{\mathrm{III}}_{n_f}\theta_{sb,\nu}\right)\right), \tag{3.98}$$

$$C^{m,\nu}_{cos,r} = \left(c^{\mathrm{III}}_{n_f} r_g^{2n_f} + d^{\mathrm{III}}_{n_f} r_g^{-2n_f}\right)\left(\cos\left(w^{\mathrm{III}}_{n_f}\theta_{re,\nu}\right) - \cos\left(w^{\mathrm{III}}_{n_f}\theta_{rb,\nu}\right)\right). \tag{3.99}$$

Finally, the magnetizing flux linkage per stator phase is obtained as

$$\bar{\lambda}_{m,A}^{MMT} = C_{per} \sum_{\forall \nu \in N_A} c_{dir}^{\nu} \bar{\lambda}_{m,ss}^{MMT}, \tag{3.100}$$

$$\bar{\lambda}_{m,B}^{MMT} = C_{per} \sum_{\forall \nu \in N_B} c_{dir}^{\nu} \bar{\lambda}_{m,ss}^{MMT}, \tag{3.101}$$

$$\bar{\lambda}_{m,C}^{MMT} = C_{per} \sum_{\forall \nu \in N_C} c_{dir}^{\nu} \bar{\lambda}_{m,ss}^{MMT}. \tag{3.102}$$

In Figure 3.17, a comparison of the flux linkages calculated from the MMT, linear FEA and nonlinear FEA models is shown. These results are obtained at no-load operation for various stator current values, increasing from 10% to 100% of the nominal current. It can be seen that a very good agreement is obtained between the total phase flux linkage calculated by the MMT model and the linear FEA predictions. With respect to the FEA results obtained for nominal current, an error less than 3% is obtained for all benchmark motors. Also, it can be seen that the fundamental phase flux linkage is very close to the total flux linkage. The small difference between the fundamental and total flux linkage calculated by the MMT model represents the stator leakage flux. However, a large discrepancy between the linear and nonlinear models is observed due to the neglected saturation effect. As previously discussed, this discrepancy will be significantly reduced for full-load operating conditions.

3.4.5 Electromagnetic torque

As previously discussed in Section 3.3.6, an analytical expression for the produced electromagnetic torque, T_{em}, can be calculated by integrating Maxwell's Stress Tensor along the rotor surface in the air-gap region. For the MMT model, the expression for T_{em} is obtained as

$$T_{em} = \frac{2\pi l_{stk}}{\mu_0} \sum_{n=1}^{N_{sh}^{\mathrm{III}}} \left[b_n^{\mathrm{III}} c_n^{\mathrm{III}} - a_n^{\mathrm{III}} d_n^{\mathrm{III}} \right]. \tag{3.103}$$

To validate T_{em} predicted by the MMT model, calculation results are obtained for all four benchmark motors. A static current distribution is applied to the stator windings and rotor bars using (3.4) to (3.6) and (3.8), respectively, where $I_{ph} = I_{ph}^N$ and $I_{bar} = I_{bar}^N$ are used. The rotor is then rotated along one mechanical period in steps and for each step, T_{em} is calculated using (3.103). Similar predictions are also obtained from the linear 2D FEA models. A comparison of the results is shown in Figure 3.18. It can be seen that the calculation results are in good agreement, although some discrepancies are observed at the peaks of the waveforms. These mismatches are attributed to the truncation of the Fourier series, and lead to local errors typically ranging from 10% up to 25% with respect to the nominal torque of the benchmark motors. However, the rms value of the error along the entire waveform, is 10% or less.

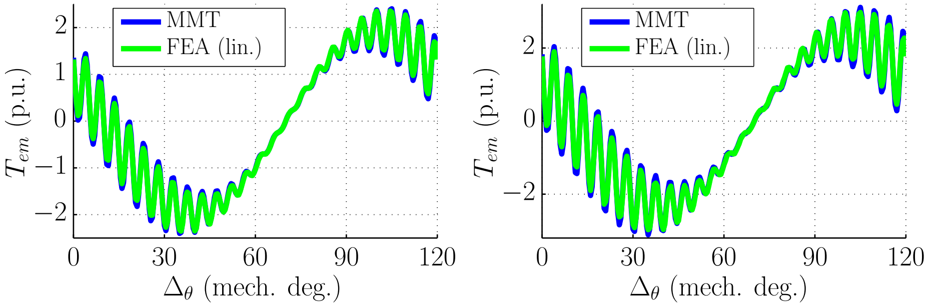

(a) Benchmark motor "one"   (b) Benchmark motor "two"

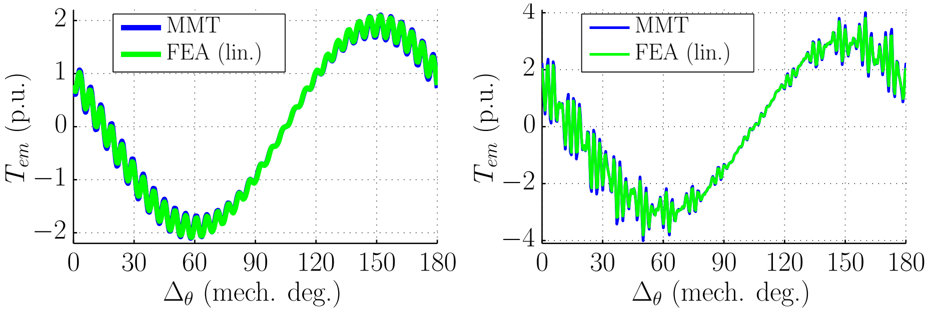

(c) Benchmark motor "three"   (d) Benchmark motor "four"

Figure 3.18: Comparison of the electromagnetic torque calculated by MMT and linear 2D FEA for various rotor positions and static stator and rotor current distributions.

Chapter 4

Electric-circuit coupling

The contents of this chapter are published in:

R. L. J. Sprangers, B. L. J. Gysen, J. J. H. Paulides, J. Waarma, and E. A. Lomonova, "Calculation of induced rotor current in induction motors using a slotted semi-analytical harmonic model," in *Proceedings of the XXIth International Conference on Electrical Machines (ICEM)*, September 2014.

R. L. J. Sprangers, J. J. H. Paulides, B. L. J. Gysen, J. Waarma, and E. A. Lomonova, "Electric circuit coupling of a slotted semi-analytical model for induction motors based on harmonic modeling," in *Proceedings of IEEE Energy Conversion Congress and Expo (ECCE)*, September 2014.

4.1 Introduction

In Chapter 3, two harmonic models for IM analysis have been discussed. These models can be used to analyse the magnetic-field distribution in an IM for a predefined distribution of the stator and rotor currents. However, they do not include the interactions that take place between the electric and magnetic domain. These interactions are therefore investigated in this chapter in terms of a coupling between the magnetic models and electric-circuit models of the stator and rotor windings. As a results, two methods are defined to calculate the fundamental time harmonic of the induced rotor-bar current for a given stator current distribution. Both these methods are applied to calculate the rotor-bar current and electromagnetic torque for the four benchmark motors, and the computation results are validated against 2D FEA calculations. Finally, the second calculation method is also applied for voltage-fed simulations.

4.2 Induced voltage and current

According to Faraday's law of induction, a time-varying magnetic field is always accompanied by an electric field. A generalised expression for this principle is given by the quasi-static Maxwell-Faraday equation, expressed in differential form as

$$\nabla \times \vec{E} = -\frac{\partial \vec{B}}{\partial t}, \tag{4.1}$$

where $\vec{E}$ represents the electric field strength vector. For all electromagnetic motors and actuators, the principle of induction is of fundamental importance. For IMs, the induction principle plays a double role. Firstly, it produces an induced voltage in the stator windings. Secondly, it also produces an induced voltage in the rotor bars, which leads to an induced current in the closed rotor circuit. The rotor current generates an opposing secondary magnetic field. Without this secondary field, the motor would mainly draw reactive power and no active power is converted into mechanical power. Once the secondary magnetic field becomes apparent, however, the phase angle of the stator induced voltage changes such that mainly active power is drawn for energy conversion.

The amplitude and phase angle of the induced rotor current depend on the slip, s, between the rotor and the rotating magnetic field of the stator. By assuming that the stator excitation frequency and the mechanical angular velocity of the rotor, $w_{r,m}$, are known, s is obtained as

$$s = \frac{w_{syn} - w_{r,m}}{w_{syn}}, \tag{4.2}$$

where w_{syn} is the synchronous angular velocity of the stator magnetic field, given by

$$w_{syn} = \frac{2\pi f_s}{p}. \tag{4.3}$$

Furthermore, the rotor current also depends on the magnitude and the orientation of the magnetic flux in the motor. In turn, however, the magnetic flux depends on the stator and rotor current. Thus, to calculate the rotor current, both its own magnetic field and the magnetic field of the stator should be considered.

Two methods to calculate the fundamental time harmonic of the induced rotor current are presented in this chapter. The first method is an indirect one and can only be applied to a linear magnetic-field model, i.e. the MMT model in this case. Further, it also limits the model to current-fed simulations, which means that the stator phase currents should be known a-priori. The second method presents a direct coupling between the magnetic-field model and the electric-circuit models of the stator and rotor. It can be applied to both linear and nonlinear magnetic-field models and allows for current-fed as well as voltage-fed simulations. Also, both methods take the resistance and inductance of the rotor end rings into account. It should be noted, however, that the influence of higher time harmonics in the rotor are currently neglected. Due to the discrete distribution of the stator windings and the permeance variations caused by stator and rotor slotting, such harmonics can become apparent. In practice, they lead to parasitic effects such as additional Ohmic losses in the rotor, increased skin effect and parasitic components in the torque-speed characteristic of the motor. Fortunately, the influence of these effects can be significantly reduced by means of appropriate design choices [37]. Furthermore, the models presented in Chapter 3 can be used to predict the rotor current time harmonics and their influence on the torque-speed characteristic as well. However, this is beyond the scope of this thesis.

An alternative approach to calculate the induced currents in the rotor bars is by solving the magnetic field in the rotor bars using the diffusion equation, which is given in terms of $\vec{A}$ by

$$\nabla^2\vec{A} - \mu\sigma\frac{d\vec{A}}{dt} = 0. \tag{4.4}$$

The advantage of such an approach is that a nonuniform current distribution in the rotor bars, for example due to skin effect, can be accounted for. However, a different representation of the rotor bars, in comparison to the ones proposed in Chapter 3, is most likely required. Further, the time-dependence can be accounted for by considering a steady-state solution and assuming that the rotor position is fixed. For polar coordinates, the resulting magnetic-field solution can then be expressed in terms of Fourier series by using Bessel functions to describe the radial dependence of the magnetic field. These Bessel functions presents additional challenges to the model implementation, although solutions to some common problems are provided in literature. For example, the numerical convergence of higher-order Bessel functions can be improved by employing the method described in [159]. Also, if the Bessel functions need to be evaluated for various order numbers, but with the same argument, recurrence relations can be used to quickly obtain numerical values. An extensive treatise on the theory of Bessel functions is given in [160]. On the other hand, Bessel functions can be omitted if the magnetic-field problem is described in Cartesian coordinates. For example, a Cartesian implementation of a single rotor slot can be used to estimate the skin effect due to various rotor current time harmonics. Such a model, however, is not considered here.

An implementation of the diffusion equation for an ALT model in polar coordinates is presented in [71]. In this publication, an equivalent conductivity is specified for the rotor slotting region, such that the current induced in the rotor can be calculated directly as a function of the rotor slip. However, due to the homogenization of the material properties, an incorrect rotor current-density distribution is obtained for high slip values. Also, the rotor end-ring resistance and inductance cannot be easily accounted for.

Additionally, an implementation of the diffusion equation for an MMT model in polar coordinates is presented in [142], under the assumption of a smooth stator surface (no stator slotting) and single stator spatial harmonic excitation. A similar approach could be applied to the double slotted MMT model discussed in Chapter 3, to calculate the fundamental time harmonic of the induced rotor current. The methods presented in this thesis could consecutively be used to couple the electromagnetic model to an external electric circuit to account for the rotor end rings [161]. However, the implementation of the diffusion equation for the MMT model is not within the scope of this thesis. Therefore, this chapter mainly focuses on calculating the interaction between the magnetic models described in Chapter 3 and the electric-circuit models of the stator and rotor windings.

4.3 Indirect rotor current calculation

The indirect rotor current calculation method divides the computation of the induced current in the ν^{th} rotor bar, $\bar{I}_{bar}^{\nu}$, into three steps, namely:

1. Calculate the flux linkage in the ν^{th} rotor bar due to stator excitation.
2. Calculate the synchronous inductance of the ν^{th} rotor bar.
3. Calculate the induced current in the ν^{th} rotor bar.

The magnetic fields due to the stator and rotor currents are calculated separately during steps one and two. The results of these calculations are translated into

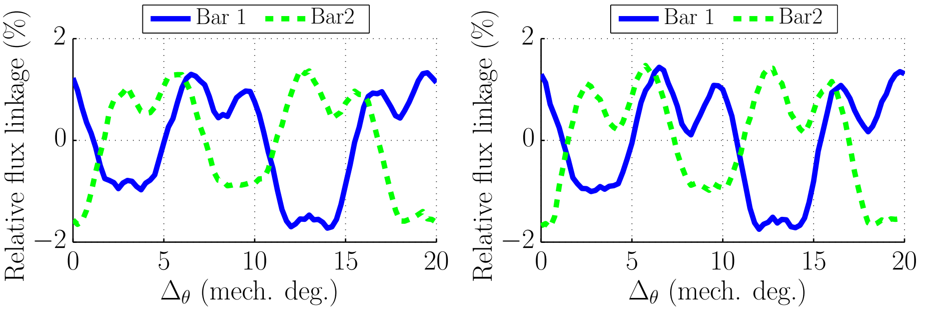

(a) Benchmark motor "one" (b) Benchmark motor "two"

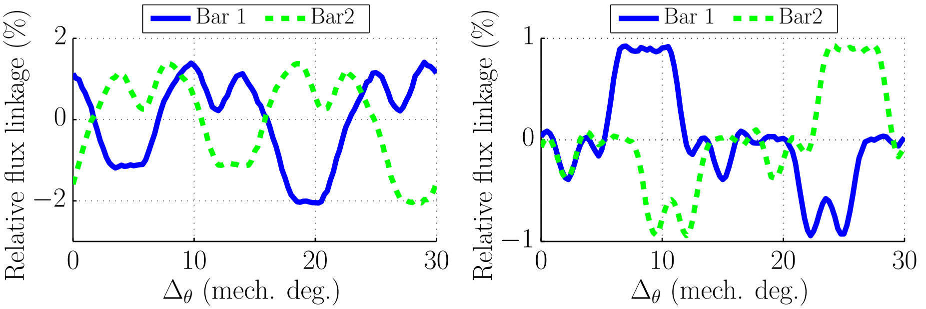

(c) Benchmark motor "three" (d) Benchmark motor "four"

Figure 4.1: Variation of the fundamental rotor-bar flux linkage due to stator excitation, relative to its average value (calculated by MMT).

circuit parameters, such that the induced rotor-bar current can be calculated during step three. It should be noted that such an approach can only be applied to a linear model, since the stator excitation current does not influence the magnetic field produced by the rotor current, and vice-versa. Therefore, the following calculations are only applied to the MMT model.

4.3.1 Rotor-bar flux linkage due to stator excitation

The purpose of step one is to calculate the amplitude of the fundamental flux linkage in the ν^{th} rotor bar, $\left|\bar{\lambda}^{\nu}_{sr}\right|$, due to the stator excitation current using the MMT model. Therefore, a three-phase current distribution is applied to the stator windings, whereas the rotor current is set to zero. The flux linkage phasor $\bar{\lambda}^{\nu}_{sr}$ is obtained using (3.82). However, due to the stator and rotor slotting, the obtained flux linkage value varies with rotor position. This variation repeats itself periodically and the period angle is equal to the number of stator slots per pole per phase, q, times the stator slot pitch angle, $\theta_{sp,s} = 2\pi/Q_s$. In Figure 4.1, the variation of $\left|\bar{\lambda}^{\nu}_{sr}\right|$ is shown, relative to its average value, $\lambda^{\nu,av}_{sr}$, for two rotor bars of each benchmark motor. It can be seen that the influence of the rotor position

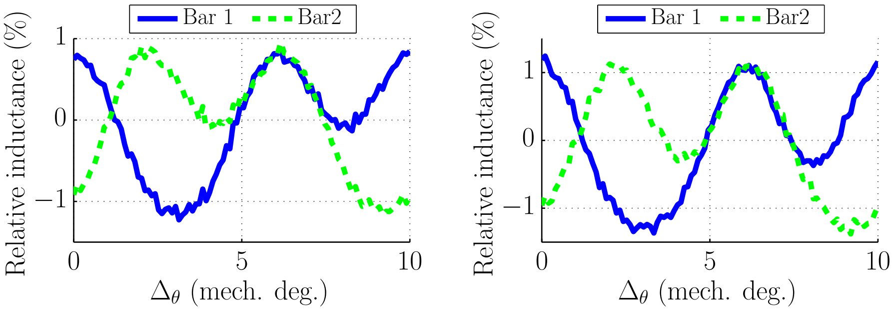

(a) Benchmark motor "one" (b) Benchmark motor "two"

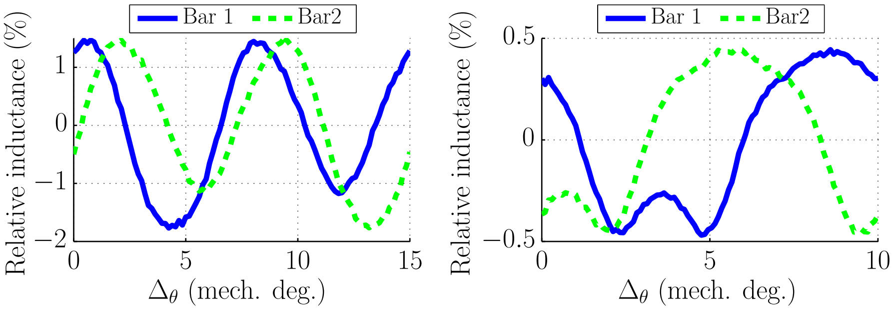

(c) Benchmark motor "three" (d) Benchmark motor "four"

Figure 4.2: Variation of the rotor-bar synchronous inductance, relative to its average value (calculated by MMT).

is small, i.e. 2% or less for the benchmark motors. This suggests that $\left|\bar{\lambda}_{sr}^{\nu}\right|$ can be calculated for a single rotor position, e.g. $\Delta_\theta = 0$, and used in the calculations of step three without introducing a significant error.

Additionally, it can also be seen that the results obtained for $\left|\bar{\lambda}_{sr}^{2}\right|$ are approximately equal to the results obtained for $\left|\bar{\lambda}_{sr}^{1}\right|$, but shifted with respect to Δ_θ. The discrepancies between the waveforms, due to the truncation of the Fourier series and the limited numerical accuracy of the results, are small enough to be neglected. Therefore, the flux linkage amplitude obtained for one rotor bar can be used for all other rotor bars as well. In total, the number of model runs required during step one can thus be reduced to one, which significantly decreases the required computation time. Nevertheless, such an approach should be used with caution during machine design. Especially when the number of stator or rotor slots, or the slot opening dimensions are varied, it should be checked whether the previous assumptions are still valid. Alternatively, the average value of $\left|\bar{\lambda}_{sr}^{\nu}\right|$ obtained for various rotor positions can be used.

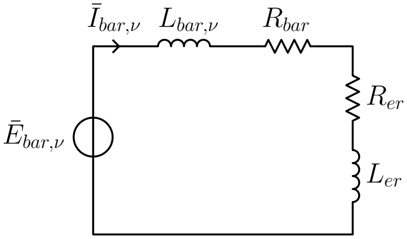

Figure 4.3: Rotor-bar circuit used to calculate the rotor-bar currents with the indirect method.

4.3.2 Rotor-bar synchronous inductance

The purpose of the second calculation step is to determine the rotor-bar synchronous inductance, $L_{bar,\nu}$. Therefore, the stator current is set to zero, whereas a sinusoidal current distribution is applied to the rotor bars, using (3.8). Then, the rotor-bar flux linkage phasor, $\bar{\lambda}_{sr}^{\nu}$, is obtained using (3.82), such that $L_{bar,\nu}$ can be calculated as

$$L_{bar,\nu} = \frac{\left|\bar{\lambda}_{sr}^{\nu}\right|}{\sqrt{2}I_{bar}}. \tag{4.5}$$

Since the MMT model is linear, the value of I_{bar} does not influence the obtained inductance, and is therefore set to its nominal value for convenience. Further, $L_{bar,\nu}$ depends on the rotor position and behaves periodically along one stator slot pitch angle, $\theta_{sp,s}$. Figure 4.2 shows the variation in $L_{bar,\nu}$ with rotor position relative to its average value for two rotor bars of each benchmark motor. Similar to the results of step one, it can be seen that $L_{bar,\nu}$ does not vary significantly with the rotor position, i.e. 2% or less for the benchmark motors. Also, the results obtained for $L_{bar,2}$ are approximately equal to $L_{bar,1}$, but shifted with respect to Δ_θ. Therefore, it is assumed that $L_{bar,\nu}$ can be obtained for each rotor bar by performing the calculation on one rotor bar for a single rotor position, e.g. $\Delta_\theta = 0$. The results of step two could thus be obtained from a single model run as well, albeit with care.

4.3.3 Induced rotor-bar current

During calculation step three, $\bar{I}_{bar,\nu}$ is calculated for given stator excitation and slip using the rotor-bar electric circuit shown in Fig. 4.3. The voltage phasor $\bar{E}_{bar,\nu}$ represents the voltage induced in the ν^{th} rotor bar due to the stator excitation, and is calculated as

$$\bar{E}_{bar,\nu} = jsw_s\left|\bar{\lambda}_{sr}^{\nu}\right|, \tag{4.6}$$

where $w_s = 2\pi f_s$. Further, the parameters R_{er} and L_{er} are the equivalent resistance and inductance of the rotor end ring. To calculate R_{er} and L_{er}, firstly, the resistance and inductance of an end-ring segment between two adjacent rotor bars are calculated as [37]

$$R_{ring} = \frac{l_{ring}}{\sigma_r S_{ring}}, \tag{4.7}$$

$$L_{ring} = \frac{\mu_0 Q_r}{3mp^2}\left(0.18\frac{\pi D_{ring}}{2p}\right), \tag{4.8}$$

where D_{ring} and S_{ring} are the average diameter and the cross-section area of the rotor end ring, respectively, σ_r is the conductivity of the rotor conductive material and l_{ring} is the length of an end-ring segment, given by

$$l_{ring} = \frac{\pi D_{ring}}{Q_r}. \tag{4.9}$$

Secondly, R_{er} and L_{er} are obtained as

$$R_{er} = \frac{R_{ring}}{2\sin^2\left(\frac{\pi p}{Q_r}\right)}, \tag{4.10}$$

$$L_{er} = \frac{L_{ring}}{2\sin^2\left(\frac{\pi p}{Q_r}\right)}. \tag{4.11}$$

Finally, R_{bar} represents the rotor-bar resistance and is calculated as

$$R_{bar} = k_R\frac{l_{bar}}{\sigma_r S_{bar}}, \tag{4.12}$$

where S_{bar} is the cross-section area of the actual rotor bar. Since the rotor skin effect is not accounted for by the MMT and ALT models, a resistance correction factor, k_R, is used. Several methods to calculate k_R are presented in literature [37] and here, a well-known analytical expression is used, given by

$$k_R = \xi\frac{\sinh(2\xi)+\sin(2\xi)}{\cosh(2\xi)-\cos(2\xi)}, \tag{4.13}$$

where

$$\xi = h_{sr}\sqrt{\frac{1}{2}sw_s\mu_0\sigma_r}. \tag{4.14}$$

When all parameters of the circuit in Figure 4.3 are calculated, the rotor-bar current phasor is obtained as

$$\bar{I}_{bar,\nu} = \frac{\bar{E}_{bar,\nu}}{jsw_s\left(L_{bar,\nu}+L_{er}\right)+R_{bar}+R_{er}}. \tag{4.15}$$

4.3.4 Electromagnetic torque and power

From the classical IM equivalent circuit model, it is known [37] that the electromagnetic power, P_{em}, and the electromagnetic torque, T_{em}, of a three-phase IM can be calculated as

$$P_{em} = 3I_r^2 R_r' \frac{1-s}{s}, \tag{4.16}$$

$$T_{em} = \frac{P_{em} p}{(1-s)\, w_s} = \frac{3I_r^2 R_r' p}{s w_s}, \tag{4.17}$$

where I_r and R_r' are the stator referred rotor current and resistance, respectively. Following a similar approach, the contribution of each rotor bar to P_{em} and T_{em} can be calculated using the presented model as

$$P_{em,\nu} = \left(\frac{\hat{I}_{bar,\nu}}{\sqrt{2}}\right)^2 (R_{bar} + R_{er}) \frac{1-s}{s}, \tag{4.18}$$

$$T_{em,\nu} = \frac{\left(\frac{\hat{I}_{bar,\nu}}{\sqrt{2}}\right)^2 (R_{bar} + R_{er})\, p}{s w_s}, \tag{4.19}$$

The total electromagnetic power and torque are then calculated as

$$P_{em} = C_{per} \sum_{\nu=1}^{N_{sr}} P_{em,\nu}, \tag{4.20}$$

$$T_{em} = C_{per} \sum_{\nu=1}^{N_{sr}} T_{em,\nu}, \tag{4.21}$$

where N_{sr} is the number of rotor slots within one periodic section of the motor.

4.4 Direct electric-circuit coupling

The second approach to calculate the induced rotor current is the direct circuit coupling method. The voltage equations of the stator and rotor electric-circuit models are expressed in terms of electric model parameters and magnetic-field coefficients, such that they can be added to the boundary-condition equation matrix given by (2.85). The currents in the stator phases and the rotor end rings are considered as unknowns and added to the matrix **X**, such that they can be calculated during the solving process. Hence, this method is not only suitable for calculation of the induced rotor currents, but can also be applied to perform simulations of a voltage-fed IM.

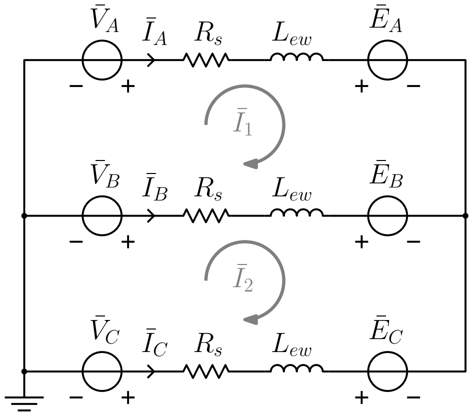

Figure 4.4: Electric circuit of an induction motor stator.

4.4.1 Stator circuit coupling

The stator circuit is represented by the electric-circuit model shown in Figure 4.4. Three voltages phasors, $\bar{V}_A$, $\bar{V}_B$ and $\bar{V}_C$, represent the stator excitation in the frequency domain and are defined as

$$\bar{V}_A = \sqrt{2}V_{ph} \qquad \leftrightarrow \qquad v_A(t) = \mathrm{Re}\left\{\bar{V}_A e^{jw_s t}\right\}, \tag{4.22}$$

$$\bar{V}_B = \sqrt{2}V_{ph} e^{-j\frac{2\pi}{3}} \qquad \leftrightarrow \qquad v_B(t) = \mathrm{Re}\left\{\bar{V}_B e^{jw_s t}\right\}, \tag{4.23}$$

$$\bar{V}_C = \sqrt{2}V_{ph} e^{j\frac{2\pi}{3}} \qquad \leftrightarrow \qquad v_C(t) = \mathrm{Re}\left\{\bar{V}_C e^{jw_s t}\right\}. \tag{4.24}$$

For clarity, the time domain representations of the phase voltages are also given, and represented by $v_A(t)$, $v_B(t)$ and $v_C(t)$. Further, R_s is the stator phase resistance and L_{ew} represents the stator end-winding inductance. Both R_s and L_{ew} are estimated analytically and calculated here using the equations given in [37]. It is assumed that the ac resistance of the stator winding is equal to its dc resistance, since only stranded stator windings for low-power, low-speed IMs are considered in this thesis. Finally, $\bar{E}_A$, $\bar{E}_B$ and $\bar{E}_C$ represent the induced voltage of each stator phase and are calculated as

$$e_A(t) = \mathrm{Re}\left\{\bar{E}_A e^{jw_s t}\right\} = \frac{d\lambda_A(t)}{dt} \leftrightarrow \bar{E}_A = jw_s C_{per} \sum_{\forall \nu \in N_A} c_{dir}^{\nu} \bar{\lambda}_{ss}^{\nu}, \tag{4.25}$$

$$e_B(t) = \mathrm{Re}\left\{\bar{E}_B e^{jw_s t}\right\} = \frac{d\lambda_B(t)}{dt} \leftrightarrow \bar{E}_B = jw_s C_{per} \sum_{\forall \nu \in N_B} c_{dir}^{\nu} \bar{\lambda}_{ss}^{\nu}, \tag{4.26}$$

$$e_C(t) = \mathrm{Re}\left\{\bar{E}_C e^{jw_s t}\right\} = \frac{d\lambda_C(t)}{dt} \leftrightarrow \bar{E}_C = jw_s C_{per} \sum_{\forall \nu \in N_C} c_{dir}^{\nu} \bar{\lambda}_{ss}^{\nu}. \tag{4.27}$$

Using Kirchhoff's voltage law (KVL), the stator voltage-equations are then obtained as

$$\bar{V}_A - \bar{V}_B = \bar{E}_A - \bar{E}_B + (R_s + jw_s L_{ew}) \left(\bar{I}_A - \bar{I}_B\right), \tag{4.28}$$

$$\bar{V}_B - \bar{V}_C = \bar{E}_B - \bar{E}_C + (R_s + jw_s L_{ew}) \left(\bar{I}_B - \bar{I}_C\right). \tag{4.29}$$

Finally, to complete the set of stator equations, the sum of the currents $\bar{I}_A$, $\bar{I}_B$ and $\bar{I}_C$ should be equal to zero, which is expressed as

$$\bar{I}_A + \bar{I}_B + \bar{I}_C = 0. \tag{4.30}$$

To include (4.28) and (4.29) in the system equation matrix, the induced voltages, $\bar{E}_A$, $\bar{E}_B$ and $\bar{E}_C$, should be expressed in terms of magnetic-field coefficients, a_n, b_n, c_n and d_n. These coefficients and their corresponding regions differ for the ALT model and the MMT model. Therefore, the voltage equations obtained for the ALT model and the MMT model are described separately.

Anisotropic Layer model

For the ALT model, the flux linkage phasor per stator slot is given by (3.36). Substituting (3.36) into (4.28) and (4.29), the stator voltage-equations can be rewritten for the ALT model as

$$\begin{aligned}
\bar{V}_A - \bar{V}_B = {} & C_{x,s} \sum_{\forall n} \left[\left(\sum_{\forall \nu \in N_A} \left\{ c^{\nu}_{dir} C^{\nu}_{sn,s} \right\} - \sum_{\forall \nu \in N_B} \left\{ c^{\nu}_{dir} C^{\nu}_{sn,s} \right\} \right) C^{\mathrm{IV}}_{an} a^{\mathrm{IV}}_n \right] \\
& + C_{x,s} \sum_{\forall n} \left[\left(\sum_{\forall \nu \in N_A} \left\{ c^{\nu}_{dir} C^{\nu}_{sn,s} \right\} - \sum_{\forall \nu \in N_B} \left\{ c^{\nu}_{dir} C^{\nu}_{sn,s} \right\} \right) C^{\mathrm{IV}}_{bn} b^{\mathrm{IV}}_n \right] \\
& + C_{x,s} \sum_{\forall n} \left[\left(\sum_{\forall \nu \in N_A} \left\{ c^{\nu}_{dir} C^{\nu}_{cn,s} \right\} - \sum_{\forall \nu \in N_B} \left\{ c^{\nu}_{dir} C^{\nu}_{cn,s} \right\} \right) C^{\mathrm{IV}}_{cn} c^{\mathrm{IV}}_n \right] \\
& + C_{x,s} \sum_{\forall n} \left[\left(\sum_{\forall \nu \in N_A} \left\{ c^{\nu}_{dir} C^{\nu}_{cn,s} \right\} - \sum_{\forall \nu \in N_B} \left\{ c^{\nu}_{dir} C^{\nu}_{cn,s} \right\} \right) C^{\mathrm{IV}}_{dn} d^{\mathrm{IV}}_n \right] \\
& + \left(C_{x,s} \left[\sum_{\forall \nu \in N_A} \left\{ c^{\nu}_{dir} C^{\nu}_{y,A} \right\} - \sum_{\forall \nu \in N_B} \left\{ c^{\nu}_{dir} C^{\nu}_{y,A} \right\} \right] + Z_s \right) \bar{I}_A \\
& + \left(C_{x,s} \left[\sum_{\forall \nu \in N_A} \left\{ c^{\nu}_{dir} C^{\nu}_{y,B} \right\} - \sum_{\forall \nu \in N_B} \left\{ c^{\nu}_{dir} C^{\nu}_{y,B} \right\} \right] - Z_s \right) \bar{I}_B \\
& + C_{x,s} \left[\sum_{\forall \nu \in N_A} \left\{ c^{\nu}_{dir} C^{\nu}_{y,C} \right\} - \sum_{\forall \nu \in N_B} \left\{ c^{\nu}_{dir} C^{\nu}_{y,C} \right\} \right] \bar{I}_C,
\end{aligned} \tag{4.31}$$

$$
\begin{aligned}
\bar{V}_B - \bar{V}_C = {} & C_{x,s} \sum_{\forall n} \left[\left(\sum_{\forall \nu \in N_B} \left\{ c^{\nu}_{dir} C^{\nu}_{sn,s} \right\} - \sum_{\forall \nu \in N_C} \left\{ c^{\nu}_{dir} C^{\nu}_{sn,s} \right\} \right) C^{\mathrm{IV}}_{an} a^{\mathrm{IV}}_n \right] \\
& + C_{x,s} \sum_{\forall n} \left[\left(\sum_{\forall \nu \in N_B} \left\{ c^{\nu}_{dir} C^{\nu}_{sn,s} \right\} - \sum_{\forall \nu \in N_C} \left\{ c^{\nu}_{dir} C^{\nu}_{sn,s} \right\} \right) C^{\mathrm{IV}}_{bn} b^{\mathrm{IV}}_n \right] \\
& + C_{x,s} \sum_{\forall n} \left[\left(\sum_{\forall \nu \in N_B} \left\{ c^{\nu}_{dir} C^{\nu}_{cn,s} \right\} - \sum_{\forall \nu \in N_C} \left\{ c^{\nu}_{dir} C^{\nu}_{cn,s} \right\} \right) C^{\mathrm{IV}}_{cn} c^{\mathrm{IV}}_n \right] \\
& + C_{x,s} \sum_{\forall n} \left[\left(\sum_{\forall \nu \in N_B} \left\{ c^{\nu}_{dir} C^{\nu}_{cn,s} \right\} - \sum_{\forall \nu \in N_C} \left\{ c^{\nu}_{dir} C^{\nu}_{cn,s} \right\} \right) C^{\mathrm{IV}}_{dn} d^{\mathrm{IV}}_n \right] \\
& + C_{x,s} \left[\sum_{\forall \nu \in N_B} \left\{ c^{\nu}_{dir} C^{\nu}_{y,A} \right\} - \sum_{\forall \nu \in N_C} \left\{ c^{\nu}_{dir} C^{\nu}_{y,A} \right\} \right] \bar{I}_A \\
& + \left(C_{x,s} \left[\sum_{\forall \nu \in N_B} \left\{ c^{\nu}_{dir} C^{\nu}_{y,B} \right\} - \sum_{\forall \nu \in N_C} \left\{ c^{\nu}_{dir} C^{\nu}_{y,B} \right\} \right] + Z_s \right) \bar{I}_B \\
& + \left(C_{x,s} \left[\sum_{\forall \nu \in N_B} \left\{ c^{\nu}_{dir} C^{\nu}_{y,C} \right\} - \sum_{\forall \nu \in N_C} \left\{ c^{\nu}_{dir} C^{\nu}_{y,C} \right\} \right] + Z_s \right) \bar{I}_C,
\end{aligned}
\tag{4.32}
$$

where $Z_s = R_s + jw_s L_{ew}$, $C_{x,s} = jw_s C_{per}$ and $C^{\nu}_{y,A}$, $C^{\nu}_{y,B}$ and $C^{\nu}_{y,C}$ are given by

$$
C^{\nu}_{y,A} = \sum_{\forall n} \left[C^{\nu}_{sn,s} \sum_{\forall \nu_s \in N_A} C^{\mathrm{IV},\nu_s}_{gcn} + C^{\nu}_{cn,s} \sum_{\forall \nu_s \in N_A} C^{\mathrm{IV},\nu_s}_{gsn} \right], \tag{4.33}
$$

$$
C^{\nu}_{y,B} = \sum_{\forall n} \left[C^{\nu}_{sn,s} \sum_{\forall \nu_s \in N_B} C^{\mathrm{IV},\nu_s}_{gcn} + C^{\nu}_{cn,s} \sum_{\forall \nu_s \in N_B} C^{\mathrm{IV},\nu_s}_{gsn} \right], \tag{4.34}
$$

$$
C^{\nu}_{y,C} = \sum_{\forall n} \left[C^{\nu}_{sn,s} \sum_{\forall \nu_s \in N_C} C^{\mathrm{IV},\nu_s}_{gcn} + C^{\nu}_{cn,s} \sum_{\forall \nu_s \in N_C} C^{\mathrm{IV},\nu_s}_{gsn} \right]. \tag{4.35}
$$

Mode-Matching model

For the MMT model, the flux linkage phasor per stator slot is given by (3.81). Substituting (3.81) into (4.28) and (4.29), the stator voltage-equations can be rewritten as

$$\begin{aligned}
\bar{V}_A - \bar{V}_B = {} & C_{x,s} \sum_{\forall \nu \in N_A} \left[C_{\lambda,s}^{\nu} \left(C_{B,s}^{\mathrm{V}_\nu} \bar{B}_0^{\mathrm{V}_\nu} + C_{A,s}^{\mathrm{V}_\nu} \bar{A}_0^{\mathrm{V}_\nu} \right) \right] \\
& - C_{x,s} \sum_{\forall \nu \in N_B} \left[C_{\lambda,s}^{\nu} \left(C_{B,s}^{\mathrm{V}_\nu} \bar{B}_0^{\mathrm{V}_\nu} + C_{A,s}^{\mathrm{V}_\nu} \bar{A}_0^{\mathrm{V}_\nu} \right) \right] \\
& + \left(C_{x,s} \sum_{\forall \nu \in N_A} \left[C_{\lambda,s}^{\nu} C_{I,s}^{\mathrm{V}_\nu} \right] + Z_s \right) \bar{I}_A \\
& - \left(C_{x,s} \sum_{\forall \nu \in N_B} \left[C_{\lambda,s}^{\nu} C_{I,s}^{\mathrm{V}_\nu} \right] + Z_s \right) \bar{I}_B,
\end{aligned} \tag{4.36}$$

$$\begin{aligned}
\bar{V}_B - \bar{V}_C = {} & C_{x,s} \sum_{\forall \nu \in N_B} \left[C_{\lambda,s}^{\nu} \left(C_{B,s}^{\mathrm{V}_\nu} \bar{B}_0^{\mathrm{V}_\nu} + C_{A,s}^{\mathrm{V}_\nu} \bar{A}_0^{\mathrm{V}_\nu} \right) \right] \\
& - C_{x,s} \sum_{\forall \nu \in N_C} \left[C_{\lambda,s}^{\nu} \left(C_{B,s}^{\mathrm{V}_\nu} \bar{B}_0^{\mathrm{V}_\nu} + C_{A,s}^{\mathrm{V}_\nu} \bar{A}_0^{\mathrm{V}_\nu} \right) \right] \\
& + \left(C_{x,s} \sum_{\forall \nu \in N_B} \left[C_{\lambda,s}^{\nu} C_{I,s}^{\mathrm{V}_\nu} \right] + Z_s \right) \bar{I}_B \\
& - \left(C_{x,s} \sum_{\forall \nu \in N_C} \left[C_{\lambda,s}^{\nu} C_{I,s}^{\mathrm{V}_\nu} \right] + Z_s \right) \bar{I}_C,
\end{aligned} \tag{4.37}$$

$$\tag{4.38}$$

where

$$C_{\lambda,s}^{\nu} = \frac{c_{dir}^{\nu} z_{Q,s} l_{sl} \theta_{ss}}{2 S_{ss}}. \tag{4.39}$$

4.4.2 Rotor circuit coupling

A segment of the electric circuit representing the rotor squirrel cage is shown in Figure 4.5. Each rotor bar is represented by the bar resistance, R_{bar}, and the induced rotor-bar voltage, $\bar{E}_{bar,\nu}$. The bars are connected by the end rings of the squirrel cage, which are modeled by the end-ring-segment resistance, R_{ring}, and inductance, L_{ring}. Values for E_{bar}, R_{bar}, R_{ring} and L_{ring} are calculated from (4.6), (4.7), (4.8) and (4.12), respectively.

Between each rotor bar, ν, and its adjacent rotor bar, $\nu + 1$, a loop current can be identified that is equal to the end-ring-segment current, $\bar{I}_{ring,\nu}$. The currents in the rotor bars, $\bar{I}_{bar,\nu}$, can be expressed in terms of $\bar{I}_{ring,\nu}$ as

$$\bar{I}_{bar,\nu} = \bar{I}_{ring,\nu} - \bar{I}_{ring,\nu-1}. \tag{4.40}$$

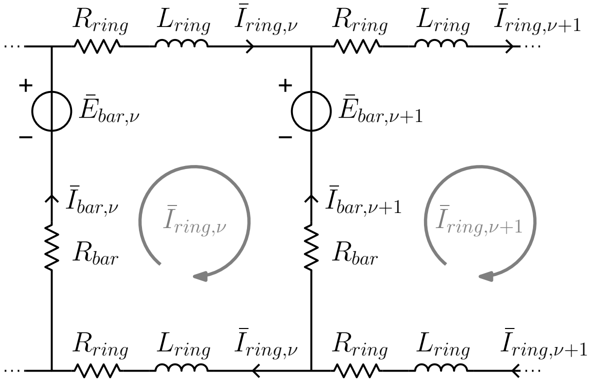

Figure 4.5: Electric circuit of an induction motor rotor.

Using the KVL along the loop as indicated in Figure 4.5, the circuit voltage-equation is then obtained as

$$\begin{aligned}&\bar{E}_{bar,\nu+1} - \bar{E}_{bar,\nu} + 2\left(R_{bar} + Z_{ring}\right)\bar{I}_{ring,\nu} - R_{bar}\bar{I}_{ring,\nu-1} \\ &\qquad - R_{bar}\bar{I}_{ring,\nu+1} = 0, \end{aligned} \tag{4.41}$$

where $Z_{ring} = R_{ring} + jsw_sL_{ring}$. Equation (4.41) can be used for all but one rotor current loop. Therefore, the resulting system of equations is under-determined, and one additional equation is required to solve the rotor current. This equation is obtained by applying the KVL to the end-ring loop. Since the impedance of each end-ring segment is assumed to be equal, the resulting equation can be written as

$$\sum_{\nu=1}^{N_{sr}} \bar{I}_{ring,\nu} = 0, \tag{4.42}$$

The equations given by (4.41) and (4.42) are expressed in terms of the magnetic-field coefficients and rotor-end-ring current. The resulting expressions of the rotor voltage-equation are obtained for the ALT model and the MMT model separately.

Anisotropic Layer model

For the ALT model, the rotor-bar flux linkage phasor is given by (3.37) and is used to obtain the induced rotor-bar voltage using (4.6). Substituting (3.37) and (4.6) into (4.41), the rotor voltage-equation can be rewritten for each current loop as

$$\begin{aligned}&C_{x,r}\sum_{\forall n}\left[\left(C^{\nu+1}_{sn,r} - C^{\nu}_{sn,r}\right)\left(C^{\mathrm{II}}_{an}a^{\mathrm{II}}_n + C^{\mathrm{II}}_{bn}b^{\mathrm{II}}_n\right)\right] + \\ &C_{x,r}\sum_{\forall n}\left[\left(C^{\nu+1}_{cn,r} - C^{\nu}_{cn,r}\right)\left(C^{\mathrm{II}}_{cn}c^{\mathrm{II}}_n + C^{\mathrm{II}}_{dn}d^{\mathrm{II}}_n\right)\right] + \end{aligned}$$

$$
\begin{aligned}
&C_{x,r}\sum_{\forall n}\left[\left(C_{sn,r}^{\nu+1}-C_{sn,r}^{\nu}\right)\sum_{\nu_r=1}^{N_{sr}}\left\{C_{gcn}^{\mathrm{II},\nu_r}\left(\bar{I}_{ring,\nu_r}-\bar{I}_{ring,\nu_r-1}\right)\right\}\right]+\\
&C_{x,r}\sum_{\forall n}\left[\left(C_{cn,r}^{\nu+1}-C_{cn,r}^{\nu}\right)\sum_{\nu_r=1}^{N_{sr}}\left\{C_{gsn}^{\mathrm{II},\nu_r}\left(\bar{I}_{ring,\nu_r}-\bar{I}_{ring,\nu_r-1}\right)\right\}\right]+\\
&2\left(R_{bar}+Z_{ring}\right)\bar{I}_{ring,\nu}-R_{bar}\bar{I}_{ring,\nu-1}-R_{bar}\bar{I}_{ring,\nu+1}=0, \qquad (4.43)
\end{aligned}
$$

where $C_{x,r} = jsw_s$. It should be noted here that for $\nu = 1$ it holds that $\nu - 1 = N_{sr}$, and for $\nu = N_{sr}$ it holds that $\nu+1 = 1$, to account for the physical connection and periodicity of the rotor cage. Similarly, this also holds for ν_r.

Mode-Matching model

For the MMT model, the rotor-bar flux linkage phasor is given by (3.82). Substituting (3.82) and (4.6) into (4.41), the rotor voltage-equation can be rewritten for each current loop as

$$
\begin{aligned}
&C_{x,r}C_{\lambda,r}\left(C_{B,r}^{\nu+1}B_0^{\mathrm{I}_{\nu+1}}+C_{A,r}^{\nu+1}A_0^{\mathrm{I}_{\nu+1}}\right)-C_{x,r}C_{\lambda,r}\left(C_{B,r}^{\nu}B_0^{\mathrm{I}_{\nu}}+C_{A,r}^{\nu}A_0^{\mathrm{I}_{\nu}}\right)+\\
&\left[C_{x,r}C_{\lambda,r}\frac{C_{I,r}^{\nu}}{S_{sr}}-R_{bar}\right]\bar{I}_{ring,\nu-1}+\left[C_{x,r}C_{\lambda,r}\frac{C_{I,r}^{\nu+1}}{S_{sr}}-R_{bar}\right]\bar{I}_{ring,\nu+1}-\\
&\left[C_{x,r}\left(\frac{C_{\lambda,r}C_{I,r}^{\nu+1}}{S_{sr}}+\frac{C_{\lambda,r}C_{I,r}^{\nu}}{S_{sr}}\right)-2\left(R_{bar}+Z_{ring}\right)\right]\bar{I}_{ring,\nu}=0, \qquad (4.44)
\end{aligned}
$$

where

$$
C_{\lambda,r}=\frac{l_{sl}\theta_{sr}}{2S_{sr}}. \qquad (4.45)
$$

Again, it should be noted here that for $\nu = 1$ it holds that $\nu - 1 = N_{sr}$, and for $\nu = N_{sr}$ it holds that $\nu + 1 = 1$.

4.4.3 Electromagnetic torque

Two methods are considered to calculate the electromagnetic torque, T_{em}, from the results of the direct circuit coupling model. Firstly, since both the stator and the rotor currents are considered in the magnetic-field solution, T_{em} can be obtained from Maxwell's Stress Tensor. For the ALT model and the MMT model, (3.54) and (3.103) are used, respectively. Secondly, T_{em} is obtained in a similar manner as described in Section 4.3.4, namely using (4.18) to (4.21). This method is referred to as the circuit method.

Table 4.1: Parameters and simulation settings used for the ALT calculations.

Symbol	Value				Unit	Description
-	1	2	3	4	-	Benchmark motor
C_{it}	0.3	0.3	0.3	0.3	-	Relaxation constant
ε_{des}	1e-3	1e-3	1e-3	1e-3	-	Maximum convergence error
L_{ring}	1.9	0.83	2.1	0.49	nH	Rotor end-ring inductance
R_{ring}	3.8	2.1	6.6	3.5	$\mu\Omega$	Rotor end-ring resistance
L_{ew}	38	4.2	25	4.5	mH	Stator end-winding inductance
R_s	47	9.3	21	4.0	Ω	Stator winding resistance

Table 4.2: Parameters and simulation settings used for the MMT calculation.

Symbol	Value				Unit	Description
-	1	2	3	4	-	Benchmark motor
N_{sh}^{III}	150	150	120	100	-	Air-gap spatial harmonics
N_{sh}^{ss}	5	5	5	4	-	Stator slot spatial harmonics
N_{sh}^{sr}	3	3	3	2	-	Rotor slot spatial harmonics
L_{ring}	1.9	0.83	2.1	0.49	nH	Rotor end-ring inductance
R_{ring}	3.8	2.1	6.6	3.5	$\mu\Omega$	Rotor end-ring resistance
L_{ew}	38	4.2	25	4.5	mH	Stator end-winding inductance
R_s	47	9.3	21	4.0	Ω	Stator winding resistance

4.5 Validation of the calculation methods

To validate the induced-current calculation methods, simulations are performed for the benchmark motors and compared to 2D FEA predictions. During these simulations, the stator current is increased from 10% to 150% of its nominal value and applied to the benchmark motors for operating slips of $s = s_N/2$, $s = s_N$ and $s = 2s_N$. The results are validated in terms of the rms rotor-bar current, I_{bar}, rotor-bar current angle, ϕ_{bar}, and electromagnetic torque, T_{em}. An overview of important parameters and simulation settings for the ALT and MMT models is provided in Tables 4.1 and 4.2, respectively.

4.5.1 Indirect method

To obtain the results of the indirect method, both the rotor-bar flux linkage due to stator excitation and the rotor-bar synchronous inductance are calculated for $\Delta_\theta = 0$. The same rotor position is also used to perform linear FEA simulations. A comparison of the rotor-bar current, $\bar{I}_{bar}$, obtained from the MMT and linear FEA models, is shown in Figures 4.6 and 4.7. It can be seen that both the rms value and the phase angle of $\bar{I}_{bar}$ are in good agreement for all benchmark motors. Some small discrepancies are observed, but the maximum error is approximately 5%, which is acceptable. Further, Figure 4.8 shows that a good agreement is also obtained in terms of T_{em}.

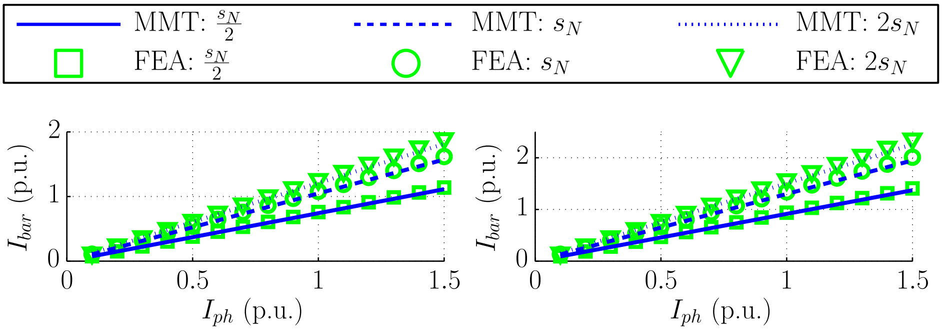

(a) Benchmark motor ”one” (b) Benchmark motor ”two”

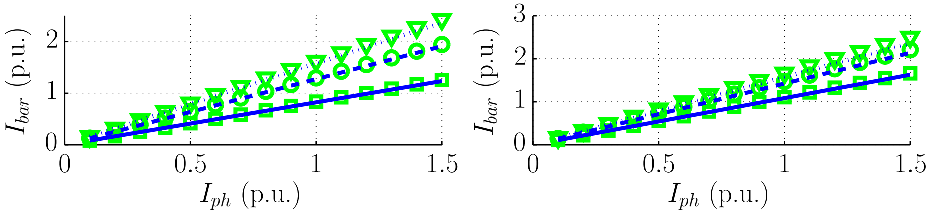

(c) Benchmark motor ”three” (d) Benchmark motor ”four”

Figure 4.6: Comparison of the rms rotor-bar current, I_{bar}, calculated by MMT and linear 2D FEA, using the indirect method.

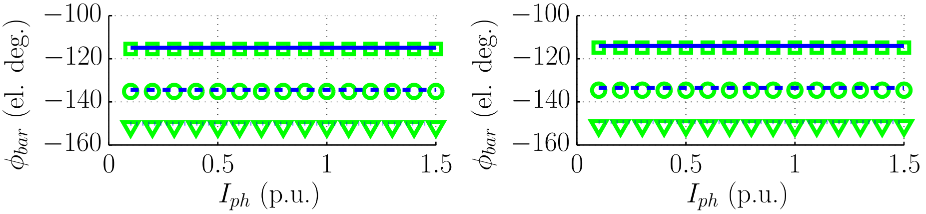

(a) Benchmark motor ”one” (b) Benchmark motor ”two”

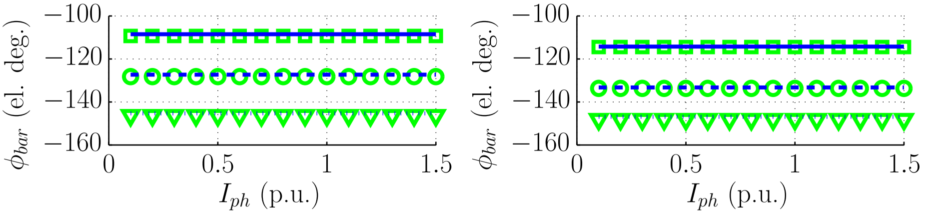

(c) Benchmark motor ”three” (d) Benchmark motor ”four”

Figure 4.7: Comparison of the rotor-bar current angle, ϕ_{bar}, calculated by MMT and linear 2D FEA, using the indirect method.

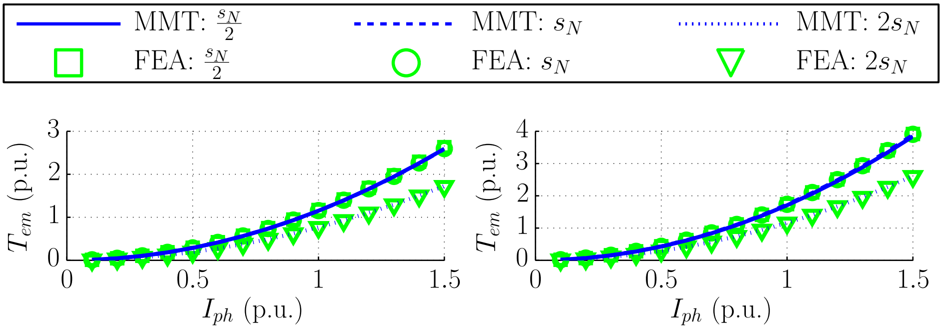

(a) Benchmark motor "one" (b) Benchmark motor "two"

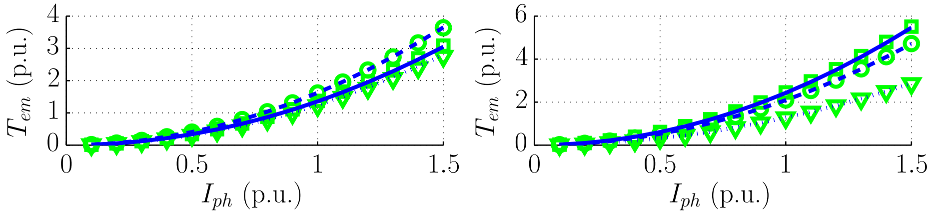

(c) Benchmark motor "three" (d) Benchmark motor "four"

Figure 4.8: Comparison of the electromagnetic torque, T_{em}, calculated by MMT and linear 2D FEA, using the indirect method.

4.5.2 Direct method: current-fed simulations

For the current-fed simulations, the same operating conditions are used as those of the indirect method validation. The validation results of the ALT and MMT models are discussed separately.

Anisotropic Layer model

Since the ALT model includes the global effect of the nonlinear behavior of the motor, its calculation results are compared to nonlinear FEA predictions. It can be seen from Figure 4.9 and Figure 4.10 that the obtained rms values and phase angles of $\bar{I}_{bar}$ are in good agreement for all benchmark motors. Further, a comparison of T_{em}, obtained from FEA and the ALT model using MST, is shown in Figure 4.11. It can be seen that a relatively good agreement is obtained, although small discrepancies can be observed. These discrepancies are attributed to the fact that the FEA model calculates T_{em} based on a more accurate representation of the magnetic-flux-density distribution, including not only the fundamental, but also higher spatial harmonics. Finally, it should be noted that T_{em} calculated by the circuit method is identical to T_{em} calculated by the MST in this case, and therefore only the results obtained from MST are shown here.

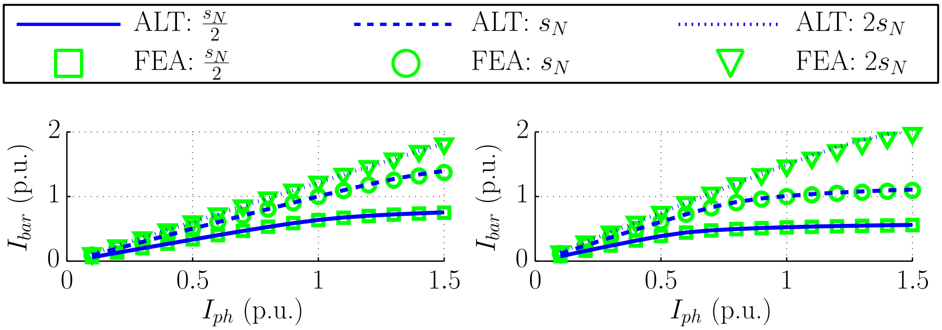

(a) Benchmark motor "one" (b) Benchmark motor "two"

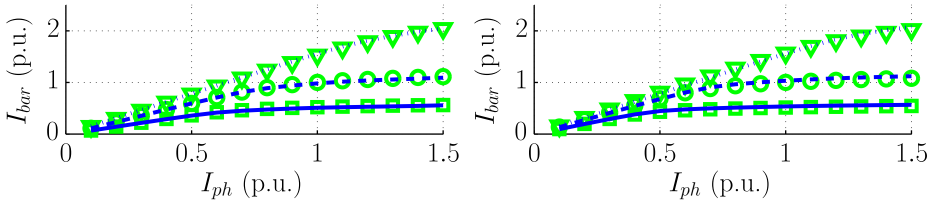

(c) Benchmark motor "three" (d) Benchmark motor "four"

Figure 4.9: Comparison of the rms rotor-bar current, I_{bar}, calculated by ALT and nonlinear 2D FEA, using the direct method (current-fed).

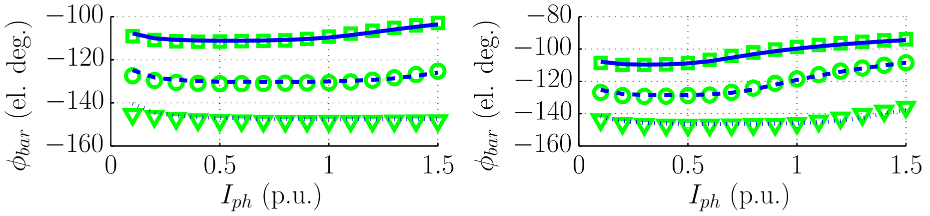

(a) Benchmark motor "one" (b) Benchmark motor "two"

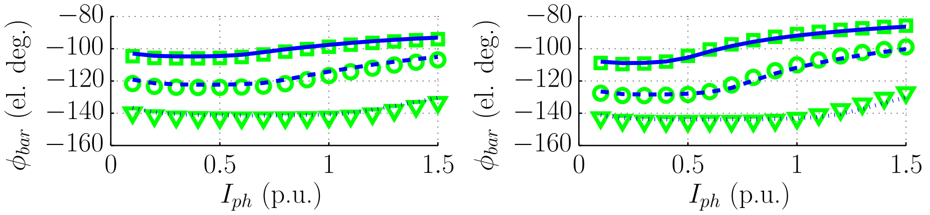

(c) Benchmark motor "three" (d) Benchmark motor "four"

Figure 4.10: Comparison of the rotor-bar current angle, ϕ_{bar}, calculated by ALT and nonlinear 2D FEA, using the direct method (current-fed).

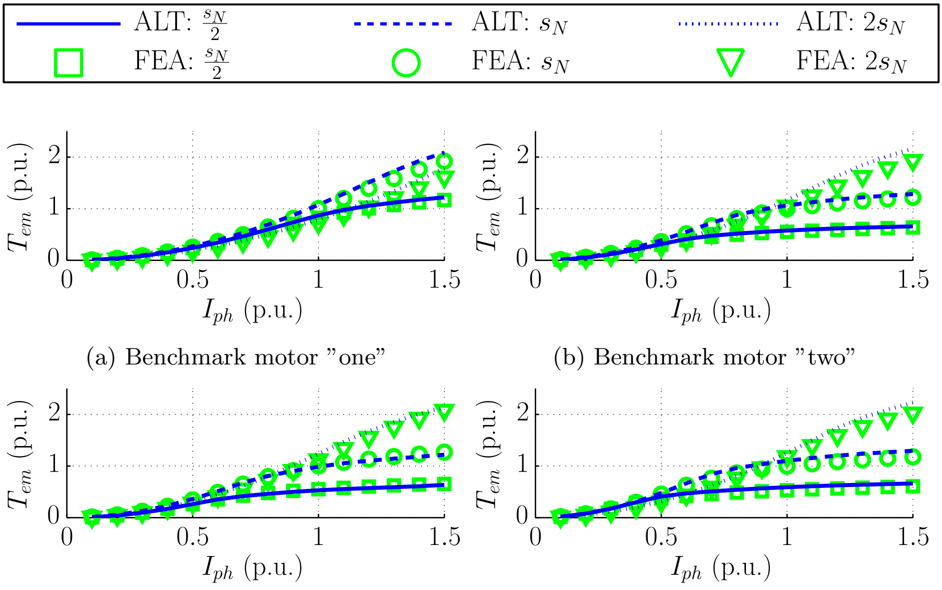

(a) Benchmark motor ”one”

(b) Benchmark motor ”two”

(c) Benchmark motor ”three”

(d) Benchmark motor ”four”

Figure 4.11: Comparison of the torque calculated by ALT and nonlinear 2D FEA, using the direct method (current-fed).

Mode-matching model

For the MMT model, the results of the direct method are validated against linear FEA predictions. A comparison of the results in terms of the rms value and current angle of $\bar{I}_{bar}$ is shown in Figure 4.12 and Figure 4.13, respectively. It can be seen that a very good agreement is obtained. Further, a comparison of the results in terms of T_{em} is shown in Figure 4.14 and Figure 4.15, calculated using Maxwell's Stress Tensor and the circuit method, respectively. It can be seen that a very good agreement is obtained using the circuit method for torque calculation, whereas the results obtained from Maxwell's Stress Tensor show significant discrepancies for benchmark motors ”one” and ”two”. These discrepancies are discussed in more detail in Section 4.6.

4.5.3 Direct method: voltage-fed simulations

For the voltage-fed simulations, the voltage applied to the stator phase windings is fixed to its nominal value, whereas the rotor slip is increased from $s = 0.01$ to $s = 1$ in 30 steps. Further, the position of the rotor is set to $\Delta_\theta = 0$ and similar calculations are performed using FEA. The results of the ALT model and the MMT model are again discussed separately.

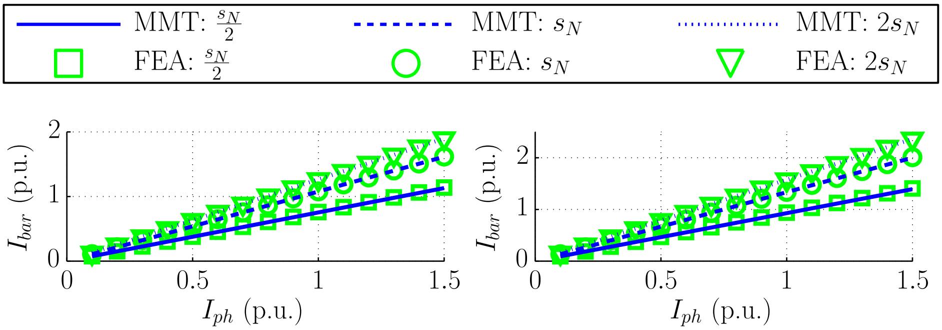

(a) Benchmark motor "one" (b) Benchmark motor "two"

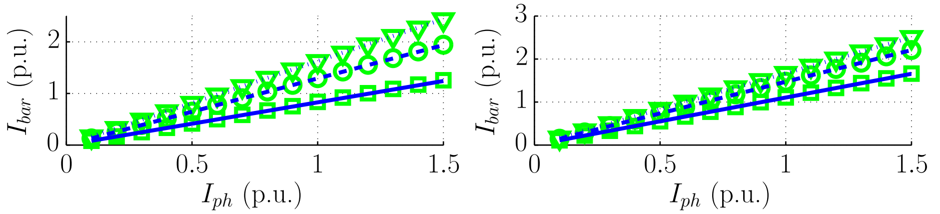

(c) Benchmark motor "three" (d) Benchmark motor "four"

Figure 4.12: Comparison of the rms rotor-bar current, I_{bar}, calculated by MMT and linear 2D FEA, using the direct method (current-fed).

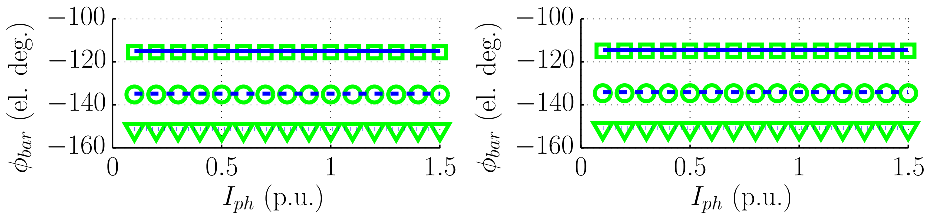

(a) Benchmark motor "one" (b) Benchmark motor "two"

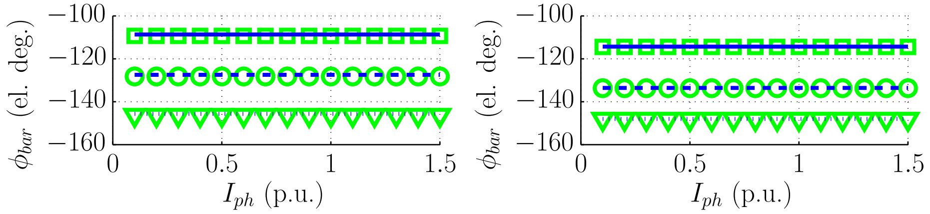

(c) Benchmark motor "three" (d) Benchmark motor "four"

Figure 4.13: Comparison of the rotor-bar current angle, ϕ_{bar}, calculated by MMT and linear 2D FEA, using the direct method (current-fed).

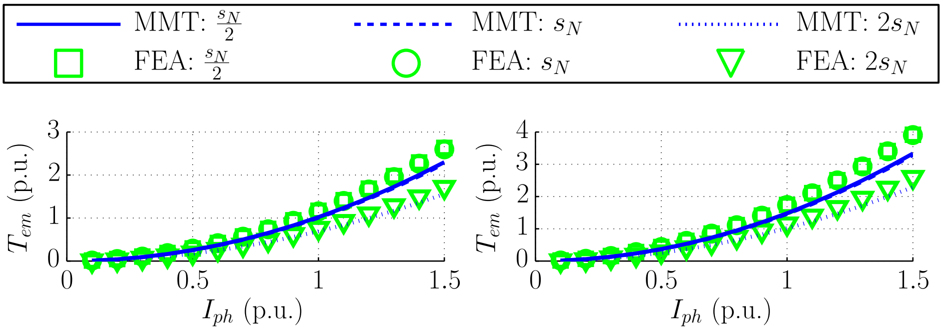

(a) Benchmark motor ”one” (b) Benchmark motor ”two”

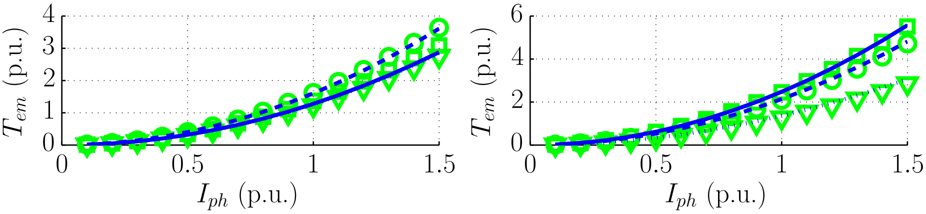

(c) Benchmark motor ”three” (d) Benchmark motor ”four”

Figure 4.14: Comparison of the electromagnetic torque, T_{em}, calculated by MMT (using the MST method) and linear 2D FEA, using the direct method (current-fed).

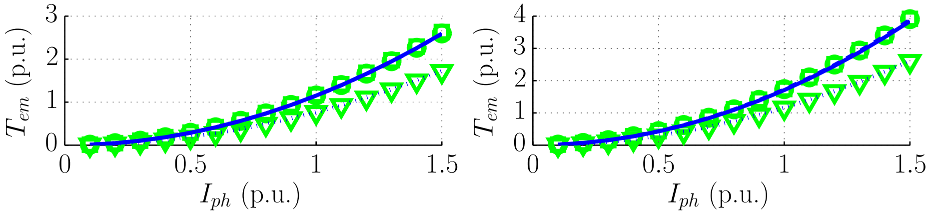

(a) Benchmark motor ”one” (b) Benchmark motor ”two”

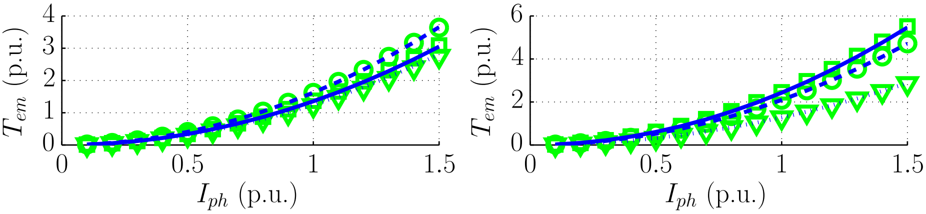

(c) Benchmark motor ”three” (d) Benchmark motor ”four”

Figure 4.15: Comparison of the electromagnetic torque, T_{em}, calculated by MMT (using the circuit method) and linear 2D FEA, using the direct method (current-fed).

Anisotropic layer model

A comparison between voltage-fed results obtained from the ALT model and nonlinear FEA predictions is shown in Figure 4.16 and Figure 4.17 in terms of rms stator phase current and electromagnetic torque. From Figure 4.16, it can be seen that a good agreement is obtained for benchmark motors "one", "two" and "four" up to approximately $s = 0.3$. For this operating region, the magnetizing inductance is relatively dominant with respect to the phase impedance, such that any error in the predicted rotor leakage inductance does not influence the stator current significantly. For larger slip values, the contribution of the rotor leakage inductance to the total phase impedance becomes more significant. The discrepancy in I_{ph} for large slip values is therefore attributed to an inaccurate estimation of the rotor leakage inductance. Furthermore, benchmark motor "three" shows a significant discrepancy in terms of stator current for low slip values. It was found that this error is caused by deep saturation of the rotor teeth. Apparently, the ALT model overestimates the influence of the soft-magnetic iron on the fundamental flux density for this case, which leads to an increased stator current. Finally, it can be seen from Figure 4.17 that T_{em}, obtained using MST, is predicted accurately up to approximately $s = 0.15$. For larger slip values, errors in the leakage flux predictions lead to incorrect results.

Mode-matching model

The results of the voltage-fed simulations performed using the MMT model are compared to the results obtained from both linear and nonlinear FEA predictions in Figure 4.18 and Figure 4.19. From Figure 4.18, it can be seen that a good agreement is obtained between the linear FEA model and the MMT model in terms of stator phase current. However, as expected, the nonlinear FEA model does not match well with the linear calculation results. For small slip values, near the no-load operating region, this is caused by global saturation in the main flux path, whereas for large slip values, this is caused by saturation in the leakage flux paths. In between these two extremes, the soft-magnetic material is not heavily saturated and therefore, a relatively good agreement is obtained for this operating region. Further, a comparison in terms of T_{em} is shown in Figure 4.19, where T_{em} was obtained for the MMT model using the circuit method. It can be seen that there is a good agreement between the linear FEA model and the MMT model up to $s = 0.3$ for benchmark motors "one", "three" and "four", and up to $s = 0.2$ for benchmark motor "two". For larger slip values, the error increases due to a difference in the predicted leakage flux. This difference is most likely caused by the simplifications applied to the MMT model geometry. However, the resulting error in T_{em} remains within acceptable limits, i.e. within 6% in the linear operating region and within 20% for $s = 1$.

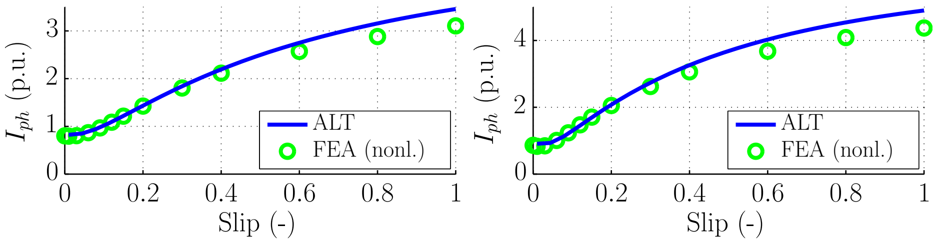

(a) Benchmark motor "one" (b) Benchmark motor "two"

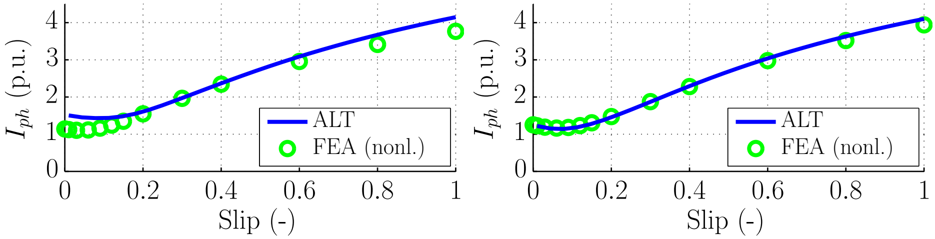

(c) Benchmark motor "three" (d) Benchmark motor "four"

Figure 4.16: Comparison of the rms stator phase current, I_{ph}, calculated by ALT and nonlinear 2D FEA, using the direct method (voltage-fed).

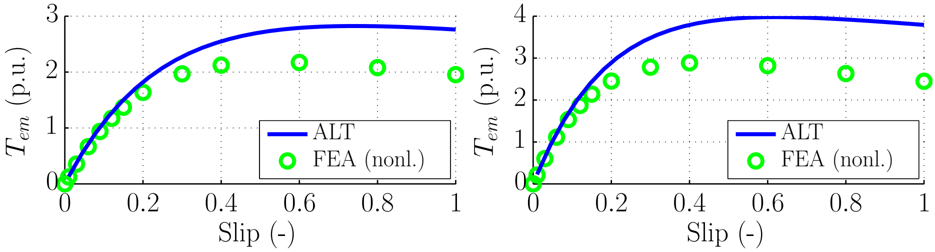

(a) Benchmark motor "one" (b) Benchmark motor "two"

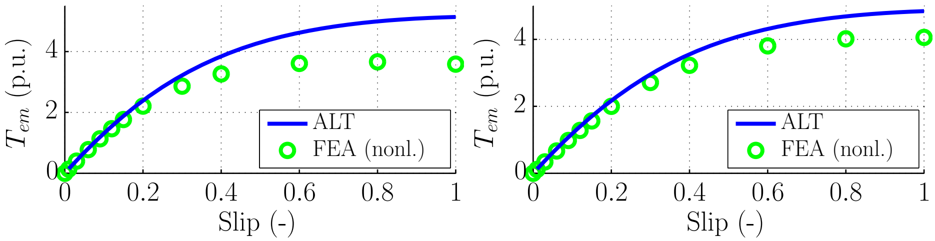

(c) Benchmark motor "three" (d) Benchmark motor "four"

Figure 4.17: Comparison of the electromagnetic torque, T_{em}, calculated by the ALT and nonlinear 2D FEA, using the direct method (voltage-fed).

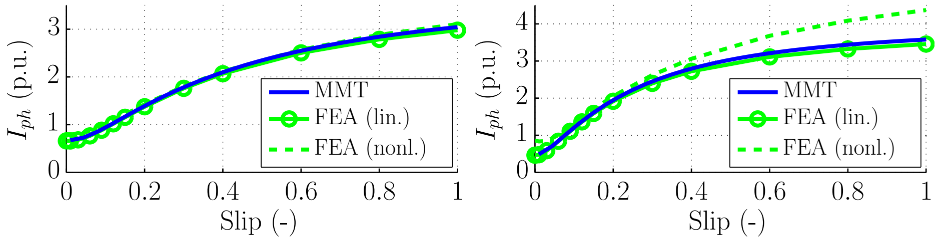

(a) Benchmark motor "one" (b) Benchmark motor "two"

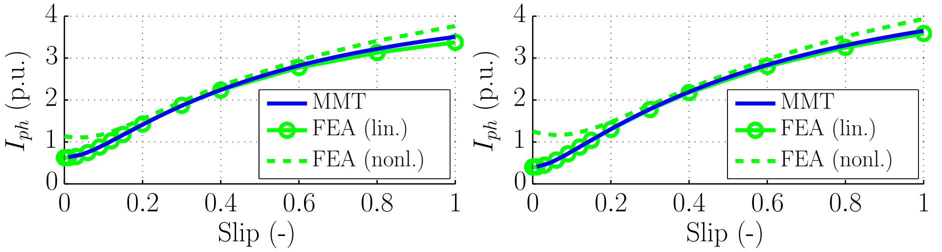

(c) Benchmark motor "three" (d) Benchmark motor "four"

Figure 4.18: Comparison of the rms stator phase current, I_{ph}, calculated by MMT and linear 2D FEA, using the direct method (voltage-fed).

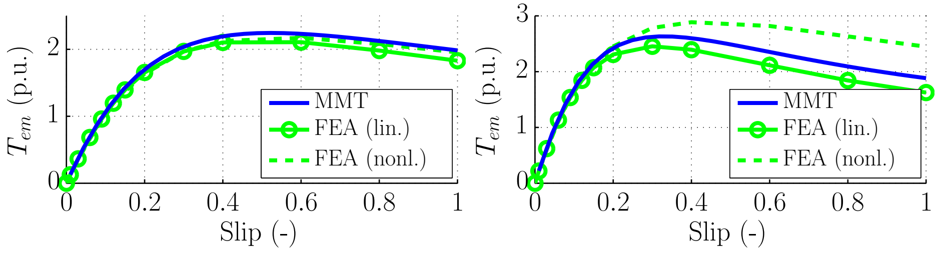

(a) Benchmark motor "one" (b) Benchmark motor "two"

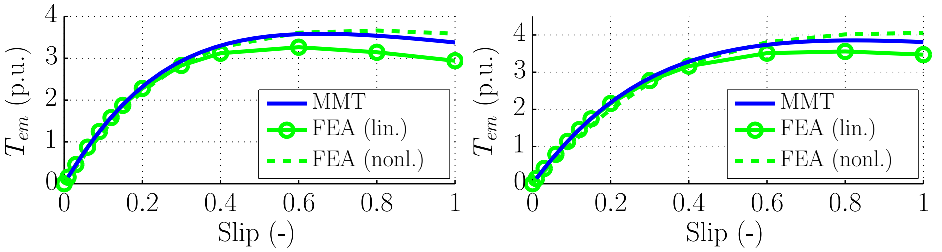

(c) Benchmark motor "three" (d) Benchmark motor "four"

Figure 4.19: Comparison of the electromagnetic torque, T_{em}, calculated by MMT (using MST) and linear 2D FEA, using the direct method (voltage-fed).

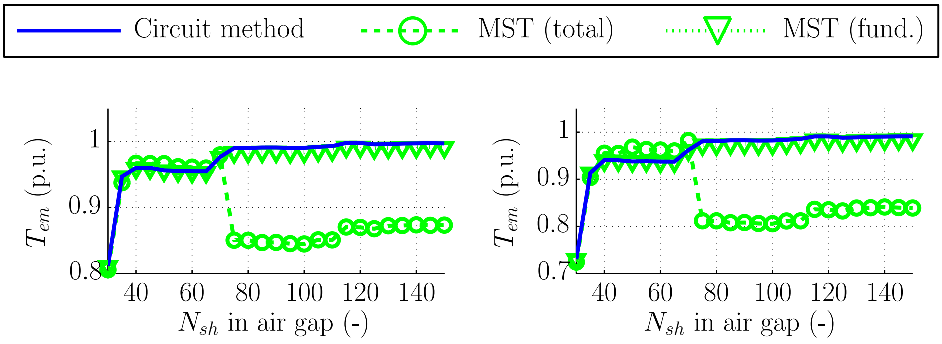

(a) Benchmark motor ”one”

(b) Benchmark motor ”two”

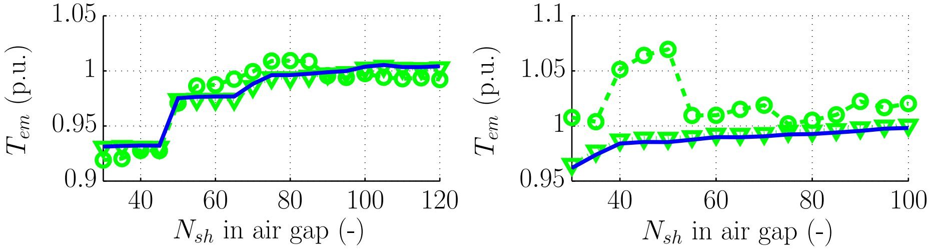

(c) Benchmark motor ”three”

(d) Benchmark motor ”four”

Figure 4.20: Number of spatial harmonics, N_{sh}, in the air gap versus electromagnetic torque, T_{em}, computed by MST and the circuit method, normalized against the nominal value of T_{em} obtained from FEA.

4.6 Convergence of MST calculations

In the previous section, it was shown that Maxwell's Stress Tensor does not always predict the correct torque value for the MMT model, whereas it does calculate the correct value for the ALT model. To further investigate this problem, additional calculations are performed using the MMT model for each benchmark motor. The stator phase current and the rotor slip are fixed to the nominal value of each benchmark motor, whereas N_{sh}^{III} is increased from 30 up to the maximum number of harmonics given in Table 4.2. For each simulation, T_{em} is computed using both the MST and the circuit method. Moreover, two cases of the MST calculation are considered. The first case (total) includes all spatial harmonics in the calculation, whereas the second case (fund.) includes only the fundamental spatial harmonic. A comparison of the results is shown in Figure 4.20, where all obtained values of T_{em} are normalized to the value obtained by the linear FEA models for equal operating conditions. It can be seen that for each benchmark motor, the results calculated by the circuit method and the fundamental MST calculation converge approximately to the linear FEA predictions. For the results obtained from the total MST calculation, however, it can be seen that T_{em} does not converge to the correct value. Especially for benchmark motors "one" and "two", large discrepancies become apparent after N_{sh} passes a certain point. Further, since the effect is not observed for the fundamental MST calculations, it is expected that the problem is caused by the contribution of higher spatial harmonics in the total MST calculation. The exact origin of the observed discrepancies should be investigated in more detail. However, this is beyond the scope of this thesis.

Chapter 5

Framework for Induction-Motor analysis

5.1 Introduction

In Chapter 3, the advantages and disadvantages of the ALT and MMT models for the analysis of the magnetic field in an IM were investigated. In this chapter, a combination of these models is described to form a framework for induction-motor analysis. This framework aims to combine the advantages of both modeling approaches. Moreover, it uses the direct circuit coupling presented in Chapter 4 to connect the magnetic and electric domains. An extension of this coupling to account for multiple slices of the ALT model is also presented, such that a skewed rotor structure can be approximated. The results of the models are then used to calculate performance characteristics, which are thoroughly validated against 2D FEA calculations, skewed FEA calculations and measurements. First, however, an overview of several challenges in induction-motor analysis and a description of the framework implementation is discussed.

5.2 Challenges in induction-motor analysis

Accurate performance prediction is a challenging task for IMs, especially due to the large number of physical phenomena that influence their performance. These phenomena are generally influencing each other as well, which leads to a complex interaction between the desired motor behavior and parasitic effects. Additionally, one of the biggest uncertainties in electric-motor modeling are the properties of the soft-magnetic material, especially in terms of magnetization and losses. These properties may vary throughout a lamination due to processing, for example after cutting the lamination or after shrink-fitting a housing onto the stator.

Several challenges encountered during IM analysis are addressed in this chapter. An overview of the considered phenomena and the extend of their implementation in the developed models are presented below:

Leakage and fringing flux: In an ideal IM, the distribution of the magnetic-flux density in the air gap is purely sinusoidal and all magnetic flux links both the stator winding and the rotor squirrel cage. In practice, however, the distributed nature of the conductors and the disruption of the soft-magnetic material due to stator and rotor slotting significantly distorts the flux distribution. Consequently, a part of the magnetic flux does not contribute to useful torque production and is therefore considered leakage flux. Furthermore, the presence of slot openings in the magnetic structure causes the magnetic flux to fringe when crossing the air gap, thereby increasing the effective air-gap length. As a result, the magnetizing inductance decreases and the required magnetizing current increases.

Global saturation: Due to the physical properties of soft-magnetic materials, the ability to magnetize them generally reduces as the magnetizing field strength increases. At some point, which varies for different types of materials, the increase in magnetization drops rapidly and the material is said to be saturated. The global saturation effect reflects the average saturation level of the teeth and yokes and is primarily important for the calculation of the IM magnetization behaviour and its associated magnetizing current. The influence of local saturation is currently neglected.

Skin effect: For low-power IMs, skin effect generally takes place in the rotor conductors only. If the frequency of the induced rotor-bar current is sufficiently high (and thus the slip is sufficiently low), the currents induced by rotor slot-leakage flux tend to push the total current towards the top of the conductor (air-gap side). Consequently, the effective surface area of the conductor decreases and the effective resistance increases. For small slip values, for example near nominal slip, the influence of skin effect is often small in low-power IMs. However, for high slip values, the influence of skin effect can be considerable, especially for deep-bar and double-cage motors. Therefore, an analytical approximation of the influence of skin effects on the effective resistance of the rotor bars is included in the model.

End windings and rings: The end windings and rings of the stator and rotor contribute to the total resistance and inductance of the stator and rotor, respectively. The magnetic field produced by the stator end winding and rotor end rings is considered as an additional leakage component, as it does not contribute to useful torque production. However, since the end windings and rings are only partially surrounded by soft-magnetic material and their geometry is relatively complex, the distribution of the end-winding magnetic flux and the associated inductance are difficult to predict. Therefore, empirical estimations of their values are usually employed and a similar approach is used here. Furthermore, the resistance of the end windings and rings add to the Ohmic losses and are calculated based on an approximation of their geometry. Any skin effect occurring in the rotor end rings is neglected.

Skewing: To reduce parasitic torques during motor start-up and to decrease the torque ripple amplitude, the rotor of low-power IMs is often skewed. However, skewing also reduces the mutual flux linkage between the stator and rotor and, consequently, torque production decreases. Further, since the rotor conductors are spatially shifted in the axial direction, the global saturation level will also vary in the axial direction. These effects can be taken into account by using multiple slices of a 2D model, each with a slightly displaced rotor position. Other undesired effects, such as parasitic currents between the rotor bars (inter-bar current) and axial magnetic flux may also become apparent due to skewing. However, such effects are not considered in this thesis.

Soft-magnetic material characteristics: The properties of the soft-magnetic materials are often measured on an Epstein frame or using ring samples of the magnetic material. The results are expressed in terms of the BH-characteristics and iron-loss characteristics. These are then used in simulations to predict the magnetization behaviour and iron losses of a motor for a specific operating point. However, the properties of the materials in a real motor generally differ from those obtain from the measurements. Especially for the prediction of the iron losses, these discrepancies can lead to large errors, even when an accurate estimation of the magnetic-field distribution is available. The origin of the discrepancies is often a combination of various factors. For example, the loss characteristics of the magnetic materials are generally determined for a pulsating magnetic field, whereas the magnetic field in an IM is ideally a rotating one. Also, manufacturing steps such as lamination punching, stacking, shrink-fitting and milling can significantly influence the properties of the magnetic materials, or lead to undesired short-circuits for example at the outer surface of the rotor. Therefore, the calculation of iron losses is often limited during design to the ones calculated for the fundamental magnetic-flux distribution. These losses are then corrected by means of empirical coefficients, determined by the motor manufacturer for a large set of motors, to include the remaining iron losses. Finally, the discrepancies in the material properties also lead to errors in the predicted magnetization behaviour. For IMs, these errors mainly influence the required magnetizing current, which in turn influences the stator Ohmic losses.

It should be noted that the aforementioned phenomena do not present an exclusive overview. Many additional challenges, such as local saturation, stator and rotor current harmonics, parasitic torques, proximity effect, rotor-cage material variation etc. are currently not considered in the framework. Further, the operating temperatures of the stator and rotor conductors are assumed to be fixed. However, the developed electromagnetic models can be coupled to a thermal model to obtain a more accurate estimation of the operating temperatures.

5.3 Overview of the analysis framework

In Chapter 3, two different IM models were presented, namely the ALT model and the MMT model. Furthermore, methods to calculate the induced rotor current for both models were discussed in Chapter 4. It was shown that both models have advantages and disadvantages when it comes to IM analysis. Therefore, in this chapter, the advantages of both methods are combined to implement a semi-analytical analysis tool for low-power, low-speed, three-phase IMs. A schematic overview of the proposed analysis tool is shown in Figure 5.1.

For a given geometry, the MMT model is used to calculate the stator and rotor leakage inductances, $L_{\sigma,s}$ and $L_{\sigma,bar}$ respectively, and the effective air-gap lengthening coefficient, k_C. These parameters will be referred to as leakage and fringing flux parameters. Also, analytical and empirical calculations are used to estimate the stator and rotor resistance and end-winding inductance. Further, the

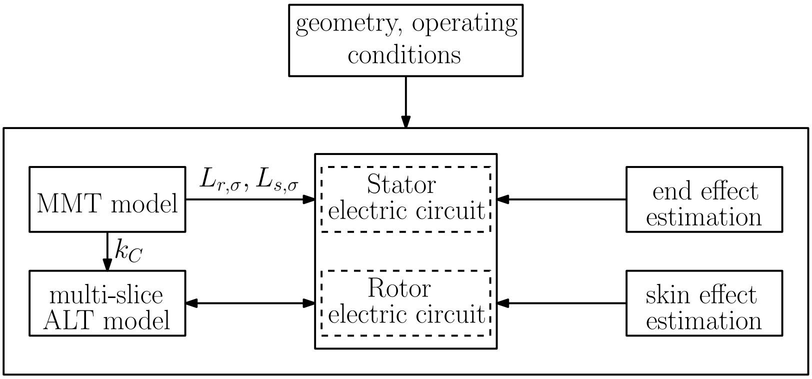

Figure 5.1: Schematic overview of the induction-motor modeling approach.

stator and rotor electric circuits are redefined, such that they include the leakage inductance calculated by the MMT model, and coupled to the ALT model using the methods described in Chapter 4. Small modifications are made to the ALT model to minimize its slot-leakage flux, since this leakage component is already accounted for by the MMT model. For simulation of skewed rotors, the ALT model is divided into a variable number of slices. Each slice is included in the circuit coupling with a different rotor position, such that the influence of skewing on the fundamental torque production is accounted for.

5.4 Leakage and fringing flux parameters

In this section, the calculation of the leakage and fringing flux parameters is discussed. These calculations are separated into three aspects, namely stator phase leakage inductance, rotor-bar leakage inductance and Carter's factor. The obtained parameters are applied in the next section to implement a skewed electromagnetic model.

5.4.1 Stator-phase leakage-inductance

For the stator-phase leakage-inductance calculation, a three-phase current distribution is applied to the stator windings, whereas the rotor current is set to zero. Since the MMT model is linear, the inductance is independent of the excitation magnitude. Therefore, I_{ph} is set to its nominal value for convenience. The synchronous and magnetizing flux linkage phasors are obtained using (3.89) to (3.91) and (3.100) to (3.102), respectively. The leakage flux linkage phasor of each stator phase x is then calculated as

$$\lambda_{\sigma,x} = \lambda_x - \lambda_{m,x}. \tag{5.1}$$

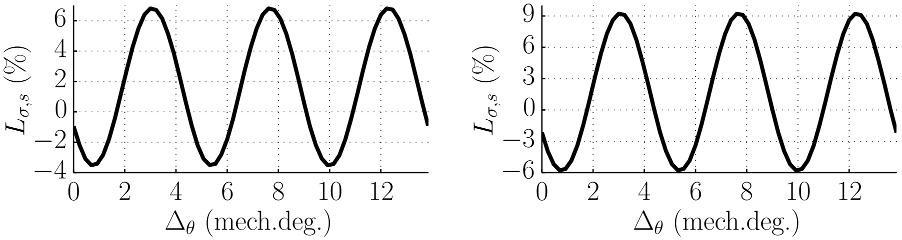

(a) Benchmark motor ”one” (b) Benchmark motor ”two”

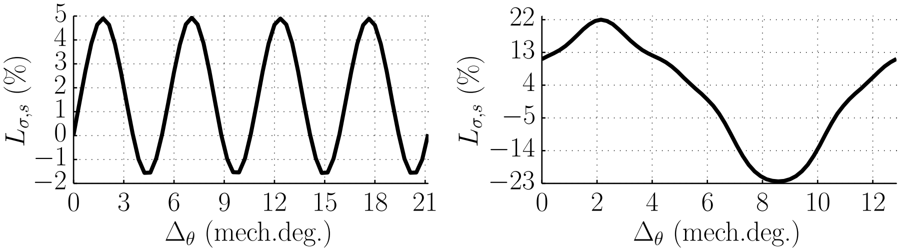

(c) Benchmark motor ”three” (d) Benchmark motor ”four”

Figure 5.2: Variation of the stator leakage inductance, $L_{\sigma,s}$, with respect to its average value, calculated as a function of rotor position, Δ_θ.

Finally, the phase leakage inductance is obtained as

$$L^x_{\sigma,s} = \frac{|\bar{\lambda}_{\sigma,x}|}{\sqrt{2} I_{ph}}. \tag{5.2}$$

Due to slotting, $L^x_{\sigma,s}$ varies as a function of the rotor position. To analyse the inductance variation, $L^A_{\sigma,s}$ is calculated for various values of the rotor displacement angle, Δ_θ. From the stator point of view, the magnetic structure behaves periodically with respect to Δ_θ along one rotor slot angle. Therefore, the calculations are performed for Δ_θ ranging from 0° to $360°/Q_r$. The results for each benchmark motor are shown in Figure 5.2, in terms of the relative variation of $L^A_{\sigma,s}$ with respect to its average value. It can be seen that this variation is significant for all benchmark motors, especially for number ”four”. Therefore, it is concluded that $L^A_{\sigma,s}$ can not be determined by considering only a single value of Δ_θ, but should be averaged along several rotor positions instead. For the considered balanced operating conditions, the average value of $L^x_{\sigma,s}$ is equal for each phase.

5.4.2 Rotor-bar leakage-inductance

For the rotor-bar leakage-inductance calculation, the stator phase currents are set to zero, whereas a sinusoidal current distribution is applied to the rotor bars, as given by (3.8). The value of I_{bar} is set to its nominal value, since it does

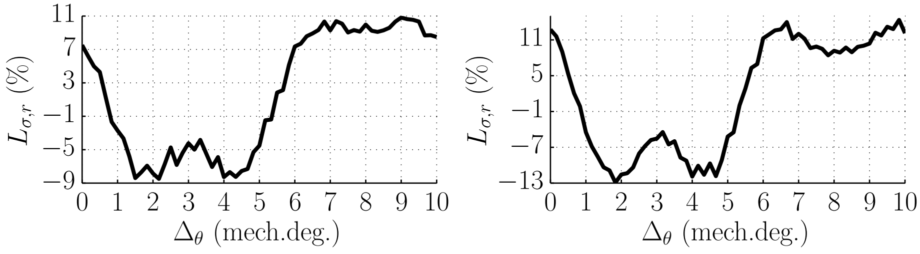

(a) Benchmark motor "one" (b) Benchmark motor "two"

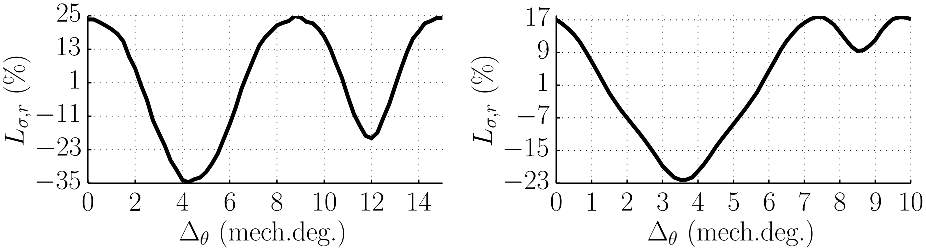

(c) Benchmark motor "three" (d) Benchmark motor "four"

Figure 5.3: Variation of the rotor leakage inductance, $L_{\sigma,r}$, with respect to its average value, calculated as a function of rotor position, Δ_θ.

not influence the inductance in the considered linear case. The synchronous and magnetizing inductance of each rotor bar are calculated using (3.82) and (3.95), respectively. Then, the leakage flux linkage phasor of each rotor bar is calculated as

$$\bar{\lambda}^{\nu}_{\sigma,bar} = \bar{\lambda}^{\nu}_{sr} - \bar{\lambda}^{\nu}_{m,sr}. \tag{5.3}$$

Finally, the leakage inductance of each rotor bar is obtained as

$$L^{\nu}_{\sigma,bar} = \frac{\left|\bar{\lambda}^{\nu}_{\sigma,bar}\right|}{\sqrt{2}I_{bar}}. \tag{5.4}$$

$L^{\nu}_{\sigma,bar}$ also varies as a function of rotor position due to slotting. From the rotor point of view, the magnetic structure varies periodically along one stator slot angle. Therefore, $L^{\nu}_{\sigma,bar}$ is calculated for various values of Δ_θ, ranging from 0° to $360°/Q_s$. The results of these calculations are shown in Figure 5.3, in terms of the relative variation of $L^{\nu}_{\sigma,bar}$ with respect to its average value. Again, it can be seen that the variation is significant. Therefore, $L^{\nu}_{\sigma,bar}$ should also be averaged along several rotor positions to obtain a suitable value for the analysis framework.

Table 5.1: Comparison of Carter's factor obtained for four benchmark motors using analytical calculation, the MMT model and the FEA model.

Benchmark	Analytical	MMT model	FEA model
1	1.26	1.28	1.26
2	1.29	1.30	1.28
3	1.19	1.20	1.19
4	1.29	1.29	1.29

5.4.3 Carter's factor

Carter's factor, k_C, represents the effective increase in the air-gap length seen by the fundamental travelling wave in an electric motor due to stator and rotor slotting. The effect is caused by the absence of highly permeable material in the slots and slot openings, which forces the flux that crosses the air gap to travel an effectively longer distance. An analytical approximation of k_C was first derived by Carter [162] from a simplified slot model by means of conformal mapping and the obtained results have been widely used in literature [37, 40]. For single-slotted machines, having either stator or rotor slotting, an expression for k_C is given by

$$k_C = \frac{\tau_u}{\tau_{sp} - \kappa b_o}, \tag{5.5}$$

where τ_{sp} is the slot pitch, b_o is the slot opening width and κ is given by

$$\kappa = \frac{2}{\pi}\left[\arctan\left(\frac{b_o}{2g}\right) - \left(\frac{2g}{b_o}\right)\ln\left(\sqrt{1+\left(\frac{b_o}{2g}\right)^2}\right)\right], \tag{5.6}$$

where $g = r_{si} - r_{ro}$ is the mechanical air-gap length. In case of double slotted machines, having both stator and rotor slotting, k_C is approximated as

$$k_C \approx k_{C,s} k_{C,r}, \tag{5.7}$$

where $k_{C,s}$ and $k_{C,r}$ represent Carter's factor due to stator and rotor slotting, respectively, both calculated separately using (5.5), assuming that the opposing side of the air gap is smooth.

As an alternative, k_C can be calculated using the MMT model. Since the required calculations are already performed for various rotor positions to obtain the average stator leakage inductances, the same analysis results can be used to determine k_C. To this extent, the peak value of the fundamental radial air-gap flux-density, $\hat{B}_{g,n_f}$, is calculated for each rotor position as

$$\hat{B}_{g,n_f} = \frac{1}{2}\left|-c_{n_f}^{\mathrm{III}} r^{2n_f-1} - d_{n_f}^{\mathrm{III}} r^{-2n_f-1} + j a_{n_f}^{\mathrm{III}} r^{2n_f-1} + j b_{n_f}^{\mathrm{III}} r^{-2n_f-1}\right|, \tag{5.8}$$

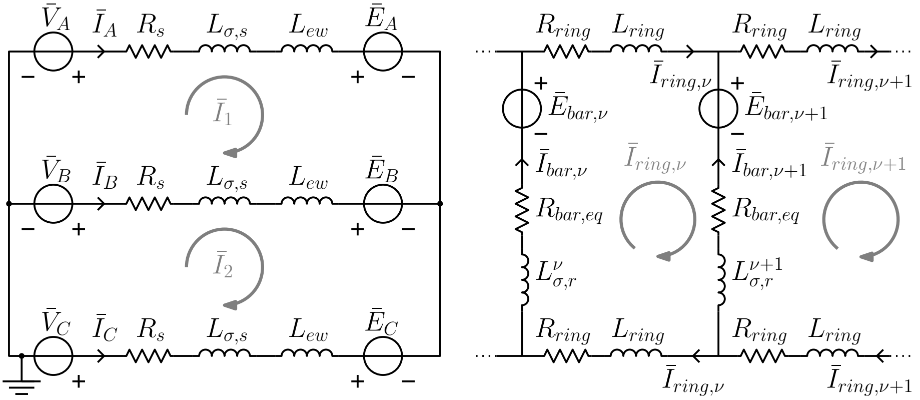

(a) Stator circuit

(b) Rotor circuit

Figure 5.4: Modified stator and rotor electric-circuit models including leakage inductance.

In the ideal case, where the stator and rotor air-gap surfaces are completely smooth and the soft-magnetic material is infinitely permeable, the fundamental radial air-gap flux-density of a three-phase IM is obtained as

$$\hat{B}_{g,ideal} = \sqrt{2} I_{ph} \frac{\mu_0 m k_{w1} N_{ph}}{\pi p g}, \tag{5.9}$$

where k_{w1} is the fundamental winding factor and N_{ph} is the number of winding turns per phase. A detailed overview of the calculation of k_{w1} is presented in [37] for various types of windings. Finally, k_C can be calculated as

$$k_C = \frac{\hat{B}_{g,ideal}}{\hat{B}_{g,slotted}}, \tag{5.10}$$

where $\hat{B}_{g,slotted}$ represents the average of $\hat{B}_{g,n_f}$ along the considered rotor positions. A comparison of Carter's factor calculated by (5.5), the MMT model, and linear FEA is shown in Table 5.1 for each benchmark motor. It can be seen that a close correspondence is obtained between the results. In the ALT model, k_C is used to correct the air-gap permeability, as discussed in Section 3.3.1.

5.5 Skewed electromagnetic model

Since the leakage flux is modeled by the MMT model, the resulting leakage-inductance components should be represented in the electric-circuit models that are coupled to the ALT model. Therefore, the stator and rotor electric circuits are modified such that they include $L_{\sigma,s}$ and $L^{\nu}_{\sigma,bar}$, as shown in Figure 5.4. Furthermore, the ALT model should be modified such that its predicted leakage flux is

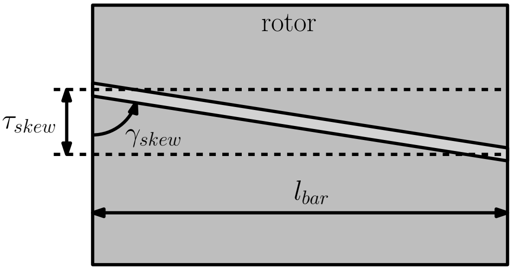

Figure 5.5: Graphical overview of rotor skewing to illustrate the skew pitch, τ_{skew}, and the rotor-bar inclination angle, γ_{skew}.

minimal. To this extent, non-physical values are assumed for the circumferential magnetic permeabilities of regions II and IV in the ALT model, namely $\mu_0/1000$.

To take rotor skewing into account in the coupled electromagnetic model, several measures are taken. Firstly, rotor skewing increases the total length of the rotor bar, whereas it decreases its effective cross-section area [38]. The equivalent rotor-bar length, $l_{bar,eq}$, and rotor-bar surface area, $S_{bar,eq}$, are calculated as

$$l_{bar,eq} = \frac{l_{bar}}{\cos\left(\gamma_{skew}\right)}, \tag{5.11}$$

$$S_{bar,eq} = S_{bar}\cos\left(\gamma_{skew}\right), \tag{5.12}$$

where γ_{skew} is the rotor-bar inclination angle, shown in Figure 5.5 and given by

$$\gamma_{skew} = \tan^{-1}\left(\frac{\tau_{skew}}{l_{bar}}\right), \tag{5.13}$$

where τ_{skew} represents the skew pitch at the rotor air-gap radius. Using the equivalent values, the rotor-bar resistance is then calculated as

$$R_{bar,eq} = k_R \frac{l_{bar,eq}}{\sigma_r S_{bar,eq}}. \tag{5.14}$$

Secondly, the influence of rotor skewing on the fundamental magnetic coupling between the stator and rotor should be taken into account. Therefore, the geometry of the motor is divided into N_{slice} slices along the axial direction. The axial length of each slice is calculated as

$$l_{slice} = \frac{l_{stk}}{N_{slice}}. \tag{5.15}$$

The rotor positions of subsequent slices are shifted with respect to each other. To determine the average rotor position of each slice, firstly the total skewing angle of the rotor bars is calculated as

$$\theta_{skew} = \frac{t_{skew}}{r_{ro}}. \tag{5.16}$$

Then, the rotor position of the first slice is determined as

$$\Delta_{\theta,slice,1} = -\frac{\theta_{skew}}{2} + \frac{\theta_{slice}}{2}, \tag{5.17}$$

where $\theta_{slice} = \theta_{skew}/N_{slice}$ is the amount of skewing per slice. Finally, the rotor angle of the remaining slices is obtained as

$$\Delta_{\theta,slice,n_{slice}} = \Delta_{\theta,slice,1} + (n_{slice} - 1)\,\theta_{slice}, \tag{5.18}$$

where n_{slice} represents the considered slice number. For odd N_{slice}, the rotor position of the middle slice should be equal to zero.

Finally, all slices are represented by separate ALT models, which are coupled to each other through the stator and rotor electric-circuit models. The boundary-condition equations of each of these ALT models are included in the system matrix equations. By summing the induced voltage of each slice for both the stator phases and the rotor bars, expressions for the induced voltages required for the voltage equations are obtained. The coupling equations derived in Chapter 4 can therefore be reused for each model slice.

5.6 Motor performance calculation

To use the coupled electromagnetic model as a tool for motor design, the losses of the machine should be predicted. Methods to calculate these losses are presented in this section, including Ohmic losses, iron losses, mechanical losses and stray losses. Performance parameters, such as efficiency and power factor, can then be determined. Further, a brief overview of methods to determine the Steinmetz Equivalent Circuit parameters from no-load and locked-rotor tests is also provided. These parameters will be used in the next sections to validate the IM analysis framework against FEA simulation results and measurements.

5.6.1 Stator and rotor Ohmic losses

The Ohmic losses of the stator and rotor can be determined relatively easily. Assuming that the resistance and rms current are known for the stator and rotor windings, their Ohmic losses are determined as

$$P_{Ohm,s} = \sum_{x=A,B,C} \frac{\left|\bar{I}_x\right|^2}{2} R_s, \tag{5.19}$$

$$P_{Ohm,r} = C_{per} \sum_{\nu=1}^{N_{sr}} \frac{\left|\bar{I}_{bar,\nu}\right|^2}{2} \left(R_{bar,eq} + R_{er}\right). \tag{5.20}$$

During motor design, the wire length of a stator phase winding, l_{wire}, needs to be estimated, for example using the equations given in [37]. Furthermore, the conductivity of the stator and rotor conductors strongly depends on the operating temperature. For initial design, the conductor temperatures can be estimated, but for accurate performance calculation, the operating temperatures should be predicted by a thermal model. Finally, the total Ohmic losses are calculated as

$$P_{Ohm} = P_{Ohm,s} + P_{Ohm,r}. \tag{5.21}$$

5.6.2 Iron losses

In general, an accurate prediction of the iron losses is difficult to obtain. Even if an accurate description of the magnetic-field variation is available, for example from FEA simulations, significant discrepancies between measured and calculated values are often observed. These discrepancies are mainly caused by the influence of manufacturing processes on the iron-loss characteristics of soft-magnetic material. Therefore, iron-loss predictions are usually limited to the iron losses due to the fundamental magnetic flux in design calculations, whereas the remaining part of the iron losses is accounted for by empirical corrections. In the analysis framework, a similar approach is used.

The iron losses are mathematically separated into three different component, namely static hysteresis losses, dynamic eddy-current losses, and excess losses [163]. The iron-loss density in each motor part is then described as

$$p_{Fe} = p_{hys} + p_{eddy} + p_{exc}. \tag{5.22}$$

The static hysteresis-loss density, assumed proportional to the area of the hysteresis loop obtained for near-zero frequency excitation, is represented by p_{hys}. Its value is calculated as

$$p_{hys} = k_{hys}\hat{B}^2 f, \tag{5.23}$$

where $\hat{B}$ is the peak flux-density in the motor part, f is the excitation frequency, and k_{hys} is the hysteresis-loss coefficient.

Further, the dynamic eddy-current loss density, p_{eddy}, represents the macroscopic induced currents in the soft-magnetic material due to the variation of the magnetic field. By assuming that the flux density in each motor part varies sinusoidally in time with frequency f, p_{eddy} can be obtained as

$$p_{eddy} = k_{eddy}\frac{\pi^2 d_{lam}^2 \sigma_{iron}}{6}\left(\hat{B}f\right)^2, \tag{5.24}$$

where d_{lam} is the lamination thickness, σ_{iron} is the conductivity of the soft-magnetic material and k_{eddy} is the eddy-current loss coefficient.

Finally, p_{exc} represents the excess losses, which accounts for additional iron losses not considered by p_{hys} and p_{eddy}. An expression for p_{exc} is given by

$$p_{exc} = 8.67k_{exc}\left(\hat{B}f\right)^{1.5}, \tag{5.25}$$

where k_{exc} represents the excess loss coefficient. The values of k_{hys}, k_{eddy} and k_{exc} are determined from measurement results, for example obtained from ring samples of the soft-magnetic material. These measurements are discussed in more detail in Appendix B.

The calculation of the iron losses is performed separately for four motor parts, namely the stator yoke, the stator teeth, the rotor yoke and the rotor teeth. The peak value of the magnetic-flux density in each motor part is calculated using (3.28), (3.29), (3.30) and (3.31), respectively. The iron losses are then calculated as

$$\begin{aligned} P_{Fe,ys} =& k_{Fe,ys}V_{ys}\left(k_{hys}\hat{B}_{ys}^2 f_s + k_{eddy}\frac{\pi^2 d_{lam}^2\sigma_{iron}}{6}\left(\hat{B}_{ys}f_s\right)^2 + \right. \\ & \left. 8.67k_{exc}\left(\hat{B}_{ys}f_s\right)^{1.5}\right), \end{aligned} \tag{5.26}$$

$$\begin{aligned} P_{Fe,ds} =& k_{Fe,ds}V_{ds}\left(k_{hys}\hat{B}_{ds}^2 f_s + k_{eddy}\frac{\pi^2 d_{lam}^2\sigma_{iron}}{6}\left(\hat{B}_{ds}f_s\right)^2 + \right. \\ & \left. 8.67k_{exc}\left(\hat{B}_{ds}f_s\right)^{1.5}\right), \end{aligned} \tag{5.27}$$

$$\begin{aligned} P_{Fe,yr} =& k_{Fe,yr}V_{yr}\left(k_{hys}\hat{B}_{yr}^2 sf_s + k_{eddy}\frac{\pi^2 d_{lam}^2\sigma_{iron}}{6}\left(\hat{B}_{yr}sf_s\right)^2 + \right. \\ & \left. 8.67k_{exc}\left(\hat{B}_{yr}sf_s\right)^{1.5}\right), \end{aligned} \tag{5.28}$$

$$\begin{aligned} P_{Fe,dr} =& k_{Fe,dr}V_{dr}\left(k_{hys}\hat{B}_{dr}^2 sf_s + k_{eddy}\frac{\pi^2 d_{lam}^2\sigma_{iron}}{6}\left(\hat{B}_{dr}sf_s\right)^2 + \right. \\ & \left. 8.67k_{exc}\left(\hat{B}_{dr}sf_s\right)^{1.5}\right), \end{aligned} \tag{5.29}$$

where V_{ys}, V_{ds}, V_{yr} and V_{dr} are the volumes of each motor part, which are approximated using geometric parameters as

$$V_{ys} = k_{sf}l_{stk}\pi\left(\left(r_{si}+h_{ss}+h_{ys}\right)^2 - \left(r_{si}+h_{ss}\right)^2\right), \tag{5.30}$$

$$V_{ds} = k_{sf}l_{stk}h_{ss}b_{ds}Q_s, \tag{5.31}$$

$$V_{yr} = k_{sf}l_{stk}\pi\left(\left(r_{ro}-h_{sr}\right)^2 - \left(r_{ro}-h_{sr}-h_{yr}\right)^2\right), \tag{5.32}$$

$$V_{dr} = k_{sf}l_{stk}h_{sr}b_{dr}Q_r, \tag{5.33}$$

where k_{sf} is the lamination stacking factor. Further, $k_{Fe,yr}$, $k_{Fe,ys}$, $k_{Fe,dr}$ and $k_{Fe,ds}$ represent iron-loss correction-coefficients. If these empirical factors are set to unity, the calculated iron losses only considers losses due to a sinusoidally varying, fundamental magnetic field. In practice, however, the iron losses are generally much larger than the ones predicted for the fundamental magnetic field. On the one hand, this increase is caused by loss mechanisms that have not been taken into account, such as dynamic losses due to high-frequency field harmonics. On the other hand, inaccuracy of the obtained loss parameters with respect to the application influences the results. For example, the iron losses produced by a rotating magnetic field, such as in an IM, differ from the ones produced by a pulsating magnetic field. However, most material-identification tests are performed using pulsating magnetic fields. Furthermore, mechanical stress, e.g. due to lamination punching and shrink-fitting of the motor housing, can significantly increase iron losses. To deal with these effects in design calculations, the empirical coefficients $k_{Fe,yr}$, $k_{Fe,ys}$, $k_{Fe,dr}$ and $k_{Fe,ds}$ are usually determined from no-load test results, performed on a large set of test machines [37]. However, if such measurements are not available, the values given in [37] could be used for a first estimation.

Finally, in case $N_{slice} > 1$, l_{stk} should be replaced by l_{slice} in (5.30) to (5.33), and (5.26) to (5.29) should be evaluated for each model slice separately. The total iron losses are then obtained as

$$P_{Fe} = P_{Fe,ys} + P_{Fe,ds} + P_{Fe,yr} + P_{Fe,dr}. \tag{5.34}$$

5.6.3 Mechanical losses

For the mechanical losses, only the bearing-friction losses are considered in this thesis. Due to the low speed of the considered machines, the air-gap windage losses are considered negligible. Furthermore, it is assumed that no cooling fan is attached to the motor shaft and that the rotor end rings do not have cooling fins. For this case, the mechanical losses are determined as

$$P_{ml} = P_{bearing} = C_{bearing} n_{mech}, \tag{5.35}$$

where $C_{bearing}$ is the bearing-loss coefficient and n_{mech} is the mechanical speed of the rotor, given by

$$n_{mech} = \frac{w_{r,m}}{2\pi} C_{spm}, \tag{5.36}$$

where $C_{spm} = 60\,\mathrm{s\,min}^{-1}$. A value for $C_{bearing}$ can be determined from no-load measurements, performed on a machine of approximately the same size with a similar bearing type. The torque corresponding to the mechanical loss is given by

$$T_{ml} = \frac{P_{ml}}{w_{r,m}}, \tag{5.37}$$

which should be subtracted from the produced electromagnetic torque, such that the mechanical torque, T_{mech}, and output power, P_{mech}, can be obtained as

$$T_{mech} = T_{em} - T_{ml}, \tag{5.38}$$

$$P_{mech} = T_{mech} w_{r,m}. \tag{5.39}$$

5.6.4 Stray losses

Besides the loss components described above, unaccounted stray losses are usually produced in electric machines. Generally, these losses depend on the load applied to the machine, but they are difficult to quantify by means of calculation or measurement. Therefore, the IEC standard for indirect loss measurement assumes that the stray losses amount up to 0.5% of the motor input power. A similar assumption is made here, such that the stray losses can be determined as

$$P_{stray} = \frac{0.005\left(P_{mech} + P_{ml} + P_{Fe} + P_{Ohm}\right)}{0.995}. \tag{5.40}$$

5.6.5 Efficiency and power factor

The total active input power of the motor is determined as

$$P_{in} = P_{mech} + P_{ml} + P_{Fe} + P_{Ohm} + P_{stray}, \tag{5.41}$$

such that the efficiency can be calculated as

$$\eta = \frac{P_{mech}}{P_{in}} 100\%. \tag{5.42}$$

To determine the power factor, firstly the total reactive input power, Q_{in}, should be determined. From the results of the ALT model, Q_{in} is calculated as

$$Q_{in} = \sqrt{m\left(V_{ph}I_{ph}\right)^2 - \left(P_{mech} + P_{ml} + P_{Ohm}\right)^2}, \tag{5.43}$$

where I_{ph} and V_{ph} are the rms stator phase current and voltage. It should be noted that P_{Fe} and P_{stray} are not included in (5.43), since these losses are not taken into account directly by the ALT model. For current-fed simulations, V_{ph} can be obtained as

$$V_{ph} = \frac{\left|\bar{E}_{ph} + \bar{I}_{ph}\left(R_s + jw_s L_{\sigma,s} + jw_s L_{ew}\right)\right|}{\sqrt{2}}. \tag{5.44}$$

Finally, the power factor, pf, is obtained as

$$pf = \frac{P_{in}}{\sqrt{P_{in}^2 + Q_{in}^2}}. \tag{5.45}$$

5.6.6 Steinmetz equivalent circuit parameters

A common approach to separate the influence of different phenomena that take place in IMs is to calculate its SEC parameters by means of no-load and locked-rotor tests. These tests can be performed on a real machine by means of measurements to obtain more insight in the behaviour of the motor. However, they can also be applied to a motor in simulation to obtain more insight in the capabilities of the model. Moreover, a comparison of different models based on these parameter values is possible as well.

To perform the locked-rotor test, the position of the IM rotor is fixed and the excitation frequency is set to the nominal frequency of the motor. The locked-rotor test is then executed for various stator phase voltages, such that the resulting parameters can be evaluated for various rotor current amplitudes. Finally, the rotor resistance, R'_r, and the stator and rotor leakage inductances, $L_{\sigma,s}$ and $L'_{\sigma,r}$, are calculated from the active and reactive input power, $P_{in,LR}$ and $Q_{in,LR}$ respectively, as

$$R'_r = \left(\frac{P_{in,LR}}{3I_{ph}^2} - R_s\right)\left(\frac{1}{1+\alpha_{T,r}\left(T_{op,r}-20\right)}\right), \tag{5.46}$$

$$L_{\sigma,s} = \frac{1}{2}\frac{Q_{in,LR}}{6\pi f_s I_{ph}^2}, \tag{5.47}$$

$$L'_{\sigma,r} = \frac{1}{2}\frac{Q_{in,LR}}{6\pi f_s I_{ph}^2}, \tag{5.48}$$

where $\alpha_{T,r}$ is the temperature coefficient of the rotor-bar material conductivity and $T_{op,r}$ is the operating temperature of the rotor bars. It is assumed here that during locked-rotor operation, the rms stator current, I_{ph}, is equal to the rotor current, I'_r. Further, the split ratio between the stator and rotor inductance is assumed to be 1:1.

In order to obtain the no-load characteristics, the IM is operated near its synchronous speed. The frequency of the excitation voltage is again fixed to its nominal value, whereas the rms phase voltage is increased in steps up to approximately 130% of its nominal value. For each voltage level, the magnetizing inductance, L_m, can be determined from $Q_{in,NL}$ as

$$L_m = \frac{Q_{in,NL}}{6\pi f_s I_{ph^2}} - L_{\sigma,s}. \tag{5.49}$$

It is assumed that the current through the magnetizing inductance, I_m, is equal to I_{ph}. Further, in case of real motor measurements, the no-load iron losses, $P_{Fe,NL}$, can be determined from $P_{in,NL}$ as

$$P_{Fe,NL} = P_{in,NL} - 3I_{ph}^2 R_s - P_{mech}. \tag{5.50}$$

Additionally, P_{mech} can be determined from no-load measurements as well. Using the input power obtained for low values of V_{ph}, linear extrapolation can be applied to find $P_{in,NL}$ for $V_{ph} = 0$, which represents P_{mech}.

5.7 Finite Element validation

To asses the capabilities of the IM analysis framework, the results of calculations performed on the benchmark motors are validated against FEA results. The results of these validations are presented in terms of performance characteristics, namely electromagnetic torque and rms stator phase current versus slip, and motor parameters obtained from no-load and locked-rotor tests. Firstly, a comparison between the framework and 2D FEA calculations is discussed for each benchmark motor without considering the influence of skewing. The goal of this comparison is to reflect on the performance of the combined 2D semi-analytical model with respect to a 2D FEA model without disturbance of 3D effects. Secondly, a comparison between the framework and skewed FEA calculations is discussed for benchmark motors "two" and "four". Both these validation steps serve to obtain more insight in discrepancies that might arise in a comparison between the framework and measurement results, which will be presented in Section 5.8.

5.7.1 Comparison without skewing

In Figure 5.6, a comparison between the IM analysis framework and 2D FEA is presented in terms of electromagnetic torque without considering skewing. For benchmark motors "one", "three" and "four", the stable operating region spans from $s = 0$ up to approximately $s = 0.4$, whereas it spans from $s = 0$ up to approximately $s = 0.2$ for benchmark motor "two". Within these stable regions, it can be seen that a good agreement is obtained between the framework and 2D FEA calculations. However, for larger slip values, the error between the models increases and is most notable for $s = 1$.

A similar trend can be observed for the rms stator phase current in Figure 5.7, although the magnitude of the discrepancies for large slip values is smaller. Further, an additional discrepancy is observed for low slip values in benchmark motors "three" and "four". For number "three", a similar discrepancy was also observed in Figure 4.16 and is caused by deep saturation of the rotor teeth. For benchmark motor "four", a similar discrepancy is not observed in Figure 4.16. However, it can be seen from Figure 4.18 that the discrepancy between the linear and nonlinear FEA models is large at low slip values. This suggests that benchmark motor "four" is generally saturated in the stable operating region, especially near $s = 0$. On the one hand, the influence of this saturation on the stator leakage inductance is accounted for by the original ALT model. Consequently, Figure 4.16 shows a good agreement. On the other hand, the modified ALT model used in the framework utilizes the MMT model to estimate the stator leakage inductance, and does not consider saturation in the leakage-inductance calculation. Therefore, the discrepancy observed for benchmark motor "four" near $s = 0$ in Figure 5.7 is attributed to saturation of the stator leakage flux paths.

Additionally, characteristics for the magnetizing current and magnetizing inductance as a function of stator phase voltage are shown in Figures 5.8 and 5.9, respectively. These results are obtained from no-load tests and it can be seen that the framework is in relatively good agreement with the FEA calculations for voltage levels below the nominal voltage. However, for voltage levels close to and above the nominal voltage, the discrepancy between the models increases. In this operating region, the motor is heavily saturated and local saturation effects have an increased influence on the magnetizing characteristics. During the design of low-power IMs, this operating region is often omitted to increase the efficiency of the motor, unless the motor is being designed for a high power density.

Finally, characteristics for the total leakage inductance ($L_{\sigma,s} + L'_{\sigma,r}$) and the rotor resistance as a function of stator phase voltage are shown in Figures 5.10 and 5.11, respectively. These results are obtained from locked-rotor tests. For the leakage inductance, it can be seen that the framework and the FEA results are in good agreement for low voltage values. For increasing voltage, however, the discrepancy increases, especially for benchmark motor "two". These discrepancies are attributed to saturation of the stator and rotor leakage inductances. Additionally, they can be identified as the origin of the discrepancies observed in Figures 5.6 and 5.7 for high-slip operation. For the rotor resistance, it can be seen that the framework and the FEA results are in good agreement. This shows that the skin effect due to the fundamental rotor time harmonic is not the origin of the discrepancies observed in Figures 5.6 and 5.7.

5.7.2 Comparison with skewing

In this section, the results of the IM analysis framework including the influence of skewing are compared to results obtained from a skewed (multi-slice) FEA model for benchmark motors "two" and "four". The number of slices used in the skewed FEA model is selected equal to the number of slices used in the framework, namely $N_{slice} = 7$. In Figures 5.12 and 5.13, it can be seen that skewing has a significant influence of the torque versus slip and current versus slip characteristics. For benchmark motor "two", the discrepancies between the framework and the skewed FEA results are approximately similar to the discrepancies observed for the unskewed case. A good agreement is observed for the stable operating region, whereas the discrepancy increases for high slip values due to leakage path saturation. For benchmark motor "four", a relatively good agreement is obtained along the entire torque and current characteristics, although the error between the framework and the FEA model is slightly larger in the stable operating region of the motor.

Additionally, a comparison in terms of magnetizing current and inductance is shown in Figures 5.14 and 5.15, respectively. As expected, the skewing does not significantly influence the no-load characteristics of the benchmark motors. Therefore, approximately the same results are obtained as the ones obtained for the unskewed case. Further, a comparison in terms of leakage inductance and

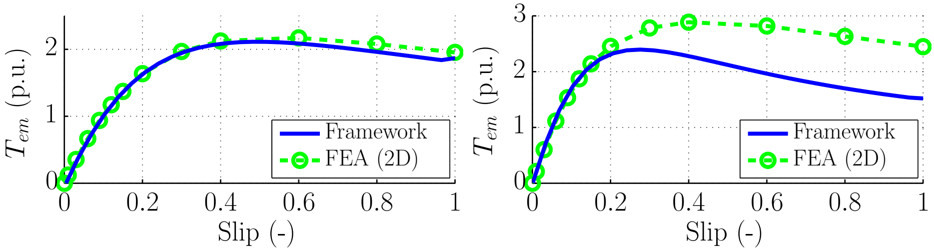

(a) Benchmark motor "one" (b) Benchmark motor "two"

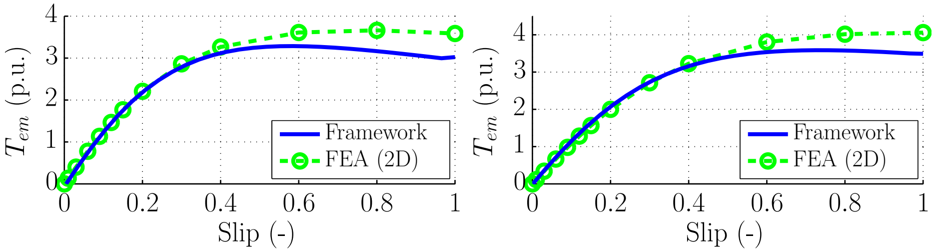

(c) Benchmark motor "three" (d) Benchmark motor "four"

Figure 5.6: Comparison of the electromagnetic torque, T_{em}, versus slip, calculated by the framework and 2D FEA without skewing.

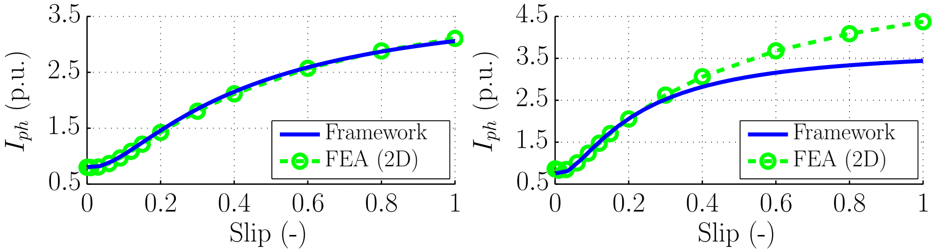

(a) Benchmark motor "one" (b) Benchmark motor "two"

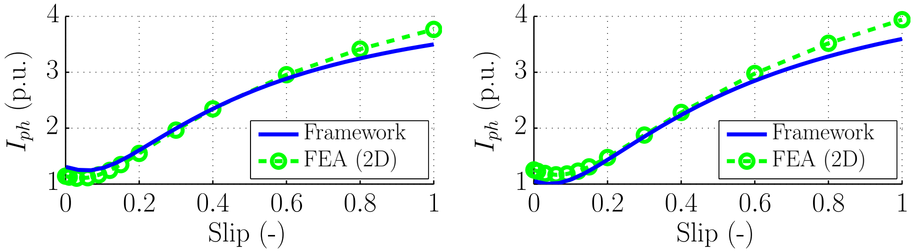

(c) Benchmark motor "three" (d) Benchmark motor "four"

Figure 5.7: Comparison of the rms stator phase current, I_{ph}, versus slip, calculated by the framework and 2D FEA without skewing.

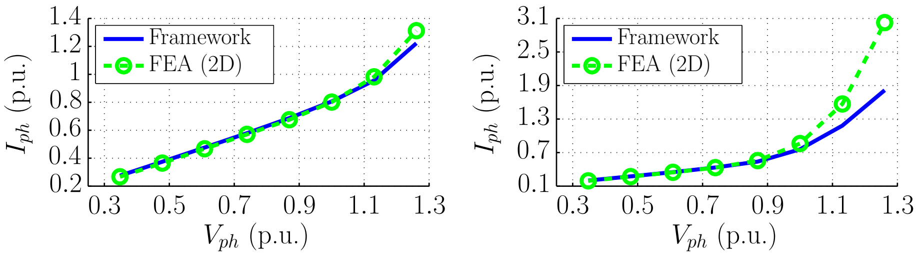

(a) Benchmark motor "one" (b) Benchmark motor "two"

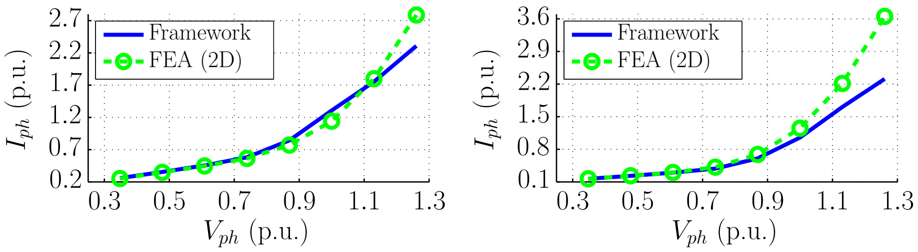

(c) Benchmark motor "three" (d) Benchmark motor "four"

Figure 5.8: Comparison of the rms stator phase current, I_{ph}, calculated by the framework and 2D FEA at no-load operation without skewing.

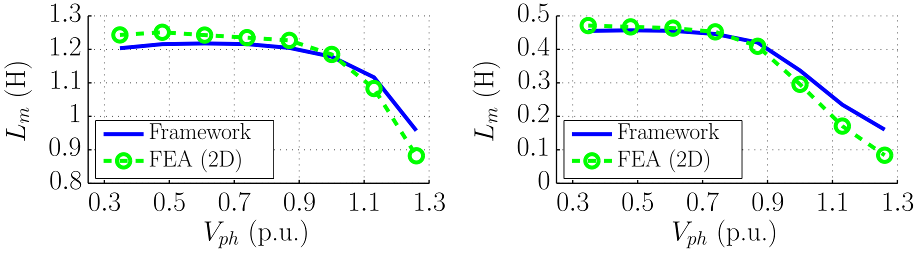

(a) Benchmark motor "one" (b) Benchmark motor "two"

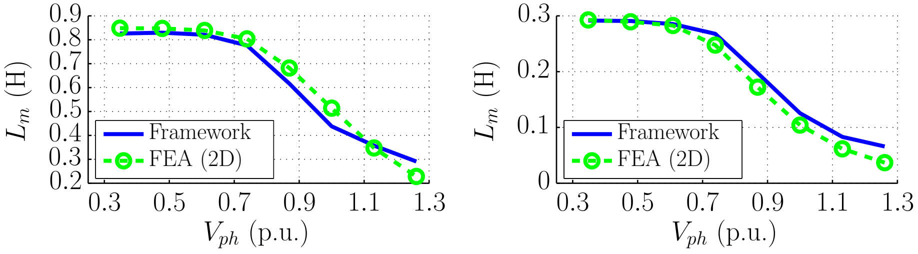

(c) Benchmark motor "three" (d) Benchmark motor "four"

Figure 5.9: Comparison of the magnetizing inductance, L_m, calculated by the framework and 2D FEA at no-load operation without skewing.

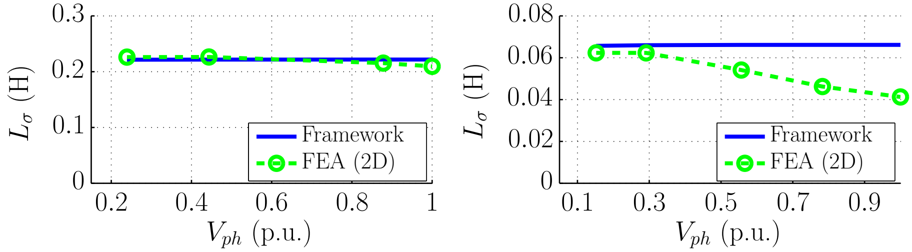

(a) Benchmark motor ”one” (b) Benchmark motor ”two”

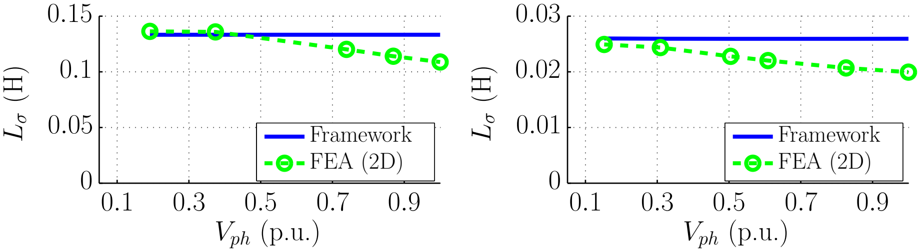

(c) Benchmark motor ”three” (d) Benchmark motor ”four”

Figure 5.10: Comparison of the leakage inductance, L_σ, calculated by the framework and 2D FEA at locked-rotor operation without skewing.

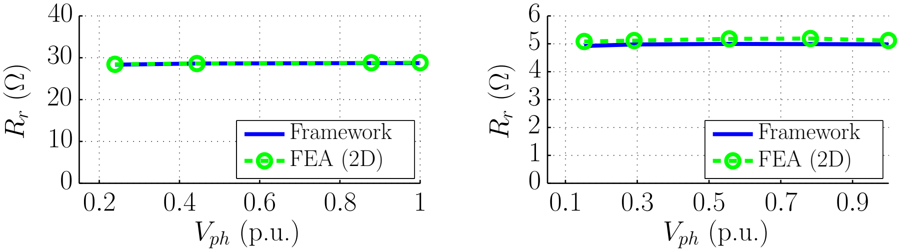

(a) Benchmark motor ”one” (b) Benchmark motor ”two”

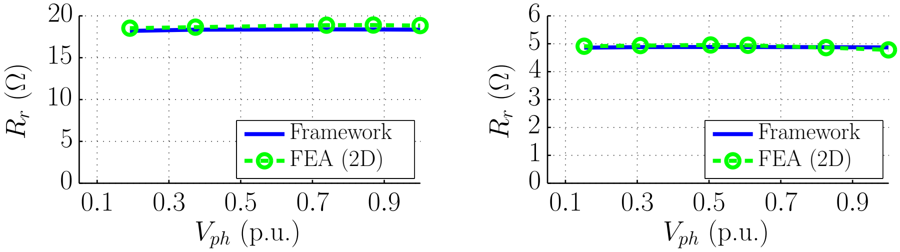

(c) Benchmark motor ”three” (d) Benchmark motor ”four”

Figure 5.11: Comparison of the rotor resistance, R_r, calculated by the framework and 2D FEA at locked-rotor operation without skewing.

rotor resistance is shown in Figures 5.16 and 5.17, respectively. It can be seen that the skewing significantly increases the leakage inductance of the motor. Also, it can be seen that the increase predicted by the framework is approximately equal to the increase predicted by the skewed FEA model. Finally, the skewing does not significantly influence the rotor resistance. Therefore, the results of the framework, 2D FEA and skewed FEA are approximately equal.

5.8 Experimental validation

In this section, the IM analysis framework is validated against measurements performed on prototypes of the four benchmark motors. A description of the setup and measurements is provided first, followed by the validation results. The comparison between framework and measured values is presented in terms of performance characteristics, as a function of slip, and SEC parameters obtained from no-load and locked-rotor tests.

5.8.1 Setup and measurement description

To validate the IM analysis framework, measurements were performed on a Magtrol motor test bench for each benchmark motor. This measurement setup uses an eddy-current brake to apply a load torque to the IM under test. The applied load torque is controlled by the Magtrol system and has a maximum value of approximately 10 Nm. During the measurements, all required signals, such as stator voltages and currents, mechanical torque, T_{mech}, speed, n, end-winding temperature, T_{wind}, and ambient temperature, T_{amb}, were monitored and stored by the Magtrol system. Also, the IM under test was fed by a variable three-phase transformer, such that the supply voltage for the IM could be regulated. A schematic overview of the measurement setup is shown in Figure 5.18.

To obtain performance characteristics for each benchmark motor, automated measurements were performed for a large number of operating points between synchronous speed and standstill. During these measurements, V_{ph} and f_s remained fixed to their nominal values. Using the measured voltages, currents, torque and speed, the input power and output power of the tested motor were calculated, such that efficiency and power factor could be determined. Prior to each measurement, the motor under test was heated up to its approximate operating temperature. Furthermore, each measurement was executed within several seconds to prevent large parameters variation due to increasing stator and rotor temperature.

Additional to the performance characteristic measurements, no-load and locked-rotor measurements were performed. For the no-load measurements, the IM under test was disconnected from any mechanical load such that it can rotate freely.

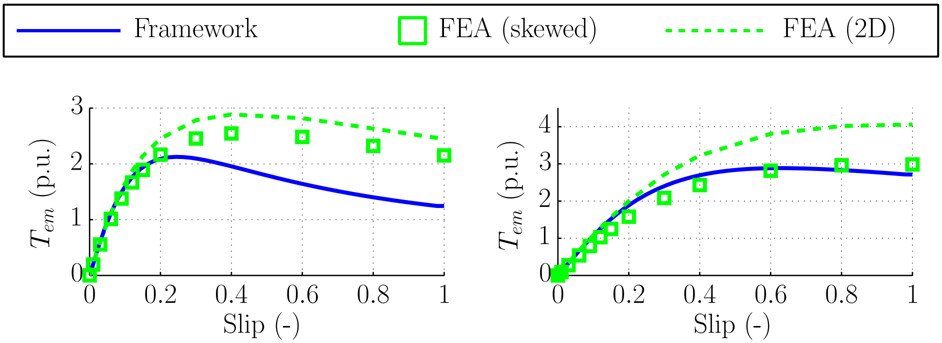

(a) Benchmark motor ”two”

(b) Benchmark motor ”four”

Figure 5.12: Comparison of the electromagnetic torque, T_{em}, versus slip, calculated by the framework and 2D FEA with skewing.

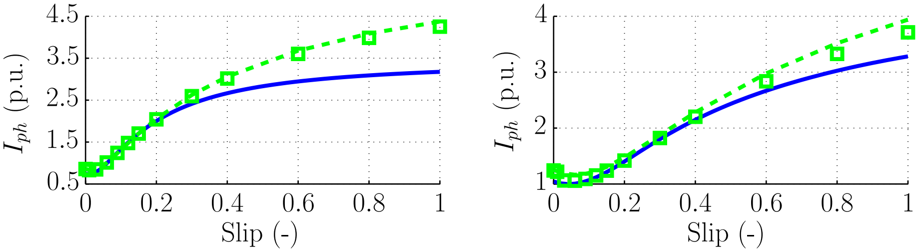

(a) Benchmark motor ”two”

(b) Benchmark motor ”four”

Figure 5.13: IM analysis framework versus FEA with skewing: stator phase current comparison.

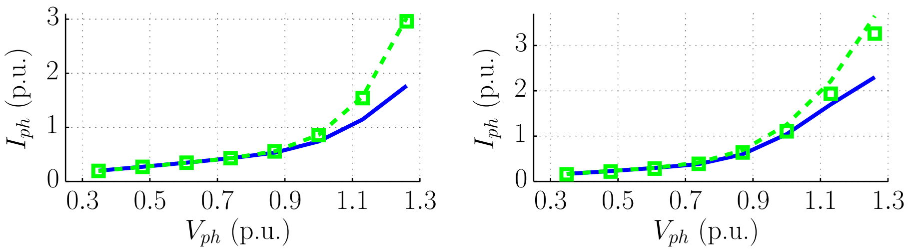

(a) Benchmark motor ”two”

(b) Benchmark motor ”four”

Figure 5.14: Comparison of the rms stator phase current, I_{ph}, versus slip, calculated by the framework and 2D FEA with skewing.

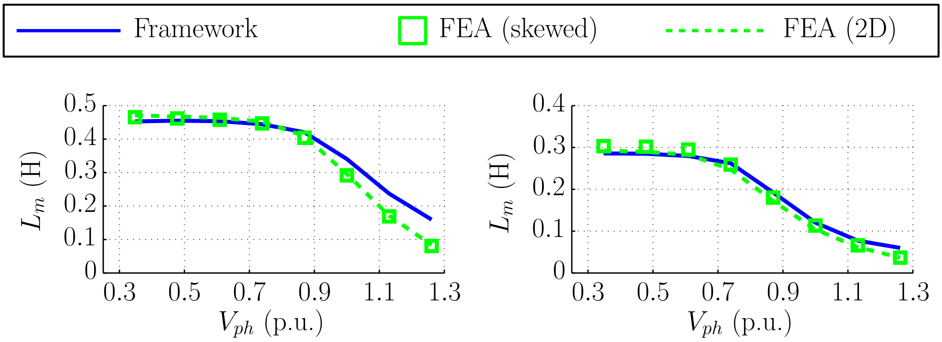

(a) Benchmark motor "two" (b) Benchmark motor "four"

Figure 5.15: Comparison of the magnetizing inductance, L_m, calculated by the framework and 2D FEA at no-load operation without skewing.

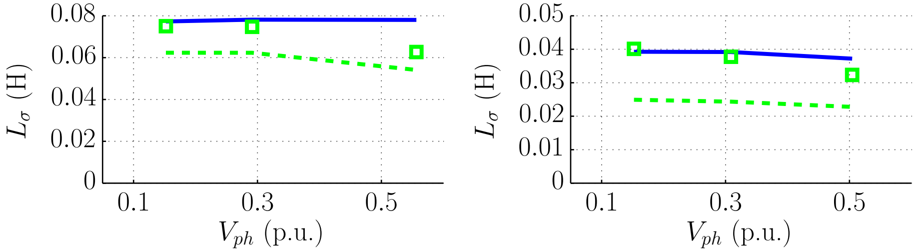

(a) Benchmark motor "two" (b) Benchmark motor "four"

Figure 5.16: Comparison of the leakage inductance, L_σ, calculated by the framework and 2D FEA at locked-rotor operation without skewing.

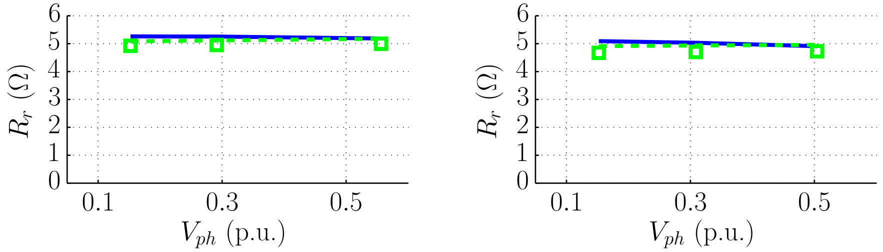

(a) Benchmark motor "two" (b) Benchmark motor "four"

Figure 5.17: Comparison of the rotor resistance, R_r, calculated by the framework and 2D FEA at locked-rotor operation without skewing.

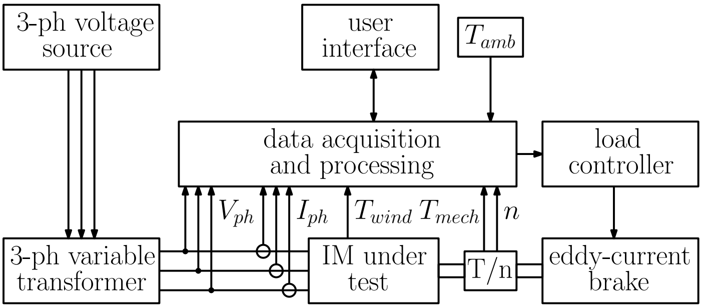

Figure 5.18: Schematic overview of the induction-motor measurement setup.

The stator voltage was then increased in steps and for each step, a number of measurements was performed. From the results, L_m and $P_{Fe,NL}$ were determined using (5.49) and (5.50), respectively. Further, for the locked-rotor measurements, the shaft of the rotor was mechanically fixed and the rms phase voltage that gives approximately nominal stator current, $V_{ph,LR}$, was determined. The locked-rotor measurements were then obtained for three different voltage levels, namely $V_{ph} = 0.5V_{ph,LR}$, $V_{ph} = V_{ph,LR}$ and $V_{ph} = 2V_{ph,LR}$. For each of these voltage levels, the results were averaged over multiple measurements, performed at different rotor positions. Finally, R'_r, $L_{\sigma,s}$ and $L'_{\sigma,r}$ were determined using (5.46), (5.47) and (5.48), respectively.

5.8.2 Validation results

A comparison between the characteristics obtained from the framework and measurements is shown in Figures 5.19 to 5.22 in terms of mechanical torque, rms stator phase current, efficiency and power factor. The number of slices used in the framework is set to $N_{slice} = 7$, similar to the skewed comparison discussed in Section 5.7.2. For the mechanical torque, depicted in Figure 5.19, it can be seen that a very good agreement is obtained in the stable operating region, with errors typically less that 5%. Only benchmark motor "one" shows a slightly higher error, but it is limited to 10%. Further, it can be seen than the error increases for high slip values in benchmark motors "one" and "three". For benchmark motors "two" and "four", these results are not shown due to the torque limitation of the measurement setup. For the rms stator phase current, shown in Figure 5.20, the error obtained for the nominal operating point is typically less than 10%. For benchmark motor "three", however, a slightly larger error is observed. A similar error was observed for this motor in the 2D FEA comparison presented in Section 5.7.1, and was found to be caused by severe rotor tooth saturation. Also, a larger error is apparent near no-load operation. This indicates that the saturation behaviour of the actual motors differs from the simulated ones. Finally, it can be seen from Figures 5.21 and 5.22 that a good agreement is obtained for the power factor and the efficiency, respectively. For the power factor, the error is typically less than 10% in the stable operating region, whereas the error in the efficiency is typically less than 5%. However, benchmark motor "three" again presents an exception to these numbers.

A comparison of the parameters obtained from the no-load and locked-rotor tests is shown in Figures 5.23 to 5.26. It can be seen from Figure 5.23 that the discrepancies observed for L_m follow a similar trend as those observed in Figure 5.9. However, the magnitude of the error obtained for the saturated conditions is larger. This indicates that the magnetic material properties in the actual motors differ from the ones used in the simulation. As a result, the magnetization behaviour of the motor is influenced. This also explains why the stator phase current is overestimated by the framework in the stable operating region of benchmark motor "three". Further, a comparison of the no-load iron losses is shown in Figure 5.24. For the two largest benchmark motors, "two" and "four", it can be seen that a good agreement is obtained for voltage levels up to the nominal stator voltage. Near and above the nominal stator voltage, saturation of the soft-magnetic material leads to a significant increase in the iron losses, which is not accounted for by the framework. For the two shorter benchmark motors, "one" and "three", the obtained error is more significant. Finally, a comparison of the leakage inductance and rotor resistance parameters obtained from the locked-rotor tests are shown in Figures 5.25 and 5.26, respectively. For the leakage inductance, it can be seen that a relatively good agreement is obtained for benchmark motors "one", "two" and "three". Similar to the FEA comparisons, the influence of saturation on the leakage inductance can be observed, although the error for low voltage levels is larger. This is likely caused by material property variations. For benchmark motor "four", however, a large discrepancy between the framework and measurements is observed for all voltage levels. It is not exactly known why this discrepancy is so large. However, it was not observed in the comparisons against FEA. Additionally, relatively large discrepancies are also obtained for the rotor resistance of each benchmark motor. Since the presented values describe the rotor resistance at room temperature, it could be that the operating temperature of the rotor during the measurements was incorrectly estimated. On the other hand, it could also be that the conductivity of the rotor-cage material is lower than expected.

5.9 Extension of the IM analysis framework

The developed framework focuses on the calculation of the fundamental, steady-state motor performance. An overview of the phenomena that are accounted for during these calculations is provided in Section 5.2. However, it is also noted that a number of other side-effects may occur, which are currently not included in the framework. The influence of such effects on the performance of IMs has received a significant amount of attention in literature. In many research works, suggestions for design choices are made in order to reduce undesired phenomena.

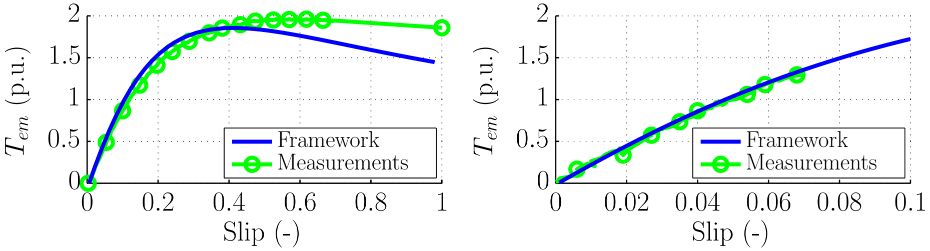

(a) Benchmark motor ”one” (b) Benchmark motor ”two”

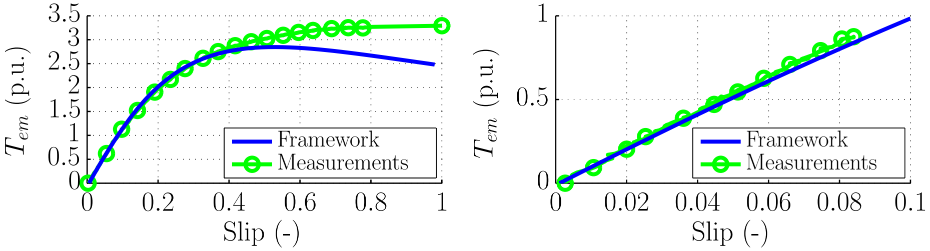

(c) Benchmark motor ”three” (d) Benchmark motor ”four”

Figure 5.19: IM analysis framework versus measurements: mechanical torque.

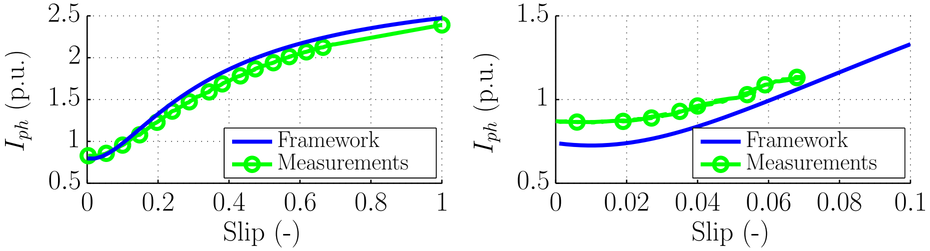

(a) Benchmark motor ”one” (b) Benchmark motor ”two”

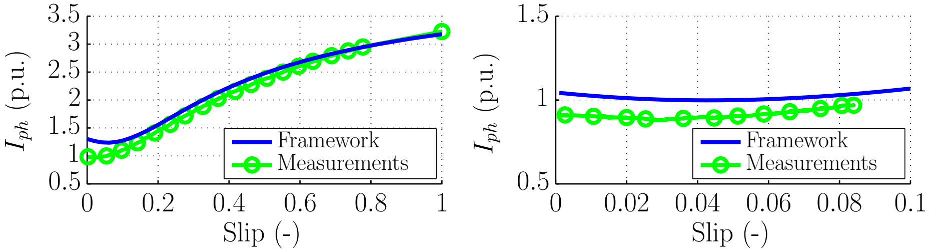

(c) Benchmark motor ”three” (d) Benchmark motor ”four”

Figure 5.20: IM analysis framework versus measurements: rms stator phase current.

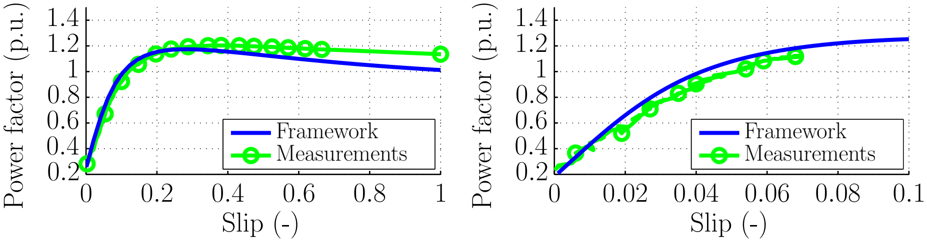

(a) Benchmark motor ”one” (b) Benchmark motor ”two”

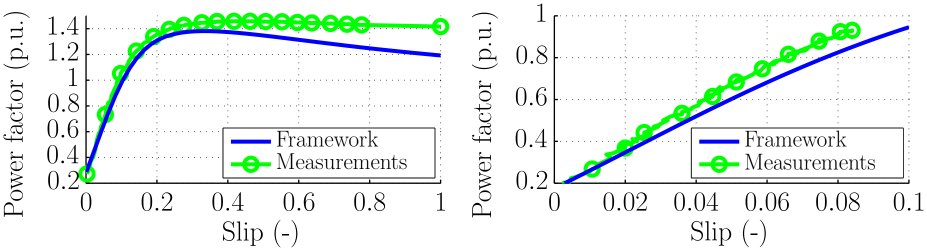

(c) Benchmark motor ”three” (d) Benchmark motor ”four”

Figure 5.21: IM analysis framework versus measurements: power factor.

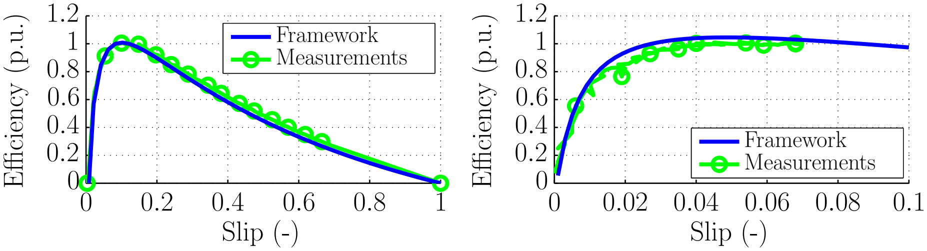

(a) Benchmark motor ”one” (b) Benchmark motor ”two”

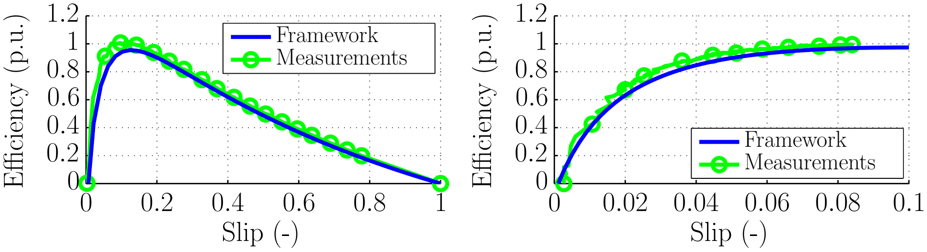

(c) Benchmark motor ”three” (d) Benchmark motor ”four”

Figure 5.22: IM analysis framework versus measurements: efficiency.

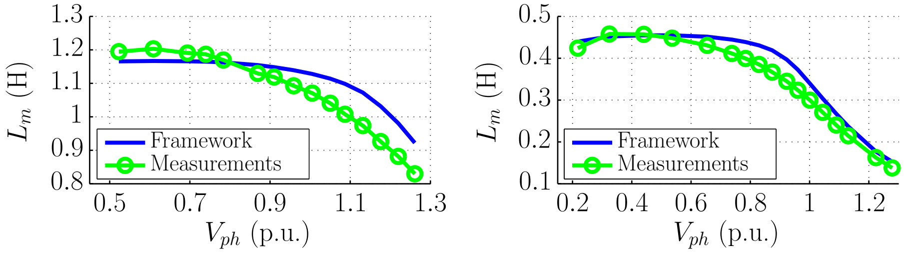

(a) Benchmark motor ”one” (b) Benchmark motor ”two”

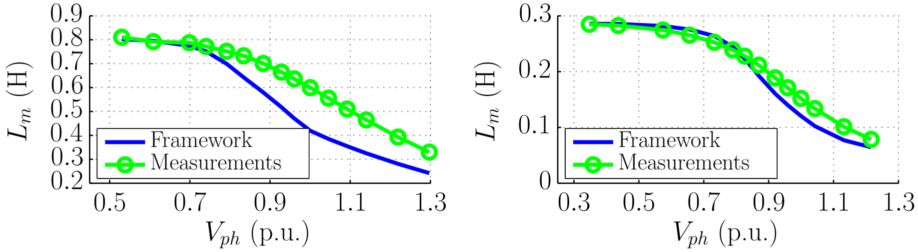

(c) Benchmark motor ”three” (d) Benchmark motor ”four”

Figure 5.23: IM analysis framework versus measurements: magnetizing inductance.

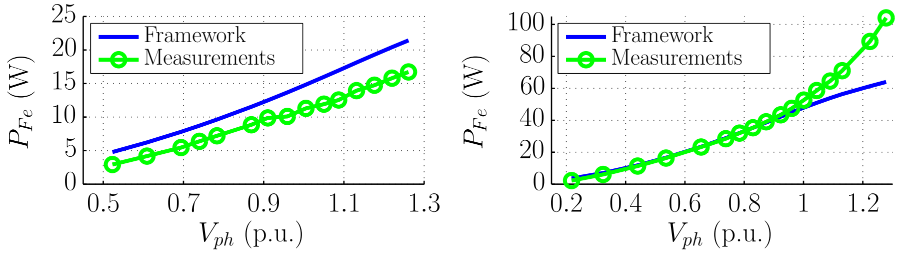

(a) Benchmark motor ”one” (b) Benchmark motor ”two”

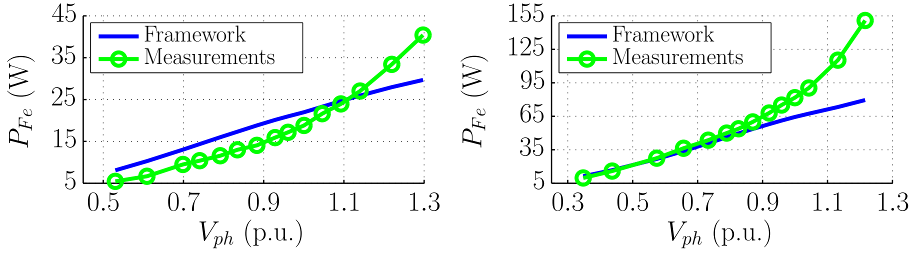

(c) Benchmark motor ”three” (d) Benchmark motor ”four”

Figure 5.24: IM analysis framework versus measurements: no-load iron losses.

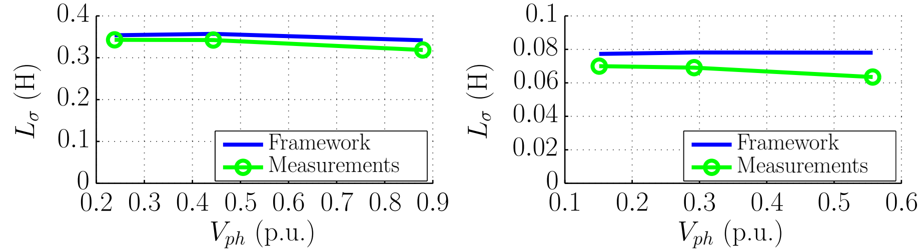

(a) Benchmark motor ”one” (b) Benchmark motor ”two”

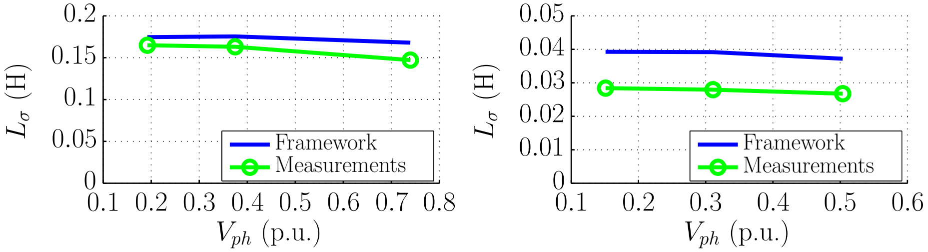

(c) Benchmark motor ”three” (d) Benchmark motor ”four”

Figure 5.25: IM analysis framework versus measurements: leakage inductance.

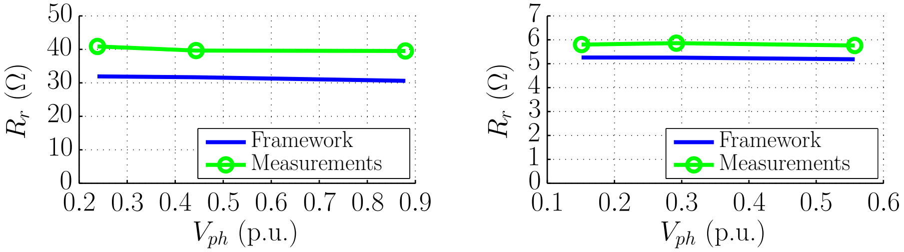

(a) Benchmark motor ”one” (b) Benchmark motor ”two”

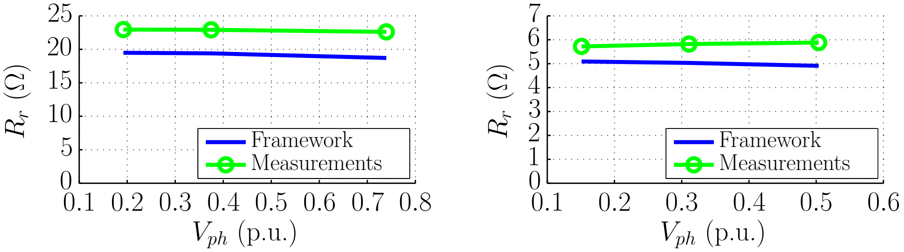

(c) Benchmark motor ”three” (d) Benchmark motor ”four”

Figure 5.26: IM analysis framework versus measurements: rotor resistance.

For example, rules to minimize the stray load losses in IMs have been proposed in [164] and a number of facts about parasitic torques, and how to deal with them, have been presented in [165]. However, these publications only show how to avoid certain effects, whereas FEA results generally show many effects all-in-one. This makes it difficult to analyse the exact cause of a phenomenon. On the other hand, (semi-)analytical models, such as the ones presented here, allow more control over the model itself. Therefore, they are very suitable to study specific effects in electric machines.

For example, in existing induction-motor theory, the influence of spatial air-gap harmonics on the steady-state torque-slip characteristic is often considered through a number of mechanically connected, harmonic induction machines [35, 37, 166]. Each of these harmonic machines represents a single spatial harmonic and, accordingly, has its own number of poles. Further, a time-harmonic rotor current is associated with each spatial harmonic, which can possibly lead to undesired parasitic torques and rotor Ohmic losses. Using the models presented in this thesis, the behavior is the harmonic machines can be estimated. An example of such an implementation is described in [67] for IMs with multi-layer rotors in Cartesian coordinates. Since the MMT model accounts for stator and rotor slotting, the influence of permeance harmonics on parasitic torques can also be studied. To fully utilize the capabilities of the presented models, extension of the IM analysis framework should be further investigated in future work.

Chapter 6

Harmonic modeling for Synchronous Reluctance Motors

The contents of this chapter are published in:

R. L. J. Sprangers, J. J. H. Paulides, B. L. J. Gysen, J. Waarma, and E. A. Lomonova, "Semi-analytical framework for synchronous reluctance motor analysis including finite soft-magnetic material permeability," *IEEE Trans. Magn.*, accepted: to be published.

6.1 Introduction

In this chapter, the capabilities and limitations of harmonic modeling for analysis of Synchronous Reluctance Motors (SynRMs) are investigated. First, however, a short introduction of this motor type is provided. The SynRM is a synchronous motor, which means that its rotor and the fundamental magnetic field produced by the stator winding are revolving in synchronism. The principles of its operation and control can be explained using dq-axis theory [167]. In Figure 6.1a, a simplified two-pole SynRM topology, with a three-phase stator windings and a soft-magnetic rotor, is shown. Due to the shape of the rotor, it provides a low-reluctance magnetic-flux path along the d-axis, whereas there is a high-reluctance magnetic-flux path along the q-axis. Consequently, when an external magnetizing field is applied, a reluctance torque starts acting on the rotor that tends to align the d-axis with the direction of the magnetizing field. Once aligned, the reluctance, observed by the source of the magnetizing field, is at its minimum, magnetic flux is maximized and the torque acting on the rotor reduced to zero.

To control the SynRM, the orientation of the stator magnetic field with respect to the d- and q-axis of the rotor should thus be regulated. The magnetomotive force (mmf) of each stator phase is represented on the axes A, B and C in the ABC stator reference frame, as shown in Figure 6.1a. For a given stator current distribution, the current on each ABC-axis can then be projected onto the dq-axis reference frame of the rotor using Park's transformation [167], given here in its amplitude invariant form by

$$I_d = \frac{2}{3}\left[\cos\left(\theta_r\right) I_A + \cos\left(\theta_r - \frac{3\pi}{2}\right) I_B + \cos\left(\theta_r + \frac{3\pi}{2}\right) I_C\right], \tag{6.1}$$

$$I_q = -\frac{2}{3}\left[\sin\left(\theta_r\right) I_A + \sin\left(\theta_r - \frac{3\pi}{2}\right) I_B + \sin\left(\theta_r + \frac{3\pi}{2}\right) I_C\right], \tag{6.2}$$

where θ_r is the angle between the A-axis of the ABC-reference frame and the d-axis of the dq reference frame. Furthermore, I_d and I_q are the d- and q-axis currents, respectively. Assuming that the stator phase currents vary sinusoidally in time with a phase shift of $2\pi/3$ rad between the phases and considering that the stator magnetic field and the rotor are in synchronism, I_d and I_q are time-invariant. Their resultant current vector, I_s, is shown in the vector diagram depicted by Figure 6.1b and represents the orientation of the stator magnetic field. The angle between I_s and the d-axis is denoted as the current angle, δ_c.

An expression for the torque produced by the SynRM in terms of I_s and δ_c is given by [168]

$$T_{em} = \frac{3}{4} p \left(L_d - L_q\right) \left|I_s\right|^2 \sin\left(2\delta_c\right), \tag{6.3}$$

where p is the number of pole pairs, and L_d and L_q are the d- and q-axis inductance, respectively. It can be seen that L_d should be significantly larger than

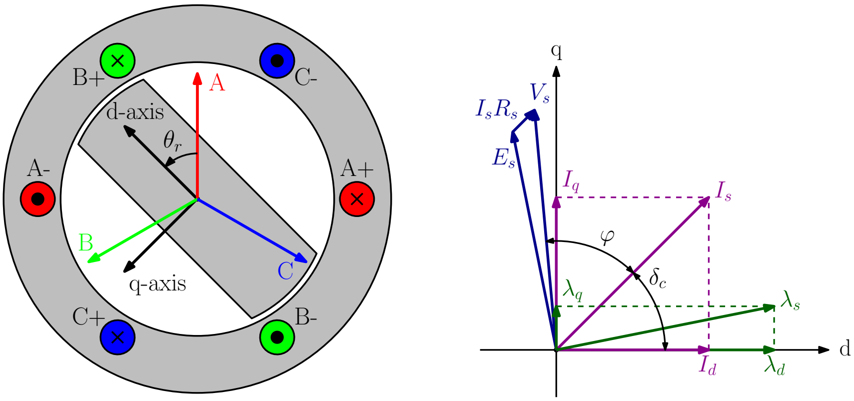

(a) (b)

Figure 6.1: Example of (a) a simplified two-pole SynRM and (b) its vector diagram.

L_q in order to produce torque, which corresponds to a low d-axis and high q-axis reluctance. If the soft-magnetic materials are assumed to be linear, L_d and L_q are independent of the current. For this case, T_{em} increases quadratically as a function of the current magnitude, $|I_s|$ and maximum torque production is obtained for $\delta_c = \pi/4$ rad. In practice, however, L_d decreases for increasing I_d due to saturation of the d-axis magnetic-flux path. The effect of d-axis saturation on L_q is small since the q-axis reluctance is already large. Therefore, maximum torque production is obtained for $\delta_c > \pi/4$ rad for saturated operating conditions.

For given I_d and I_q, the d- and q-axis flux linkage, λ_d and λ_q respectively, are given by

$$\lambda_d = L_d I_d, \tag{6.4}$$

$$\lambda_q = L_q I_q. \tag{6.5}$$

As shown in Figure 6.1b, λ_d and λ_q represent the stator flux linkage vector, λ_s, and can be used to obtain the induced stator voltage vector, E_s. Finally, after adding the voltage drop across the stator resistance, the stator voltage vector, V_s, is obtained. The angle between V_s and I_s is given by φ, such that the power factor is obtained as $\cos(\varphi)$. An expression for $\cos(\varphi)$ in terms of I_d, I_q, L_d and L_q is given by

$$\cos(\varphi) = \frac{(L_d - L_q) I_d I_q}{\sqrt{(L_d I_d)^2 + (L_q I_q)^2}\sqrt{I_d^2 + I_q^2}}. \tag{6.6}$$

Finally, for control purposes, $|I_s|$ and δ_c are selected according to the required motor performance and used to calculate reference values for I_d and I_q. The reference values are compared to the actual values of I_d and I_q, obtained from current and rotor-position measurements, and the difference is fed into a controller, e.g. a PI controller. The output of the controller represents the required d- and q-axis stator voltage, V_d and V_q respectively. Using Park's inverse transformation, V_d and V_q are then transformed to the ABC-stator reference frame and supplied as a reference for the power amplifier.

6.2 Modeling approach

An accurate prediction of the magnetic-field distribution inside the SynRM for a given excitation is important to obtain accurate performance predictions. As shown in the previous section, the magnetic reluctance of the stator and rotor soft-magnetic material can not be neglected, especially when small air-gap sizes are used. Following the approach used for IM analysis, a combination of the MMT and ALT approaches could be considered. Using a suitable polar representation of the complex SynRM geometry, an MMT model could be implemented to calculate L_q. In addition, an ALT model could be used to predict the magnetization behaviour of the d-axis. However, the nature of the ALT model would only allow for a global estimation of the soft-magnetic material saturation, not a local one. As a result, the distribution of the magnetic-flux density along the flux guides would not be physically correct, which is undesirable from a designer point of view. Also, the influence of cross-saturation on L_q due to d-axis flux would not be taken into account.

To obtain a more complete model, capable of predicting both L_d and L_q, the IRM modeling approach is used for the SynRM harmonic model. This approach still requires a polar representation of the SynRM geometry in order to divide it into regions, but the circumferential variation of the material permeability can be taken into account. Moreover, the magnetic-field distribution inside the entire motor is obtained, including the soft-magnetic parts. The implementation of the model is described based on a parameterized example of the geometry. Also, a benchmark motor is defined based on the considered parameters and used to validate the harmonic-modeling results against FEA predictions.

6.3 Geometry and benchmark definitions

The geometry of a typical low-power SynRM with Transverse Laminated Anisotropy (TLA) rotor can roughly be divided into the following parts:

1. The stator core, consisting of a yoke, teeth and tooth tips
2. The stator slots with the stator windings
3. The stator slot openings
4. The air gap between the stator and rotor
5. The rotor inner web
6. The rotor flux guides
7. The rotor flux barriers
8. The rotor cut-out (optional)
9. The connection bridges between the rotor flux guides

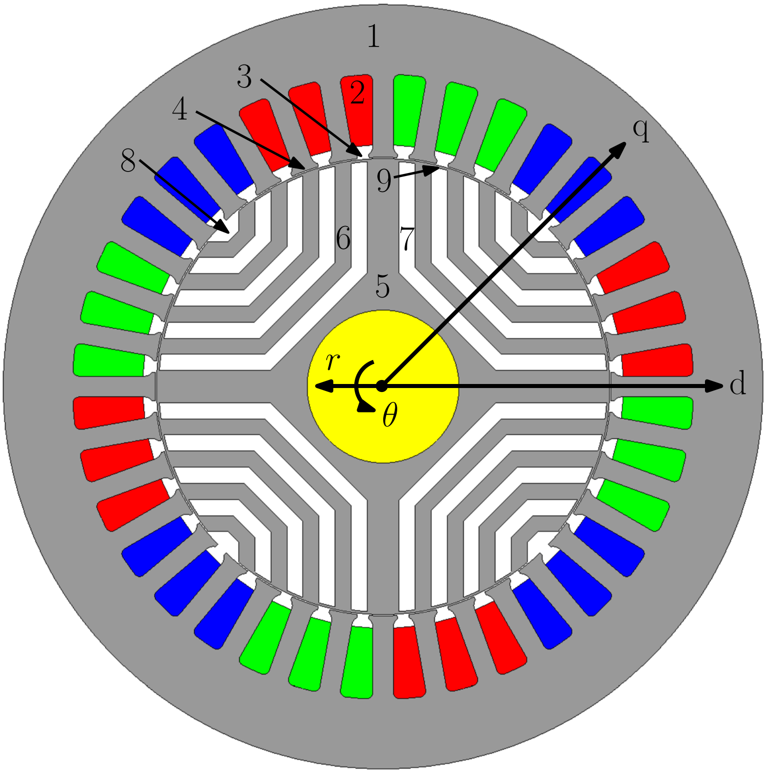

Figure 6.2: Cross-section geometry of the four-pole benchmark SynRM topology.

An example of the cross-section geometry of a SynRM is shown for the benchmark topology depicted in Figure 6.2. It can be seen that the stator is similar to the stator of the IM, whereas the rotor is completely different. On the one hand, the inner web and the rotor flux guides are made of soft-magnetic material and provide a low-reluctance path for the d-axis magnetic flux. On the other hand, the rotor cut-out and rotor flux barriers generally consist of air in order to provide a high-reluctance for the q-axis magnetic flux. Finally, thin soft-magnetic bridges are used to connect the rotor flux guides and provide mechanical stability to the rotor. The disadvantage of these bridges is that they increase the q-axis flux, and thereby L_q. However, the influence on the motor performance is limited, since only a small portion of magnetic flux is required to saturate the bridges. Also, the bridges tend to smoothen the air-gap flux-density, leading to a considerably lower torque ripple.

6.3.1 SynRM geometry parameters

Based on the typical SynRM geometry, a number of geometric parameters is defined. An overview of these parameters is shown in Table 6.1, including their values for the benchmark topology discussed in Section 6.3.2. Additionally, a graphical overview of the geometry parameters is shown in Figure 6.3. For a given rotor position, Δ_θ, the orientation of the stator magnetic field is determined by the distribution of the phase currents, which is given by

$$I_A = \sqrt{2} I_{ph} \cos\left(\delta_c + \theta_{offset} + \frac{\Delta_\theta}{p}\right), \tag{6.7}$$

$$I_B = \sqrt{2} I_{ph} \cos\left(\delta_c + \theta_{offset} - \frac{2\pi}{3} + \frac{\Delta_\theta}{p}\right), \tag{6.8}$$

$$I_C = \sqrt{2} I_{ph} \cos\left(\delta_c + \theta_{offset} + \frac{2\pi}{3} + \frac{\Delta_\theta}{p}\right). \tag{6.9}$$

The parameter θ_{offset} represents the electrical offset between the magnetic field produced by phase A and the rotor d-axis for $\Delta_\theta = 0$. For example, θ_{offset} is calculated for the benchmark topology as

$$\theta_{offset} = -\frac{pq\theta_{sp,s}}{2} - \frac{\pi}{2} = -\frac{2\pi}{3}\,\text{rad}. \tag{6.10}$$

6.3.2 Benchmark topology

The considered benchmark topology, shown in Figure 6.2, is a four-pole SynRM with 36 stator slots, containing a single layer, distributed, three-phase winding. The rms value of the total current per slot is given by $z_Q I_N$. Its rotor consists of an inner web, four flux guides, four flux barriers and a cut-out. The widths of these elements are equally distributed, and given in Table 6.1.

Table 6.1: Parameters of the SynRM geometry

Symbol	Value	Unit	Description
r_{sh}	15	mm	Shaft radius
r_{si}	45	mm	Stator inner radius
h_r	29.75	mm	Rotor lamination height
h_w	3.0	mm	Inner web height
b_w	3.2	mm	Inner web width
b_{bq}^n	3.0	mm	n^{th} barrier width, q-axis
b_{gq}^n	3.0	mm	n^{th} guide width, q-axis
b_{bd}^n	3.2	mm	n^{th} barrier width, d-axis
b_{gd}^n	3.2	mm	n^{th} guide width, d-axis
h_c	2.75	mm	Cut-out height
h_{ss}	16.3	mm	Stator slot height
h_{ys}	13.7	mm	Stator yoke height
h_{os}	0.64	mm	Stator slot opening height
b_{os}	2.3	mm	Circumferential stator slot opening width
b_{ds}	4.1	mm	Stator tooth width
$z_Q I_N$	180	A-t	Nominal rms stator excitation
p	2	-	Number of pole pairs
l_{stk}	120	mm	Stack length

To perform validation calculations, two magnetostatic, 2D FEA models were implemented for the benchmark topology. The first FEA model represents the actual SynRM geometry, as shown in Figure 6.2, whereas the second FEA model represents a polar representation of the SynRM geometry. Furthermore, the magnetic permeability of the soft-magnetic material is assumed linear in the current implementation of the harmonic SynRM model and therefore, the connection bridges between the rotor flux guides are disregarded. The same assumptions are applied to the FEA models, where I_{ph}, δ_c and Δ_θ are variable, such that the motor performance can be evaluated for various operating conditions.

6.4 The inhomogeneous region model

To implement the IRM model, the SynRM geometry is divided into a finite number of radial regions. Within each region, material properties and excitation sources should only vary in the circumferential direction. For the geometry shown in Figure 6.3, a large number of thin regions would be required to approximate the actual geometry. Consequently, the size of the resulting matrix equation and the required computation time of this model would be prohibitive. Therefore, it is more practical to use a polar representation of the SynRM geometry. For the one depicted in Figure 6.3, such a polar representation is shown in Figure 6.4.

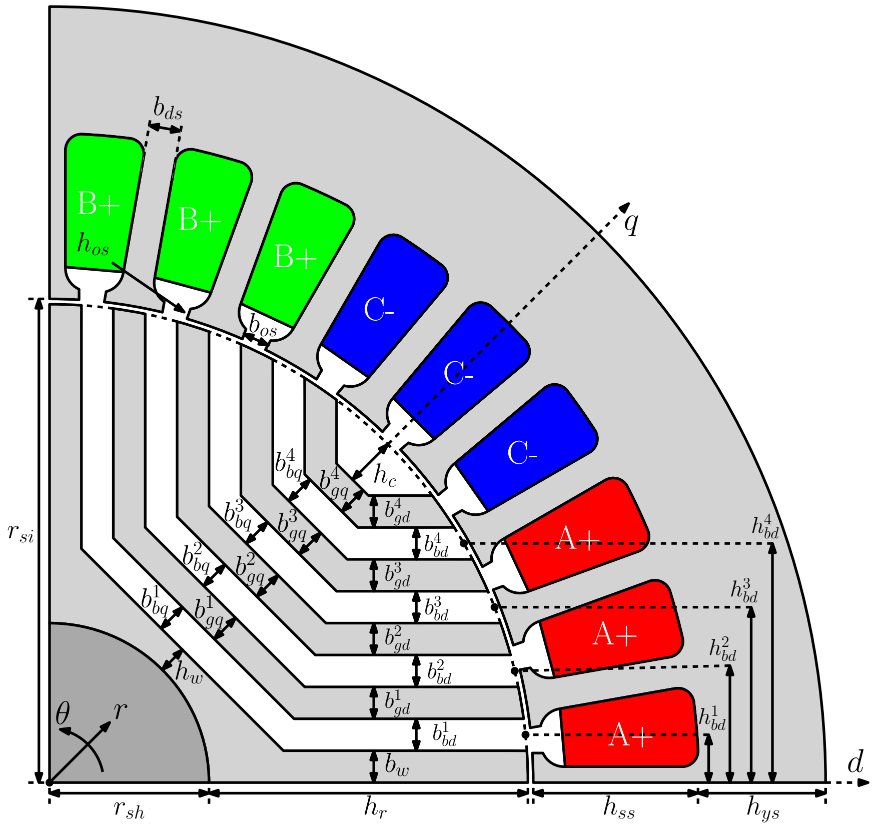

Figure 6.3: Parameters of the actual SynRM geometry.

6.4.1 Model representation of the geometry

To define the polar representation, several parameters are introduced in Figure 6.4. Their values can be calculated from the parameters used in Figure 6.3. For the stator, the fixed tooth width is replaced by a fixed tooth angle, θ_{ds}, calculated as

$$\theta_{ds} = \frac{2b_{ds}}{2r_{si} + h_{os} + h_{ss}}, \tag{6.11}$$

whereas the fixed slot opening width is replaced by a fixed slot opening angle angle, θ_{so}, calculated as

$$\theta_{os} = \frac{b_{os}}{r_{si}}. \tag{6.12}$$

The curved corners of the slots are replaced by straight corners, and the current density is considered to be homogeneously distributed along the entire slot underneath the tooth tips.

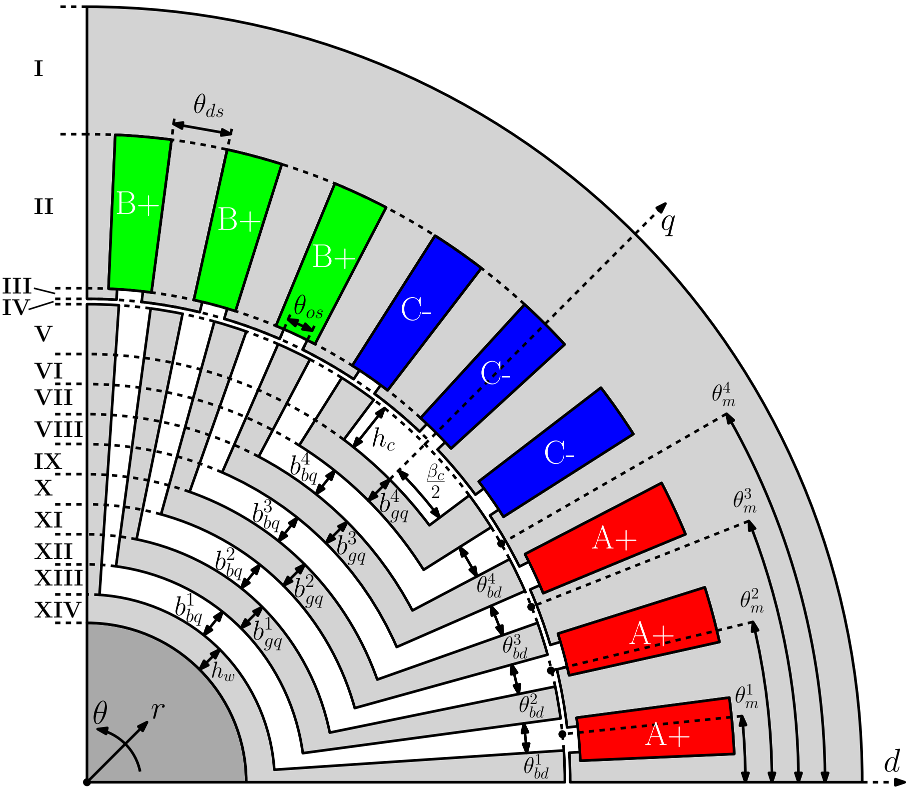

Figure 6.4: Parameters of the SynRM polar geometry representation.

For the rotor, the flux barriers and guides are reshaped into circumferential and radial segments. All circumferential segments follow a circumferential arc around the origin and are radially distributed according to the depth of the flux barriers and guides in the actual geometry, as shown in Figure 6.4. All radial segments follow a radial line starting from the origin and are circumferentially distributed according to the angles indicated in Figure 6.4. The rotor cut-out angle, β_c, is calculated as

$$\beta_c = 2\left(\frac{\pi}{2p} - \arcsin\left(\frac{\sum_{\upsilon=1}^{\Upsilon_{bar}}\left[b_{gd}^{\upsilon} + b_{bd}^{\upsilon}\right] + b_w}{r_{si} - g}\right)\right), \tag{6.13}$$

where Υ_{bar} represents the number of flux barriers or guides in the rotor. The average angle of the υ_{th} radial barrier segment, θ_{bd}^{υ}, is obtained as

$$\theta_{bd}^{\upsilon} = \frac{2b_{bd}^{\upsilon}}{r_{si} - g + r_b^{\upsilon}}, \tag{6.14}$$

where r_b^{υ} is the outer radius of the υ^{th} circumferential barrier segment, calculated

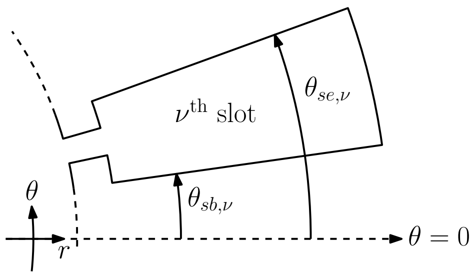

Figure 6.5: Starting and ending angles of the ν^{th} slot, $\theta_{sb,\nu}$ and $\theta_{se,\nu}$ respectively.

as

$$r_b^\upsilon = \begin{cases} r_{sh} + h_w + b_{bq}^1 & \upsilon = 1, \\ r_{sh} + h_w + \sum_{\upsilon'=1}^{\upsilon-1} b_{gq}^{\upsilon'} + \sum_{\upsilon'=1}^{\upsilon} b_{bq}^{\upsilon'} & \upsilon > 1. \end{cases} \tag{6.15}$$

Finally, the circumferential midpoint angle of the υ^{th} radial barrier segment, represented by θ_m^υ in Figure 6.4, is calculated as

$$\theta_m^\upsilon = \arcsin\left(\frac{h_{bd}^\upsilon}{r_{ro}}\right), \tag{6.16}$$

where h_{bd}^υ is the average barrier height in the d-axis, as indicated in Figure 6.3, given by

$$h_{bd}^\upsilon = \begin{cases} b_w + \frac{b_{bd}^1}{2} & \upsilon = 1, \\ b_w + \sum_{\upsilon'=1}^{\upsilon-1} \left[b_{bd}^{\upsilon'} + b_{gd}^{\upsilon'}\right] + \frac{b_{bd}^\upsilon}{2} & \upsilon > 1. \end{cases} \tag{6.17}$$

Based on the polar geometry representation, a layered region-division is defined. As shown in Figure 6.4, regions I to III describe the stator yoke, the stator teeth/slots and the stator tooth tips/slot openings, whereas region IV represents the air gap of the motor. Furthermore, all remaining regions represent the SynRM rotor. The total number of model regions thus depends on the number of considered flux barriers and guides. For the benchmark topology, a total of 14 model regions is considered.

6.4.2 Magnetic-field solution

In Section 2.4, general expressions are derived for the magnetic-field solution of an inhomogeneous region in a polar coordinate system. For the SynRM model, no permanent-magnet materials are considered and therefore, $\mathbf{G}_2^k = \mathbf{0}$ for each region k. The Fourier coefficients of A_z^k are then given in matrix form by

$$\mathbf{A}_z^k = \mathbf{W}^k r^{\boldsymbol{\lambda}^k} \mathbf{a}^k + \mathbf{W}^k r^{-\boldsymbol{\lambda}^k} \mathbf{b}^k + r^2 \mathbf{G}_1^k, \tag{6.18}$$

whereas the Fourier coefficients of B_r^k and B_θ^k are given in matrix form by

$$\mathbf{B}_r^k = -j\frac{1}{r}\left(\mathbf{K}_\theta \mathbf{W}^k r^{\boldsymbol{\lambda}^k}\mathbf{a}^k + \mathbf{K}_\theta \mathbf{W}^k r^{-\boldsymbol{\lambda}^k}\mathbf{b}^k + r^2 \mathbf{K}_\theta \mathbf{G}_1^k\right), \tag{6.19}$$

$$\mathbf{B}_\theta^k = -\mathbf{W}^k \boldsymbol{\lambda}^k r^{\boldsymbol{\lambda}^k - 1}\mathbf{a}^k + \mathbf{W}^k \boldsymbol{\lambda}^k r^{-\boldsymbol{\lambda}^k - 1}\mathbf{b}^k - 2r\mathbf{G}_1^k. \tag{6.20}$$

Only region II contains a current excitation source, such that $\mathbf{G}_1^k$ is given by

$$\mathbf{G}_1^k = \begin{cases} -\left(4\mathbf{I} - \mathbf{V}^{\mathrm{II}}\right)^{-1} \boldsymbol{\mu}_{c,\theta}^{\mathrm{II}} \mathbf{J}_z^{\mathrm{II}} & \text{for } k = \mathrm{II}, \\ \mathbf{0} & \text{otherwise}, \end{cases} \tag{6.21}$$

where $\mathbf{J}_z^{\mathrm{II}}$ denotes the Fourier-coefficient matrix of the current-density distribution. For each spatial harmonic n, the corresponding element in $\mathbf{J}_z^{\mathrm{II}}$ is calculated by summing the contributions of each stator phase as

$$J_{zn}^{\mathrm{II}} = \sum_{x=A,B,C} C_{zn,x} I_x, \tag{6.22}$$

where I_x is the current of phase x and $C_{zn,x}$ is obtained for each phase as

$$C_{zn,A} = C_{per} \sum_{\forall \nu \in N_A} \frac{c_{dir}^{\nu} z_{Q,s}}{2\pi n j S_{ss}} \left(e^{jnC_{per}\theta_{se,\nu}} - e^{jnC_{per}\theta_{sb,\nu}}\right), \tag{6.23}$$

$$C_{zn,B} = C_{per} \sum_{\forall \nu \in N_B} \frac{c_{dir}^{\nu} z_{Q,s}}{2\pi n j S_{ss}} \left(e^{jnC_{per}\theta_{se,\nu}} - e^{jnC_{per}\theta_{sb,\nu}}\right), \tag{6.24}$$

$$C_{zn,C} = C_{per} \sum_{\forall \nu \in N_C} \frac{c_{dir}^{\nu} z_{Q,s}}{2\pi n j S_{ss}} \left(e^{jnC_{per}\theta_{se,\nu}} - e^{jnC_{per}\theta_{sb,\nu}}\right). \tag{6.25}$$

Here, it is assumed that each slot contains conductors of only one phase. For the ν^{th} stator slot, $\theta_{sb,\nu}$ and $\theta_{se,\nu}$ are the beginning and ending angles between which the slot is spanned, as depicted in Figure 6.5. The surface area of the stator slots, S_{ss}, is calculated as

$$S_{ss} = \left(\frac{\pi}{Q_s} - \frac{\theta_{ds}}{2}\right)\left(\left(r_o^{\mathrm{II}}\right)^2 - \left(r_i^{\mathrm{II}}\right)^2\right), \tag{6.26}$$

where r_o^{II} and r_i^{II} represent the outer and inner radius of region II.

Further, each region has a certain permeability distribution. For regions I and IV, the magnetic permeability is assumed homogeneous and therefore, no permeability Toeplitz matrices are required. This also holds for the most inner region (region XIV for the benchmark topology). For all other regions, however, the magnetic permeability varies as a function of θ. To calculate the Fourier-series coefficients of an inhomogeneous region, its relative permeability distribution is divided into K sections. An example of such a division is shown in Figure 6.6. Each section κ is characterised by its relative permeability value, μ_r^κ, and its circumferential position. The latter is represented by the beginning and ending

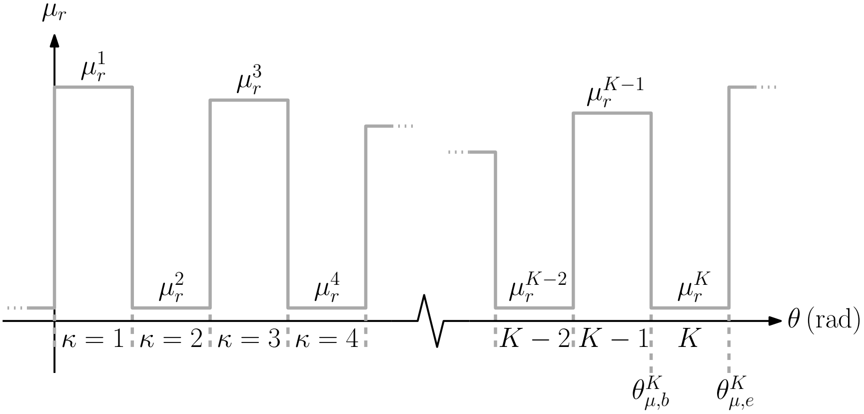

Figure 6.6: Example of the relative permeability distribution, divided into K-sections.

angles, $\theta_{\mu,b}^\kappa$ and $\theta_{\mu,e}^\kappa$, respectively, as illustrated in Figure 6.6 for section K. The contribution of each section to the Fourier-series coefficient of the n^{th} spatial harmonic is given by

$$\hat{\mu}_{r,n}^\kappa = \begin{cases} \frac{\mu_r^\kappa}{2\pi n j}\left(e^{jnC_{per}\theta_{\mu,e}^\kappa} - e^{jnC_{per}\theta_{\mu,b}^\kappa}\right) & \text{for } n \neq 0, \\ C_{per}\frac{\theta_{\mu,e}^\kappa - \theta_{\mu,b}^\kappa}{2\pi} & \text{for } n = 0, \end{cases} \tag{6.27}$$

where $\hat{\mu}_{r,0}^\kappa$ represents the contribution of section κ to the average value of μ_r. To obtain the Fourier coefficients of μ_r for the entire region, the coefficients of each section are summed as

$$\hat{\mu}_{r,n} = \sum_{\kappa=1}^{K} \hat{\mu}_{r,n}^\kappa. \tag{6.28}$$

Finally, (6.27) and (6.28) are used to calculate $\hat{\mu}_{r,n}$ for n ranging from $-2N_{sh}$ to $2N_{sh}$. The resulting relative permeability coefficients are multiplied by μ_0 to obtain the permeability coefficients. Then, subsets of the permeability coefficient array are used to fill each row of the radial permeability Toeplitz matrix, $\boldsymbol{\mu}_{c,r}$. A similar approach is also used to obtain the circumferential permeability Toeplitz matrix, $\boldsymbol{\mu}_{c,\theta}$. However, in this case, the reciprocal of the permeability distribution is used and μ_r^κ is replaced by $1/\mu_r^\kappa$ in (6.27). The resulting coefficient array is multiplied by $1/\mu_0$ and its subsets are used to fill the inverse circumferential Toeplitz matrix, $\boldsymbol{\mu}_{r,\theta}^{rec}$. If required, $\boldsymbol{\mu}_{c,\theta}$ is then obtained by inverting $\boldsymbol{\mu}_{r,\theta}^{rec}$.

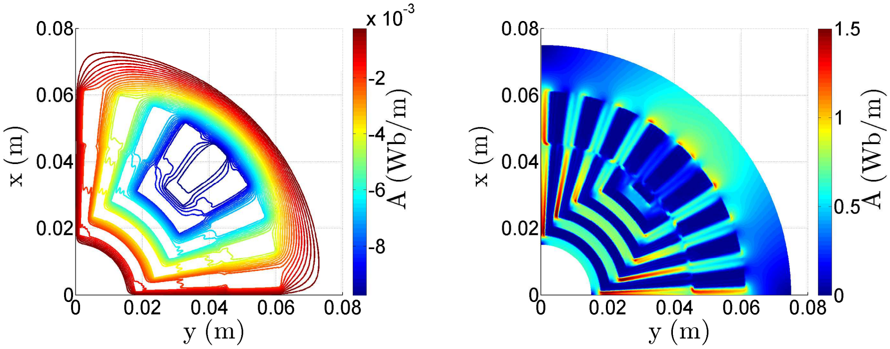

(a) (b)

Figure 6.7: Visualization of (a) the magnetic-flux-line distribution and (b) the magnetic-flux-density distribution in the polar geometry representation predicted by the harmonic model for a current angle of 0 rad with respect to the d-axis.

6.4.3 Magnetic-field validation

The proposed model is implemented for the benchmark topology and used to predict the magnetic-field distribution using $N_{sh} = 80$. Firstly, the stator is excited with the nominal current and $\delta_c = 0$ rad, such that only d-axis current is produced. The relative permeability of the soft-magnetic material, $\mu_{r,iron}$, is set to 1000. The resulting distributions of the magnetic-flux lines and the magnetic-flux density are shown in Figure 6.7. It can be seen that the magnetic flux is mostly confined to the soft-magnetic material of the motor.

Secondly, δ_c is increased to $\pi/4$ rad and the magnetic-field distribution is predicted for $\mu_{r,iron} = 1000$ and $\mu_{r,iron} = 100$. Similar calculations are also performed using the FEA model of the actual motor geometry. A comparison of the results is shown in Figure 6.8 in terms of radial air-gap flux-density. It can be seen that a relatively good match is obtained between the FEA predictions and the harmonic modeling results. Small deviations can be attributed to the simplified polar representation of the geometry and the finite number of harmonics used in the harmonic model.

6.5 Performance calculation and validation

To validate the SynRM harmonic model, simulations are performed on the benchmark topology for a fixed set of operating conditions. The current in the stator windings is calculated using (6.7) to (6.9), whereas I_{ph} is set to its nominal value. Further, δ_c is fixed to $\pi/4$ rad in order to generate maximum torque, whereas Δ_θ

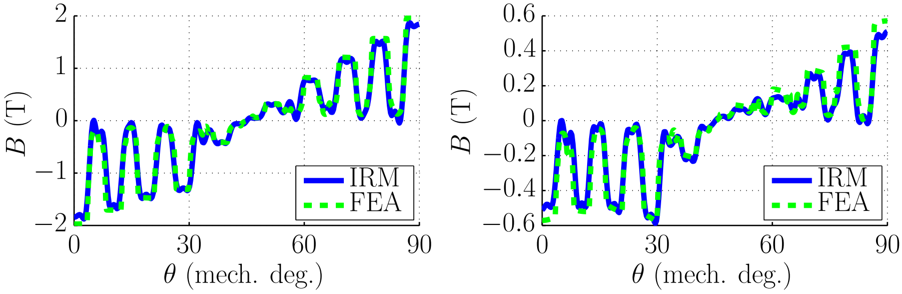

(a) (b)

Figure 6.8: Radial magnetic-flux density in the air gap calculated by the harmonic model for the polar geometry representation and by the FEA model of the actual geometry for a current angle of $\pi/4$ rad using a relative magnetic permeability of (a) $\mu_{r,iron} = 1000$ and (b) $\mu_{r,iron} = 100$.

is increased from 0 up to 30°in steps of 0.5°. For each rotor step, the inductances L_d and L_q and the electromagnetic torque, T_{em}, are calculated. All calculations are performed with three different models, namely the harmonic model, the FEA model of the polar geometry representation and the FEA model of the actual geometry representation.

6.5.1 Flux linkage and inductance

The flux linkage of the ν^{th} stator slot, λ_{ss}^{ν}, is calculated using (3.35). For the given magnetic-field solution, evaluating (3.35) reduces the expression for λ_{ss}^{ν} to

$$\lambda_{ss}^{\nu} = \frac{z_{Q,s} l_{sl}}{S_{ss}} \sum_{n=-N_{sh}}^{N_{sh}} \left[-\frac{1}{jn} C_{zn} \left(e^{-jn\theta_{se,\nu}} - e^{-jn\theta_{sb,\nu}} \right) \right], \tag{6.29}$$

where $l_{sl} = l_{stk} + 2\left(r_{si} - r_{ro}\right)$ is the effective stack length of the motor and the coefficient C_{zn} is given in matrix form by

$$\mathbf{C}_z = \mathbf{W}^k \frac{1}{2\mathbf{I} + \boldsymbol{\lambda}^k} \left(\left(r_o^k\right)^{2\mathbf{I}+\boldsymbol{\lambda}^k} - \left(r_i^k\right)^{2\mathbf{I}+\boldsymbol{\lambda}^k} \right) \mathbf{a}^k \tag{6.30}$$

$$+ \mathbf{W}^k \frac{1}{2\mathbf{I} - \boldsymbol{\lambda}^k} \left(\left(r_o^k\right)^{2\mathbf{I}-\boldsymbol{\lambda}^k} - \left(r_i^k\right)^{2\mathbf{I}-\boldsymbol{\lambda}^k} \right) \mathbf{b}^k \tag{6.31}$$

$$+ \frac{1}{4} \left(\left(r_o^k\right)^4 - \left(r_i^k\right)^4 \right) \mathbf{G}_1^k + \frac{1}{3} \left(\left(r_o^k\right)^3 - \left(r_i^k\right)^3 \right) \mathbf{G}_2^k. \tag{6.32}$$

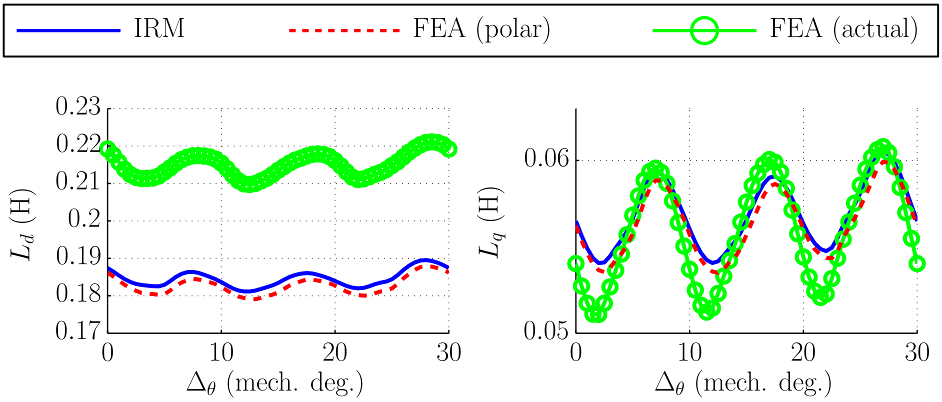

(a) (b)

Figure 6.9: Inductance of (a) the d-axis, L_d, and (b) the q-axis, L_q, calculated by the IRM model and FEA for $\mu_{r,iron} = 100$.

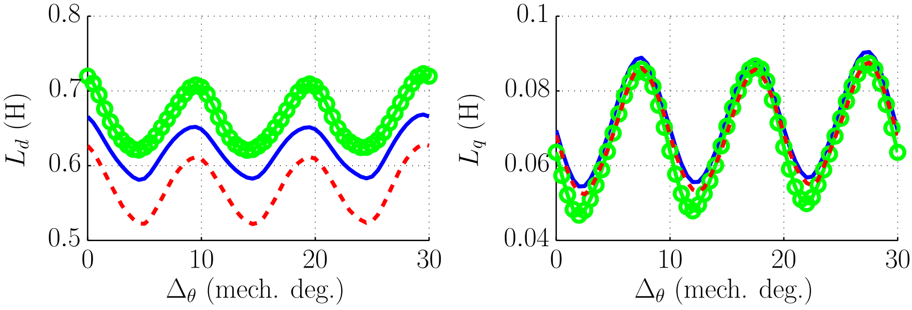

(a) (b)

Figure 6.10: Inductance of (a) the d-axis, L_d, and (b) the q-axis, L_q, calculated by the IRM model and FEA for $\mu_{r,iron} = 1000$.

For each stator phase, the flux linkage is then obtained as

$$\lambda_A = C_{per} \sum_{\forall \nu \in N_A} c_{dir}^{\nu} \lambda_{ss}^{\nu}, \tag{6.33}$$

$$\lambda_B = C_{per} \sum_{\forall \nu \in N_B} c_{dir}^{\nu} \lambda_{ss}^{\nu}, \tag{6.34}$$

$$\lambda_C = C_{per} \sum_{\forall \nu \in N_C} c_{dir}^{\nu} \lambda_{ss}^{\nu}. \tag{6.35}$$

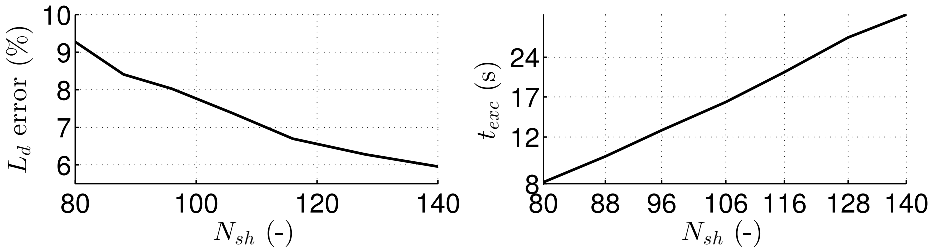

(a) (b)

Figure 6.11: The number of spatial harmonics versus (a) the error in d-axis inductance (linear scale) and (b) the required computation time (logarithmic scale).

Using Park's transformation, λ_d and λ_q are calculated from λ_A, λ_B and λ_C as

$$\lambda_d = \frac{2}{3}\left[\cos\left(\theta_r\right)\lambda_A + \cos\left(\theta_r - \frac{3\pi}{2}\right)\lambda_B + \cos\left(\theta_r + \frac{3\pi}{2}\right)\lambda_C\right], \tag{6.36}$$

$$\lambda_q = -\frac{2}{3}\left[\sin\left(\theta_r\right)\lambda_A + \sin\left(\theta_r - \frac{3\pi}{2}\right)\lambda_B + \sin\left(\theta_r + \frac{3\pi}{2}\right)\lambda_C\right], \tag{6.37}$$

where the angle θ_r is calculated as

$$\theta_r = p\left(\Delta_\theta - \frac{q\theta_{sp,s}}{2}\right). \tag{6.38}$$

The currents I_d and I_q are calculated using (6.1) and (6.2) using the same value of θ_r. Finally, L_d and L_q are obtained using (6.4) and (6.5).

To assess the accuracy of L_d and L_q calculated by the harmonic model, their values are calculated for various rotor positions and validated against FEA predictions. A comparison of the results is shown in Figures 6.9 and 6.10. For $\mu_{r,iron} = 100$, it can be seen that a good agreement is obtained between the harmonic model and the FEA model of the polar geometry. However, in comparison to the FEA model of the actual geometry, an error of approximately 15% is observed for L_d, whereas the maximum error in L_q is limited to 6%. The origin of these discrepancies is attributed to the polar geometry representation, which leads to longer and more narrow rotor flux guides.

Further, it can be seen that L_d deviates from both FEA simulations for $\mu_{r,iron} = 1000$. The error with respect to the FEA model of the polar geometry is attributed to the truncation of the complex Fourier series. Additional simulations have been performed for various values of N_{sh}. The resulting error in L_d, with respect to the FEA model of the polar geometry, is shown in Figure 6.11a. It can be seen that the error decreases for increasing N_{sh}. Additionally, a comparison of the required calculation time is shown in Figure 6.11b on a logarithmic scale. It can be seen that the calculation time is relatively large, even for $N_{sh} = 80$. Moreover, it increases approximately quadratically as a function of N_{sh}.

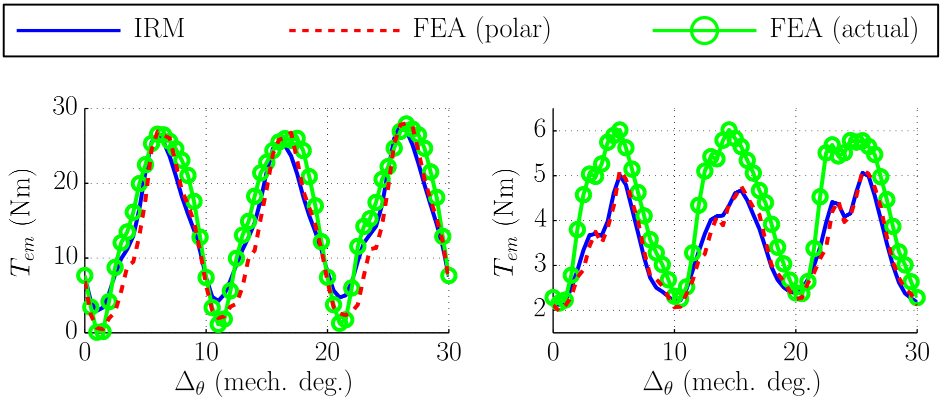

(a) (b)

Figure 6.12: Electromagnetic torque calculated at various rotor positions using MST for (a) $\mu_{r,iron} = 1000$ and (b) $\mu_{r,iron} = 100$.

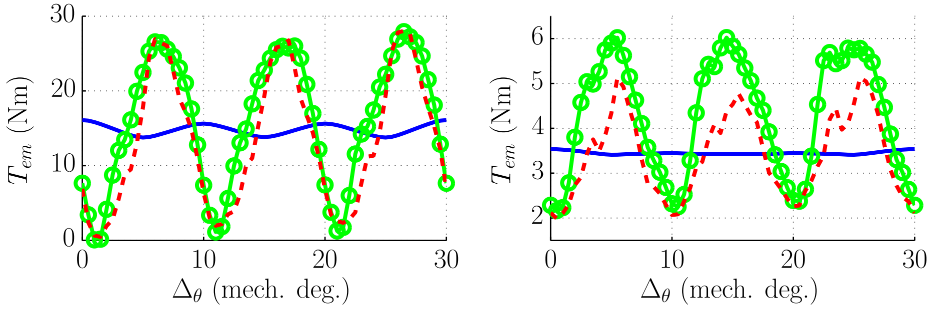

(a) (b)

Figure 6.13: Electromagnetic torque calculated at various rotor positions using L_d and L_q for (a) $\mu_{r,iron} = 1000$ and (b) $\mu_{r,iron} = 100$.

6.5.2 Electromagnetic torque

The electromagnetic torque of the SynRM can either be calculated by means of Maxwell's Stress Tensor or using (6.3). In the first case, T_{em} is expressed for the given magnetic-field solution as

$$T_{em} = -\frac{\pi l_{sl}}{\mu_0} \sum_{n=-N_{sh}}^{N_{sh}} \left[\mathrm{Im}(X_n)\,\mathrm{Re}(Y_n) + \mathrm{Im}(X_n)\,\mathrm{Re}(Y_{-n}) \right.$$
$$\left. - \mathrm{Re}(X_n)\,\mathrm{Im}(Y_n) + \mathrm{Re}(X_n)\,\mathrm{Im}(Y_{-n})\right], \qquad (6.39)$$

where

$$X_n = nC_{per} r_{g,m}^{(nC_{per})} a_n + nC_{per} r_{g,m}^{(-nC_{per})} b_n, \tag{6.40}$$

$$Y_n = nC_{per} r_{g,m}^{(nC_{per})} a_n - nC_{per} r_{g,m}^{(-nC_{per})} b_n, \tag{6.41}$$

where $r_{g,m}$ is the radius at the middle of the air gap. A comparison between FEA predictions and the calculation results obtained from the harmonic model using MST is presented in Figure 6.12. It can be seen that a relatively good match is obtained between the harmonic model and the FEA model of the polar geometry for $\mu_{r,iron} = 100$. However, as already suggested by the error obtained for the d- and q-axis inductances, the FEA model of the actual geometry shows a significant discrepancy with respect to the harmonic model. In terms of average torque, the error between the harmonic model and the polar FEA geometry is approximately 1%, whereas the error with respect to the actual FEA geometry is 20%. Furthermore, T_{em} obtained for $\mu_{r,iron} = 1000$ shows a moderate agreement between the models. The average value of T_{em} obtained from the harmonic model deviates less than 10% from the values predicted by the FEA models. Finally, in Figure 6.13, T_{em} calculated using (6.3) is compared to the FEA predictions. It can be seen that this method does not properly include the torque ripple. The average values, however, show the same error with respect to the FEA calculations as the average value of torque calculated using the MST.

To obtain a more accurate prediction of the inductance and electromagnetic torque, improvement of the polar geometry representation should be considered. For example, the polar transformation could select equal average flux-guide width instead of equal average flux-barrier width. Such an approach will most likely lead to a better prediction of L_d, although the accuracy of L_q will probably decrease. Alternatively, the relative permeabilities of the modeled materials could be varied artificially throughout the rotor. This will lead to an improved representation for the reluctance of the rotor flux-barriers and guides, and consequently, to more accurate calculation results. Such a method will be further investigated in future research.

Chapter 7

Conclusions, contributions and recommendations

7.1 Conclusions

During the design of electric machines, engineers generally need to select suitable values for a large number of parameters. The time available to perform this task is usually limited and should therefore be used as efficiently as possible. On the one hand, machine designers thus require fast and accurate models to predict the machine performance for a large set of parameter combinations. On the other hand, their modeling tools should also provide physical insight in the behaviour of the machine, such that the design space can be reduced systematically. Various modeling approaches have been proposed in literature, although Finite Element Analysis (FEA) remains one of the most popular choices. This is mainly due to its ability to accurately include nonlinear magnetic material-characteristics and its flexibility with respect to complex geometrical shapes. In recent literature, however, harmonic modeling is proposed as a suitable alternative to FEA, both in terms of accuracy and computational efficiency. The development and research of this modeling technique can only be undertaken considering detailed physical insight in electrical machines. Besides a fast and accurate modeling tool, harmonic modeling can thus also provide engineers and researchers with an increased understanding of the machine under study. Therefore, the applicability of harmonic modeling to analyse the performance of induction motors (IMs) and synchronous reluctance motors (SynRMs) has been thoroughly investigated in this thesis.

7.1.1 Towards accurate harmonic modeling for analysis and design of electric machines

One of the main challenges of harmonic modeling is to properly deal with the finite, nonlinear magnetic permeability of soft-magnetic materials. This is especially true for electric machines with slotted stator or rotor structures, due to the difference in permeability between the slots and teeth. The research presented in this thesis has led to an extension of the harmonic modeling method. This extension allows for circumferential variation of the magnetic material-permeability and includes its influence directly in the magnetic-field solution. Therefore, it embodies an important step towards incorporating nonlinear soft-magnetic materials in harmonic modeling.

Three modeling approaches for slotted electric-machine structures have been discussed, namely Anisotropic Layer Theory (ALT), Mode-Matching Theory (MMT) and Inhomogeneous Region Modeling (IRM). The magnetic-field solutions required for each modeling approach are provided by harmonic modeling and separated into homogeneous and inhomogeneous cases. The homogeneous case represents the state-of-the-art and assumes a homogeneous material-property distribution within every model region. The inhomogeneous case represents the extended magnetic-field solution and allows for a circumferential variation of the magnetic permeability. In both cases, separation of variables is applied, and the circumferential dependency of the magnetic field is expressed in terms of Fourier series. Further, the radial dependency of the magnetic field is derived analytically from Maxwell's equations in quasi-static form. To obtain the final magnetic-field solution, the unknown coefficients in the aforementioned expressions are solved using boundary conditions. The exact definition of the boundary conditions depends on the considered magnetic structure and therefore, the presented methods can be applied to a large variety of electric machines.

To compare the three modeling approaches, a quantitative study has been performed by analysing the magnetic-field distribution in a slotted benchmark topology. Two values of relative soft-magnetic material-permeability, $\mu_{r,iron} = 100$ and $\mu_{r,iron} = 1000$, have been considered, where the number of spatial harmonics in the air gap has been kept equal for each model. The results have been validated against 2D FEA calculations and compared in terms of the fundamental air-gap flux-density, rms air-gap flux-density and required computation time. The following conclusions are drawn:

- The IRM produces the most accurate calculation results.
- For $\mu_{r,iron} = 1000$, the results calculated by the MMT are nearly identical to the ones obtained from the IRM. However, this does not hold for $\mu_{r,iron} = 100$, due to the fact that the MMT does not account for finite soft-magnetic material-permeability.
- The results of the ALT model show a large error with respect to the FEA calculations, which is mainly attributed to the neglected influence of flux fringing. However, this mismatch can be compensated for by an artificial correction of the air-gap magnetic permeability using Carter's factor.
- The IRM requires significantly more computation time than the other approaches, namely seven times more than the MMT and 20 times more than the ALT for the considered benchmark topology. This increase is mainly associated to the complexity of the system equation matrix, which requires more effort to be solved.
- The ALT requires the shortest computation time. This is especially true if only the fundamental spatial harmonic is considered.

The geometry of the benchmark topology has been selected such that it can be implemented in polar coordinates without changes. For practical electric machine geometries, however, this generally does not hold. Therefore, to date, a suitable polar representation of the considered electromagnetic structure is still required and should be developed on a case-to-case basis using expert knowledge.

7.1.2 Anisotropic Layer model for IM analysis

Based on the ALT method, an ALT model has been implemented for induction-motor (IM) analysis. This model takes only the fundamental spatial harmonic into account, and represents the geometry of the motor by five model regions. The material properties are homogenized in the slotted motor-regions, and the magnetic permeability of each saturable region is updated iteratively, as previously suggested in [68]. Further, the permeability of the air gap is divided by Carter's factor to consider the average influence of flux fringing on the fundamental flux-density distribution. The ALT model has been used to analyse the magnetic-field distribution in four benchmark motor topologies under no-load operating conditions. The results have been validated against nonlinear 2D FEA calculations and the following is concluded:

- The fundamental radial air-gap flux-density predicted by the ALT model and the FEA model for no-load operating conditions are in very good agreement for all four benchmark motors, with less than 4% error. This indicates that the proposed approach to correct for flux fringing is valid for the considered benchmark motors. Also, it can be concluded that the implemented model represents the influence of saturation on the fundamental air-gap flux successfully.
- The stator flux-linkage calculated using the ALT model is in good agreement with the FEA calculations for no-load operating conditions. The maximum obtained error is typically within 5%, although benchmark motor "three" shows a slightly increased error of 8%. This difference is caused by deep saturation of the rotor teeth.

To predict IM performance under loaded operating conditions, a direct coupling between the ALT model and electric-circuit models representing the stator and rotor windings has been implemented. The induced voltages of the stator phase windings and the rotor bars are expressed in terms of the unknown coefficients of the ALT model. Then, the voltage equations of the electric circuits are included in the system equation matrix. Further, the stator phase currents and the rotor end-ring currents are considered to be unknown coefficients as well, such that their values can be obtained simultaneously with the coefficients of the ALT model.

To validate the rotor circuit-coupling, simulations have been performed for various predetermined stator-current values. Three slip values have been considered, namely nominal slip, half the nominal slip and twice the nominal slip. Based on a comparison to nonlinear 2D FEA calculations, it has been concluded that a very good agreement is obtained for the induced rotor-bar current. The maximum error obtained for the rms rotor-bar current is within 4%, where the rotor-bar current-angle error is less than 2%. Further, the electromagnetic torque obtained for nominal operating conditions shows a maximum discrepancy of 10%. For locked-rotor conditions, however, an inaccurate estimation of the leakage inductance leads to large differences between the ALT model and FEA predictions.

7.1.3 Mode-Matching model for IM analysis

The second model that has been considered for IM analysis is based on the MMT and is referred to as the MMT model. This model assumes infinitely permeable soft-magnetic material, where the slots of the stator and rotor are represented by separate, nonperiodic regions. A suitable polar approximation of the slots has been studied. As a result, a slot representation consisting of two regions has been proposed, where special measures have been taken to properly account for both slot-leakage flux and air-gap flux-fringing. It has been shown that such a representation is favorable over a single region slot model in terms of accuracy and implementation.

The MMT model has been used to analyse the magnetic-field distribution of the four benchmark motors under no-load operating conditions. The results have been validated against linear 2D FEA calculations, obtained under the assumption of infinite soft-magnetic material-permeability. A comparison of the radial air-gap flux-density distribution shows that the Gibbs phenomenon leads to local discrepancies, especially for benchmark motors ”one” and ”two”. These discrepancies, however, do not significantly influence the fundamental air-gap flux-density and stator flux-linkage. For these quantities, a maximum error less than 3% is obtained in comparison to FEA results.

To simulate loaded operating conditions with the MMT model, two different methods have been implemented to calculate the induced rotor-bar current, namely the direct method and the indirect method. The direct method is similar to the approach used for the ALT model, where the indirect model requires separate analysis of the magnetic field produced by the stator current and the magnetic field produced by the rotor current. The advantage of the indirect method is that each magnetic-field distribution needs to be calculated only once, after which the induced current and electromagnetic torque can be calculated for other operating conditions as well. However, its use is restricted to linear models, and it can only be applied to perform simulations with fixed stator currents.

Finally, the direct and the indirect methods have been used to calculate the induced rotor-bar current of the benchmark motors. The results of both approaches are in very good agreement with linear 2D FEA calculations, with errors less than 4% and 1% for the indirect and direct calculations, respectively. Additionally, the electromagnetic torque predicted by the indirect method is in very good agreement with FEA as well, where the torque obtained from the direct method using Maxwell’s Stress Tensor shows significant deviation for benchmark motors ”one” and ”two”. Further investigation reveals that the calculated torque does not converge well for an increasing number of spatial air-gap harmonics. As an alternative, the electromagnetic torque has been calculated using rotor circuit parameters. This approach shows errors less than 1% with respect to linear 2D FEA calculations.

7.1.4 Induction-motor analysis framework

The main advantage of the ALT model is its ability to predict the influence of saturation on the fundamental magnetic-flux distribution, where the advantage of the MMT model is an accurate prediction of leakage and fringing fluxes. Both these advantages have been combined in the IM analysis framework. The MMT model has been used to calculate Carter's factor, and the leakage inductance of the stator phase windings and the rotor bars. The circuit coupling of the ALT model has been modified to include these leakage-inductance parameters. Additionally, rotor skewing has been taken into account by considering multiple ALT model slices in the electric-circuit coupling, each with a slightly displaced rotor. Finally, since the leakage inductance is already included, the ALT model is modified such that it only includes radial magnetic-flux in the slotting regions.

Performance calculations have been made for the benchmark motors using the framework, 2D FEA and skewed FEA. To allow for a fair comparison, skewing is not considered in the framework during the validation against 2D FEA. The obtained simulation results show a good agreement between the 2D models in the stable operating region of the motor. For high slip values, however, the error increases. Using the results of locked-rotor simulations, it is shown that this increased mismatch is caused by saturation of the leakage flux-paths. Further, a comparison between the framework and FEA is performed including skewing. The obtained results reveal that the proposed method to account for skewing in the framework works relatively well. With respect to the 2D comparison, the discrepancy in terms of electromagnetic torque increases slightly in the stable operating region, where the difference in terms of stator phase current reduces. Also, the locked-rotor results of the framework and skewed FEA show a similar increase in leakage inductance due to skewing.

Finally, the results of the framework are validated against measurements performed on a prototype of each benchmark motor. In general, a relatively good agreement is obtained between the measurements and calculations. As expected, however, the disparity increases for large slip values due to saturation of the leakage flux-paths. Also, a comparison of the no-load magnetizing inductance shows larger discrepancies than the ones obtained from the 2D and skewed FEA comparisons. This indicates that the magnetizing behaviour of the soft-magnetic material in the actual motor is different than the magnetizing behaviour assumed in the models. This deviation also leads to a small mismatch in the stator phase current near no-load and nominal operating conditions.

7.1.5 Harmonic model for synchronous reluctance motors

A harmonic model has been implemented for analysis of synchronous reluctance motors (SynRMs). The model is based on the IRM, such that finite soft-magnetic material-permeability can be taken into account. To implement the IRM model, a polar representation of the SynRM geometry has been presented, focusing on equal average flux-barrier width and equal placement of the rotor-barrier openings at the interface of the air gap. The model has been applied to a benchmark topology, which is analysed for two different values of relative soft-magnetic material-permeability, namely $\mu_{r,iron} = 100$ and $\mu_{r,iron} = 1000$. The calculation results have been validated against calculations obtained from two different 2D FEA models. The first one represents the actual SynRM geometry, and the second one embodies a polar approximation of the SynRM. Based on a comparison of the results in terms of d-axis inductance, L_d, q-axis inductance, L_q, and electromagnetic torque, T_{em}, the following conclusions are derived:

- For $\mu_{r,iron} = 100$, the results of the harmonic model are in good agreement with the FEA calculations obtained for the polar geometry representation. With respect to the FEA results obtained for the actual geometry, an error of approximately 15% is obtained for L_d, whereas an error less than 6% is obtained for L_q. The error in L_d is attributed to the polar representation of the geometry, which leads to longer and more narrow flux guides in the rotor.
- For $\mu_{r,iron} = 1000$, the d-axis inductance, obtained from the harmonic model, deviates from the results of both FEA models. When the number of spatial harmonics is significantly increased, the error with respect to the FEA model of the polar geometry decreases. Therefore, the mismatch is associated to the truncation of the Fourier series.
- With the selected number of spatial harmonics, the required computation time is considerable for the current implementation of the model (seven seconds on a modern PC). Therefore, increasing the number of spatial harmonics to improve the model accuracy is not desirable, unless the computational efficiency of the model can be enhanced.

The implementation of the SynRM harmonic model has shown that the IRM is capable of modeling a complex electric-motor geometry. The current implementation of the model, however, requires a computation time in the same order of magnitude as a linear 2D FEA simulation of the same geometry. Therefore, future research should include an investigation on how to improve the computational efficiency of the model implementation. Further, convergence problems may arise for the Fourier-series representation of the magnetic material-properties is case of narrow slots or teeth. This problem limits the applicability of the method for relative soft-magnetic material-permeabilities of 1000 or higher. On the other hand, the MMT approach can be considered instead of the IRM approach for high permeability values.

7.2 Scientific contributions

The scientific contributions presented in this thesis can be summarized as follows:

- **The inclusion of variable magnetic material-properties in the magnetic-field solution obtained by harmonic modeling**
  Instead of assuming homogenized material-properties or infinite soft-magnetic material-permeability, a magnetic-field solution is formulated that allows for circumferential variation of the materials. This contribution facilitates the use of finite soft-magnetic material-permeability in slotted electromagnetic structures. Therefore, it presents an important step forward in harmonic modeling of electromagnetic motors and actuators. The results of the research are published in [169]. Currently, only linear soft-magnetic materials have been considered. However, using an iterative method, nonlinear soft-magnetic material behavior can be modeled as well.

- **Harmonic modeling of induction motors**
  Neither the use of Mode-Matching Theory to analyse slotted motor-structures, nor the application of Anisotropic Layer Theory to induction-motor analysis is new. However, the implementation of a double slotted induction-motor model based on Mode-Matching Theory is unique. The contributions presented on this subject include a detailed investigation of the polar representation of the IM, the influence of parasitic effects and the calculation of performance parameters. The results of this investigation have been published in [71, 170, 171, 172].

- **Modeling the interaction between the harmonic models and the electric domain**
  The interactions between the magnetic and electric domains have been studied for decades. However, suitable approaches to account for induced rotor-bar currents in induction-motor models based on harmonic modeling are scarcely represented in literature. Therefore, two methods have been presented in this thesis to calculate these currents using the developed harmonic techniques. One of these methods can be applied to calculate the stator phase current in voltage-fed simulations as well. The results of this contribution have been published in [71, 153, 170, 173], and can also be applied to many other types of electromagnetic motors and actuators.

- **Implementation and experimental verification of a semi-analytical framework for induction-motor analysis**
  A unique combination of Anisotropic Layer Theory and Mode-Matching Theory is used to implement a semi-analytical framework for induction-motor analysis. This framework unifies the advantages of both approaches and is thoroughly validated against results obtained from 2D Finite Element Analysis, skewed Finite Element Analysis, and measurements.

- **Harmonic modeling of synchronous reluctance motors**
  The use of harmonic modeling to analyse the magnetic field in a synchronous

reluctance motor has not been found in previous literature. Therefore, a harmonic model for analysis of these motors has been examined in this thesis. The presented model is based on the extended magnetic-field solution and takes the finite permeability of the soft-magnetic materials into account. The contributions of the research focus on the geometrical representation of the motor, calculation of the performance parameters and identification of the factors that influence the accuracy of the model. These results are published in [174].

7.3 Recommendations

Based on the research presented in this thesis, the following recommendations for future research are made:

- **Harmonic modeling with nonlinear soft-magnetic material-properties**
  In this thesis, an extension of the harmonic modeling method for electric machines is presented that takes the finite permeability of the soft-magnetic materials in slotted machine structures into account. Currently, however, only linear soft-magnetic materials have been considered. To make full use of the presented extension, nonlinear soft-magnetic material-properties should be considered. For example, the BH-characteristic of a soft-magnetic material can be linearized locally in terms of a remanent magnetic-flux density and a differential permeability. For a given excitation, the material parameters in each region can then be solved using an iterative algorithm, e.g. based on the Newton-Raphson method. Additionally, methods to increase the computational efficiency of the model implementation should also be investigated.

- **3D harmonic modeling**
  Numerical methods to model 3D magnetic-field distributions, such as 3D-FEA, are inefficient in terms of time-consumption. As an alternative, a 3D extension of the IRM method, presented in Chapter 2, can be considered. For rotating electric machines, the complexity of the magnetic structure is generally low along that axial direction. Several issues, however, need to be addressed, including a suitable approach to account for laminated structures and a method to deal with skewed magnetic structures. Examples of 3D implementations of the ALT and MMT are presented in [64] and [144, 145], respectively.

- **Accurate identification of soft-magnetic material-properties, including the influence of manufacturing processes**
  One of the main sources of error in electromagnetic analysis is introduced by inaccurate material-property estimations. Material manufacturers usually specify typical magnetization and loss characteristics, based on measurement performed using an Epstein frame. However, manufacturing processes, such as punching and stacking, lead to local stresses in the magnetic materials, which distort the magnetization behavior and locally promote large iron-losses. To assess the influence of such manufacturing processes, a detailed investigation of

the material properties should be performed, using samples of different sizes, shapes and materials. Measurements should be performed before and after each manufacturing step. Additionally, a similar approach should be applied to identify the effect of annealing, which is often performed after a manufacturing step to restore the properties of the magnetic materials up to some degree. Previous work on identification of the influence of manufacturing processes is, for example, discussed in [163, 175]. A detailed analysis of magnetic hysteresis phenomena is presented in [176].

- **Extension of the IM analysis framework**
  In the presented IM analysis framework, only steady-state calculation of the fundamental motor performance is considered. However, the developed harmonic models can be used to predict undesired side-effects as well, such as rotor current harmonics and parasitic torques. It is therefore suggested to investigate the extension of the framework to include these effects. Further, the steady-state circuit coupling can be extended to transient circuit coupling using a time-stepping approach, as presented in [153]. For example, transient simulations could then be performed to predict dynamic iron-losses, as proposed for tubular PM actuators in [177]. Also, the transient harmonic model could be coupled to a mechanical model to study start-up behavior for various Direct-On-Line motors, including IMs and line-start synchronous machines.

- **Improved implementation of the SynRM model**
  To obtain a better estimation of the d-axis magnetic-flux, different polar geometry representations should be considered. For example, the geometry transformation could be focussed on equal average flux-guide width rather that equal average flux-barrier width. Also, an artificial correction of the flux-guide permeability could be applied to account for the increased flux-guide length. Finally, the angular width of the flux guides and barriers could be varied per model region, in order to obtain a more accurate approximation of the actual geometry.

- **Investigation of alternative applications for harmonic modeling**
  Harmonic modeling is generally used to analyse electric-machine performance during a design procedure. However, it can provide a useful tool in other application areas as well. For example, it could be used for diagnostic purposes in electric drives, in order to determine an accurate estimation of magnetic-field distribution for a measured set of operating conditions. This could greatly improve the performance of online parameter and performance estimators. Additional alternative applications for harmonic modeling should be investigated.

- **Maxwell's Stress Tensor convergence problem**
  In Section 4.6, it is shown that a convergence problem can appear for the electromagnetic torque calculated by MST, in case of narrow slotting and a high number of spatial harmonics. The origin of this problem should be investigated in more detail.

Appendix A

Boundary conditions

A.1 Anisotropic Layer Theory for IMs

In this section, the boundary conditions for the ALT model, implemented for IM analysis, are given. The model consists of five periodic regions and therefore, interface boundary conditions are applied at the interface between two such regions, k and $k+1$. For each harmonic n, the resulting boundary-condition equations are given by

$$\begin{aligned} &a_n^{k+1} r_{bnd}^{\alpha^{k+1} w_n^{k+1}-1} + b_n^{k+1} r_{bnd}^{-\alpha^{k+1} w_n^{k+1}-1} + G_{rsn}^{k+1}\left(r_{bnd}\right) = \\ &\qquad a_n^{k} r_{bnd}^{\alpha^{k} w_n^{k}-1} + b_n^{k} r_{bnd}^{-\alpha^{k} w_n^{k}-1} + G_{rsn}^{k}\left(r_{bnd}\right), \end{aligned} \tag{A.1}$$

$$\begin{aligned} &-c_n^{k+1} r_{bnd}^{\alpha^{k+1} w_n^{k+1}-1} - d_n^{k+1} r_{bnd}^{-\alpha^{k+1} w_n^{k+1}-1} + G_{rcn}^{k+1}\left(r_{bnd}\right) = \\ &\qquad -c_n^{k} r_{bnd}^{\alpha^{k} w_n^{k}-1} - d_n^{k} r_{bnd}^{-\alpha^{k} w_n^{k}-1} + G_{rcn}^{k}\left(r_{bnd}\right), \end{aligned} \tag{A.2}$$

$$\begin{aligned} &\alpha^{k+1} c_n^{k+1} r_{bnd}^{\alpha^{k+1} w_n^{k+1}-1} - \alpha^{k+1} d_n^{k+1} r_{bnd}^{-\alpha^{k+1} w_n^{k+1}-1} + G_{\theta sn}^{k+1}\left(r_{bnd}\right) = \\ &\qquad \frac{\mu_\theta^{k+1}}{\mu_\theta^{k}} \left[\alpha^{k} c_n^{k} r_{bnd}^{\alpha^{k} w_n^{k}-1} - \alpha^{k} d_n^{k} r_{bnd}^{-\alpha^{k} w_n^{k}-1} + G_{\theta sn}^{k}\left(r_{bnd}\right)\right], \end{aligned} \tag{A.3}$$

$$\begin{aligned} &\alpha^{k+1} a_n^{k+1} r_{bnd}^{\alpha^{k+1} w_n^{k+1}-1} - \alpha^{k+1} b_n^{k+1} r_{bnd}^{-\alpha^{k+1} w_n^{k+1}-1} + G_{\theta cn}^{k+1}\left(r_{bnd}\right) = \\ &\qquad \frac{\mu_\theta^{k+1}}{\mu_\theta^{k}} \left[\alpha^{k} a_n^{k} r_{bnd}^{\alpha^{k} w_n^{k}-1} - \alpha^{k} b_n^{k} r_{bnd}^{-\alpha^{k} w_n^{k}-1} + G_{\theta cn}^{k}\left(r_{bnd}\right)\right], \end{aligned} \tag{A.4}$$

where r_{bnd} is the radius of the boundary. Furthermore, at the inner boundary of region I and the outer boundary of region V, the normal Neumann boundary conditions are given by

$$a_n^{\mathrm{I}} r_{sh}^{\alpha^{\mathrm{I}} w_n^{\mathrm{I}} - 1} + b_n^{\mathrm{I}} r_{sh}^{-\alpha^{\mathrm{I}} w_n^{\mathrm{I}} - 1} + G_{rsn}^{\mathrm{I}} \left(r_{sh} \right) = 0, \tag{A.5}$$

$$- c_n^{\mathrm{I}} r_{sh}^{\alpha^{\mathrm{I}} w_n^{\mathrm{I}} - 1} - d_n^{\mathrm{I}} r_{sh}^{-\alpha^{\mathrm{I}} w_n^{\mathrm{I}} - 1} + G_{rcn}^{\mathrm{I}} \left(r_{sh} \right) = 0, \tag{A.6}$$

$$a_n^{\mathrm{V}} r_{so}^{\alpha^{\mathrm{V}} w_n^{\mathrm{V}} - 1} + b_n^{\mathrm{V}} r_{so}^{-\alpha^{\mathrm{V}} w_n^{\mathrm{V}} - 1} + G_{rsn}^{\mathrm{V}} \left(r_{so} \right) = 0, \tag{A.7}$$

$$- c_n^{\mathrm{V}} r_{so}^{\alpha^{\mathrm{V}} w_n^{\mathrm{V}} - 1} - d_n^{\mathrm{V}} r_{so}^{-\alpha^{\mathrm{V}} w_n^{\mathrm{V}} - 1} + G_{rcn}^{\mathrm{V}} \left(r_{so} \right) = 0, \tag{A.8}$$

where $r_{sh} = r_{ro} - h_{sr} - h_{yr}$ represents the shaft radius and $r_{so} = r_{si} + h_{ss} + h_{ys}$ is the stator outer radius.

A.2 Mode-Matching Theory for IMs

In this section, the boundary conditions of the MMT model, implemented for IM analysis, are given. This model consists of a periodic air gap region and a variable number of nonperiodic regions, representing the stator and rotor slots. Each of these slots is divided into a slot opening region and a conductor region. To connect the air gap region, k, to the slot opening regions, j_ν, mode-matching is applied. For each air gap harmonic n and slot opening harmonic m, the boundary-condition equations obtained from mode-matching are given by

$$\begin{aligned} c_n^k r_{bnd}^{w_n^k - 1} - d_n^k r_{bnd}^{-w_n^k - 1} = - \sum_{\nu=1}^{K} \frac{\mu^k}{\mu^{j_\nu}} \Bigg\{ \frac{1}{r_{bnd}} \kappa_0^{k,j_\nu} \left(n \right) A_0^{j_\nu} + \\ \sum_{m=1}^{M_{sh}^\nu} \left[-a_m^{j_\nu} r_{bnd}^{w_m^{j_\nu} - 1} \kappa_c^{k,j_\nu} \left(n, m \right) + b_m^{j_\nu} r_{bnd}^{-w_m^{j_\nu} - 1} \kappa_c^{k,j_\nu} \left(n, m \right) \right] \Bigg\}, \end{aligned} \tag{A.9}$$

$$\begin{aligned} a_n^k r_{bnd}^{w_n^k - 1} - b_n^k r_{bnd}^{-w_n^k - 1} = - \sum_{\nu=1}^{K} \frac{\mu^k}{\mu^{j_\nu}} \Bigg\{ \frac{1}{r_{bnd}} \zeta_0^{k,j_s} \left(n \right) B_0^{j_\nu} \\ \sum_{m=1}^{M_{sh}^\nu} \left[-a_m^{j_\nu} r_{bnd}^{w_m^{j_\nu} - 1} \zeta_c^{k,j_\nu} \left(n, m \right) + b_m^{j_\nu} r_{bnd}^{-w_m^{j_s} - 1} \zeta_c^{k,j_s} \left(n, m \right) \right] \Bigg\}, \end{aligned} \tag{A.10}$$

$$\begin{aligned} a_m^{j_\nu} r_{bnd}^{w_m^{j_\nu} - 1} + b_m^{j^\nu} r_{bnd}^{-w_m^{j_\nu} - 1} = \sum_{n=1}^{\infty} \Big[a_n^k r_{bnd}^{w_n^k - 1} \epsilon_s^{k,j_\nu} \left(m, n \right) + \\ b_n^k r_{bnd}^{-w_n^k - 1} \epsilon_s^{k,j_\nu} \left(m, n \right) - c_n^k r_{bnd}^{w_n^k - 1} \epsilon_c^{k,j_\nu} \left(m, n \right) - d_n^k r_{bnd}^{-w_n^k - 1} \epsilon_c^{k,j_\nu} \left(m, n \right) \Big], \end{aligned} \tag{A.11}$$

where r_{bnd} represents the radius of the boundary, ν is the slot number, K denotes the number of slot present at the boundary, N_{sh} is the number of spatial harmonics in the air gap and M_{sh}^ν is the number of spatial harmonics in the ν^{th} slot region.

The terms $\kappa_c^{k,j_\nu}(n,m)$, $\zeta_c^{k,j_\nu}(n,m)$, $\kappa_0^{k,j_\nu}(n)$, $\zeta_0^{k,j_s}(n)$, $\epsilon_s^{k,j_\nu}(m,n)$ and $\epsilon_c^{k,j_\nu}(m,n)$ represent correlation functions and are given in Appendix A.4. Additionally, to obtain the average magnetic vector potential in each slot opening, continuity of the magnetic vector potential is applied at the interface between the air gap and the ν^{th} slot opening as

$$\sum_{n=1}^{N_{sh}^k}\left\{C_{an}^k a_n^k + C_{bn}^k b_n^k + C_{cn}^k c_n^k + C_{dn}^k d_n^k\right\} = \ln\left(r_{bnd}\right) B_0^{j_\nu} + A_0^{j_\nu} = 0, \tag{A.12}$$

where

$$C_{an}^k = -\frac{1}{\theta_s^{j_\nu}\left(w_n^k\right)^2} r_{bnd}^{w_n^k}\left[\sin\left(w_n^k\left(\theta^{j_\nu}+\theta_s^{j_\nu}\right)\right) - \sin\left(w_n^k\theta^{j_\nu}\right)\right], \tag{A.13}$$

$$C_{bn}^k = -\frac{1}{\theta_s^{j_\nu}\left(w_n^k\right)^2} r_{bnd}^{-w_n^k}\left[\sin\left(w_n^k\left(\theta^{j_\nu}+\theta_s^{j_\nu}\right)\right) - \sin\left(w_n^k\theta^{j_\nu}\right)\right], \tag{A.14}$$

$$C_{cn}^k = \frac{1}{\theta_s^{j_\nu}\left(w_n^k\right)^2} r_{bnd}^{w_n^k}\left[\cos\left(w_n^k\left(\theta^{j_\nu}+\theta_s^{j_\nu}\right)\right) - \cos\left(w_n^k\theta^{j_\nu}\right)\right], \tag{A.15}$$

$$C_{dn}^k = \frac{1}{\theta_s^{j_\nu}\left(w_n^k\right)^2} r_{bnd}^{-w_n^k}\left[\cos\left(w_n^k\left(\theta^{j_\nu}+\theta_s^{j_\nu}\right)\right) - \cos\left(w_n^k\theta^{j_\nu}\right)\right], \tag{A.16}$$

where θ^{j_ν} represents the circumferential position of the slot and $\theta_s^{j_\nu}$ is the angular width of the slot.

Furthermore, interface boundary conditions are applied at the boundary between a slot opening region, j_ν, and a conductor region, i_ν. For each spatial harmonic m, the boundary-condition equations are therefore given by

$$a_m^{j_\nu} r_{bnd}^{w_m^{j_\nu}-1} + b_m^{j_\nu} r_{bnd}^{-w_m^{j_\nu}-1} = a_m^{i_\nu} r_{bnd}^{\alpha^{i_\nu} w_m^{i_\nu}-1} + b_m^{i_\nu} r_{bnd}^{-\alpha^{i_\nu} w_m^{i_\nu}-1}, \tag{A.17}$$

$$a_m^{j_\nu} r_{bnd}^{w_m^{j_\nu}-1} - b_m^{j_\nu} r_{bnd}^{-w_m^{j_\nu}-1} = \frac{\alpha^{i_\nu}\mu_\theta^{i_\nu}}{\mu^{j_\nu}}\left(a_m^{i_\nu} r_{bnd}^{\alpha^{i_\nu} w_m^{i_\nu}-1} - b_m^{i_\nu} r_{bnd}^{-\alpha^{i_\nu} w_m^{i_\nu}-1}\right), \tag{A.18}$$

$$\frac{1}{r_{bnd}} B_0^{j_\nu} = -\frac{\mu_\theta^{i_\nu}}{\mu^{j_\nu}}\mu_\theta^{i_\nu}\frac{r_{bnd}}{2} J^{i_\nu} + \frac{\mu_\theta^{i_\nu}}{\mu^{j_\nu}}\frac{1}{r_{bnd}} B_0^{i_\nu}. \tag{A.19}$$

Also, to obtain the average magnetic vector potential in the ν^{th} conductor region, continuity of the magnetic vector potential is applied at the interface between the slot opening region and the conductor region as

$$\ln\left(r_{bnd}\right) B_0^{j_\nu} + A_0^{j_\nu} = \mu_{i_\nu}\frac{r_{bnd}^2}{4} J^{i_\nu} - \ln\left(r_{bnd}\right) B_0^{i_\nu} - A_0^{i_\nu}. \tag{A.20}$$

Finally, tangential Neumann boundary conditions are applied at the inner boundary of the rotor conductor regions and the outer boundary of the stator conductor regions. For the each harmonic m of the ν^{th} conductor regions, this boundary condition is given by

$$a_m^{i_\nu} r_{bnd}^{w_m^{i_\nu}-1} - b_m^{i_\nu} r_{bnd}^{-w_m^{i_\nu}-1} = 0, \tag{A.21}$$

$$\mu^{i_\nu}\frac{r_{bnd}}{2}J^{i_\nu} - B_0^{i_\nu}\frac{1}{r_{bnd}} = 0. \tag{A.22}$$

A.3 Inhomogeneous Region Modeling for SynRMs

In this section, the boundary conditions of the IRM model, implemented for SynRM analysis, are given. The model consists of 14 periodic regions and therefore, interface boundary conditions are used between two adjacent regions. Since the magnetic-field solution is derived in matrix form, the boundary-condition equations are presented in matrix form as well, and given by

$$\begin{aligned}
&-j\frac{1}{r_{bnd}}\left(\mathbf{K}_\theta \mathbf{W}^l r_{bnd}^{\boldsymbol{\lambda}^l}\mathbf{a}^l + \mathbf{K}_\theta \mathbf{W}^l r_{bnd}^{-\boldsymbol{\lambda}^l}\mathbf{b}^l + r_{bnd}^2\mathbf{K}_\theta \mathbf{G}_1^l\right) = \\
&\quad -j\frac{1}{r_{bnd}}\left(\mathbf{K}_\theta \mathbf{W}^{l+1} r_{bnd}^{\boldsymbol{\lambda}^{l+1}}\mathbf{a}^{l+1} + \mathbf{K}_\theta \mathbf{W}^{l+1} r_{bnd}^{-\boldsymbol{\lambda}^{l+1}}\mathbf{b}^{l+1} + r_{bnd}^2\mathbf{K}_\theta \mathbf{G}_1^{l+1}\right),
\end{aligned} \tag{A.23}$$

$$\begin{aligned}
&-\left(\boldsymbol{\mu}_{c,\theta}^l\right)^{-1}\mathbf{W}^l\boldsymbol{\lambda}^l r_{bnd}^{\boldsymbol{\lambda}^l-1}\mathbf{a}^l + \left(\boldsymbol{\mu}_{c,\theta}^l\right)^{-1}\mathbf{W}^l\boldsymbol{\lambda}^l r_{bnd}^{-\boldsymbol{\lambda}^l-1}\mathbf{b}^l - \\
&\quad 2r_{bnd}\left(\boldsymbol{\mu}_{c,\theta}^l\right)^{-1}\mathbf{G}_1^l = -\left(\boldsymbol{\mu}_{c,\theta}^{l+1}\right)^{-1}\mathbf{W}^{l+1}\boldsymbol{\lambda}^{l+1} r_{bnd}^{\boldsymbol{\lambda}^{l+1}-1}\mathbf{a}^{l+1} + \\
&\quad \left(\boldsymbol{\mu}_{c,\theta}^{l+1}\right)^{-1}\mathbf{W}^{l+1}\boldsymbol{\lambda}^{l+1} r_{bnd}^{-\boldsymbol{\lambda}^{l+1}-1}\mathbf{b}^{l+1} - 2r_{bnd}\left(\boldsymbol{\mu}_{c,\theta}^{l+1}\right)^{-1}\mathbf{G}_1^{l+1},
\end{aligned} \tag{A.24}$$

where r_{bnd} is the radius of the boundary. Additionally, tangential Neumann boundary conditions are applied at the outer boundary of region I and the inner boundary of region XIV. The resulting boundary-condition equations are given in matrix form by

$$\begin{aligned}
&-\left(\boldsymbol{\mu}_{c,\theta}^{\mathrm{I}}\right)^{-1}\mathbf{W}^{\mathrm{I}}\boldsymbol{\lambda}^{\mathrm{I}} r_{so}^{\boldsymbol{\lambda}^{\mathrm{I}}-1}\mathbf{a}^{\mathrm{I}} + \\
&\quad \left(\boldsymbol{\mu}_{c,\theta}^{\mathrm{I}}\right)^{-1}\mathbf{W}^{\mathrm{I}}\boldsymbol{\lambda}^{\mathrm{I}} r_{so}^{-\boldsymbol{\lambda}^{\mathrm{I}}-1}\mathbf{b}^{\mathrm{I}} - 2r_{so}\left(\boldsymbol{\mu}_{c,\theta}^{\mathrm{I}}\right)^{-1}\mathbf{G}_1^{\mathrm{I}} = 0,
\end{aligned} \tag{A.25}$$

$$\begin{aligned}
&-\left(\boldsymbol{\mu}_{c,\theta}^{\mathrm{XIV}}\right)^{-1}\mathbf{W}^{\mathrm{XIV}}\boldsymbol{\lambda}^{\mathrm{XIV}} r_{sh}^{\boldsymbol{\lambda}^{\mathrm{XIV}}-1}\mathbf{a}^{\mathrm{XIV}} + \\
&\quad \left(\boldsymbol{\mu}_{c,\theta}^{\mathrm{XIV}}\right)^{-1}\mathbf{W}^{\mathrm{XIV}}\boldsymbol{\lambda}^{\mathrm{XIV}} r_{sh}^{-\boldsymbol{\lambda}^{\mathrm{XIV}}-1}\mathbf{b}^{\mathrm{XIV}} - 2r_{sh}\left(\boldsymbol{\mu}_{c,\theta}^{\mathrm{XIV}}\right)^{-1}\mathbf{G}_1^{\mathrm{XIV}} = 0,
\end{aligned} \tag{A.26}$$

where r_{sh} represents the shaft radius and r_{so} is the stator outer radius.

A.4 Correlation functions

The mode-matching boundary conditions, used implement the MMT model for IM analysis, are based on correlation functions. A mathematical description of the required correlation functions is given by

$$\epsilon_s^{k,j_\nu}(m,n) = 2m\pi^2 \frac{\sin(2n\theta_0^k) - (-1)^m \sin(2n(\theta_0^k + \theta_c^k))}{\pi(m^2\pi^2 - n^2(\theta_c^k)^2)}, \tag{A.27}$$

$$\epsilon_c^{k,j_\nu}(m,n) = 2m\pi^2 \frac{\cos(2n\theta_0^k) - (-1)^m \cos(2n(\theta_0^k + \theta_c^k))}{\pi(m^2\pi^2 - n^2(\theta_c^k)^2)}, \tag{A.28}$$

$$\kappa_c^{k,j_\nu}(n,m) = n(\theta_0^k)^2 \frac{(-1)^m \cos(2n(\theta_0^k + \theta_c^k)) - \cos(2n\theta_0^k)}{\pi(m^2\pi^2 - n^2(\theta_c^k)^2)}, \tag{A.29}$$

$$\zeta_c^{k,j_\nu}(n,m) = n(\theta_0^k)^2 \frac{\sin(2n\theta_0^k) - (-1)^m \sin(2n(\theta_0^k + \theta_c^k))}{\pi(m^2\pi^2 - n^2(\theta_c^k)^2)}, \tag{A.30}$$

$$\kappa_0^{k,j_\nu}(n) = \frac{\cos(2n\theta_0^k) - \cos(2n(\theta_0^k + \theta_c^k))}{n\pi}, \tag{A.31}$$

$$\zeta_0^{k,j_s}(n) = \frac{\sin(2n(\theta_0^k + \theta_c^k)) - \sin(2n\theta_0^k)}{n\pi}, \tag{A.32}$$

where θ_c is the angular width of the nonperiodic region and θ_0 is the angular position of the nonperiodic region.

Appendix B

Magnetic material identification

B.1 Measurement set-up

To determine the magnetization and iron-loss characteristics of the soft-magnetic material used in the benchmark motors, material identification measurements have been performed on a Brockhaus MPG200 Electric Steel Tester set-up, as depicted in Figure B.1a. This set-up is compliant with the IEC60404 standard and is specifically designed to identify the characteristics of electric steel samples by various methods, including Epstein frames, ring-core samples, single sheets and stator cores. In these measurements, the set-up was used to perform measurements on ring-core samples, as these give the closest approximation to the actual shape and dimensions of the material when applied in an electric motor.

The measurement set-up is schematically depicted by the block diagram shown in Fig. B.1b. In this diagram, it can be seen that two different windings are applied to a ring-core sample, namely a primary winding and a secondary winding. The primary winding is used to excite the material sample and its current is supplied by an amplifier. Further, the secondary winding is used to determine resulting magnetic-field variation by measuring the induced voltage. Based on the waveform of measured voltage, the amplitude of the current in the primary winding is regulated by a controller, such that a sinusoidal magnetic flux is obtained in the material. The measured currents and voltages are logged and processed by a data acquisition system. Then, using the predefined dimensions of the material sample, the BH-characteristic and the iron losses are determined. The operating conditions for which the characteristics are determined, such as frequency and peak magnetic flux density, can be adjusted through a Graphical User Interface (GUI).

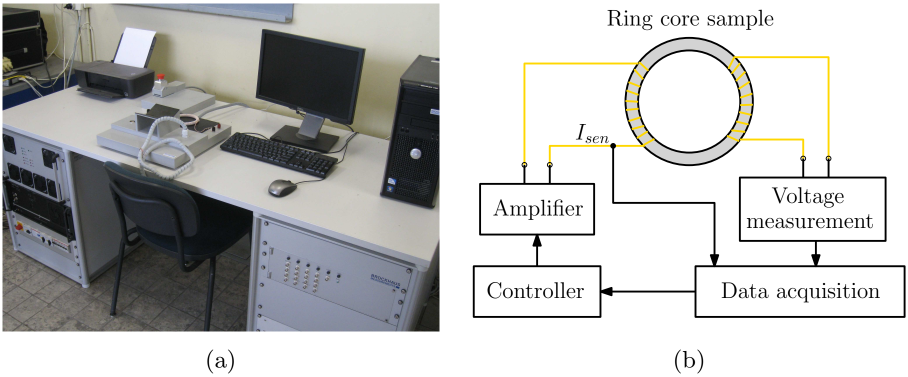

(a) (b)

Figure B.1: (a) A picture of the MPG-200 and (b) the block diagram of the material identification set-up.

B.2 Sample properties and construction

In total, magnetic material properties were determined for two different materials using four different ring samples. An overview of the properties of these ring samples is shown in Figure B.1, where samples one and two are made of soft-magnetic material one and samples three and four are made of soft-magnetic material two. The inner and outer diameters of the ring samples, D_{in} and D_{out} respectively, were selected such that

$$\frac{D_{out}}{D_{in}} \leq 1.1, \tag{B.1}$$

which is recommended by the IEC60404 standards. Furthermore, the number of primary winding turns was selected such that moderate saturation levels can be obtained within the maximum operating conditions of the amplifier, as given in Table B.2.

Figure B.2: Example of a fully wound ring sample.

Table B.1: Ring-core sample properties

Symbol	**Unit**	**Values**				**Description**
		1	2	3	4	Sample number
D_{in}	mm	99.9	99.9	99.8	99.9	Inner ring diameter
w_{rns}	mm	4.95	2.45	4.95	2.48	Ring width
h_{rns}	mm	5.16	2.72	5.16	2.53	Ring height
m_{rns}	g	61.2	14.8	62.8	15.0	Ring mass
N_{pri}	-	196	196	197	194	Number of primary windings
N_{sec}	-	300	286	291	284	Number of secondary windings
D_{pri}	mm	1	1	1	1	Primary winding diameter
D_{sec}	mm	0.7	0.7	0.7	0.7	Secondary winding diameter

Table B.2: Maximum operating conditions of the Brockhaus MPG-200

Symbol	**Unit**	**Value**	**Description**
I_{max}	A	±40	Excitation current limit
V_{max}	V	±100	Excitation voltage limit
f_{min}	Hz	3	Minimum excitation frequency
f_{max}	kHz	20	Maximum excitation frequency

The ring-core laminations were produced using a laser cutter. Then, the laminations were stacked by hand and provided with a layer of Kapton tape to keep them together. To minimize the influence leakage flux on the induced voltage measurement, the secondary winding is wound onto the sample first. Consequently, the primary winding is placed on the outside, which is also beneficial for additional cooling of the coil. Both windings are tightly distributed around the entire circumference of the sample, as shown by the picture of a fully wound ring sample in Figure B.2.

B.3 Measurement results

The magnetization characteristics and specific iron-losses of the ring samples have been measured for a peak flux density, $\hat{B}$, ranging from 0.1 - 1.8 T and a fixed excitation frequency of 50 Hz. The results obtained for soft-magnetic material one and two are shown in Figure B.3 and Figure B.4, respectively. The characteristic of soft-magnetic material two, obtained for $w_{rns} = 5\,\text{mm}$, has been used in the simulations discussed in Chapters 3 to 5.

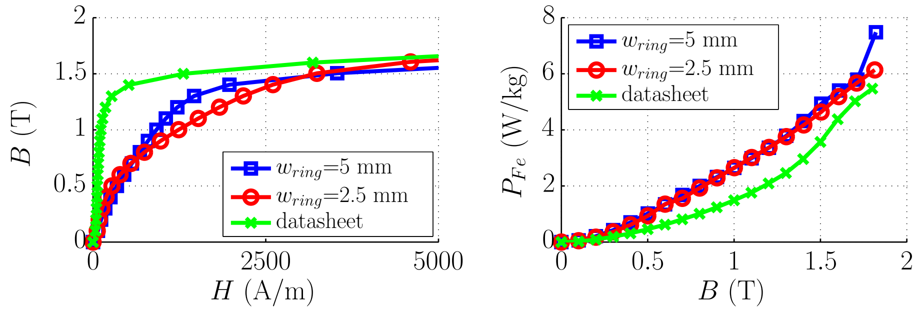

(a) (b)

Figure B.3: Soft-magnetic material one: (a) BH-characteristic and (b) specific iron-loss characteristic.

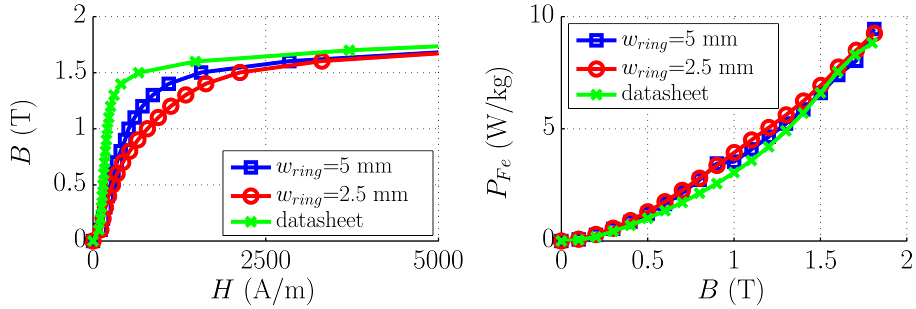

(a) (b)

Figure B.4: Soft-magnetic material two: (a) BH-characteristic and (b) specific iron-loss characteristic.

Bibliography

[1] *World Energy Outlook 2014 (Executive summary).* International Energy Agency (IEA), 2014.

[2] P. Waide and C. U. Brunner, *Energy-Efficiency Policy Opportunities for Electric Motor-Driven Systems.* International Energy Agency (IEA), 2011.

[3] *IEC 60034-30 Rotating electrical machines - Efficiency classes of single-speed, three-phase, cage-induction motors*, International Electrotechnical Commision (IEC) Std.

[4] "COMMISSION REGULATION (EC) No 640/2009," July 2009.

[5] "COMMISSION REGULATION (EU) No 4/2014," January 2014.

[6] *IEC 60034-2-1:2014 Rotating electrical machines - Standard methods for determining losses and efficiency from tests*, International Electrotechnical Commision (IEC) Std.

[7] *IEC 60034-30-1 Rotating electrical machines - Efficiency classes of line operated AC motors*, International Electrotechnical Commision (IEC) Std.

[8] F. Parasiliti, "Design strategies, new materials and technologies to improve induction motors efficiency," *Proceedings of the Electrotechnical Institute*, vol. 223, 2005.

[9] D. T. Peters, E. F. Brush, and J. L. Kirtley, "Die-cast copper rotors as strategy for improving induction motor efficiency," in *Proceedings of Electrical Insulation Conference and Electrical Manufacturing Expo (EIC/EME)*, 2007, pp. 322–327.

[10] S. Manoharan, N. Devarajan, S. M. Deivasahayam, and G. Ranganathan, "Review on efficiency improvement in squirrel-cage induction motor by DCR technology," *Journal of Electrical Engineering*, vol. 60, no. 4, pp. 227–236, 2009.

[11] K. N. Gyftakis, D. Athanasopoulos, and J. Kappatou, "Study of double cage induction motors with different rotor bar materials," in *Proceedings of*

International Conference on Electrical Machines (ICEM), 2012, pp. 1450–1456.

[12] F. Parasiliti and M. Villani, "IE3 induction motor design with aluminum and copper rotor cage: a comparison," in *Proceedings of Energy Efficiency in Motor Driven Systems (EEMODS)*, 2013.

[13] E. B. Agamloh, A. Boglietti, and A. Cavagnino, "The incremental design efficiency improvement of commercially manufactured induction motors," *IEEE Trans. Ind. Appl.*, vol. 49, no. 6, pp. 2496–2504, Nov/Dec 2013.

[14] M. V. Cistelecan, H. B. Cosan, and M. Popescu, "High efficiency general purpose small power induction motors design and development," in *Proceedings of International Aegean Conference on Electrical Machines and Power Electronics and Electromotion (ACEMP)*, 2007, pp. 536–540.

[15] J. F. Fuchsloch, W. R. Finley, and R. W. Walter, "The next generation motor," *IEEE Ind. Appl. Magazine*, vol. 14, no. 1, pp. 37–43, Jan/Feb 2008.

[16] A. T. Almeida, F. J. T. E. Ferreira, and G. Baoming, "Beyond induction motors - technology trends to move up efficiency," *IEEE Trans. Ind. Appl.*, vol. 50, no. 3, pp. 2103–2114, May/Jun 2014.

[17] E. P. Furlani, *Permanent Magnet and Electromechanical Devices.* Academic Press, 2001.

[18] M. J. Kamper and A. F. Volschenk, "Effect of rotor dimensions and cross magnetisation on Ld and Lq inductances of reluctance synchronous machine with cageless flux barrier rotor," *IEE Proceedings Electr. Power Appl.*, vol. 141, no. 4, pp. 213–220, Jul 1994.

[19] N. Bianchi, O. Bottesi, and L. Alberti, "Energy efficiency improvement adopting synchronous motors," in *Proceedings of International Conference on Ecological Vehicles and Renewable Energies (EVER)*, 2013.

[20] S. Musuroi, C. Sorandaru, M. Greconici, V. N. Olarescu, and M. Weinman, "Low-cost ferrite permanent magnet assisted synchronous reluctance rotor and permanent magnet synchronous rotor with flux concentrator: an alternative for rare earth permanent magnet synchronous motors," in *Proceedings of International Conference on Applied and Theoretical Electricity (ICATE)*, 2014.

[21] S. Taghavi and P. Pillay, "A mechanically robust rotor with transverse-laminations for a synchronous reluctance machine for traction applications," in *Proceedings of IEEE Energy Conversion Congress and Expo (ECCE)*, 2014, pp. 5131–5137.

[22] M. L. Henriksen, B. B. Jensen, N. Mijatovic, J. Kolehmainen, and J. Holboll, "Structural design of SynRM rotor and the effect on power factor," in

Proceedings of IEEE International Electric Machines and Drives Conference (IEMDC), 2015, pp. 516–522.

[23] X. Feng, L. Liu, J. Kang, and Y. Zhang, “Super premium efficient line start-up permanent magnet synchronous motor,” in *Proceedings of International Conference on Electrical Machines (ICEM)*, 2010.

[24] V. Elistratova, M. Hecquet, P. Brochet, D. Vizireanu, and M. Dessoude, “Analytical approach for optimal design of a line-start internal permanent magnet synchronous motor,” in *Proceedings of European Conference on Power Electronics and Applications (EPE)*, 2013.

[25] S. F. Rabbi and M. A. Rahman, “Determination of the synchronization criteria of line start IPM motors,” in *Proceedings of IEEE International Electric Machines and Drives Conference (IEMDC)*, 2013, pp. 1218–1224.

[26] R. T. Ugale and B. N. Chaudhari, “A new rotor structure for line start permanent magnet synchronous motor,” in *Proceedings of IEEE International Electric Machines and Drives Conference (IEMDC)*, 2013, pp. 1436–1442.

[27] M. J. Melfi, S. D. Umans, and J. E. Atem, “Viability of highly efficient multi-horsepower line-start permanent-magnet motors,” *IEEE Trans. Ind. Appl.*, vol. 51, no. 1, pp. 120–128, Jan/Feb 2015.

[28] M. Gamba, G. Pellegrino, A. Vagati, and F. Villata, “Design of a line-start synchronous reluctance motor,” in *Proceedings of IEEE International Electric Machines and Drives Conference (IEMDC)*, 2013, pp. 648–655.

[29] A. Castagnini, T. Känsäkangas, J. Kolehmainen, and P. S. Termini, “Analysis of the starting transient of a synchronous reluctance motor for direct-on-line applications,” in *Proceedings of IEEE International Electric Machines and Drives Conference (IEMDC)*, 2015.

[30] G. Ferraris, “Rotazioni elettrodinamische prodotte per mezzo di corrente alternate,” *Atti della Reale Accademia delle Scienze di Torino*, vol. 23, pp. 360–375, 1888.

[31] N. Tesla, “A new system of alternate current motors and transformers,” *Trans. AIEE*, vol. 5, no. 10, pp. 308–327, Jul 1888.

[32] M. Dolivo-Dobrovolsky, “Anker fur wechselstrommotoren,” *Deutsches Reichspatent No. 51083*, 1889.

[33] C. P. Steinmetz, “The alternating current induction motor,” *Trans. AIEE*, vol. 14, no. 1, pp. 183–217, Sep 1897.

[34] C. G. Veinott, *Theory and design of small induction motors.* McGraw-Hill, 1959.

[35] P. L. Alger, *Induction Machines: Their Behavior and Uses*, 2nd ed. Gordon and Breach, Science Publishers, Inc., 1970.

[36] M. G. Say, *Alternating Current Machines.* Pitman Publishing Ltd., 1976.

[37] J. Pyrhonen, T. Jokinen, and V. Hrabovcova, *Design of Rotating Electrical Machines.* John Wiley & Sons, Ltd, 2008.

[38] A. Boglietti, A. Cavagnino, and M. Lazzari, "Algorithms for the computation of the induction motor equivalent circuit parameters - part I," in *Proceedings of IEEE Industrial Electronics Conference (IECON)*, Orlando, Florida, USA, November 2008, pp. 2020–2027.

[39] A. Boglietti, A. Cavagnino, and M. Lazzari, "Algorithms for the computation of the induction motor equivalent circuit parameters - part II," in *Proceedings of IEEE Industrial Electronics Conference (IECON)*, Orlando, Florida, USA, November 2008, pp. 2028–2034.

[40] I. Boldea and S. A. Nasar, *The Induction Machines Design Handbook.* CRC Press, Taylor and Francis Group, 2010.

[41] V. Ostovic, *Dynamics of Saturated Electric Machines.* New York: Springer-Verlag, 1989.

[42] F. Hrusovsky and V. Hrabovcova, "Investigation of iron loss and magnetic field distribution in inverter fed induction motor," in *Proceedings of Transcom*, Zilina, Slovakia, Jun 1995, pp. 153–156.

[43] J. Perho and E. Ritchie, "A motor operation analysis using reluctance network," in *Proceedings of the International Symposium on Electric Power Engineering (PowerTech)*, Stockholm, Sweden, Jun 1995, pp. 356–361.

[44] J. Perho and E. Ritchie, "Analysis of a permanent magnet machine using reluctance network," in *Proceedings of International Conference on Electrical Machines (ICEM)*, Vigo, Spain, Sep 1996, pp. 44–48.

[45] C. Rasmussen and E. Ritchie, "Improved reluctance-mmf network for calculation of magnetic field distribution in surface-mounted permanent-magnet motors," *Electromotion*, no. 4, pp. 55–61, 1997.

[46] R. Wang and J. Gieras, "Analysis of characteristics of a permanent magnet hybrid linear stepping motor," in *Proceedings of International Conference on Electrical Machines (ICEM)*, Istanbul, Turkey, Sep 1998, pp. 833–838.

[47] B. Asghari and V. Dinavahi, "Experimental validation of a geometrical nonlinear permeance network based real-time induction machine model," *IEEE Trans. Ind. Electron.*, vol. 59, no. 11, pp. 4049–4062, Nov 2012.

[48] S. D. Sudhoff, B. T. Kuhn, K. A. Corzine, and B. T. Branecky, "Magnetic equivalent circuit modeling of induction motors," *IEEE Trans. Energy Convers.*, vol. 22, no. 2, pp. 397–405, Jun 2007.

[49] J. Perho, "Reluctance network for analysing induction machines," Ph.D. dissertation, Helsinki University of Technology, 2002.

[50] W. T. J. Atkins, "An improved electromagnetic analogue," *IEE Proceedings*, vol. 105, no. 7, pp. 151–154, Mar 1958.

[51] M. Armhein and P. T. Krein, "3-D magnetic equivalent circuit framework for modeling electromechanical devices," *IEEE Trans. Energy Convers.*, vol. 24, no. 2, pp. 397–405, Jun 2009.

[52] M. Armhein and P. T. Krein, "Force calculation in 3-D magnetic equivalent circuit networks with a maxwell stress tensor," *IEEE Trans. Energy Convers.*, vol. 24, no. 3, pp. 587–593, Sep 2009.

[53] M. Armhein and P. T. Krein, "Induction machine modeling approach based on 3-D magnetic equivalent circuit framework," *IEEE Trans. Energy Convers.*, vol. 25, no. 2, pp. 339–347, Jun 2010.

[54] A. Aden, Y. Amara, G. Barakat, S. Hlioui, O. Barriere, and M. Gabsi, "Modeling of a radial flux PM rotating machine using a new hybrid analytical model," in *Proceedings of International Conference on Electrical Sciences and Technologies (CISTEM)*, 2014.

[55] K. Pluk, J. W. Jansen, and E. A. Lomonova, "Hybrid analytical modeling: Fourier modeling combined with mesh-based magnetic equivalent circuits," *IEEE Trans. Magn.*, 2015.

[56] E. Mishkin, "Theory of the squirrel-cage induction machine derived directly from Maxwell's field equations," *Quart. J. Mech. and Appl. Math.*, vol. 7, pp. 472–487, 1954.

[57] A. L. Cullen and T. H. Barton, "A simplified electromagnetic theory of the induction motor, using the concept of wave impedance," *IEE Proceedings*, vol. 105, no. 8, pp. 331–336, 1958.

[58] J. Greig and E. M. Freeman, "Travelling-wave problem in electrical machines," *IEE Proceedings*, vol. 114, no. 11, pp. 1681–1683, 1967.

[59] E. M. Freeman, "Travelling waves in induction machines: input impedance and equivalent circuits," *IEE Proceedings*, vol. 115, no. 12, pp. 1772–1776, 1968.

[60] T. W. Preston and A. B. J. Reece, "Transverse edge effects in linear induction motors," *IEE Proceedings*, vol. 116, no. 6, pp. 973–979, 1969.

[61] E. M. Freeman, D. A. Lowther, T. W. Preston, and A. B. J. Reece, "Transverse edge effects in linear induction motors," *IEE Proceedings*, vol. 118, no. 12, pp. 1820–1821, 1971.

[62] J. F. Eastham and J. H. Alwash, "Transverse-flux tubular motors," *IEE Proceedings*, vol. 119, no. 12, pp. 1709–1718, 1972.

[63] H. Weh, "Induktionsvorgänge in anisotropen medien," *Archiv für Elektrotechnik*, vol. 52, no. 2, pp. 80–92, 1968.

[64] S. Williamson, “The anisotropic layer theory of induction machines and induction devices,” *IMA J. Appl. Math.*, vol. 17, pp. 69–84, 1976.

[65] S. Williamson and A. C. Smith, “Field analysis for rotating induction machines and its relationship to the equivalent-circuit method,” *IEE Proceedings*, vol. 127, no. 2, pp. 83–90, 1980.

[66] J. F. Gieras, “Three dimensional multilayer theory of induction machines and devices,” *Acta Technica CSAV*, vol. 28, no. 5, pp. 525–548, 1983.

[67] J. F. Gieras, “Analysis of multilayer rotor induction motor with higher space harmonics taken into account,” *IEE Proceedings*, vol. 138, no. 2, pp. 59–67, 1991.

[68] G. Madescu, I. Boldea, and T. J. E. Miller, “An analytical iterative model (AIM) for induction motor design,” in *Conference Record of the IEEE IAS Industry Applications Conference*, vol. 1, 1996, pp. 566–573.

[69] M. P. Magill and P. T. Krein, “Electric machines as metamaterials: Induction machine design using planar layer models,” in *Proceedings of IEEE International Electric Machines and Drives Conference (IEMDC)*, 2011, pp. 890–895.

[70] R. L. J. Sprangers, T. E. Motoasca, and E. A. Lomonova, “Extended anisotropic layer theory for electrical machines,” *IEEE Trans. Magn.*, vol. 49, no. 5, pp. 2217–2220, May 2013.

[71] R. L. J. Sprangers, J. J. H. Paulides, K. O. Boynov, J. Waarma, and E. A. Lomonova, “Comparison of two anisotropic layer models applied to induction motors,” *IEEE Trans. Ind. Appl.*, vol. 50, no. 4, pp. 2533–2543, July/August 2014.

[72] N. L. Schmitz and D. W. Novotny, *Introductory Electromechanics.* The Ronald Press Company, New York, 1965.

[73] H. A. Toliyat, T. A. Lipo, and J. C. White, “Analysis of a concentrated winding induction machine for adjustable speed drive applications - part I,” *IEEE Trans. Energy Convers.*, vol. 6, no. 4, pp. 679–683, Dec 1991.

[74] X. Luo, Y. Liao, H. A. Toliyat, A. El-Antably, and T. A. Lipo, “Multiple coupled circuit modeling of induction machines,” *IEEE Trans. Ind. Appl.*, vol. 31, no. 2, pp. 311–318, Mar/Apr 1995.

[75] H. A. Toliyat and T. A. Lipo, “Transient analysis of cage induction machines under stator, rotor bar and end ring faults,” *IEEE Trans. Energy Convers.*, vol. 10, no. 2, pp. 241–247, Jun 1995.

[76] J. Milimonfared, H. M. Kelk, S. Nandi, A. D. Minassians, and H. A. Toliyat, “A novel approach for broken-rotor-bar detection in cage induction motors,” *IEEE Trans. Ind. Appl.*, vol. 35, no. 5, pp. 1000–1006, Sep/Oct 1999.

[77] G. M. Joksimovic, "The detection of inter-turn short circuits in the stator windings of operating motors," *IEEE Trans. Ind. Electron.*, vol. 47, no. 5, pp. 1078–1084, Oct 2000.

[78] S. Nandi and H. A. Toliyat, "Novel frequency-domain-based technique to detect stator interturn faults in induction machines using stator-induced voltages after switch-off," *IEEE Trans. Ind. Appl.*, vol. 38, no. 1, pp. 101–109, Jan/Feb 2002.

[79] H. A. Toliyat, A. G. Arefeen, and A. G. Parlos, "A method for dynamic simulation of air-gap eccentricity in induction machines," *IEEE Trans. Ind. Appl.*, vol. 32, no. 4, pp. 910–918, Jul/Aug 1996.

[80] G. M. Joksimovic, M. D. Durovic, J. Penman, and N. Arthur, "Dynamic simulation of dynamic eccentricity in induction machines - winding function approach," *IEEE Trans. Energy Convers.*, vol. 15, no. 2, pp. 143–148, Jun 2000.

[81] N. A. Al-Nuaim and H. A. Toliyat, "A novel method for modeling dynamic air-gap eccentricity in synchronous machines based on modified winding function theory," *IEEE Trans. Energy Convers.*, vol. 13, no. 2, pp. 156–162, Jun 1998.

[82] J. Faiz and I. Tabatabaei, "Extension of winding function theory for nonuniform air gap in electric machinery," *IEEE Trans. Magn.*, vol. 38, no. 6, pp. 3654–3657, Nov 2002.

[83] S. Nandi, H. A. Toliyat, and A. G. Parlos, "Performance analysis of a single phase induction motor under eccentric conditions," in *Conference Record of the IEEE IAS Industry Applications Conference*, 1997, pp. 174–181.

[84] S. Nandi, S. Ahmed, and H. A. Toliyat, "Detection of rotor slot and other eccentricity related harmonics in a three phase induction motor with different rotor cages," *IEEE Trans. Energy Convers.*, vol. 16, no. 3, pp. 253–260, Sep 2001.

[85] S. Nandi, R. M. Bharadwaj, and H. A. Toliyat, "Performance analysis of a three-phase induction motor under mixed eccentricity condition," *IEEE Trans. Energy Convers.*, vol. 17, no. 3, pp. 392–399, Sep 2002.

[86] J. Faiz and M. Ojaghi, "Unified winding function approach for dynamic simulation of different kinds of eccentricity faults in cage induction machines," *IET Electric Power Applications*, vol. 3, no. 5, pp. 461–470, 2009.

[87] G. M. Joksimovic, M. D. Durovic, and A. B. Obradovic, "Skew and linear rise of mmf across slot modeling - winding function approach," *IEEE Trans. Energy Convers.*, vol. 14, no. 3, pp. 315–320, Sep 1999.

[88] G. Bossio, C. D. Angelo, J. Solsona, G. García, and M. I. Valla, "A 2-D model of the induction machine: An extension of the modified winding

function approach," *IEEE Trans. Energy Convers.*, vol. 19, no. 1, pp. 144–150, Mar 2004.

[89] S. Nandi, "A detailed model of induction machines with saturation extendable for fault analysis," *IEEE Trans. Ind. Appl.*, vol. 40, no. 5, pp. 1302–1309, Sep/Oct 2004.

[90] M. Ojaghi and J. Faiz, "Extension to multiple coupled circuit modeling of induction machines to include variable degrees of saturation effects," *IEEE Trans. Magn.*, vol. 44, no. 11, pp. 4053–4056, Nov 2008.

[91] J. C. Moreira and T. A. Lipo, "Modeling of saturated AC machines including air gap flux harmonic components," *IEEE Trans. Ind. Appl.*, vol. 28, no. 2, pp. 343–349, Mar/Apr 1992.

[92] N. A. Karim, J. Azzouzi, G. Barakat, and B. Dakyo, "Complete analytical modeling of an axial flux PM synchronous machine for wind energy application," in *Proceedings of International Power Electronics and Motion Control Conference (EPE-PEMC)*, 2006, pp. 996–1001.

[93] A. B. J. Reece and T. W. Preston, *Finite Element Methods in electrical power engineering.* Oxford University Press, 2000.

[94] A. Arkkio, "Analysis of induction motors based on the numerical solution of the magnetic field and circuit equations," Ph.D. dissertation, Helsinki University of Technology, 1987.

[95] J. K. Kostko, "Polyphase reaction synchronous motors," *Trans. AIEE*, vol. 42, no. 11, pp. 1162–1168, Nov 1923.

[96] A. J. O. Cruickshank, A. F. Anderson, and R. W. Menzies, "Theory and performance of reluctance motors with axially laminated anisotropic rotors," *IEE Proceedings*, vol. 118, no. 7, pp. 887–894, Jul 1971.

[97] D. A. Staton, T. J. E. Miller, and S. E. Wood, "Maximising the saliency ratio of the synchronous reluctance motor," *IEE Proceedings-B*, vol. 140, no. 4, pp. 249–259, Jul 1993.

[98] I. Boldea, Z. X. Fu, and S. A. Nasar, "Performance evaluation of axially-laminated anisotropic (ALA) rotor reluctance synchronous motors," *IEEE Trans. Ind. Appl.*, vol. 30, no. 4, pp. 977–985, Jul/Aug 1994.

[99] B. J. Chalmers and L. Musaba, "Design and field-weakening performance of a synchronous reluctance motor with axially laminated rotor," *IEEE Trans. Ind. Appl.*, vol. 34, no. 5, pp. 1035–1041, Sep/Oct 1998.

[100] A. Fratta, A. Vagati, and F. Villata, "On the evolution of AC machines for spindle drive applications," *IEEE Trans. Ind. Appl.*, vol. 28, no. 5, pp. 1081–1086, Sep/Oct 1992.

[101] I. Marongiu and A. Vagati, "Improved modelling of a distributed anisotropy synchronous reluctance machine," in *Conference Record of the IAS Annual Meeting*, vol. 1, 1991, pp. 238–243.

[102] A. Vagati, G. Franceschini, I. Marongiu, and G. P. Troglia, "Design criteria of high performance synchronous reluctance motors," in *Conference Record of the IEEE IAS Industry Applications Conference*, vol. 1, 1992, pp. 66–73.

[103] A. Fratta, G. P. Troglia, A. Vagati, and F. Villata, "Evaluation of torque ripple in high performance synchronous reluctance machines," in *Conference Record of the IEEE IAS Industry Applications Conference*, 1993, pp. 163–170.

[104] A. Vagati, M. Pastorelli, G. Franceschini, and C. Petrache, "Design of low-torque-ripple synchronous reluctance motors," in *Conference Record of the IEEE IAS Industry Applications Conference*, 1997, pp. 286–293.

[105] A. Vagati, A. Canova, M. Chiampi, M. Pastorelli, and M. Repetto, "Design refinement of synchronous reluctance motors through finite-element analysis," *IEEE Trans. Ind. Appl.*, vol. 36, no. 4, pp. 1094–1102, Jul/Aug 2000.

[106] T. Matsuo and T. A. Lipo, "Rotor design optimization of synchronous reluctance machine," *IEEE Trans. Energy Convers.*, vol. 9, no. 2, pp. 359–365, Jun 1994.

[107] X. B. Bomela and M. J. Kamper, "Effect of machine design on performance of reluctance synchronous machine," in *Conference Record of the IEEE IAS Industry Applications Conference*, 2000, pp. 515–522.

[108] H. Kiriyama, S. Kawano, Y. Honda, T. Higaki, S. Morimoto, and Y. Takeda, "High performance synchronous reluctance motor with multi-flux barrier for the appliance industry," in *Conference Record of the IEEE IAS Industry Applications Conference*, 1998, pp. 111–117.

[109] P. Hudak, V. Hrabovcova, and P. Rafajdus, "Geometrical dimension influence of multi-barrier rotor on reluctance synchronous motor performances," in *Proceedings of International Symposium on Power Electronics, Electrical Drives, Automation and Motion (SPEEDAM)*, 2006, pp. 24–29.

[110] P. Niazi, H. A. Toliyat, D. Cheong, and J. Kim, "A low-cost and efficient permanent-magnet-assisted synchronous reluctance motor drive," *IEEE Trans. Ind. Appl.*, vol. 43, no. 2, pp. 542–550, Mar/Apr 2007.

[111] K. Wang, Z. Q. Zhu, G. Ombach, M. Koch, S. Zhang, and J. Xu, "Optimal slot/pole and flux-barrier layer number combination for synchronous reluctance machines," in *Proceedings of International Conference on Ecological Vehicles and Renewable Energies (EVER)*, 2013.

[112] E. Howard, M. J. Kamper, and S. Gerber, "Asymmetric flux barrier and skew design optimisation of reluctance synchronous machines," *IEEE Trans. Ind. Appl.*, 2015.

[113] F. Parasiliti and M. Villani, "Optimisation analysis of synchronous reluctance motor design," in *Proceedings of IEE International Conference on Electrical Machines and Drives*, 1995, pp. 276–280.

[114] M. Kamper, F. S. Merwe, and S. Williamson, "Direct finite element design optimisation of the cageless reluctance synchronous machine," *IEEE Trans. Energy Convers.*, vol. 11, no. 3, Sep 1996.

[115] G. Pellegrino, F. Cupertino, and C. Gerada, "Automatic design of synchronous reluctance motors focusing on barrier shape optimization," *IEEE Trans. Ind. Appl.*, vol. 51, no. 2, pp. 1465–1474, Mar/Apr 2014.

[116] R. Moghaddam and F. Gyllensten, "Novel high-performance SynRM design method: An easy approach for a complicated rotor topology," *IEEE Trans. Ind. Electron.*, vol. 61, no. 9, pp. 5058–5065, Sep 2014.

[117] F. Parasiliti and M. Villani, "Synchronous reluctance motors design and performance prediction using an analytical procedure," *WIT Press Transactions on Engineering Sciences*, vol. 41, 2003.

[118] F. Parasiliti and M. Villani, "Magnetic analysis of flux barriers synchronous reluctance motors," in *Proceedings of International Conference on Electrical Machines (ICEM)*, 2008.

[119] B. Nikbakhtian, S. Talebi, P. Niazi, and H. A. Toliyat, "An analytical model for an n-flux barrier per pole permanent magnet-assisted synchronous reluctance motor," in *Proceedings of IEEE International Electric Machines and Drives Conference (IEMDC)*, 2009, pp. 129–136.

[120] A. Tessarolo, M. Degano, and N. Bianchi, "On the analytical estimation of the airgap field in synchronous reluctance machine," in *Proceedings of International Conference on Electrical Machines (ICEM)*, 2014, pp. 239–244.

[121] S. Yammine, C. Henaux, M. Fadel, and S. Desharnais, "Synchronous reluctance machine flux barrier design based on the flux line patterns in a solid rotor," in *Proceedings of International Conference on Electrical Machines (ICEM)*, 2014.

[122] B. Hague, *Electromagnetic Problems in Electrical Engineering.* London, U.L.: Oxford University Press, 1929.

[123] J. Pyrhonen, "The high-speed induction motor: Calculating the effects of solid-rotor material on machine characteristics," Ph.D. dissertation, Lappeenranta University of Technology, 1991.

[124] N. Boules, "Two-dimensional field analysis of cylindrical machines with permanent magnet excitation," *IEEE Trans. Ind. Appl.*, vol. IA-20, no. 5, pp. 1267–1277, Sep/Oct 1984.

[125] N. Boules, "Prediction of no-load flux density distribution in permanent magnet machines," *IEEE Trans. Ind. Appl.*, vol. IA-21, no. 4, pp. 633–643, May/Jun 1985.

[126] Q. Gu and G. Hongzhan, "Air gap field of PM electric machines," *Electric Machines and Power Systems*, vol. 10, no. 5-6, pp. 459–470, 1985.

[127] Z. Q. Zhu, D. Howe, E. Bolte, and B. Ackermann, "Instantaneous magnetic field distribution in brushless permanent magnet DC motors, part I: Open-circuit field," *IEEE Trans. Magn.*, vol. 29, no. 1, pp. 124–135, January 1993.

[128] M. Marinescu and N. Marinescu, "New concept of permanent magnet excitation for electrical machines: analytical and numerical computation," *IEEE Trans. Magn.*, vol. 28, no. 2, pp. 1390–1393, 1992.

[129] Z. Q. Zhu and D. Howe, "Instantaneous magnetic field distribution in brushless permanent magnet DC motors, part II: Armature-reaction field," *IEEE Trans. Magn.*, vol. 29, no. 1, pp. 136–142, January 1993.

[130] Z. Q. Zhu and D. Howe, "Instantaneous magnetic field distribution in brushless permanent magnet DC motors, part III: Effect of stator slotting," *IEEE Trans. on Magn.*, vol. 29, no. 1, pp. 143–151, January 1993.

[131] B. Ackermann and R. Sottek, "Analytical modeling of the cogging torque in permanent magnet motors," *Electrical Engineering*, vol. 78, no. 2, pp. 177–125, 1995.

[132] Z. J. Liu and J. T. Li, "Analytical solution of air-gap field in permanent-magnet motors taking into account the effect of pole transition over slots," *IEEE Trans. Magn.*, vol. 43, no. 10, pp. 3872–3883, October 2007.

[133] F. Dubas and C. Espanet, "Analytical solution of the magnetic field in permanent-magnet motors taking into account slotting effect: No-load vector potential and flux density calculation," *IEEE Trans. Magn.*, vol. 45, no. 5, pp. 2097–2109, May 2009.

[134] Z. Zhu, L. Wu, and Z. Xia, "An accurate subdomain model for magnetic field computation in slotted surface-mounted permanent-magnet machines," *IEEE Trans. Magn.*, vol. 46, no. 4, pp. 1100–1115, April 2010.

[135] T. Lubin, S. Mezani, and A. Rezzoug, "2-D exact analytical model for surface-mounted permeanent-magnet motors with semi-closed slots," *IEEE Trans. Magn.*, vol. 47, no. 2, pp. 479–492, Feb 2011.

[136] O. Barriere, H. Ben Ahmed, M. Gabsi, and M. LoBue, "2D analytical airgap field model of an inset permanent magnet synchronous machine, taking into account the slotting effect," *IEEE Trans. Magn.*, vol. 49, no. 4, pp. 1423–1435, Apr 2013.

[137] T. T. Overboom, J. P. C. Smeets, J. W. Jansen, and E. A. Lomonova, "Semi-analytical calculation of the torque in a linear permanent-magnet motor with finite yoke length," *IEEE Trans. Magn.*, vol. 48, no. 11, pp. 3575–3578, Nov 2012.

[138] B. L. J. Gysen, E. Ilhan, K. J. Meessen, J. J. H. Paulides, and E. A. Lomonova, "Modeling of flux switching permanent magnet machines with Fourier analysis," *IEEE Trans. Magn.*, vol. 46, no. 6, pp. 1499–1502, Jun 2010.

[139] B. Gaussens, O. Barriere, E. Hoang, J. Saint-Michel, P. Manfe, M. Lécrivain, and M. Gabsi, "Magnetic field solution in doubly slotted airgap of conventional and alternate field-excited switched-flux topologies," *IEEE Trans. Magn.*, vol. 49, no. 9, pp. 5083–5096, Sep 2013.

[140] B. Gaussens, E. Hoang, J. Saint-Michel, P. Manfe, M. Lécrivain, and M. Gabsi, "Topology exploration of static-excited cylindrical machines using a general analytical magnetic field solution," *IEEE Trans. Magn.*, vol. 50, no. 11, Nov 2014.

[141] H. Tiegna, A. Bellara, Y. Amara, and G. Barakat, "Analytical modeling of the open-circuit magnetic field in axial flux permanent magnet machines with semi-closed slots," *IEEE Trans. Magn.*, vol. 48, no. 3, pp. 1212–1226, March 2012.

[142] T. Lubin, S. Mezani, and A. Rezzoug, "Analytic calculation of eddy currents in the slots of electrical machines: Application to cage rotor induction motors," *IEEE Trans. Magn.*, vol. 47, no. 11, pp. 4650–4659, Nov 2011.

[143] B. L. J. Gysen, K. J. Meessen, J. J. H. Paulides, and E. A. Lomonova, "General formulation of the electromagnetic field distribution in machines and devices using Fourier analysis," *IEEE Trans. Magn.*, vol. 46, no. 1, pp. 39–52, Jan 2010.

[144] K. J. Meessen, B. L. J. Gysen, J. J. H. Paulides, and E. A. Lomonova, "General formulation of fringing fields in 3-D cylindrical structures using Fourier analysis," *IEEE Trans. Magn.*, vol. 48, no. 8, pp. 2307–2323, Aug 2012.

[145] J. P. C. Smeets, T. T. Overboom, J. W. Jansen, and E. A. Lomonova, "Three-dimensional analytical modeling technique of electromagnetic fields of air-cored coils surrounded by different ferromagnetic boundaries," *IEEE Trans. Magn.*, vol. 49, no. 12, pp. 5698–5708, Dec 2013.

[146] R. C. Rumpf, "Design and optimization of nano-optical elements by coupling fabrication to optical behavior," Ph.D. dissertation, University of Central Florida, 2006.

[147] B. L. J. Gysen, "Generalized harmonic modeling technique for 2D electromagnetic problems," Ph.D. dissertation, Eindhoven University of Technology, 2011.

[148] G. Granet and B. Guizal, "Efficient implementation of the coupled-wave method for metallic gratings in TM polarization," *J. Opt. Soc. Am. A*, vol. 13, no. 5, pp. 1019–1023, May 1996.

[149] P. Lalanne and G. M. Morris, "Highly improved convergence of the coupled-wave method for TM polarization," *J. Opt. Soc. Am. A*, vol. 13, no. 4, pp. 779–784, Apr 1996.

[150] L. Li, "Use of Fourier series in the analysis of discontinuous periodic structures," *J. Opt. Soc. Am. A*, vol. 13, no. 9, pp. 1870–1876, Sep 1996.

[151] S. W. Lee, W. R. Jones, and J. J. Campbell, "Convergence of numerical solutions of iris-type discontinuity problems," vol. 19, no. 6, pp. 528–536, June 1971.

[152] R. Mittra, T. Itoh, and T. Li, "Analytical and numerical studies of the relative convergence phenomenon arising in the solution of an integral equation by the moment method," *IEEE Transactions on Microwave Theory and Techniques*, vol. 20, no. 2, pp. 96–104, February 1972.

[153] R. L. J. Sprangers, J. J. H. Paulides, B. L. J. Gysen, J. Waarma, and E. A. Lomonova, "Electric circuit coupling of a slotted semi-analytical model for induction motors based on harmonic modeling," in *Proceedings of IEEE Energy Conversion Congress and Expo (ECCE)*, September 2014.

[154] F. W. Carter, "The magnetic field of the dynamo-electric machine," *IEE Journal*, vol. 64, no. 359, pp. 1115–1138, Nov 1926.

[155] J. Gibbs, "Fourier's Series," *letter in Nature*, vol. 59, p. 200, 1898.

[156] J. Gibbs, "Fourier's Series," *letter in Nature*, vol. 59, p. 606, 1899.

[157] M. Bocher, "Introduction to the theory of Fourier's series," *Annals of Mathematics*, vol. 7, no. 3, pp. 81–152, Apr 1906.

[158] K. Raeen, "A study of the Gibbs phenomenon in Fourier series and wavelets," Master's thesis, University of New Mexico, 2008.

[159] A. Lange, "Analytische method zur berechnung elektromagnetischer und thermischer probleme in elektrische maschinen," Ph.D. dissertation, Technische Universität Braunschweig, 2000.

[160] G. Watson, *A treatise on the theory of Bessel functions*, 2nd ed. Cambridge University Press, 1966.

[161] S. J. Salon, M. J. DeBortoli, and R. Palma, "Coupling of transient fields, circuits and motion using finite element analysis," *Journal of Electromagnetic Waves and Applications*, vol. 4, no. 11, pp. 1077–1106, 1990.

[162] F. W. Carter, "Air-gap induction," *Electrical World and Engineering*, vol. XXXVIII, pp. 884–888, 1901.

[163] A. Krings, “Iron losses in electrical machines,” Ph.D. dissertation, KTH Royal Institute of Technology, 2014.

[164] K. Oberretl, “13 Rules to minimize stray load losses in induction motors,” *Oerlikon Bulletin*, no. 389/390, pp. 2–12, 1969.

[165] K. Oberretl, “New facts about parasitic ttorque in squirrel cage induction motors,” *Oerlikon Bulletin*, no. 348, pp. 130–155, 1962.

[166] B. Heller and V. Hamata, *Harmonic Field Effects in Induction Machines.* Elsevier Scientific Publishing Company, 1977.

[167] R. H. Park, “Two-reaction theory of synchronous machines: Generalized method of analysis,” *Trans. AIEE*, vol. 48, no. 3, pp. 716–727, Jul 1929.

[168] J. Haataja, “A comparative performance study of four-pole induction motors and synchronous reluctance motors in variable speed drives,” Ph.D. dissertation, Lappeenranta University of Technology, 2003.

[169] R. L. J. Sprangers, J. J. H. Paulides, B. L. J. Gysen, and E. A. Lomonova, “Towards magnetic saturation in semi-analytical harmonic modeling,” *IEEE Trans. Magn., under review*, 2015.

[170] R. L. J. Sprangers, J. J. H. Paulides, K. O. Boynov, J. Waarma, and E. A. Lomonova, “Comparison of two anisotropic layer models applied to induction motors,” in *Proc. of IEMDC 2013*, Chicago, IL, USA, May 2013, pp. 701–708.

[171] R. L. J. Sprangers, J. J. H. Paulides, B. L. J. Gysen, and E. A. Lomonova, “A fast semi-analytical model for the slotted structure of induction motors with 36/28 stator/rotor slot combination,” in *Proceedings of Electrimacs 2014*, May 2014, pp. 209–214.

[172] R. L. J. Sprangers, J. J. H. Paulides, B. L. J. Gysen, and E. A. Lomonova, “A fast semi-analytical model for the slotted structure of induction motors,” *Elsevier Mathematics and Computers in Simulation, under review.*

[173] R. L. J. Sprangers, B. L. J. Gysen, J. J. H. Paulides, J. Waarma, and E. A. Lomonova, “Calculation of induced rotor current in induction motors using a slotted semi-analytical harmonic model,” in *Proceedings of the XXIth International Conference on Electrical Machines (ICEM)*, September 2014.

[174] R. L. J. Sprangers, J. J. H. Paulides, B. L. J. Gysen, J. Waarma, and E. A. Lomonova, “Semi-analytical framework for synchronous reluctance motor analysis including finite soft-magnetic material permeability,” *IEEE Trans. Magn., accepted.*

[175] G. Crevecoeur, P. Sergeant, L. Dupré, L. Vandenbossche, and R. Walle, “Analysis of local material degradation near cutting edges of electric steel sheets,” *IEEE Trans. Magn.*, vol. 44, no. 11, pp. 3173–3176, Nov 2008.

[176] N. H. Vrijsen, “Magnetic hysteresis phenomena in electromagnetic actuation systems,” Ph.D. dissertation, Eindhoven University of Technology, 2014.

[177] Y. Amara, J. Wang, and D. Howe, “Stator iron loss of tubular permanent-magnet machines,” *IEEE Trans. Ind. Appl.*, vol. 41, no. 4, pp. 989–995, Jul/Aug 2005.

Samenvatting

Towards Increased Understanding of Low-Power Induction and Synchronous Reluctance Machines

Harmonic Modeling of Complex Electromagnetic Phenomena

Door de toenemende rol van elektronica in onze maatschappij neemt de wereldwijde vraag naar elektrische energie toe. Deze uitdagende trend vereist een significante toename in de elektriciteitsproductie, bij voorkeur uit hernieuwbare energiebronnen. Naar verwachting zal het aandeel van dergelijke bronnen in 2040 toenemen tot één derde van de wereldwijde energie productie. In de tussentijd moet de beschikbare elektrische energie zo efficiënt mogelijk gebruikt worden, zodat de druk op bestaande productiefaciliteiten afneemt. Daarnaast zorgt dit er ook voor dat de kosten voor de eindgebruiker binnen de perken blijven.

Naar schatting wordt tussen de 43% en 46% van de mondiaal geproduceerde elektrische energie omgezet naar mechanische energie door middel van systemen die aangedreven worden door elektrische motoren. Om de energetische efficiëntie van zulke systemen te verbeteren zijn wereldwijd minimum energy performance standards (MEPS) gedefinieerd. Deze MEPS forceren elektromotorfabrikanten tot het herzien van bestaande motortechnologieën, zoals inductiemotoren (IMs), of het omarmen van andere motortechnologieën, zoals permanent-magneet synchroonmotoren (PMSMs) of synchrone reluctantiemotoren (SynRMs). Tijdens het ontwerp van zulke motoren is de beschikbaarheid van snelle, nauwkeurige en betrouwbare rekenmodellen van fundamenteel belang. Om het gat tussen sterk vereenvoudige analytische modellen en tijdrovende numerieke modellen te dichten wordt de ontwikkeling van semi-analytische modellen, gebaseerd op een harmonische modelleringstechniek, besproken in dit proefschrift. Het werk richt zich in het bijzonder op het harmonische modelleren van het magnetisch veld in de vertande structuren van inductie- en synchroon-reluctantiemotoren.

In Hoofdstuk 2 wordt een uitbreiding van de bestaande magnetische veldoplossing voor een 2D polair coördinaatsysteem gepresenteerd. De nieuwe fomulering neemt peripherale variaties van de magnetische permeabiliteit mee in de veldoplossing en vertegenwoordigt daarmee een belangrijke stap voorwaarts ten aanzien van het modelleren van magnetische saturatie. Bestaande methoden voor het harmonische modelleren van vertande structuren, te weten Anisotropic Layer Theory (ALT)

en Mode-Matching Theory (MMT), worden vergeleken met de nieuwe methode, welke aangeduid wordt als Inhomogeneous Region Modeling (IRM). Dit vergelijk is gebaseerd op resultaten verkregen voor een benchmark topologie. Het laat zien dat ALT voornamelijk geschikt is voor het modelleren van globale magnetische saturatie, terwijl MMT voornamelijk geschikt is voor het berekenen van lekflux en fluxverbuiging door vertanding. Daarentegen kan IRM voor beide doeleinden gebruikt worden. Echter, de resultaten laten ook zien dat de benodigde rekentijd van IRM ongeveer zeven keer langer is dan die van de traagste bestaande methode, namelijk MMT.

De implementatie van ALT en MMT modellen voor IM analyse wordt uitgebreid besproken in Hoofdstuk 3. Eén van de uitdagingen hierbij is de representatie van de motorgeometrie in het polaire coördinaatsysteem voor de MMT methode. Twee verschillende representaties worden geanalyseerd en de meest geschikte wordt geïdentificeerd. Verder wordt ook de berekening van de fundamentele fluxdichtheid in de luchtspleet, de gekoppelde flux en het elektromagnetisch koppel voor elke methode uitgelegd. De resultaten van de berekeningen worden gevalideerd ten opzichte van 2D Finite Element Analysis (2D FEA) berekeningen voor vier benchmark inductiemotoren, en laten een goede overeenkomst zien.

Om de inductiemotoren ook onder belasting te kunnen analyseren worden in Hoofstuk 4 twee verschillende aanpakken beschreven voor het berekenen van de geïnduceerde stroom in de rotorstaven. De eerste aanpak maakt gebruik van een equivalent circuit voor één rotorstaaf. De parameters van dit circuit vertegenwoordigen de geïnduceerde spanning in de rotorstaaf door de statorexcitatie en de synchrone inductie van de rotorstaaf door het magnetisch veld van de rotor. De waarden van deze parameters worden berekend met het MMT model in twee rekenstappen, zodat tijdens de derde rekenstap de geïnduceerde stroom in de rotorstaaf indirect kan worden bepaald. Voor de tweede aanpak wordt gebruik gemaakt van een directe koppeling tussen het magnetisch model en elektrische circuitmodellen van de volledige stator- en rotorwindingen. Beide methodieken worden gevalideerd ten opzichte van 2D FEA in termen van geïnduceerde stroom en elektromagnetisch koppel voor verschillende bedrijfstoestanden, en laten een zeer goede overeenstemming zien.

In Hoofdstuk 5 wordt de implementatie van een semi-analytische structuur voor prestatie-analyse van IM gepresenteerd, gebaseerd op een combinatie van de ALT en MMT modellen. Het MMT model wordt gebruikt om parameters te bepalen die de lekflux en fluxverbuiging beschrijven, welke worden uitgedrukt in termen van lekinductie en de Carter factor. Verder wordt het ALT model gebruikt voor het bepalen van de globale verzadigingstoestand van de motor en worden de resultaten van het MMT model aan het ALT model geknoopt met behulp van een aangepast circuitkoppeling. Door meerdere lagen van het ALT model te gebruiken, elk met een andere rotorpositie, kan ook verdraaiing van de rotor worden meegenomen. Tenslotte worden de resultaten van berekeningen aan vier benchmark motoren vergeleken met de resultaten van FEA simulaties en metingen. Dit vergelijk laat zien dat de nauwkeurigheid van de semi-analytische berekeningen acceptabel is, alhoewel afwijkingen in de materiaaleigenschappen leiden tot verschillen ten opzichte van de meetresultaten.

Als laatste wordt in Hoofdstuk 6 een semi-analytisch model voor analyse van SynRMs gepresenteerd, gebaseerd op IRM. De polaire representatie van de geometrie wordt besproken en richt zich op het gelijkhouden van de gemiddelde breedte en positie van de fluxbarrières in de rotor. Verder wordt ook de berekening van het elektromagnetisch koppel, de d- en q-as inductie en de d- en q-as gekoppelde flux beschreven. De berekeningen worden gevalideerd ten opzichte van 2D FEA simulaties voor een benchmark SynRM topologie. Deze validatie laat zien dat de gekozen polaire representatie leidt tot afwijkingen in de schatting van de d-as parameters, terwijl de verkregen q-as parameters goed overeen komen met de FEA resultaten.

Dankwoord

Een promotieonderzoek vergt tijd, inspanning en doorzettingsvermogen. Nu ik het einde ervan bereikt heb, kan ik terugkijken op een viertal mooie jaren, waarin ik veel geleerd en gedaan heb en mezelf regelmatig tot het uiterste heb gedreven. Gedurende dit traject zijn er veel mensen geweest die me gesteund, geholpen en gemotiveerd hebben. Daarom wil ik gráág de gelegenheid nemen om deze personen hartelijk te danken voor hun bijdrage.

Allereerst wil ik mijn dank betuigen aan Elena, voor het herkennen van mijn capaciteiten en voor het vertrouwen dat ze mij gegeven heeft gedurende het gehele PhD onderzoek. Tijdens onze vele voortgangsgesprekken was je altijd erg geïnteresseerd in zowel mijn professionele als persoonlijke ontwikkelingen, wat ik als erg prettig ervaren heb. Ik ben dankbaar voor alle discussies die we hebben mogen voeren, omdat deze vaak tot nieuwe ideeën en inzichten hebben geleid.

Johan, jou wil ik graag bedanken voor alle begeleiding die je me gedurende ruim twee jaar van mijn PhD gegeven hebt. Met je ervaring, creativiteit en positieve instelling heb je me geholpen richting te geven aan mijn werk, hetgeen mij extra gemotiveerd heeft in de uitvoering ervan. Ik heb veel van je kunnen leren, zowel op het technische als op het niet-technische vlak. Ook wil ik graag Bart Gysen bedanken voor de ondersteunende begeleiding, met name op het gebied van harmonisch modeleren. Jouw kennis en ervaring hebben mij geholpen de theorie beter te begrijpen. Tenslotte wil ik Konstantin Boynov bedanken voor zijn bijdrage in de begeleiding en de invulling van mijn PhD project.

I would also like to express my gratitude to the other members of my defense committee, prof. dr. J. Pyrhönen, prof. dr. M.J. Kamper, dr. ir. M.C. van Beurden and Dr.-Ing A. Lange, for their time and effort to read, and comment on, my thesis.

Een belangrijk onderdeel van een promotieonderzoek zijn de personen waar je dagelijks mee omgaat. Ik wil graag al mijn kamergenoten, te weten Maarten, Sultan, Yang, Bart, Koen, Kevin, Bob, Dave, Marko en Hans, hartelijk danken voor de fijne tijd die zij mij bezorgd hebben. Naast alle zinnige discussies was er ook altijd ruimte voor grappige, schunnige en vaak flauwe humor, wat een mooie afleiding heeft geboden van het serieuze onderzoekswerk. Buiten mijn kamergenoten wil ik ook de rest van mijn collega's binnen de EPE groep danken voor de prettige jaren. Marijn, Rutger en Wim, jullie hulp bij het opzetten van mijn testopstellingen is erg waardevol geweest. Ben Bron, bedankt voor je inzet als student onder mijn supervisie.

Ik wil ook graag grote dank uitspreken naar Vostermans Ventilation B.V. voor hun vertrouwen in mij en de vakgroep. Onze samenwerking heb ik altijd als zeer prettig ervaren en het heeft mij de mogelijkheid gegeven om naast theoretische ervaring ook praktische ervaring op te doen. In het bijzonder wil ik Jeroen Waarma, Raymond van As en Henk Vostermans bedanken.

Buiten het werk om heb ik ook veel steun gehad aan familie en vrienden. Ik wil hen daarom allen bedanken voor alles wat zij voor mij betekend hebben, zowel bewust als onbewust. Speciale dank betuig ik aan mijn ouders, Gerard en Magda, voor hun onvoorwaardelijke liefde, hulp en steun die ik al mijn hele leven mag ontvangen. Zij hebben mij de mogelijkheid gegeven te worden wie ik nu ben. Verder wil ik ook mijn zus Loes en broer Bas bedanken voor de fijne band die we altijd hebben gehad. Tenslotte bedank ik mijn schoonouders, Henk en Joke, voor alle ondersteuning die jullie de afgelopen jaren in en rondom huis hebben geboden.

Als laatste wil ik nog graag een woordje kwijt aan mijn eigen gezin. Angela, we hebben in de laatste jaren samen veel meegemaakt, vaak mooie dingen en soms ook minder mooie. Ik ben je onmetelijk dankbaar voor het begrip dat je altijd getoond hebt wanneer ik weer eens 's avonds of in het weekend moest doorwerken. Dankzij jou heb ik me nooit druk hoeven maken over het 'thuisfront', zodat ik me volledig op mijn werk kon concentreren wanneer dat nodig was. Revy, je bent nog te jong om het je te realiseren, maar jij bent het grootste wonder dat ik tot nu toe heb mogen meemaken. Bedankt voor alle keren dat je me hebt, en zult, laten lachen.

Allen bedankt!

Author biography

Ruud Sprangers was born on October 17th, 1986 in Waspik, The Netherlands. After finishing his secondary school at Dr. Mollercollege in Waalwijk, he started studying Electrical Engineering at Eindhoven University of Technology in 2004. He received his B.Sc. degree in 2009. During his master program at the same university, he did an internship at the Austrian Institute of Technology in Vienna, where he worked on modeling of demagnetization phenomena in permanent magnet synchronous machines. Finally, he received his M.Sc. degree in Electrical Engineering in 2011, after graduating on the development of an expert system for three-phase induction motor design.

From May 2011, he started his Ph.D. research at the Electromechanics and Power Electronics group of the Eindhoven University of Technology, in cooperation with Vostermans Ventilation B.V. The results of this research are presented in this dissertation. He was also the first author of eight conference publications and four journal publication. One additional journal publication is currently under review.